

Photoluminescence Enhancement of Ge Quantum Dots by Exploiting  
the Localized Surface Plasmon of Epitaxial Ag Islands

by

Dexin Kong

A Dissertation Presented in Partial Fulfillment  
of the Requirements for the Degree  
Doctor of Philosophy

Approved June 2015 by the  
Graduate Supervisory Committee:

Jeffery Drucker, Chair  
Tingyong Chen  
Robert Ros  
David Smith

ARIZONA STATE UNIVERSITY

August 2015

## ABSTRACT

This dissertation presents research findings regarding the exploitation of localized surface plasmon (LSP) of epitaxial Ag islands as a means to enhance the photoluminescence (PL) of Germanium (Ge) quantum dots (QDs). The first step of this project was to investigate the growth of Ag islands on Si(100). Two distinct families of Ag islands have been observed. “Big islands” are clearly faceted and have basal dimensions in the few hundred nm to  $\mu\text{m}$  range with a variety of basal shapes. “Small islands” are not clearly faceted and have basal diameters in the 10s of nm range. Big islands form via a nucleation and growth mechanism, and small islands form via precipitation of Ag contained in a planar layer between the big islands that is thicker than the Stranski-Krastanov layer existing at room-temperature.

The pseudodielectric functions of epitaxial Ag islands on Si(100) substrates were investigated with spectroscopic ellipsometry. Comparing the experimental pseudodielectric functions obtained for Si with and without Ag islands clearly identifies a plasmon mode with its dipole moment perpendicular to the surface. This observation is confirmed using a simulation based on the thin island film (TIF) theory. Another mode parallel to the surface may be identified by comparing the experimental pseudodielectric functions with the simulated ones from TIF theory. Additional results suggest that the LSP energy of Ag islands can be tuned from the ultra-violet to the infrared range by an amorphous Si ( $\alpha$ -Si) cap layer.

Heterostructures were grown that incorporated Ge QDs, an epitaxial Si cap layer and Ag islands grown atop the Si cap layer. Optimum growth conditions for distinct Ge dot ensembles and Si cap layers were obtained. The density of Ag islands grown on the

Si cap layer depends on its thickness. Factors contributing to this effect may include the average strain and Ge concentration on the surface of the Si cap layer.

The effects of the Ag LSP on the PL of Ge coherent domes were investigated for both  $\alpha$ -Si capped and bare Ag islands. For samples with low-doped substrates, the LSPs reduce the Ge dot-related PL when the Si cap layer is below some critical thickness and have no effect on the PL when the Si cap layer is above the critical thickness. For samples grown on highly-doped wafers, the LSP of bare Ag islands enhanced the PL of Ge QDs by  $\sim 40\%$ .

## ACKNOWLEDGMENTS

First, I would like to thank my supervisor, Dr. Jeff Drucker, for giving me this opportunity to work in his group. Dr. Drucker's expertise, attitude to research, and patience significantly benefit my professional life. Aside from being an excellent researcher, he is a great friend-like mentor. Under his guidance, I have gained enormous knowledge and skills in experimental solid state physics.

I would also like to express my sincere appreciation to Dr. Dave Smith, Dr. Robert Ros and Dr. Tingyong Chen for serving on my dissertation committee. A special thanks to Dr. Smith for all TEM characterization. I would like to thank Christian Poweleit for the assistance in all photoluminescence and Raman measurements, and to Grant Baumgardner for his help with electronics in the lab. I also want to thank Dr. Maxim Sukharev for the useful discussion.

I would like to thank my current group members Chad Lunceford, Mark Wirth, Emanuel Borcean, Shantanu Das and former group members Dr. SomilKumar Rathi and Michael Christiansen for their encouragement and support.

Many colleagues, co-works and friends have helped me in various ways. I would like to thank them all for their help and support. I am obliged to Zhaofeng Gan, Patrick Bookjans, Harn Chi Lim, Olaf Schulz, Liying Jiang, Chufeng Li and Xinyang Wang. Their help made my research life more fun.

It would be extremely difficult for me to accomplish the PhD without my wife's support, understanding and encouragement. I would like to express my great appreciation to my wife, Xiuli Zhao, for her love and sacrifice. I am thankful to my parents for their support.



Finally, I acknowledge the funding for the research work. The research project described in this dissertation is supported by National Science Foundation under award DMR 1005958.

# TABLE OF CONTENTS

	Page
LIST OF TABLES .....	iv
LIST OF FIGURES .....	v
CHAPTER	
1 INTRODUCTION .....	1
1.1 Background and Motivation .....	1
1.2 Epitaxial Ge/Si(100) Quantum Dots .....	4
1.2.1 Quantum Dot.....	4
1.2.2 Growth of Epitaxial Ge/Si(100) Quantum Dots .....	6
1.2.3 Coarsening Mechanisms During Post-growth Annealing .....	14
1.2.4 Dot Morphology Evolution During Si Capping .....	15
1.2.5 Novel Properties of Ge/Si(100) Quantum Dots .....	18
1.2.5.1 Electronic Properties.....	18
1.2.5.2 Optical Properties .....	20
1.3 Epitaxial Ag/Si(100) Islands .....	24
1.3.1 Growth of Ag/Si(100) Islands .....	25
1.3.2 Nucleation and Kinetics.....	27
1.3.3 Plasmonic Properties of Ag Nanoparticles .....	31
1.3.4 Applications of Localized Surface Plasmon Resonance .....	37
2 EXPERIMENTAL METHODS .....	41
2.1 Introduction .....	42
2.1.1 Molecular Beam Epitaxy Systems .....	42

CHAPTER	Page
2.1.2 Sample Characterization.....	43
2.2 Small Molecular Beam Epitaxy and Calibrations.....	44
2.2.1 Small Molecular Beam Epitaxy System .....	44
2.2.2 Bake out Procedure for the Small Molecular Beam Epitaxy System.....	47
2.2.3 Calibrations and Sample Preparation .....	48
2.3 SVTA MBE System and Components .....	52
2.3.1 SVTA MBE System .....	52
2.3.1.1 Load Lock Chamber .....	52
2.3.1.2 Prep/Ag Chamber and Components.....	56
2.3.1.3 Growth Chamber and Components.....	60
2.3.2 Bake out Procedure and Degassing.....	68
2.3.3 Calibration of Sources .....	70
2.4 Growth Procedure of Epitaxial Heterostructure .....	72
2.4.1 Wafer Cleaning .....	73
2.4.2 Substrate Degassing and Growth Preparation.....	76
2.4.3 Si Buffer Layer, Ge Quantum Dot, Si Cap Layer Growth .....	78
2.4.4 Ag Island Growth.....	81
2.4.5 Amorphous Si Layer Growth .....	81
2.5 Sample Characterization .....	81
2.5.1 Atomic Force Microscopy.....	82
2.5.2 Rutherford Back Scattering .....	83

CHAPTER	Page
2.5.3 Scanning Electron Microscopy .....	85
2.5.4 Transmission Electron Microscopy.....	87
2.5.5 Photoluminescence .....	87
2.5.6 Spectroscopic Ellipsometry .....	90
2.5.7 X-ray Photoelectron Spectroscopy .....	91
2.5.8 Raman Spectroscopy .....	92
3 RESULTS AND DISCUSSION .....	94
3.1 Ag/Si(100) Epitaxial Island Growth .....	95
3.1.1 As-grown Ag/Si(100) Islands.....	96
3.1.2 Growth Temperature Annealing.....	107
3.2 Tuning the Localized Surface Plasmon of Ag/Si(100) Islands .....	116
3.2.1 Bare Ag/Si(100) Islands .....	117
3.2.1.1 The Mie Theory .....	117
3.2.1.2 Thin Island Film Thoery.....	127
3.2.2 Ag/Si(100) Islands Capped With an $\alpha$ -Si Layer.....	138
3.3 Ag Growth on Si-capped Ge/Si(100) .....	140
3.3.1 Ge/Si(100) Quantum Dot Growth .....	141
3.3.2 Si Capping of Ge Quantum Dots .....	147
3.3.3 Ag Growth on Si Cap Layer.....	154
3.4 Effect of Ag Localize Surface Plasmon on the Photoluminescence of Ge Dots .....	164
3.4.1 Photoluminescence of Ge Quantum Dots .....	165

CHAPTER	Page
3.4.1.1 Photoluminescence of a Ge Quantum Well.....	165
3.4.1.2 Photoluminescence of Flattened Ge Coherent Domes .....	169
3.4.1.3 Solving the Non-uniform Photoluminescence Intensity Problem .....	173
3.4.2 Effect of Localized Surface Plasmon of Capped Ag Islands .....	176
3.4.3 Effect of Localized Surface Plasmon of Bare Ag Islands .....	186
4 CONCLUSIONS AND FUTURE WORK .....	195
4.1 Epitaxial Ag Island Growth on Si(100).....	196
4.2 Tuning the Localized Surface Plasmon of Ag/Si(100) Islands .....	198
4.3 Growth of the Heterostructure .....	200
4.4 Plasmonic Effect of Ag Islands on the Photoluminescence of Ge Quantum Dots .....	203
REFERENCES.....	210

## LIST OF TABLES

Table		Page
1	Existing Island Types on Samples Grown to the Indicated Coverages on Si(100) Heated to 500 °C. N = No Islands; S = Small Islands Only; B, S = Big and Small Islands .....	106

## LIST OF FIGURES

Figure		Page
1.1	Schematic of the Three Film Growth Modes. (a) Frank-van Der Merwe (FvdM) or Layer-by-layer Growth, (b) Volmer-Weber (V-W) or 3D Island Growth and (c) Stranski-Krastanov (S-K) or Layer Plus Island Growth. ....	8
1.2	Schematic of the Strain Effect During Ge Growth on Si. Both Si and Ge Crystallize in the Diamond Cubic Structure, but with Different Lattice Constants ( $a_{\text{Ge}}=5.65 \text{ \AA}$ and $a_{\text{Si}}=5.43 \text{ \AA}$ ). Initially, Ge Grows Pseudomorphically with the In-plane Lattice Constant of the Ge Film Compressed to Match That of the Si Substrate. The Ge Lattice Constant Normal to the Interface Increases. ....	9
1.3	AFM Images of Different Ge/Si(100) Quantum Dot Morphologies. (a) Huts and Pyramids, (b) Domes, and (c) Dislocated Domes. Height Profiles along the Indicated Lines in the Individual AFM Images Are Shown in (d). The Line Scans Are All along $\langle 100 \rangle$ . ....	11
1.4	Summary of Facet Evolution During Ge/si(100) Quantum Dot Growth by Deposition of Pure Ge. Facet Evolution along $\langle 100 \rangle$ and $\langle 110 \rangle$ Directions Through the Dot Center Is Displayed. The Vertical Position of Horizontal Bars Represents the Contact Angle of Dominant Facets to the Si(100) Substrate. The Horizontal Extent of These Bars Indicates the Size Range for Each Morphology. This Figure Is Adapted from [18]. ....	12

Figure	Page
1.5	<p>XTEM Images of Domes Capped with Si Deposited at <math>T = 300\text{ }^{\circ}\text{C}</math> (a), <math>450\text{ }^{\circ}\text{C}</math> (B) and <math>550\text{ }^{\circ}\text{C}</math> (C). It Clearly Shows That Growing the Si Cap Layer at Above <math>450\text{ }^{\circ}\text{C}</math> Causes a Drastic Flattening of Ge Dots. This Figure Is Adapted from Ref. [55]. ....</p>
1.6	<p>Schematics of Two Possible Band Alignments in Semiconductor QDs. The Conduction and Valence Band Edges Across the QD from A to A' as Indicated in the Top Figure Are Shown in (a) and (b). (a) Is the Type I Band Alignment for Which Both Electrons and Holes Are Confined in the QD. (b) Shows the Type II Band Alignment, Which Occurs for Strained Ge/Si(100) QDs. Note That the Reduction of Both the Conduction Band (Cb) and Valence Band (Vb) Edges at the QD Boundary Is Strain Induced. For Ge/si(100) QDs, Electrons Are Confined to the Tensile Strained Si Adjacent to the QD, and Holes Are Confined in the Ge QD. ....</p>
1.7	<p>A Typical Si-capped Ge QD Photoluminescence (PL) Spectrum, Adapted from Ref. [71]. The Ge QDs Were Grown by Depositing 5 ML of Ge at <math>630\text{ }^{\circ}\text{C}</math>. ....</p>
1.8	<p>SEM Image of Ag Islands Grown on Si(111) (a). The Scale bar Is <math>10\text{ }\mu\text{m}</math>. (b) Shows a SEM Micrograph of Ag Islands Grown on Si(100). The Scale Bar is <math>1\text{ }\mu\text{m}</math>. Note That Ag/Si(111) Islands Have Hexagonal Bases, While Ag/(100) Islands Have Rectangular Bases. These Two SEM Images Are Adapted from Ref. [115]. ....</p>



Figure	Page
1.9	Schematic of Atomic Process Responsible for Island Nucleation Adapted from Ref [118]. ..... 28
1.10	Schematics of Bulk, Surface and Localized Surface Plasmons Are Shown in (a), (b) and (c), Respectively. In (b), Only the <i>p</i> -polarized Component of Incident Light Contributes to the Excitation of a Surface Plasmon Propagating along the <i>x</i> -direction at the Infinite Interface Between Dielectric ( $\epsilon_d$ ) and Metal ( $\epsilon_m$ ). The <i>s</i> -component Is Perpendicular to the Incident Plane, as Shown in (b) the Black Dot Centered in the Circle. .... 32
1.11	(a) Illustration of PL Enhancement by the LSPR of a Metal NP Is Shown (Adapted from Fig. 1 of Ref. [132]). (b) Shows How the Enhancement Factor to Radiative Emission (top), Nonradiative Decay (middle) and to the Quantum Efficiency (Bottom) Depend on the Distance Between a CdS QD and an Au NP. They Are Adapted from Ref. [134] ..... 38
2.1	Schematic of the Small MBE System Employed for Ag Deposition. The Base Pressure in Growth Chamber Is about $2 \times 10^{-10}$ Torr. .... 45
2.2	Temperature vs. Sample Current Measured Using a k-type Thermocouple Bonded to the Back Side of the Resistively Heated Si Substrate and an Infrared Pyrometer in Both 1-color and 2-color Mode. The Emissivity Setting of the Pyrometer Was Set at 0.59 so That the Pyrometer Reading Matched That of the Thermocouple. The 3 Temperature Readings Agree to Within about 10 °C. .... 50

Figure	Page
2.3	Ag Deposition Rate vs. C-type Thermocouple Temperature. The Ag Coverage Was Determined by RBS. The Deposition Rate Monotonically Increases With Temperature. The Curve Is a Fourth Order Polynomial Fit to the Experimental Data Points. .... 51
2.4	MBE System Used for Heterostructure Growth. .... 53
2.5	Opposing Views of the MBE Loadlock With Various Components Labeled. 55
2.6	Different Views of the Prep/Ag Chamber With Various Components Labeled. .... 57
2.7	Schematic of Prep/Ag Chamber Stage Showing Detail of C-ring Support That Accepts Mo Wafer Blocks. .... 59
2.8	Views of the Growth Chamber With Various Components Labeled. .... 61
2.9	Two-pocket E-gun Employed for Si Deposition. (a) External View. (b) Shows the Two-pocket E-gun Removed from the Chamber for Maintenance With Various Components Labeled. .... 64
2.10	Schematic of Quartz Crystal Microbalance (QCM) Assembly. .... 66
2.11	Main Features of the Sample Stage. Adapted from SVTA Operation Manual. .... 67
2.12	The Normalized RBS Spectrum for a Si/Cu Film Deposited onto Si Used for Calibrating the Si E-gun Deposition Rate. The Black Curve Is the Raw RBS Data and the Red Curve Is the RUMP Simulation. The Best Match Was Obtained for a Si Layer 92.6 nm-thick Atop a Cu Layer 150 nm-thick. .... 71

Figure	Page
2.13	Schematic of a Typical Heterostructure Showing the Buffer Layer, Ge Dot Layer, Epitaxial Si Cap Layer, Ag Island Layer and $\alpha$ -Si Layer. .... 73
2.14	(a) Growth Timing Diagram for a Typical Sample. T Is the Substrate Temperature, and Si (Ge) Represents Si (Ge) E-gun Power. (b) Plots Log Files Generated by Robo MBE Corresponding to the Timing Diagrams in (a). .... 79
2.15	A Schematic Showing the Basic Components of a Standard AFM. .... 83
2.16	Schematic of RBS Main Chamber. $\alpha$ Particles Are Scattered from the Sample and Are Collected by Detector. By Analyzing the Energy Loss of The Scattered Particles, the Mass Spectrum of the Target Material Can Be Easily Generated. ....84
2.17	Schematic of a Typical SEM Column. This Diagram Is Adapted from Ref [143]. .... 86
2.18	Schematic of PL System. Most PL Spectra Were Acquired Using the Nd: YAG Laser. Some Were Acquired Using the HeCd Laser to Determine the Effect of Excitation Energy on the PL Spectra of Our Samples. .... 89
2.19	Schematic of Ellipsometry Measurement Geometry. .... 91
3.1	Scanning Electron Micrographs of Ag Islands Formed by Depositing 5.3 ML Ag at 2.1 ML/min onto Si(100) Heated to 300 °C. (a) Clearly Shows Two Distinct Classes of Islands. The Big Islands Are Clearly Faceted and Their Bases Are Aligned along $\langle 110 \rangle$ . The Big Islands Shown Have Rectangular Bases. The Small Islands Are Not Clearly Faceted. Note the Zone

	Surrounding the Big Islands That Is Denuded of Small Islands. The Width of This Denuded Zone Is Comparable to the Average Spacing Between the Small Islands. (b) Shows That the Big Islands Form With a Variety of Basal Shapes. The Five Distinct Shapes Are Identified in the Image: S (Square), R (Rectangular), T (Triangular), TT (Truncated Triangular) and I (Irregular). Individual Higher Resolution ( $1\ \mu\text{m} \times 1\ \mu\text{m}$ ) Images of Examples of Each of These Island Types Are Shown Below Fig. 1(b). ....	98
3.2	Height Profiles of Small (a) and Big (b) Islands Obtained from Typical Islands along the Indicated Lines in the Inset AFM Images. These Islands Are from the Same Sample Depicted in Fig. 1. The Small Islands Are Not Clearly Faceted and Appear Mound-like While the Big Island Is Clearly Faceted. These Morphologies Are Typical of Big and Small Islands for the Range of Growth and Annealing Conditions Investigated. ....	99
3.3	Island Size Distributions for Big Islands Formed via Deposition of 5.3 ML Ag at 2.1 ML/min onto Si(100) Heated to the Indicated Temperatures. Note the Vertical Scale Change at $T \geq 350^\circ\text{C}$ . At These Higher Growth Temperatures, the Data Have Been Multiplied by the Indicated Factors. For Example, the Maximum in the Areal Density for $T=350^\circ\text{C}$ Is $1.8 \times 10^6$ Islands/ $\text{cm}^2$ . The Increase in Average Size as Growth Temperature Increases Is Expected for Islands Formed via Nucleation and Growth. The Size Plotted on the Horizontal Axis Is the Square Root of the Island Area Measured from SEM Images. The Vertical Axis Plots the Island Areal Density in Islands/ $\text{cm}^2$	

Figure	Page
Using 10 nm Wide Bins. ....	102
3.4 Areal Density for Both Big and Small Islands vs. Inverse Temperature. The Linear Dependence of the Big Island Density in the Semilogarithmic Arrhenius Plot Indicates that the Big Islands Form via a Nucleation and Growth Mechanism With a Nucleation Energy of 0.73 eV. The Small Island Density Does Not Vary Systematically over the 300 – 500 °C Range, Suggesting That They Form via Some Alternate Mechanism. The Error Bar Is about the Size of the Plot Symbols. ....	103
3.5 Size Distributions for Small Islands Grown by Depositing 5.3 ML Ag at 2.1 ML/min onto Si(100) Heated to the Indicated Temperatures. The Size Plotted on the Horizontal Axis Is the Cube Root of the Island Volume Measured from AFM Images. ....	105
3.6 Areal Density of Big and Small Islands vs. Anneal Time for Both Big and Small Islands. The Apparent Increase in Small Island Density With Anneal Time Is Within the Scatter of Small Island Densities Observed in As-grown Samples. The Big Island Density Increases With Increasing Anneal Time. ....	108
3.7 Average Size of Small Islands vs. Anneal Time for 5.3 ML Ag Deposited at 2.1 ML/min onto Si(100) Heated to 400 °C and Annealed for the Indicated Times. The Small Island Density Does Not Vary Monotonically With Anneal Time. The Error Bars Are 1 Standard Deviation Long. The Size Was	

Figure	Page
Calculated Using the Cube Root of Island Volume Measured from AFM Images. ....	109
3.8 Size Distributions for Big Islands Grown by Depositing 5.3 ML of Ag at 2.1 ML/min onto Si(100) Heated to 300 °C (a) and 400 °C (b) and Annealed for the Indicated Times at the Growth Temperatures. The Average Island Sizes Decrease and the Island Areal Density Increases With Increasing Anneal Time. ....	111
3.9 The Shape Evolution of All 5 Families of Big Ag Islands Is Shown Here. It Shows That the Fraction of Each Family Islands Varies as the Anneal Progresses. ....	113
3.10 These Figures Are Double y-axis Plots With Annealing Time as x Axis. The Average Length $\langle L \rangle$ and Width $\langle W \rangle$ Are Plotted on the Right y Axis, and the Average Aspect Ratio $\langle L/W \rangle$ Is Plotted on the Left y Axis. Irregular Islands Essentially Disappear after One Hour of Annealing, so Their Shape Evolution Could Not Be Investigated over the Same Time Scale as for the Other Islands. (a), (b), (c) and (d) Show the Shape Evolution of Square, Rectangular, Triangular and Truncated Triangular Islands, Respectively. The Legend for All Panels of This Figure Is Shown in (a). ....	115
3.11 The Calculated LSPRs of a Prolate Spheroid from Mie Theory Are Plotted Against the Aspect Ratio, Defined as $a/b$ . The LSPRs of the Prolate Spheroid in Vacuum Are Plotted as Solid Curves, and the LSPRs of the Prolate Spheroid Embedded in Si Are Plotted as Dotted Curves. Blue Indicates	

Figure	Page
the Plasmon Mode Associated With Short Axes ( $z$ or $y$ ), and Red Indicates the Plasmon Mode Associated With Long Axis ( $x$ ). The Schematic of a Prolate Spheroid Is Shown in the Inset Figure. ....	119
3.12 (a) Shows a Scanning Electron Micrograph of Ag Islands With an Average Size of 25 nm, Which Are Called Smaller Big (SB) Islands. (b) Shows a SEM Image of Ag Islands With an Average Size of 100 nm, Which Are Called Bigger Big (BB) Islands. ....	122
3.13 (a) and (b) Show the Real and Imaginary Parts of the Pseudodielectric Functions Measured Using Spectroscopic Ellipsometry. The Red Curves Are the Dielectric Function of the Si Substrate. The Blue Curves Are the Measured Pseudodielectric Functions of SB Ag Islands on Si. The Green Curves Are the Measured Pseudodielectric Functions of BB Ag Islands on Si. The Incident Angle Used for Measurement Is $70^\circ$ . ....	124
3.14 (a) Shows the Comparison Between Experimental Ag-related Features (Dots) and Theoretical Calculation from Mie Theory by Approximating Ag Islands as Prolate Spheroids. (b) Shows the Schematic of a Ag Prolate Spheroid on Top of Si. The Experimental Ag Plasmon Features Are Determined by Simply Comparing the Pseudodielectric Functions of Samples Having Ag Islands on Si With That of Si the Substrate, and These Plasmonic Features Are Indicated in Fig. 3.13. ....	126

Figure	Page
3.15	(a) Shows the Schematic of an Oblate Spheroid. The Surface of the Si Substrate Is in the $x$ - $y$ Plane, and the $z$ Direction Is Perpendicular to the Substrate. (b) Shows the Schematic of the 3 Simulated Films. .... 130
3.16	(a) and (b) Show the Real and Imaginary Part of the Simulated Pseudodielectric Functions, Respectively. The Red Curves Are for the Si Substrate. The Blue Curves Are Simulated With the In-plane Parallel Plasmon Modes Turned off. The Green Curves Are Simulated With Perpendicular Plasmon Modes Turned off. (c) and (d) Compare the Real and Imaginary Part of the Experimentally Measured and Best-fit Simulated Pseudodielectric Function. The Simulated Pseudodielectric Functions Are Plotted in Blue, Experimentally Measured Are Plotted in Green and the Si Dielectric Function Is Plotted in Red. .... 137
3.17	(a) and (b) Show SEM Images of SB and BB Ag Islands Capped With 30 nm $\alpha$ -Si Layer. (c) and (d) Show the Imaginary Part of Experimental Pseudodielectric Functions for Samples With SB Ag Islands and BB Ag Islands, Respectively. In Both (c) and (d), the Red Curves With Circular Markers Are for Bare Ag Islands on Si, the Red Curves With Square Markers Are for the Si Substrate, the Blue Curves with Circular Markers Are for The $\alpha$ -Si Capped Ag Islands on Si, and the Blue Curves With Square Markers Are for the $\alpha$ -Si Capped Layer on Si. .... 139
3.18	An AFM Image of a Si Buffer Layer Is Shown in (a), Which Is a 3 $\mu\text{m}$ by $\mu\text{m}$ Scan. The Crystallographic Orientation of the AFM Image Is Indicated in (a).



Figure	Page
The Height Profile of the White Line as Indicated in (a) Is Shown in (b). It Clearly Shows the Step Height Is ~0.2 nm. ....	141
3.19 The AFM Images of a Series of Samples Grown at 550 °C Under Identical Deposition Rate of 2.7 ML/min. All of These 4 Images Have the Same Size, and the Scale Bar Is Shown in (a). The Ge Coverage Corresponding to (a), (b), (c) and (d) Are 5.6 ML, 5.9 ML, 6.3 ML and 6.8 ML, Respectively. ..	143
3.20 AFM Images of a Series of Samples Grown at 600 °C With an Identical Deposition Rate of 2.7 ML/min. All of These Images Are 1 µm by 1 µm. The Scale Bar Is Shown in (a). The Ge Coverage Corresponding to (a), (b), (c) and (d) Are 5.6 ML, 5.8 ML, 6.2 ML and 6.6 ML, Respectively. ..	146
3.21 The AFM Images of Si Cap Layer Grown at 550 and 600 °C Are Shown Here. (a) and (c) Show 10 nm and 15 nm Capping for Huts Only Ensembles Grown at 550 °C, Respectively. (b) and (d) Show 10 nm and 20 nm Si Cap Layer on Domes Only Ensembles Grown at 600 °C, Respectively. They Share the Same Scale Bar as Shown in (a). ....	149
3.22 Both (a) and (b) Show Cross Sectional TEM Images. (a) Is a TEM Image of a Sample Comprised Solely of Domes ( $1.1 \times 10^9 / \text{cm}^2$ ) Before Capping With 30 nm of Si Grown at 600 °C. There Are No Domes Remaining after Capping Using This recipe. (b) Displays the Structure of a Domes-only Sample ( $1.1 \times 10^9 / \text{cm}^2$ ) Capped With 20 nm of Si Grown Using the Second Cap Layer Growth Recipe. During Si Cap Layer Growth, Sample Temperature	

Figure	Page
Was Dropped from 600 to 500 °C as Quickly as Possible. Domes Are Still Evident after Cap Layer Growth. ....	151
3.23 AFM Images of Si Cap Layers With a Series of Thicknesses, 5 nm in (a), 10 nm in (b), 15 nm in (c) and 20 nm in (d). These AFM Images Share the Same Scale Bar as Shown in (a). The Si Cap Layer Was Grown With the New Recipe, Which Is to Drop the Substrate Temperature from 600 to 500 °C as Quickly as Possible. The Minimum Cap Layer Thickness That Produces an Atomically Flat Surface Is 15 nm. ....	153
3.24 SEM Images of Ag Islands Grown on Top of the Si Cap Layer Are Shown Here. These 4 SEM Images Share the Same Scale Bar as Shown in (a). The Ag Island Growth Conditions for the Samples Corresponding to These 4 SEM Images Is Identical. 9.6 ML of Ag Was Deposited on the Si Cap Layer at 450 °C. For Each Sample, the Ge Dots Were Grown Identically. 6.6 ML of Ge Was Deposited at 600 °C. The Thickness of the Si Cap Layer Corresponding to (a), (b), (c) and (d) Is 20, 15, 10 and 5 nm, Respectively. ....	156
3.25 Typical UV Raman Spectrum Acquired from the Sample With a 10 nm Thick Si Cap Layer Grown With New Lower Temperature Recipe. The Blue Curve Is the Best Fit Lorentzian to the Experimental Data. ....	159
3.26 XPS Spectrum Acquired from the Sample With a 10 nm Thick Si Cap Layer Grown Using the New Lower Temperature Recipe. The Elemental Peaks Are Indicated in the Figure. The Carbon and Oxygen Peaks Appear Due to	

Figure	Page
Exposure of Our Sample to Air. ....	160
3.27 The Dependence of Ag Island Density on the Thickness of Si Cap Layer Is Plotted in (a). (b) Is the Plot of Average Strain, Determined from UV Raman Spectroscopy, Against the Cap Layer Thickness. (c) Shows the Concentration of Ge on the Surface of the Si Cap Layer Is a Function of Cap Layer Thickness. ....	163
3.28 All PL Spectra in This Figure Were Acquired With 34 mW Excitation from a 532 nm Laser. The Samples Were at 10 K During Acquisition at 9 s Per Data Point With 2 mV Sensitivity. (a) Shows Spectra from a Series of Ge QWs Resulting from Si Capping of Ge QDs at the Dot-growth Temperature. In (a) the Red Spectrum Is for a Sample With a Ge QW That Resulted from Ge Domes Capped With 30 nm Si at 600 °C. The Blue Spectrum Was Acquired from a Sample With a Ge QW That Formed Due to Hut Flattening During 15 nm Si Cap Layer Growth at 550 °C. The Green Spectrum Was Acquired from a Reference Sample Grown Without Ge Deposition. The Uniformity of the PL Spectra from the Sample of Completely Flattened Domes Is Shown in (b). These Spectra Were Acquired at the Indicated Distance from the Center of the 4” Diameter Wafer. ....	167
3.29 These Spectra Were Taken from Different Spots on the Same Sample, at the Radial Distances from the Center Indicated in the Legend. 6.6 ML Ge Was Deposited on the Substrate at 600 °C, Which Generates Only Coherent	

Figure	Page
Domes. A 20 nm Thick Si Cap Layer Was Grown at 500 °C. The Spectra Were Acquired Using a 532 nm, 39 mW Laser. ....	172
3.30 (a) Shows a SEM Micrograph of the Boundary Between the Region Covered With Ag Islands and That With No Ag Coverage. The Schematic of Our Strategy to Solve Non-uniform PL Intensity Problem Is Illustrated in (b). PL Spectra Will Be Taken from Those 4 Spots as Indicated in (b), and They Will Be Horizontally Compared to Identify If the PL Intensity Is Uniform in 5 mm by 5mm Region. (c) Shows Two EDX Spectra Taken from Two Spots as Indicated in (a). The Red Spectrum Was Acquired from Spot 1 as Indicated in (a), and the Blue Spectrum Was Acquired from Spot 2 as Labeled in (a). Si K $\alpha$ is at 1739 eV, and Ag L $\alpha$ Is at 2980 eV. The Small Peak at 3500 eV Is the Sum of Si K $\alpha$ Peak Due to the Detection of Two Photons. ....	175
3.31 PL Spectra of Samples With Different Ge Dome Densities Are Shown. The Legend in Each Figure Describes the Sample Structure Corresponding to Each Spectrum. (a) Shows PL Spectra of Samples With a High Ge Dot Density of $3.5 \times 10^9$ /cm <sup>2</sup> . The Inset Figure in (a) Details the Ge Dot-related PL. (b) Plots the PL Spectra of Samples With a Low Ge Dot Density of $9 \times 10^7$ /cm <sup>2</sup> . The Inset Figure in (b) Details the Dot Related PL. These Spectra Were Acquired at 10 K Using 35 mW of 532 nm Laser Excitation, 20 mV Detector Sensitivity, and 9 Sec Per Data Point. ....	180

Figure	Page
3.32	<p>The Peak Ratio Is Defined as the Height (Area) PL Peak from the Spectra With Ag Island Divided by That of the Same Peak from Spectra Without Ag. The PL Peak Ratios of Ge Dots and Si Band-gap Transition Are Plot Against the Thickness of Epitaxial Si Cap Layer in (a), and Against the Fraction of Ag Island Area in (b). The Fraction of Area With Ag Islands in (b) Is Calculated from SEM Micrographs, by Taking the Summation of Ag Island Areas Divided by the Total Investigation Area. (b) Share the Same Legend as (a). Solid Curves With Circular (Red) and Upward Triangular (blue) Marks Are Peak Height Ratio for Ge Dot Related Peak and Si Band-gap Peak, Respectively. Dotted Curves With Square (Red) and Downward Triangular (Blue) Marks Are the Peak Area Ratio for Ge Dot Related Peak and Si Band-gap Peak, Respectively. ....</p> <p>183</p>
3.33	<p>This Figure Is to Show How the Effect of the LSPR of Bare Ag Islands Depends on the Thickness of Epitaxial Si Cap Layer and on the Fraction of Area With Ag Islands. The Definitions of Peak Ratio and Fraction of Area With Ag Islands Are Same as That in Fig. 3.32. The Legend Is Also Same as That in Fig. 3.32. ....</p> <p>189</p>
3.34	<p>The Results Shown in This Figure Are Conditional, Because They Are Not Reproducible at Different Conditions. (a) Shows the Spectra With Best Enhancement We Have Ever Got. (b) Shows the Peak Ratio of Ge Dots and Si Band-gap Transition Depends on the Fraction of Substrate Area Covered by Ag Islands. The Results Shown in (b) Are from the Samples Grown on</p>

highly Doped Si Wafers, $\sim 6 \times 10^9 / \text{cm}^3$ , Which Is Four Orders of Magnitude Higher Than the Wafers Used for Fig. 3.30. The Definition of Peak Ratio Is Same as That in Fig. 3.29. The Density of Ag Islands Corresponding Each Area Fraction Is Labeled on the Top $x$ Axis. ....	193
---	-----

## CHAPTER 1

### INTRODUCTION

#### 1.1 Background and Motivation

Silicon (Si) has dominated the semiconductor industry for more than four decades, mainly because of its excellent electronic properties for producing transistors and of its ability to easily form an  $\text{SiO}_2$  layer on its surface. The native  $\text{SiO}_2$  layer is an extremely high-quality dielectric film that can be used for isolation, passivation or as an active layer in the gate oxide. Si is the second most abundant material in the world, and billions of transistors can be integrated on a single wafer [1]. These low-cost, high-yield properties make Si ideal for the massive production of micro- and nano-electronic devices. Over 97% of semiconductor electronic devices are made from Si.

However, the low mobility of charge carriers and indirect interband transition in Si impede its successful application in the creation of Si-based optical and optoelectronic devices. It is possible to supplement Si with compounds of III-V (i.e., GaAs, GaN and InP), which exhibit high carrier mobility and have direct interband transitions. As a consequence, these materials are better candidates for building optoelectronic and microelectronic devices [2]. However, high cost, lack of a high-quality native oxide and practical deficiencies in making highly integrated circuits preclude III-V compounds from supplanting Si in the semiconductor industry. Proposals for making efficient Si-based optoelectronic devices include hybrid and monolithic optoelectronic integrated circuits [3]. Hybrid technologies integrate the optical material from Group III-V (or II-IV) with Si-based electronics. Monolithic refers to the integration of Si-based optoelectronics with only Group IV materials. Significant progress has been made in the

development of hybrid Si-based optoelectronics, but the technological challenge of combining materials from III-V with Si and the high cost of hybrid integration are obstacles that must be overcome before massive production of these devices are possible. However, the advantages of monolithic Si-based optoelectronics (i.e., easy integration of materials from Group IV with Si and low cost) continue to make this option attractive.

The topic of improving the optical properties of Si-based materials from Group IV has received a great deal of attention, and much work has been done in this field. Some studies have shown that modulation doping could promote higher mobility of charge carriers [4 – 7]. The principle of modulation doping is to physically separate the electrons from the donors so that scattering from the ionized impurities is weakened. Another approach is to utilize the coherent strain field to transform the electrical and optical properties [8 – 12]. New properties of low-dimensional nano-structures of Group IV semiconductors, such as quantum wells [13 – 15], nanowires [9,10,16,17] or quantum dots [18 – 20], have also been studied as possible means to improve the optical properties of Si-based devices. Due to their similar crystal structures, some Group IV nanostructures can be integrated with Si.

Self-assembled germanium (Ge) quantum dots (QD) on Si(100) are a promising solution for Si-based monolithic optoelectronic devices for the following reasons. Ge QDs can be epitaxially grown on Si(100), which is the substrate upon which current microchip technology is based. Ge QDs can be grown so that they are defect-free and have a narrow size distribution. These attributes are beneficial for technological applications to optoelectronic device or quantum computation. The fundamental growth



mechanism [21 – 24], electronic properties [25,26] and optical properties [27,28] of Ge QD have been studied for decades. It is fairly easy and low-cost to incorporate Ge QDs into Si-based electronics. The luminescence energy of epitaxial Ge QDs is in the technologically relevant low-loss transmission spectral region ( $\sim 1.5 \mu\text{m}$ ). However, the low luminescence efficiency of Ge QDs precludes their wide-ranging application.

The research presented in this dissertation is aimed at improving the luminescence efficiency of Ge QDs by employing the localized surface plasmon (LSP) of Ag nanoparticles (NPs). A LSP is the collective oscillation of free electrons in a metallic NP. LSPs can confine electromagnetic energy to a nanoscale region, which is far below the diffraction limit that precludes localization of visible light to regions smaller than its wavelength. Recent theoretical work predicts that the LSP of metallic NPs may significantly enhance the luminescence of semiconductor QDs, and the enhancement could be as large as two orders of magnitude [29]. By placing the QD in the vicinity of metallic NPs, the LSP can affect the luminescence efficiency of a QD. If the spacing between the QD and metallic NP is too small, the QD luminescence may be quenched. However, if the spacing is too large, the spontaneous emission rate of the QD may not be enhanced by the Purcell effect. Appropriate spacing between the QD and NP is an important factor for optimizing enhancement. Another equally important factor is that the LSP resonance energy should be closely matched with the exciton recombination energy of the QD [30,31]. Our strategy is to grow epitaxial Ag NPs on top of Si-encapsulated Ge QDs in order to improve the low luminescence efficiency of Ge QDs by utilizing the LSP of the Ag NP.

The following sections of this introductory chapter will discuss the fundamental growth physics, electronic properties and optical properties of epitaxial Ge QDs. The epitaxial growth of Ag NPs on the Si(100) surface and the plasmonic properties of metal NPs will also be described. Finally, the application of LSPs to enhance the optical performance of the QDs will be provided.

## **1.2 Epitaxial Ge/Si(100) Quantum Dots**

### **1.2.1 Quantum dots.**

Low-dimensional materials (2D, 1D and 0D) have attracted much attention since the early 1960s [32] because the electronic and optical properties of materials change significantly when their dimensions become comparable to the de Broglie wavelength. In these structures, quantum mechanics become important and the carrier energy levels can become quantized. It is known that the density of states (DOS) in bulk materials is continuous and proportional to  $E^{1/2}$ . However, the DOS of a low-dimensional structure is very different from 3D bulk materials. The DOS of a quantum well structure (2D) is a step-like function, and the quantum well already has found technological application in semiconductor lasers, which are part of every CD player [33]. The DOS of a 1D nanowire is saw-tooth shaped. Quantum dots provide potential confinement in all three dimensions, resulting in discrete atom-like energy levels. The QD has attracted much attention due to its promising potential for applications in optoelectronics and quantum information processing.

A simple model that illustrates confinement in a QD is the particle confined to a one-dimensional infinitely deep potential well. In this model, the confinement potential is

$$V(x) = \begin{cases} 0, (0 < x < a) \\ \infty, (x \geq a, x \leq 0) \end{cases} \quad (1.1)$$

By solving the Schrödinger equation for Eq 1.1, the energy levels are derived as

$$E(n) = n^2 h^2 / (8ma^2) , \quad (1.2)$$

where  $n$  is a positive integer,  $h$  is the Planck constant, and  $m$  is the particle mass. Due to quantum confinement, the energy levels are discrete. As the well width,  $a$ , increases, the gap between the energy levels becomes smaller, which redshifts the transition energy between the ground state and the first excited state. Conversely, the transition energy between the ground state and the first excited state blueshifts for smaller  $a$ . The spectroscopic response of a QD can be tuned by varying the size of the QD. The optical emission peak of an ensemble of quantum dots can be narrowed by making the size distribution of the QD ensemble sharper. The quantum confinement effect of the QD was experimentally confirmed by Ekimov and Onushenko [34].

There are several methods for forming QDs. These include the colloidal chemistry method, lithography and heteroepitaxial self-assembly. Each of these methods will be reviewed briefly. Colloidal QDs are formed using a wet chemical method. Colloidal QDs can have excellent size uniformity [35–37]. However, structural defects and difficulty of incorporating these QD into functional integrated circuits have limited their commercial applications [38]. Lithographic techniques are the most straightforward method for fabricating QDs with arbitrary size, shape and arrangement. However, these methods are complicated, time consuming and expensive. Furthermore, the etching process involved in lithography can result in significant damage to the QDs. Today, heteroepitaxial self-assembly is a popular method for forming QDs. Various sizes and shapes of

heteroepitaxial QDs can be created depending on the materials and growth conditions.

Defect-free QDs with sizes ranging from 10 to 100 nm can be formed easily.

Heteroepitaxial Ge QDs can also be integrated easily into Si-based electronics. This method is simple and compatible with existing integration technology.

Our Ge/Si(100) QDs were grown using the heteroepitaxial self-assembly method. The growth science and novel properties of Ge/Si(100) QD that are relevant to the present research will be discussed in the following sections.

### **1.2.2 Growth of epitaxial Ge/Si(100) quantum dots.**

There are three heteroepitaxial growth modes: Frank-van der Merwe (FvdM) [39], Volmer-Weber (V-W) [40] and Stranski-Krastanov (S-K) [41]. The FvdM mode refers to layer-by-layer growth, the V-W mode refers to island-only growth, and the S-K mode refers to layer-plus-island growth. Figure 1.1 presents schematics of all three modes.

In lattice-matched systems, film growth will be governed by three parameters: (i) the interfacial free energy between the substrate and the film ( $\sigma_{int}$ ), (ii) the surface energy of the film ( $\sigma_f$ ) and (iii) the surface energy of the substrate ( $\sigma_s$ ). If,  $\sigma_s < \sigma_{int} + \sigma_f$ , then 3D islands form immediately upon growth in order to minimize the surface area of the epi-layer. This situation is the V-W growth mode. On the other hand, if  $\sigma_s > \sigma_{int} + \sigma_f$ , then film growth follows either the FvdM mode or the S-K mode, depending on the material systems. For lattice matched systems, no elastic energy builds up as the film forms and the film grows in a layer-by-layer fashion following the FvdM mode

Another parameter, elastic energy, has to be considered in the case of lattice-mismatched systems. In the S-K mode, the sum of the surface energy of the film and the interfacial energy is also smaller than the substrate surface energy; therefore, the epi-

layer initially wets the substrate. However, the elastic energy accumulates as the epi-layer grows. The increase of elastic energy during the growth of the initial layer can drive the transition from layer-by-layer growth to 3D island growth after a certain “critical thickness” [41] is achieved. This is because the formation of 3D islands can relax some of the elastic energy at the cost of increasing surface energy. The growth of the Ge/Si(100) system follows the S-K growth mode.

Ge and Si have the same diamond cubic crystal structure, but with different lattice constants ( $a_{\text{Ge}}=5.65 \text{ \AA}$  and  $a_{\text{Si}}=5.43 \text{ \AA}$ ). The lattice mismatch between Ge and Si is 4.2%. Since the surface energy of Ge is lower than that of Si, the deposited Ge initially wets the Si substrate. Initially, a Ge film grows pseudomorphically on the Si substrate, which means that the Ge film is compressed to share the same in-plane lattice constant as Si. The in-plane compression in the Ge film causes an increase of lattice constant in the growth direction by a factor of Young’s modulus, as shown in fig. 1.2. The free energy of the coherent interface is small and is usually disregarded. Compared with the Ge film, the Si substrate is infinitely thick; therefore, the Si lattice constant is unaffected for pseudomorphic layer growth.

The transition to 3D island growth happens when the Ge pseudomorphic layer reaches  $\sim 3 \text{ ML}$  ( $1 \text{ ML}=6.78 \times 10^{14} \text{ atoms/cm}^2$  at the bulk terminated Si(100) surface). Coherent or defect-free Ge QDs initially form on top of the  $\sim 3 \text{ ML}$  wetting layer (WL) [42]. With further deposition, the strain energy of the coherent QD may become high enough to form dislocations.

The transition to 3D growth begins with formation of small 2D platelets on the  $\sim 3 \text{ ML}$  thick WL [42]. As additional Ge atoms are deposited, these 2D platelets rapidly

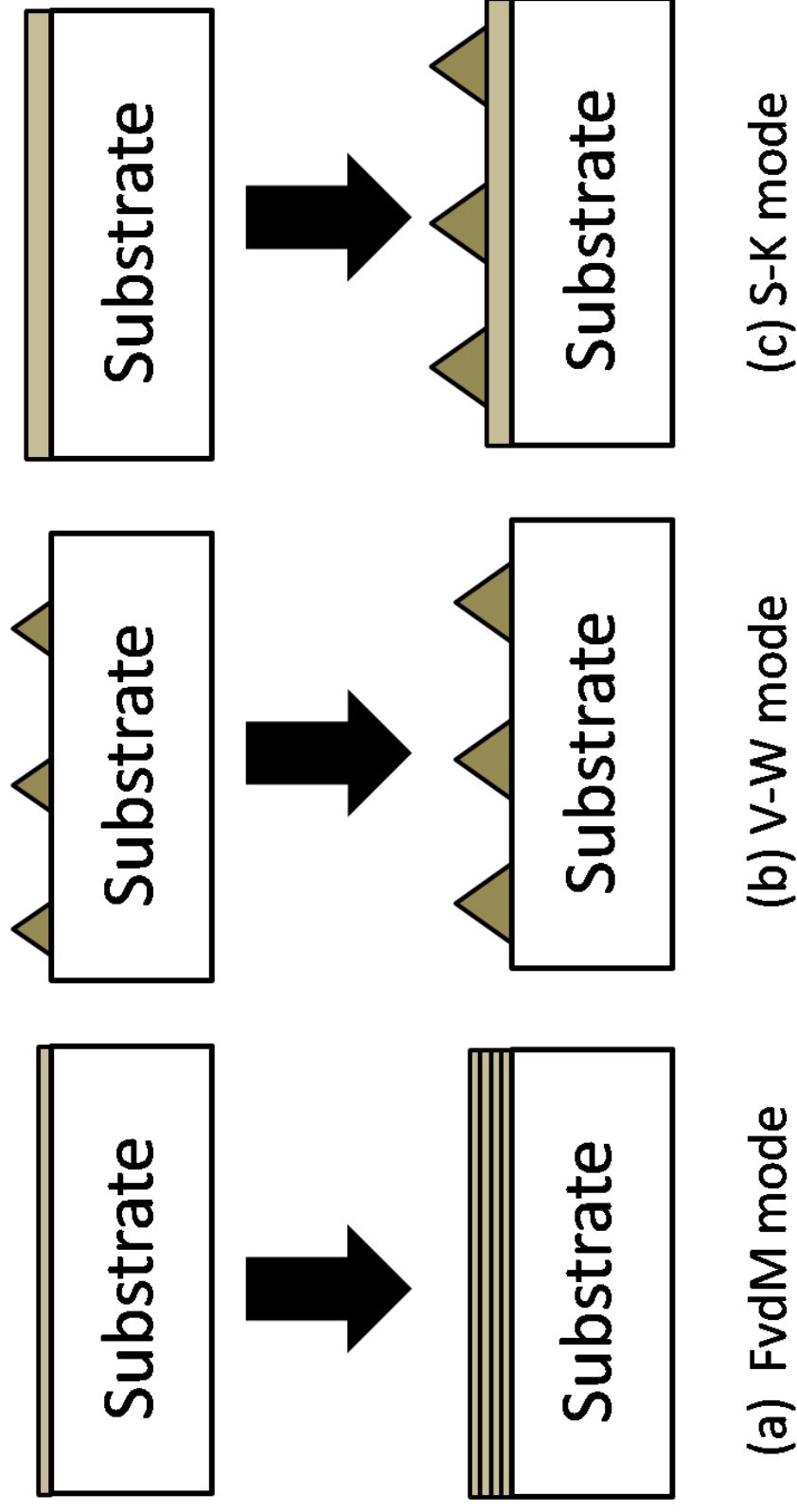


*Figure 1.1.* Schematic of the three film growth modes. (a) Frank-van der Merwe (FvdM) or layer-by-layer growth, (b) Volmer-Weber (V-W) or 3D island growth and (c) Stranski-Krastanov (S-K) or layer plus island growth.

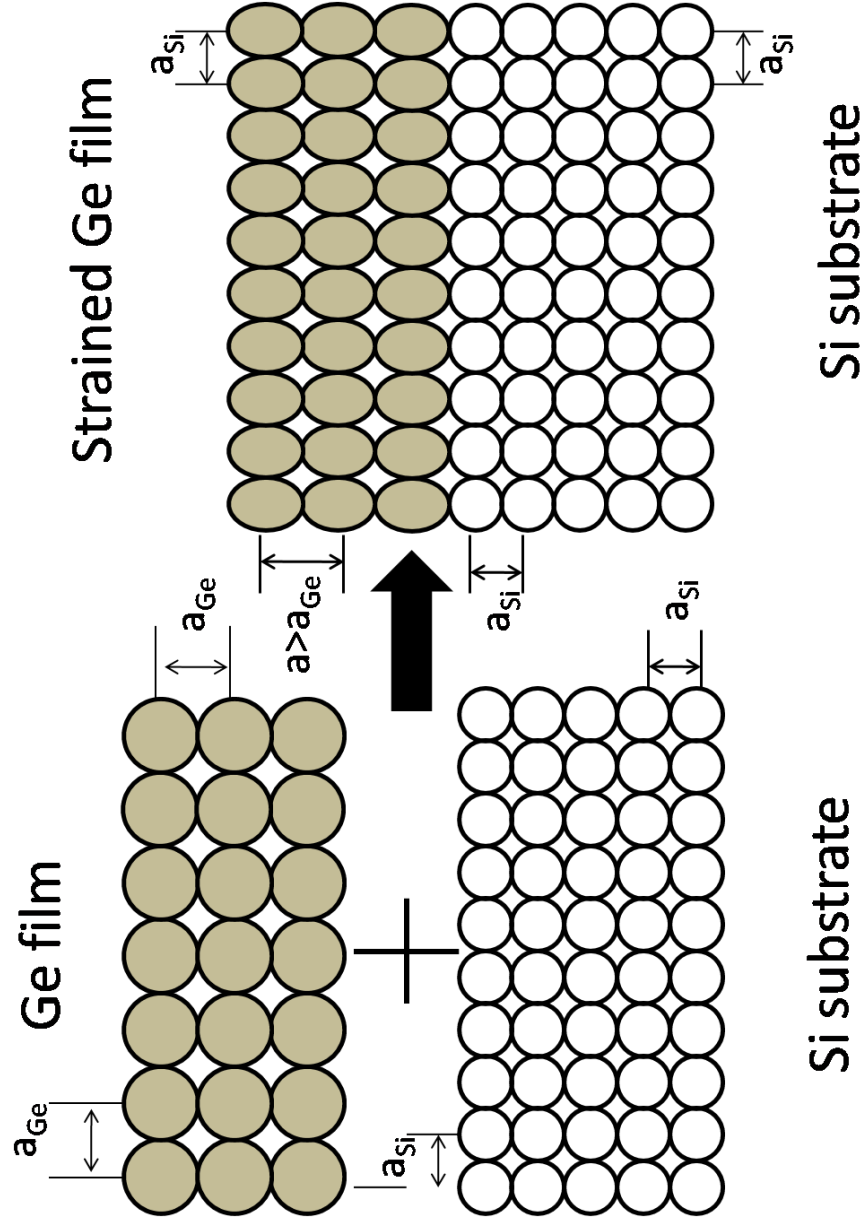


*Figure 1.2.* Schematic of the strain effect during Ge growth on Si. Both Si and Ge crystallize in the diamond cubic structure, but with different lattice constants ( $a_{\text{Ge}}=5.65 \text{ \AA}$  and  $a_{\text{Si}}=5.43 \text{ \AA}$ ). Initially, Ge grows pseudomorphically with the in-plane lattice constant of the Ge film compressed to match that of the Si substrate. The Ge lattice constant normal to the interface increases.

evolve into the so-called “prepyramid” clusters [43] with round bases and shallow contact angles ( $<11^\circ$ ). These clusters exist only when Ge coverage is between 3.5 and 4.0 ML [43]. The additional adatoms trapped by these clusters prefer to grow atop these clusters instead of sticking to the high strain energy sites at the island’s perimeter. Therefore, these clusters grow into islands with higher aspect ratios (an aspect ratio is defined as the ratio of height versus  $\frac{1}{2}$  width) as the Ge coverage increases. The first faceted islands formed on top of WL are bound by  $\{105\}$  facets.

Both rectangular-based huts [44] and square-based pyramids [45] are bound by four  $\{105\}$  facets that have a contact angle of  $11^\circ$  with the Si substrate. Figure 1.3 (a) shows an ensemble of huts and pyramids grown in our MBE system. These islands are defect-free, but the huts are metastable structures formed at lower temperatures. The huts transform to stable structures, i.e., pyramids, during post-growth annealing [45].

Further growth causes the huts and pyramids to transform into dome clusters. The morphology of a dome is shown in fig 1.3 (b), and the height profiles of the dome and pyramid are shown in fig 1.3 (d). These domes have octagonal bases and are multifaceted. In fig. 1.3 (d), it is clearly shown that the domes are bound by steeper facets, with a contact angle of  $\sim 25^\circ$  to the substrate. The dome facets that intersect the Si(100) surface along the  $\langle 110 \rangle$  direction are typically  $\{311\}$  facets, and those that intersect the substrate along the  $\langle 100 \rangle$  direction are close to  $\{102\}$ . Several other facets were observed in addition to these typical facets [46].

The evolution of facets during QD growth along the  $\langle 100 \rangle$  and  $\langle 110 \rangle$  directions is summarized in fig. 1.4, which is adapted from [18]. In early stages of growth, domes are coherent. But as they grow, dislocations form after the QD reaches a critical size to



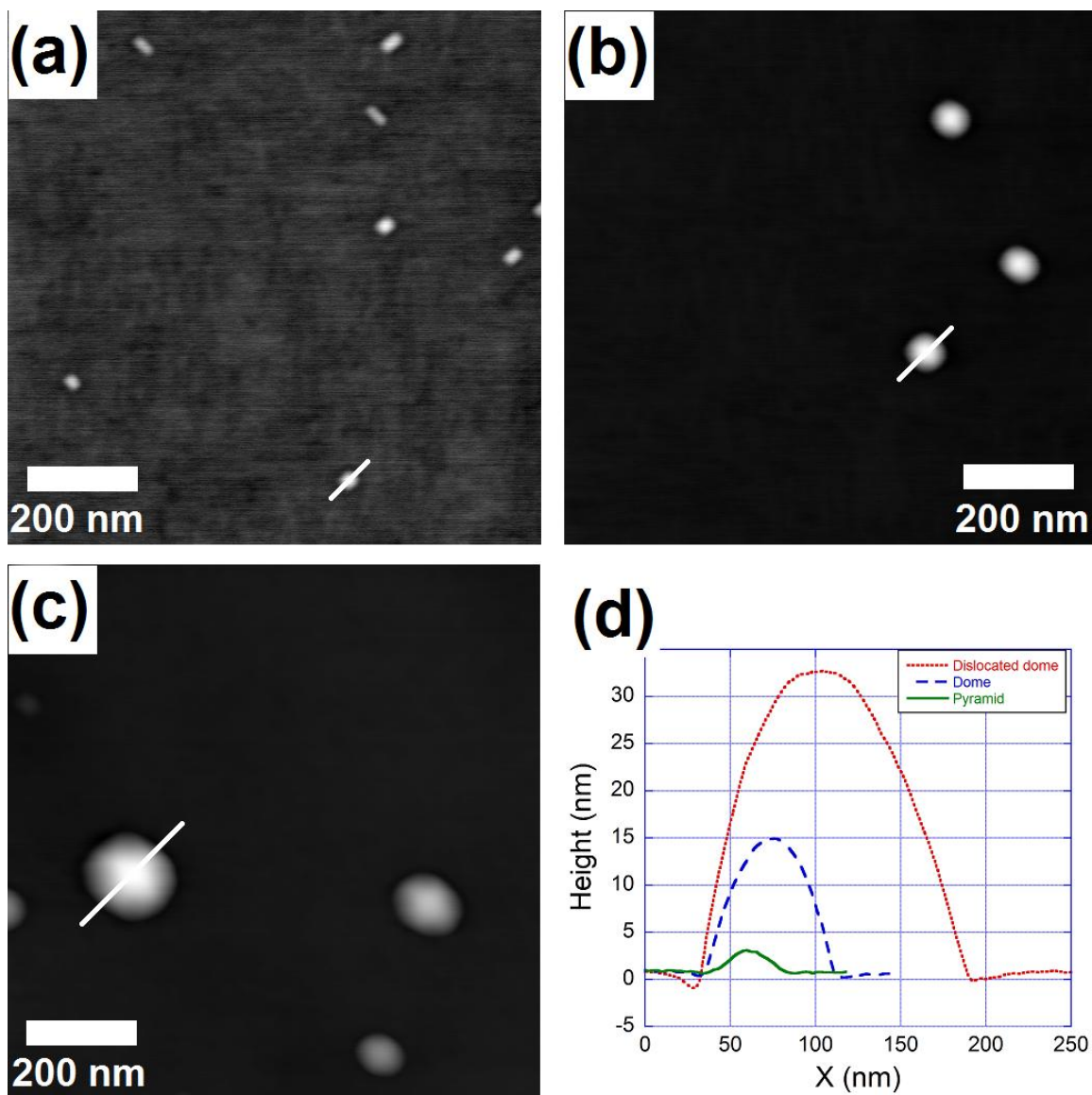


*Figure 1.3.* AFM images of different Ge/Si(100) quantum dot morphologies. (a) huts and pyramids, (b) domes, and (c) dislocated domes. Height profiles along the indicated lines in the individual AFM images are shown in (d). The line scans are all along  $\langle 100 \rangle$ .

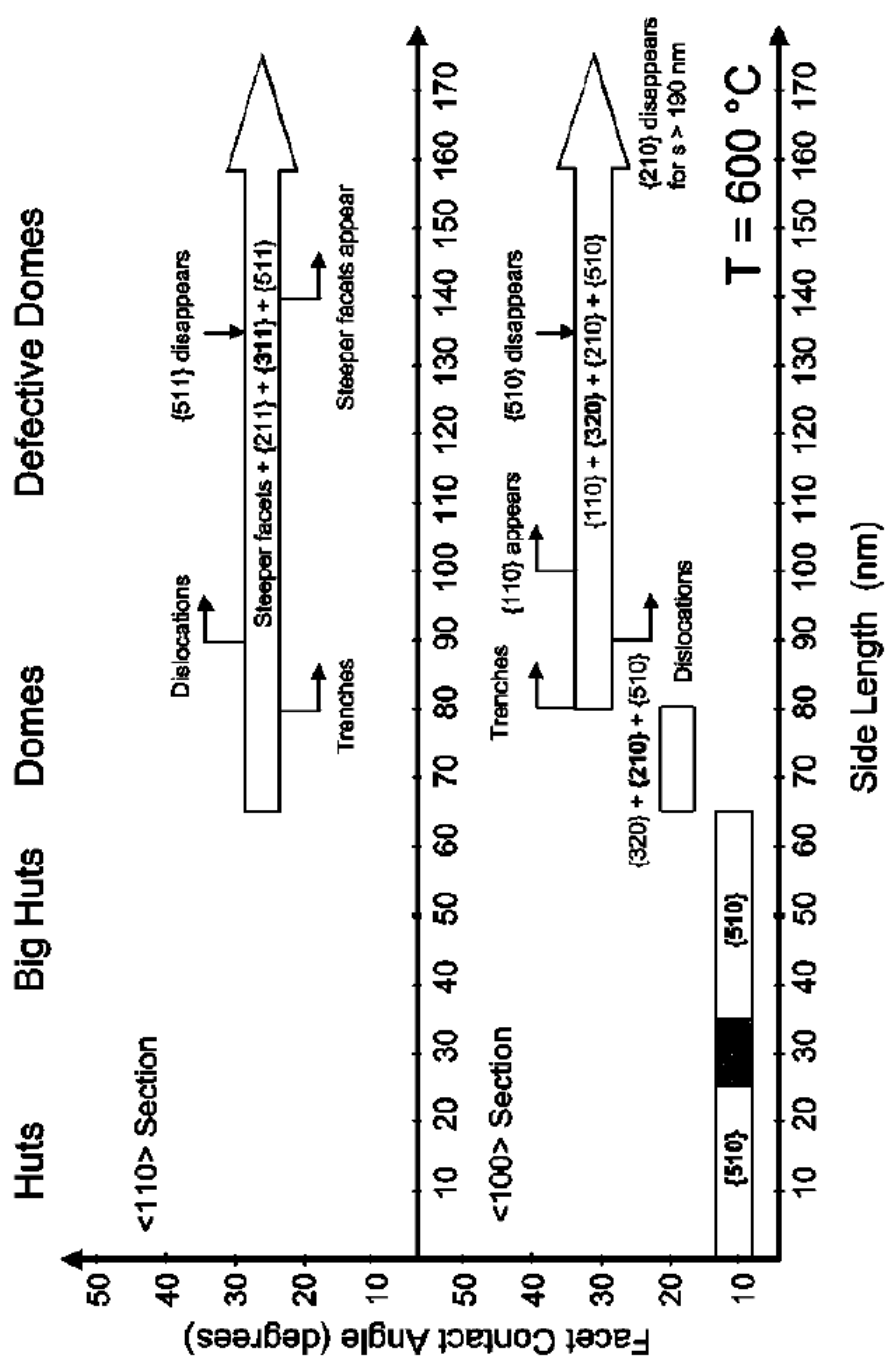


Figure 1.4. Summary of facet evolution during Ge/Si(100) quantum dot growth by deposition of pure Ge. Facet evolution along <100> and <110> directions through the dot center is displayed. The vertical position of horizontal bars represents the contact angle of dominant facets to the Si(100) substrate. The horizontal extent of these bars indicates the size range for each morphology. This figure is adapted from [18].

release some strain energy. The atomic force microscopy (AFM) image of fig. 1.3 (c) shows a dislocated dome, and fig. 1.3 (d) shows dislocated domes that are bound by even steeper facets. The chemical potential of the dislocated domes reduces dramatically, which results in a faster growth rate [47,48].

The morphology evolution of a Ge QD can be understood according to thermodynamics. The energy change that results from the shape change can be expressed as

$$\Delta E = \Delta E_{edge} + \Delta E_{surface} + \Delta E_{elastic}, \quad (1.3)$$

where  $\Delta E_{elastic}$  is negative because QD formation releases some of the strain energy and  $\Delta E_{surface}$  is positive because the surface area increases as the dot gets bigger.

All three of the terms in eq. 1.3 depend on the dot volume ( $V$ ) according to,  $\Delta E_{elastic} \propto V$ ,  $\Delta E_{surface} \propto V^{2/3}$ ,  $\Delta E_{edge} \propto V^{1/3}$ . These energies determine the dot shape during growth. In the earliest stages, pyramids have the lowest energy. As the pyramids grow, they transform into domes as they reach a critical volume, which is inversely proportional to the sixth power of misfit [49].

In summary, Ge/Si(100) QDs grow on top of a 3 ML-thick WL. The smallest QDs formed during the early stages of growth are huts and pyramids. As more Ge is deposited, the pyramids transform into coherent domes with larger contact angles to the substrate. When coherent domes reach a critical volume, dislocations form to release part of the accumulated strain energy. The chemical potential of the dislocated domes drops dramatically compared to the coherent domes, which results in a faster growth rate for the dislocated domes.

### 1.2.3 Coarsening mechanisms during post-growth annealing.

The size distribution of the Ge/Si(100) QDs also evolves during post-growth annealing, which could be useful for some technological applications. During post-growth annealing, these QD coarsen via three major mechanisms: Ostwald ripening, WL consumption and Si interdiffusion from the substrate to the QD [50–53].

Ostwald ripening is a coarsening mechanism that increases the average dot length scale. It is driven by the Gibbs-Thomson effect, which minimizes system free energy. The clusters with lower chemical potential grow at the expense of those with higher chemical potential, thus causing the latter to shrink and eventually disappear. For the Ge/Si(100) QD system, larger pyramids grow at the expense of smaller pyramids, coherent domes grow by consuming pyramids, and the size of dislocated domes increases at the expense of defect free domes [50,51]. Ostwald ripening occurs during post-growth annealing at temperatures  $\geq 400$  °C.

WL consumption during annealing is the second coarsening mechanism that happens at low temperatures (~450 °C range). In this temperature range, the diffusion of Ge atoms on the Si(100) surface is slow enough that the WL thickness exceeds the critical thickness of ~3 ML during deposition. These extra Ge atoms in the WL can be consumed by the dots with lower chemical potential. This coarsening mechanism will stop when the WL decays back to its equilibrium thickness (~ 3 ML).

The third coarsening mechanism of Si interdiffusion can occur when the annealing temperature is above 550 °C. Si atoms, can diffuse from the substrate into the Ge QD. This interdiffusion reduces the effective mismatch and results in larger dot sizes. The amount of Si interdiffusion is greater at the dot edge than at the center because the

strain is greater near the dot perimeter [51]. Si interdiffusion can even happen during dot growth if the growth temperature is  $\geq 550$  °C. Capellini et al. have reported that the average content of Si inside the dots increases from 0% at 550 °C to 72% at 850 °C [53].

When the annealing temperature is between 400 °C and 450 °C, Ostwald ripening and WL consumption can coexist. WL consumption is dominant for the rapid initial coarsening, but slower coarsening at longer annealing times occurs through Ostwald ripening [52]. Solely Ostwald ripening happens when the temperature is between 450 °C and 550 °C. As soon as the temperature goes beyond 550 °C, the Si interdiffusion and Ostwald ripening mechanisms coexist. Ostwald ripening of the SiGe alloy dots is dominant at annealing temperatures that are greater than 600 °C [52].

#### **1.2.4 Dot morphology evolution during Si capping.**

It is essential to embed the self-assembled QDs in a semiconductor matrix in order to apply them in optoelectronic devices. Encapsulating the QDs in a semiconductor matrix provides the confining potential for charge carriers, as well as surface passivation. For Ge/Si(100) QDs, the obvious choice for the matrix material is Si, which allows for the fabrication of multiple Ge/Si(100) layers [54]. Any change in dot composition and morphology during the Si capping process will affect the electronic and optical properties of the buried dot. Therefore, knowledge and control of the dot evolution is essential to obtain structures with predictable properties.

By employing cross-sectional transmission electron microscopy (XTEM), Rastelli et al. found that the shape of the initial as-grown dots can be practically preserved if the Si cap layer is grown at  $T < 300$  °C. They also found that dots become flattened if they are capped at higher temperatures ( $> 450$  °C) [55]. Dot flattening refers to an increase of base

area and a simultaneous decrease of height, as shown in fig. 1.5 (b) and (c). These figures were adapted from ref [55], which shows XTEM images of Ge dots that were capped at temperatures that range from 300 °C to 550 °C. Capping coherent domes with Si at 450 °C transforms them into truncated {105}-faceted pyramids with top surfaces that are bound by a large [100] facet. This reverse shape transition is caused by Si-Ge alloying [56]. The facets bounding capped Ge domes were carefully analyzed in ref. [55,56]. During Si capping, more Si atoms interdiffuse into the Ge QD, which causes a decrease in the Ge fraction and an increase in the Si fraction in the dots. This results in a smaller effective misfit ( $\varepsilon$ ). Since the critical volume ( $V_c$ ) for the pyramid-to-dome transition is inversely proportional to the sixth power of misfit ( $V_c \propto \varepsilon^{-6}$ ), the pyramid shape becomes energetically favorable and the domes transform into pyramids during Si capping.

It is known that the strain fields of the underlying dots can propagate through the Si cap layer. This effect can be exploited to template growth of the next Ge dot layer [54,57,58]. The strain modulation at the surface of the Si cap layer can be the driving force behind the directional migration of deposited Ge adatoms into areas with a stretched Si lattice constants (tensile strain), which causes vertical dot alignment.

Appropriate growth of the Si cap layer allows for the successful fabrication of multilayer dot stacks. By using self assembly methods, Schmidt et al. successfully grew stacked multilayers of dots, and the dots in different layers were vertically aligned for Si interlayer thicknesses of 12.5 and 25 nm [54]. They also found that perfect Ge dot position alignment can be achieved if the Si spacing layer is <25 nm. By setting the Si interlayer thickness at 10 nm, Mateeva et al. have grown up to 20 stacked dot layers with

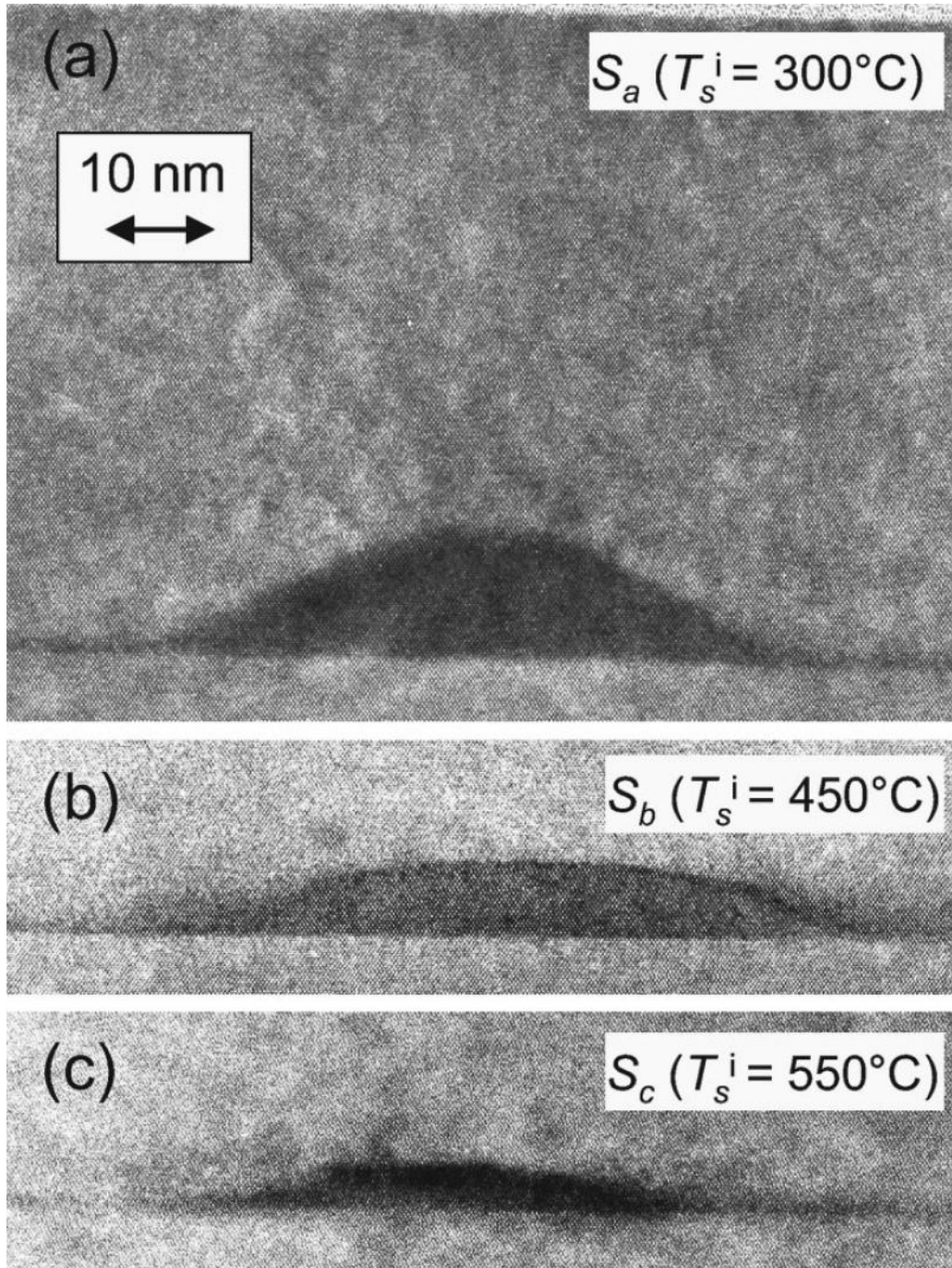


*Figure 1.5.* XTEM images of domes capped with Si deposited at  $T = 300^\circ\text{C}$  (a),  $450^\circ\text{C}$  (b) and  $550^\circ\text{C}$  (c). It clearly shows that growing the Si cap layer at above  $450^\circ\text{C}$  causes a drastic flattening of Ge dots. This figure is adapted from ref. [55].

perfect dot position alignment [58]. However, a tunneling effect may occur between stacked dot layers if the Si spacer layer is  $\leq 10$  nm, thus affecting the optical signal from the top layers [59]. The strain field propagated from the buried dots can also reduce the critical WL thickness, which can also affect the optical properties of the stacked dot layers [59].

Even though it is clear that the strain modulation on the surface of the Si cap layer can serve as a template for Ge dot growth, few investigators have addressed the effect of the strain field on Ag nucleation. Part of this project is to investigate this effect. The results will be discussed in Chapter 3.

### **1.2.5 Novel properties of Ge/Si(100) quantum dots.**

The electronic and optical properties of epitaxial Ge/Si QD have both attracted much attention due to their potential applications in Si-compatible integrated optoelectronic devices. Quantum confinement bestows novel electronic and optical properties on the Ge QD embedded in the Si matrix. In semiconductors, the knowledge of electronic properties helps to explain the optical properties. Therefore, the electronic band structure and charging behaviors of the Ge/Si QD embedded in a Si matrix will be described first.

#### ***1.2.5.1 Electronic properties.***

The interfacial band edge alignment determines the electronic and optical properties of the Ge/Si QD. Fig 1.6 shows the schematic of two main types of band alignment. Fig. 1.6(a) depicts type I band alignment, which corresponds to the band structure of III-V QD (e.g., InAs QD embedded in a GaAs matrix). Fig. 1.6(b) shows



type II strained Ge/Si(100) QD band alignment. Note that the reduction of the conduction band (CB) and valence band (VB) at the boundary of Ge QDs are strain induced.

Both electron and hole charging behavior for the Ge/Si QD system have been investigated over the last two decades. It is known that electrons and holes are confined

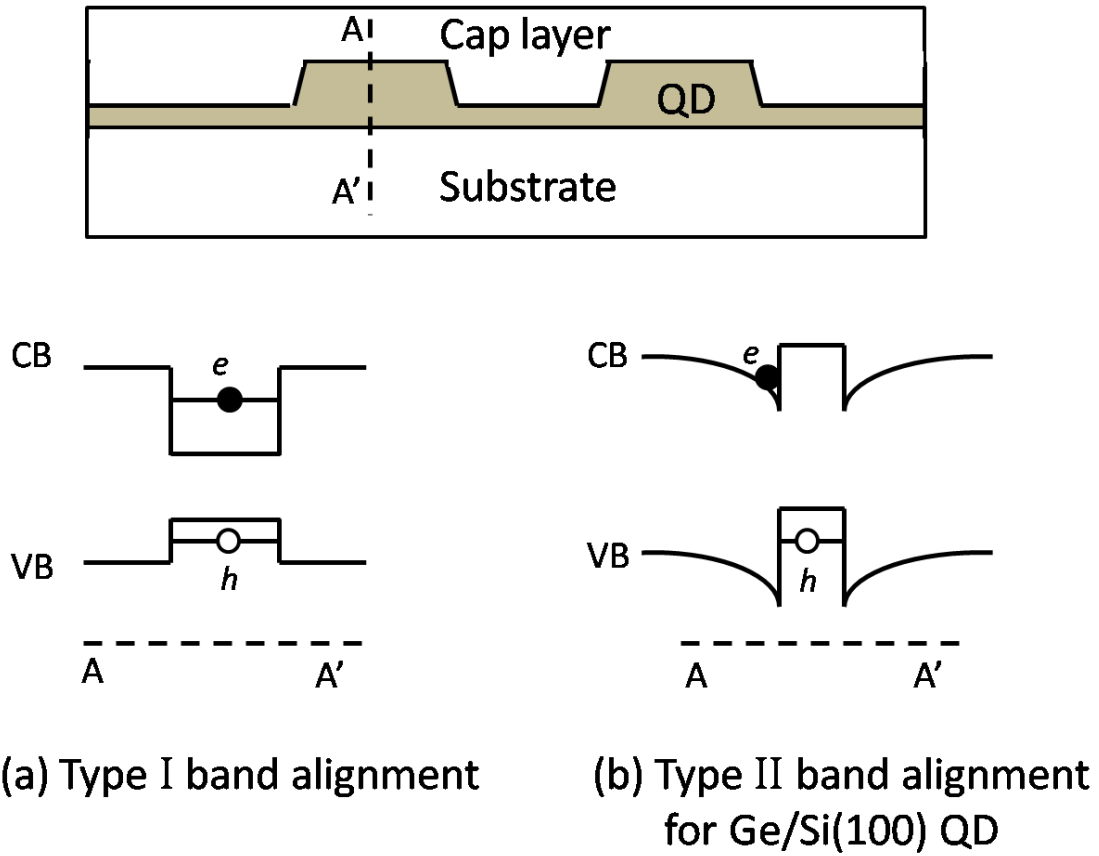


*Figure 1.6.* Schematics of two possible band alignments in semiconductor QDs. The conduction and valence band edges across the QD from A to A' as indicated in the top figure are shown in (a) and (b). (a) is the type I band alignment for which both electrons and holes are confined in the QD. (b) shows the type II band alignment, which occurs for strained Ge/Si(100) QDs. Note that the reduction of both the conduction band (CB) and valence band (VB) edges at the QD boundary is strain induced. For Ge/Si(100) QDs, electrons are confined to the tensile strained Si adjacent to the QD, and holes are confined in the Ge QD.

to different regions and are separated by a potential barrier created by the dots [60–62]. Electrons are confined to the tensile strained Si region adjacent to the dots where the conduction band has moved to lower energy by strain. Holes are confined in the Ge dots due to the higher valence band energy of Ge. The Ge/Si QD system exhibits different hole and electron charging behaviors. Hole charging was investigated extensively [63–66] before electron charging [67–70] because the small conduction band offsets make electron charging investigation more challenging. Zhang et al. showed that each hut cluster with a size of ~25 nm can contain 5–7 holes [63], but Ketharanathan et al. showed that each hut or pyramid confines ~0.7 electrons at room temperature [70]. For coherent domes with a size of ~70 nm, the density of hole states is dense and quasi-continuous [65,66]. However, only ~6 electrons can be confined in a dome cluster [70].

#### ***1.2.5.2 Optical properties.***

The optical properties of Ge QDs embedded in a Si matrix were studied extensively in the late 1990s and early 2000s using photoluminescence (PL) spectroscopy. Palange et al. [28] observed PL for uncapped Ge dots. However, the high surface-to-volume ratio of the dots and midgap Si and Ge surface states allow for the nonradiative recombination of excited electron-hole pairs, which quenches luminescence. Capping the Ge QD with an epitaxial Si layer allows for the characterization of Ge WL and dot-related luminescence.

Fig. 1.7 shows a typical PL spectrum of capped Ge/Si(100) QD, which is adapted from ref. [71]. The sample for this spectrum was grown at 630 °C, and the dots were capped with 150–170 nm Si. Two lines located at 0.998 eV and 0.942 eV in this spectrum are commonly attributed to the no-phonon assisted (NPA) and transverse-optical (TO)

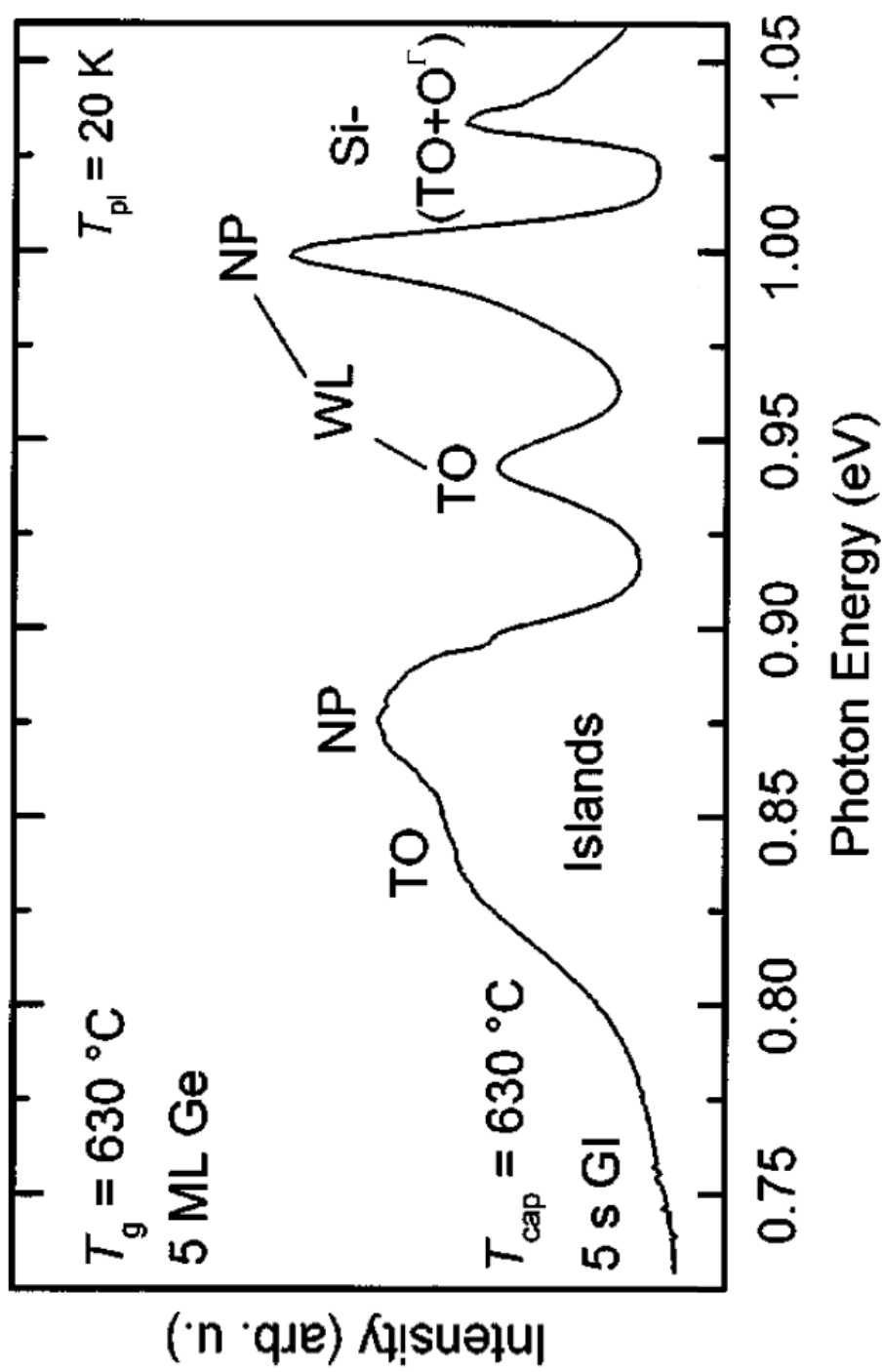


Figure 1.7. A typical Si-capped Ge QD photoluminescence (PL) spectrum, adapted from ref. [71]. The Ge QDs were grown by depositing 5 ML of Ge at 630 °C.

phonon replica of the WL. The energetic difference between these two lines is  $\sim 56$  meV, which is the Si-Si optical phonon energy [72]. The broad peak located around 0.85 eV originates from the Ge dots. This broad peak can be deconvolved into two Gaussian peaks that are attributed to dot-related NPA and TO lines, as indicated on the top of the broad peak in fig. 1.7. The energy difference between these two deconvolved PL lines is  $\sim 35$  meV, which corresponds to the Ge-Ge phonon energy [73].

PL of Ge films with different equivalent thicknesses grown on Si(100) – from the initial 2D WL to the growth of 3D dots – has been investigated systematically [74–76]. Prior to dot formation, it was found that both the NPA and TO lines from the WL red-shift as the WL thickness increases. This behavior can be explained by the reduced spacing between the quantum confined energy levels in a thicker quantum well (QW).

After dot formation, a broad dot related PL peak shows up at energies near 0.9 eV and then rapidly red-shifts and stabilizes at  $\sim 0.85$  eV as the dots grow. The PL lines from the WL blue-shift to the expected values for a 3-ML-thick Ge layer because the initial stages of dot formation consume the uncompleted fourth layer. Other researchers have reported qualitatively similar behavior [77,78].

It is understood that epitaxial Si-cap layer growth can drastically modify the morphology of Ge/Si QDs, which may have affect the luminescence. Schmidt et al. have studied the effect of overgrowth temperatures on both dot and WL PL [71]. They found that as the overgrowth temperature decreased from 630 to 460 °C, both dot-related and WL-related PL lines red-shifted by 88 meV and 27 meV, respectively. They attributed this red-shift to suppressed Si interdiffusion at lower temperatures. A smaller red-shift for the WL, as compared to the QDs can be understood easily; alloying a thin Ge QW (i.e.,

the WL) with Si will cause a smaller red-shift than in a thick QW (i.e., QD). They observe room temperature PL from Ge/Si QDs with a Si-cap layer grown at 460 °C. Other investigators have also observed room temperature PL of Ge QDs [79,80].

The dependence of Ge/Si(100) PL on temperature and power density has attracted attention of because it reveals important information about band structure and charge carrier behavior [73,81,82]. It is commonly agreed that the PL peak from the dots blue-shifts when the excitation power density increases. Boucaud et al. found that the magnitude of the dot-related PL peak shift can be as large as 80 meV when the power density changes from 4 mW/cm<sup>2</sup> to 4000 mW/cm<sup>2</sup> [73]. This energetic shift with excitation power has been attributed to band bending. A Ge/Si(100) dot has a type II band alignment where the holes are localized in dots and the electrons are confined to the tensile strained Si outside the Ge dot. Thus a dipole is formed at the interface, resulting in band bending due to the Hartree potential. At higher excitation power density, more photo-excited electron-hole pairs will result in a higher Hartree potential, which causes the PL band to blue-shift. The effect of excitation power density on the shifting of PL lines from WL is not as obvious as it is for the dots. There remains controversy about whether the band alignment for the WL is type I or type II. In ref. [81], the authors showed that as the measurement temperature increases from 8 K to 20 K, the increase of dot-related PL intensity is accompanied by a rapid decrease of WL-related PL intensity. This anomalous behavior was interpreted to mean that photo-induced charge carriers in the WL could be thermally activated to migrate to the dots, resulting in more electron-hole pairs in the dot or near the dot and fewer in the WL.

### 1.3 Epitaxial Ag/Si(100) Islands

The study of Ag NPs has attracted much attention recently due to their appealing plasmonic properties that can be used to enhance the performance of semiconductor devices and the efficiency of solar cells [83 – 85]. Since the localized surface plasmon resonance energy can be tuned by changing the size and shape of the Ag nanoparticles [86,87], it is useful to understand the dependence of Ag island size and shape on growth and annealing conditions. For the integration of plasmonic functionality with Si devices, it is also advantageous to investigate Ag epitaxy on Si. It is known that the Ge/Si(100) QDs have low luminescence efficiency, which precludes their application in optoelectronic devices. The surface plasmon of Ag NP could be a solution for significantly improving the luminescence efficiency of Ge/Si(100) QDs. Studying the growth of Ag islands on Si(100) can be useful to establish a baseline to understand effects on Ag island morphology when they are incorporated into a capped Ge/Si(100) QD structure.

The eutectic point for the Ag-Si system is at 836 °C and most investigations of Ag growth on Si are below 800 °C. Growth of Ag on Si at  $T < 800$  °C likely forms a sharp metal-semiconductor interface. Ag epitaxy on Si surfaces was studied extensively throughout the 1980s and 1990s, but the most attention was focused on Ag growth on the Si(111) surface [88–91]. In contrast, Ag island epitaxy on the Si(100) surface has been investigated less extensively, which is why it is part of this research. This section will first discuss the epitaxial growth of Ag/Si(100). This discussion will be followed by subsections discussing growth of kinetics and the plasmonic properties of Ag NPs.

### 1.3.1 Growth of Ag/Si(100) islands.

Like Ag growth on Si(111), Ag/Si(100) follows the S-K growth mode for which 3D islands form on top of the planar layer. There is a diversity of opinions about the thickness of the Ag WL, and various WL thickness values ranging from 0.3 to 1.5 ML have been reported [92–108]. To date, it is commonly believed that Ag/Si(100) growth at room temperature follows a “pseudo S-K” model. For growth at room temperature, the Ag coverage reaches 1 ML before the formation of 3D islands. Subsequent to formation of these 3D islands, Ag atoms from the metastably thick WL can be incorporated into the existing islands, leaving an undetermined thickness that is less than 1 ML [109]. The situation is different for growth at high temperatures ( $\geq 200^\circ\text{C}$ ). In this case, Ag islands form on top of a  $2\times 3$  reconstructed S-K layer with a thickness that is less than 1ML [98]. There remains a diversity of opinions about the thickness of this S-K layer [105–108].

The epitaxial relationship between the Ag islands and Si(100) substrate varies with the growth conditions, thus resulting in an uncertain misfit. It is known that Ag has a face centered cubic (FCC) crystal structure with a lattice constant of 4.08 Å. For growth at high temperatures, 3D Ag islands grow on top of a S-K layer with Ag(100)//Si(100) and Ag[011]//Si[011]. This means that the misfit would be very large, 25% if the Ag/Si interface remained coherent [98,110,111]. However, Ag islands grown at RT have an epitaxial orientation of Ag(111)//Si(100) and Ag[01-1]//Si[011] [111,112]. Kim et al. reported that 3D Ag islands formed at RT orient with Ag(011)//Si(001), and that upon annealing at high temperature, these islands transform into more stable structures of Ag(001)//Si(001) and Ag[100]//Si[100] [113]. A large fraction (~50%) of 3D Ag islands grown at high temperature contain multiple twin defects, while the rest are defect

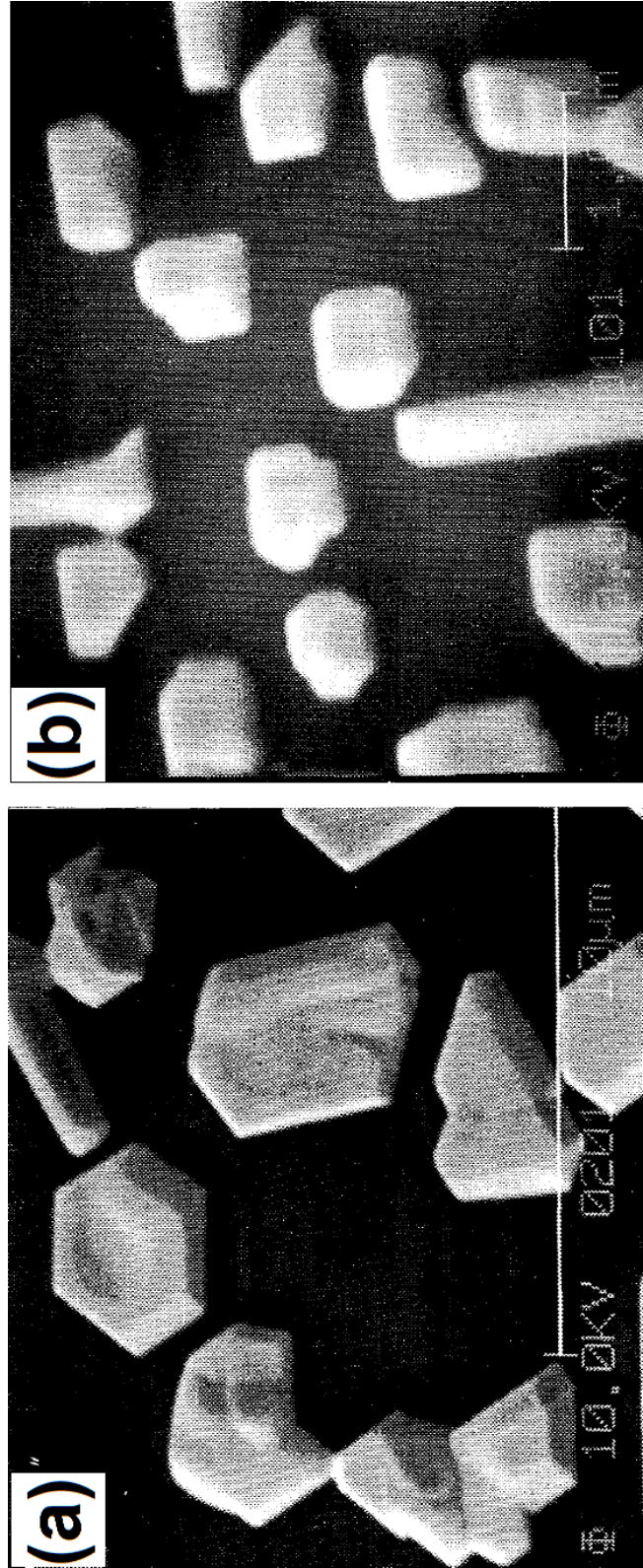


*Figure 1.8.* SEM image of Ag islands grown on Si(111) (a). The scale bar is 10  $\mu\text{m}$ . (b) shows a SEM micrograph of Ag islands grown on Si(100). The scale bar is 1  $\mu\text{m}$ . Note that Ag/Si(111) islands have hexagonal bases, while Ag/(100) islands have rectangular bases. These two SEM images are adapted from ref. [115].



free [114]. The reason why some islands are defective and others are not under the exact same growth conditions is unknown.

The shape of Ag islands grown on Si(100) are different from those grown on Si(111). Ag islands grown on Si(111) have a hexagonal base while those grown on Si(100) have a rectangular base [115]. These morphologies are clearly shown in fig. 1.8, which is adapted from ref. [115]. Besides the rectangular basal shape for Ag islands grown on Si(100), our investigation shows that there are also square, triangular, truncated triangular and irregular shaped islands [116]. Li et al. have also observed and studied the irregular shaped islands, which they have termed “bamboo-like Ag islands.” They also found that these irregular (bamboo-like) islands decompose into smaller segments during post-growth annealing [117]. We observed a similar anti-coarsening behavior during post-growth high temperature annealing, which is opposite to the coarsening behavior exhibited by Ge/Si(100) QD. The details of our investigation on the growth of Ag islands on Si(100) will be discussed in Chapter III.

### **1.3.2 Nucleation and kinetics.**

Epitaxial crystal growth is a non-equilibrium process in which there are several rate limiting steps. Kinetics and thermodynamics play key roles in island nucleation, e.g., through their influence on the areal density of the nuclei. Many of the possible atomic processes responsible for crystal growth on a substrate are illustrated in fig. 1.9. The arrival or deposition rates of atoms on the substrate surfaces are determined by the vapor pressure and source temperature. Atoms adsorbed onto the surface with adsorption energies of  $E_a$  form single adatoms, and the areal density of the adatoms increases initially with deposition time. These adatoms diffuse over the surface before participating

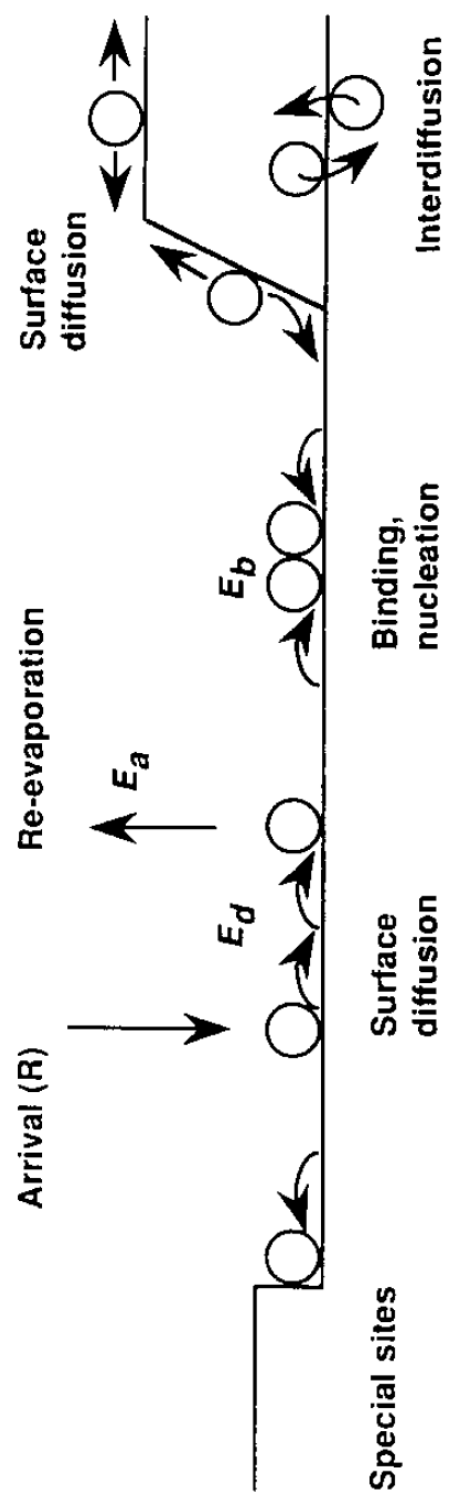


Figure 1.9. Schematic of atomic process responsible for island nucleation adapted from ref [118].

in one of the following processes: re-evaporation, binding with other adatoms to form 2D or 3D nuclei, being captured by existing clusters or special sites (i.e., defects or steps) and interdiffusion between substrate atoms. Interdiffusion is ruled out for Ag/Si growth at temperatures below 800 °C.

For substrates at high temperature, adatoms can only stay on the surface for a short adsorption time, time ( $\tau_a$ ), which is determined by

$$\tau_a^{-1} = \nu_a \exp\left(-\frac{E_a}{kT}\right), \quad (1.4)$$

where  $\nu_a$  is a surface atomic vibration frequency, which is on the order of 1-10 THz,  $k$  is the Boltzmann constant and  $T$  is the absolute temperature of the substrate. During this short adsorption residence time ( $\tau_a$ ), single adatoms diffuse over the surface with a diffusion coefficient,  $D$ , that is defined as

$$D = (\nu_D a^2) \exp\left(-\frac{E_D}{kT}\right), \quad (1.5)$$

where  $E_D$ ,  $a$  and  $\nu_D$  are the diffusion activation energy, jump distance and jump attempt frequency, respectively.

The diffusion of adatoms on the surface is like a random walk, so the net average displacement of adatoms in time  $\tau_a$  is

$$x = \sqrt{D\tau_a} \cong a(\nu_d / \nu_a)^{1/2} \exp[-(E_a - E_d) / kT]. \quad (1.6)$$

Typically,  $E_a$  is several time larger than  $E_d$ ; therefore, the adatoms will encounter other atoms when they migrate on surface. Depending on the binding energy ( $E_b$ ) between the two atoms and the areal density of the single adatom sites, they form small clusters that may then grow into large 2D or 3D islands. The binding energy ( $E_b$ ) and the energy of a

critical cluster with sizes of  $i$ ,  $E_i$ , are both important to understand nucleation and growth processes on the surface.

Epitaxial crystal growth can be divided into two stages: nucleation and cluster growth. In the beginning, random nucleation dominates growth due to the diffusion of adatoms. Once the early clusters form, they start to grow by capturing either the atoms from the supersaturated adatom phase or atoms arriving from the atomic flux. During deposition, both processes contribute to island growth. The incoming atomic flux maintains some level of supersaturation of adatoms, which is determined by the deposition rate and diffusion rate. Even though the supersaturation of adatoms will be reduced when the atomic flux is terminated, the adatom solution between the existing islands will still be supersaturated with respect to the larger islands, but not the smaller islands. This will still drive the growth of larger islands at the expense of dissolution of smaller islands, which is known as Ostwald ripening.

A detailed nucleation theory is described in ref. [118,119]. A general nucleation model is established by excluding any specific system dependent parameters (i.e., surface defects and interdiffusion). Instead of considering each individual atomic size for large clusters, grouping all clusters with  $j > i$  as stable clusters generates an equation for cluster density ( $n_x$ ). By taking appropriate approximations and considering realistic facts (i.e., loss of adatoms to growing clusters and the density limit of stable clusters), the final equation for maximum cluster density can be described as

$$n_x \approx (R/\nu)^p \exp(E_n / kT) , \quad (1.7)$$

where  $p=i/(i+2.5)$  and  $E_n=(E_i+iE_D)/(i+2.5)$  for 3D islands, and  $p=i/(i+2)$  and  $E_n=(E_i+iE_D)/(i+2)$  for 2D clusters [119].

### 1.3.3 Plasmonic properties of Ag nanoparticles.

The Lorentz model is a good starting point for understanding the plasmonic properties of Ag NPs. The equation of motion of an electron with mass  $m$  and charge  $-e$  in an external electric field of  $E_0 \exp(-i\omega t)$ , can be written as

$$m \frac{d^2 x}{dt^2} = -m\Gamma \frac{dx}{dt} - m\omega_0^2 x - eE_0 \exp(-i\omega t), \quad (1.8)$$

where  $x$  is the displacement of the electron from its bound ion. The first term on the right-hand side accounts for damping of the oscillation due to scattering from defects or phonons, where  $\Gamma$  is the damping constant. The second term is the linear restoring force from the positive ions, and  $\omega_0$  is the natural resonant frequency. Suppose the bulk density of electrons in metals is  $n_e$ , then the polarization becomes

$$P = -en_e x(t) = \alpha \epsilon_0 E(t), \quad (1.9)$$

where  $\alpha$  is the polarizability. The solution to eq. 1.8 allows us to derive the frequency-dependent dielectric function without considering interband transitions

$$\epsilon(\omega) = 1 + \frac{e^2 n_e}{\epsilon_0 m} \frac{1}{\omega_0^2 - \omega^2 - i\Gamma\omega}, \quad (1.10)$$

Conduction electrons in noble metals, i.e., silver and gold, are essentially unbound. Therefore, these electrons are assumed to respond in phase with an applied electric field. The restoring force term is zero in the Drude model; therefore, eq. 1.10 becomes

$$\epsilon(\omega) = 1 - \frac{e^2 n_e}{\epsilon_0 m} \frac{1}{\omega^2 + i\Gamma\omega} = 1 - \frac{\omega_p^2}{\omega^2 + i\Gamma\omega}, \quad (1.11)$$

where  $\omega_p^2 = \frac{e^2 n_e}{\epsilon_0 m}$ , which is known as the bulk plasmon frequency.

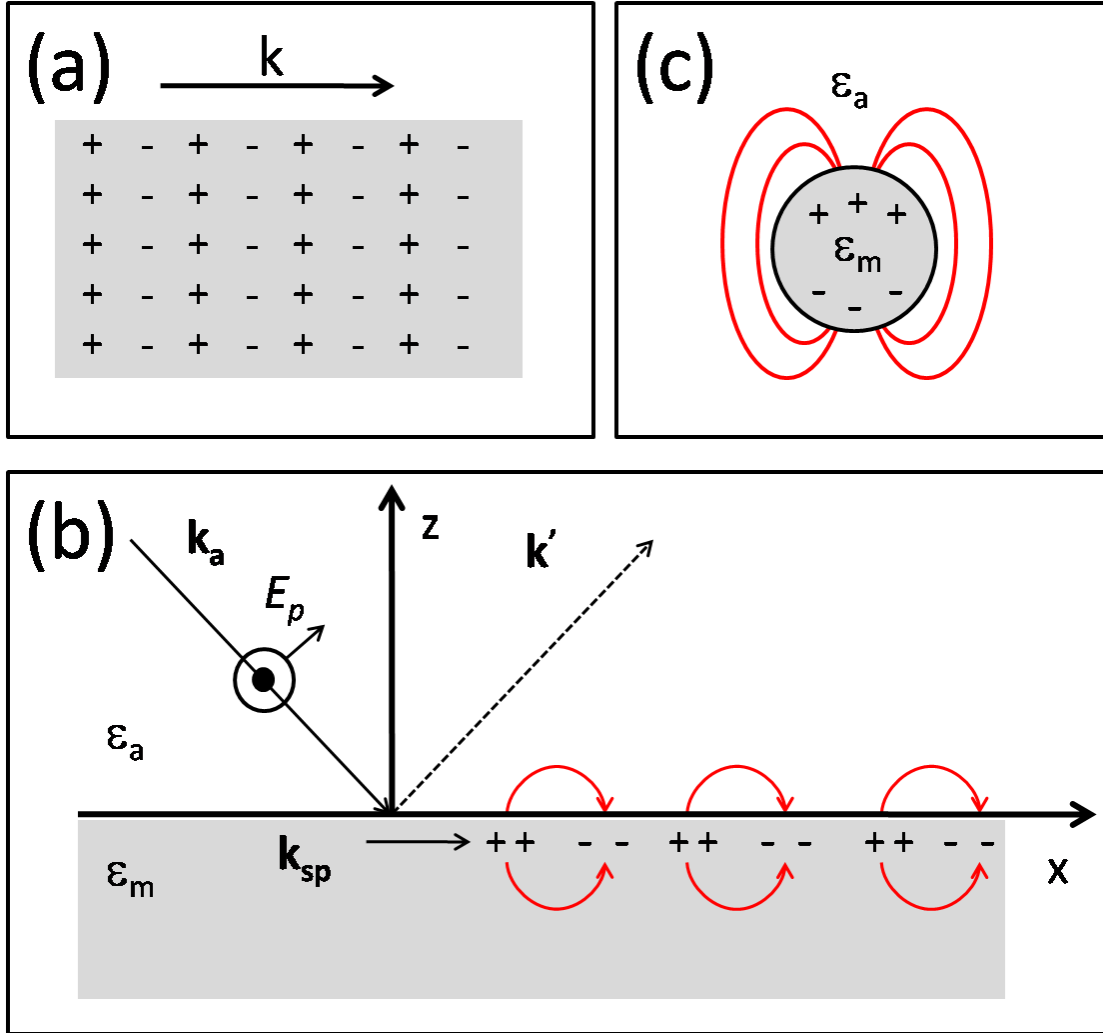


Figure 1.10. Schematics of bulk, surface and localized surface plasmons are shown in (a), (b) and (c), respectively. In (b), only the  $p$  polarized component of incident light contributes to the excitation of a surface plasmon propagating along the  $x$  direction at the infinite interface between dielectric ( $\epsilon_a$ ) and metal ( $\epsilon_m$ ). The  $s$  component is perpendicular to the incident plane, as shown in (b) the black dot centered in the circle.

Fig. 1.10(a) presents the schematic of bulk plasmon propagation. In a pure Drude metal,  $\Gamma$  is fairly small and  $\epsilon(\omega=\omega_p)$  goes to zero. Collective longitudinal optical modes can propagate in a material when  $\epsilon=0$ . This special frequency is known as “bulk plasmon frequency.”

The contribution of interband transitions to the dielectric function may be approximated by adding a constant offset,  $\epsilon_\infty$ , to the real part of eq. 1.11, so it then becomes

$$\epsilon(\omega) = \epsilon_\infty - \frac{\omega_p^2}{\omega^2 + i\Gamma\omega}. \quad (1.12)$$

In real materials, the bulk plasmon frequency is red-shifted as a result of interband transitions and damping.

When the frequency is below the bulk plasmon frequency in a metal, the real part of the dielectric function is negative. Electromagnetic wave propagation is forbidden in this situation. However, with an infinite dielectric-metal interface, a surface bound longitudinal wave can be excited, which is called surface plasmon (SP). A schematic is shown in fig. 1.10(b). Due to the fact that the SP is a longitudinal wave and the total momentum has to be conserved in the direction perpendicular to the plane of incidence, only the  $p$ -polarized component of incident light can excite the SP mode. By applying the boundary conditions at the interface, the dispersion relation in the  $x$ -direction for the SP can be derived from

$$k_{sp} = \frac{\omega}{c} \sqrt{\frac{\epsilon_a \epsilon_m}{\epsilon_a + \epsilon_m}}, \quad (1.13)$$

where  $\epsilon_a$  and  $\epsilon_m$  are the dielectric constants for the dielectric and metal, respectively. This

equation is only for surface bound SP. Ideally, the normal components of the SP mode would be imaginary. Otherwise, the SP wave would propagate in the z-direction. In the non-retarded regime,  $k_{sp}$  can be maximized when  $\epsilon_m = \epsilon_a$ , which gives the SP resonance frequency as

$$\omega_{sp}^2 = \frac{\omega_p^2}{\epsilon_\infty + \epsilon_a} . \quad (1.14)$$

For a pure Drude metal ( $\epsilon_\infty = 1$ ) interfacing with vacuum ( $\epsilon_a = 1$ ), the SP resonance frequency is  $\omega_p/\sqrt{2}$ .

Moving away from bulk metals or infinite planar dielectric-metal interfaces to an isolated spherical metal NP, the resonant frequency of a plasmon was accurately predicted by Gustav Mie who solved Maxwell's equations for spherical NP in 1908 [120]. Mie's solution provides the modern version of the theory to describe the interaction between electromagnetic radiation and a spherical metal particle. Since the plasmon is confined by the NP, the resonant frequency in NP is called the localized surface plasmon resonance (LSPR). Fig. 1.10(c) shows the schematic of LSPR. The size of the metal NP is much smaller than the optical wavelength; therefore, we can use quasistatic approximation where the phase of the electric field across the NP is the same. In the dipole limit for a metal NP ( $\epsilon_m$ ) surrounded by dielectric ( $\epsilon_a$ ), the polarizability of the metal sphere can be written as

$$\alpha = a^3 \frac{\epsilon_m - \epsilon_a}{\epsilon_m + 2\epsilon_a} , \quad (1.15)$$

where  $a$  is the radius of the sphere. Resonance occurs when



$$\varepsilon_m + 2\varepsilon_a = 0, \quad (1.16)$$

For a Drude metal, assuming the imaginary part of  $\varepsilon_m$  is small and weakly depends on the frequency, the resonance frequency can be determined by plugging eq. 1.12 into eq. 1.16,

$$\omega_{LSP}^2 = \frac{\omega_p^2}{\varepsilon_\infty + 2\varepsilon_a} - \Gamma^2. \quad (1.17)$$

Without taking the interband transition into account ( $\varepsilon_\infty = 1$ ), the LSPR for a Drude metal sphere in vacuum ( $\varepsilon_a = 1$ ) can be determined as  $\omega_{LSP} = \omega_p / \sqrt{3}$ , if  $\Gamma$  is much smaller than  $\omega_p$ .

The plasmon resonance frequency has already been derived for the Drude model, but Ag is not well approximated by a Drude metal. An easy way to find the frequency-dependent Ag dielectric properties is to fit the experimental optical data with the modified Drude model [121]

$$\varepsilon_m(\omega) = \varepsilon' - \varepsilon'' \frac{\omega_p^2}{\omega^2 + i\Gamma\omega}, \quad (1.18)$$

where  $\varepsilon'$  and  $\varepsilon''$  are fitting parameters. For Ag, the bulk plasmon resonant frequency is  $\omega_p = 1.72 \times 10^{16}$  rad/s, and the damping constant is  $\Gamma = 8.35 \times 10^{13}$  rad/s. The fitting values for  $\varepsilon'$  and  $\varepsilon''$  are 5.45 and 0.73, respectively [121]. The LSPR of the Ag sphere embedded in a dielectric ( $\varepsilon_a$ ) can be calculated by plugging eq. 1.18 into eq. 1.16

$$\omega_{LSPR}^2(Ag) = \frac{\varepsilon'' \omega_p^2}{\varepsilon' + 2\varepsilon_a} - \Gamma^2. \quad (1.19)$$

By substitution the above numbers into eq. 1.19, the LSPR of the Ag sphere in a vacuum can be calculated as  $5.38 \times 10^{15}$  rad/s ( $\sim 3.8$  eV). The resonance frequency of the Ag sphere is not dependent on the particle size because in the quasistatic limit, the size of the NP is negligible compared to the optical wavelength.

When the NP loses spherical symmetry, the NP LSP splits into two, three or even more oscillation modes. For example, spheroidal NP has two dipolar plasmon modes that have been observed in experiments [122–125]. Gan extended Mie's theory to include ellipsoidal NPs. For an ellipsoidal NP surrounded by a medium with a dielectric constant ( $\epsilon_a$ ), the dipolar polarizability becomes

$$\alpha_j(\omega) = \frac{V_e}{4\pi} \frac{\epsilon_m - \epsilon_a}{\epsilon_a + f_j(\epsilon_m - \epsilon_a)} , \quad (1.20)$$

where  $V_e$  is the volume of the ellipsoidal NP and  $f_j$  ( $j=x, y$  or  $z$ ) is the depolarization factor in the  $j$  direction. It is defined as [126]

$$f_j = \frac{L_x L_y L_z}{2} \int \frac{ds}{(s + L_j^2) \sqrt{(s + L_x^2)(s + L_y^2)(s + L_z^2)}} , \quad (1.21)$$

where  $L_j$  is the length of the  $j$  axis. The integral of Eq. 1.21 can only be evaluated analytically for spheroids. Spheroids are ellipsoids with two equal axes. The resonance condition be determined by maximizing the polarizability of eq. 1.20, which gives

$$\epsilon_a + f_j(\epsilon_m - \epsilon_a) = 0 . \quad (1.22)$$

By plugging eq. 1.18 into eq. 1.22, the LSPR of an ellipsoidal NP can be determined by

$$\omega_{LSPR}(ellipse) = \sqrt{\frac{f_j \epsilon'' \omega_p^2}{f_j \epsilon' + (1 - f_j) \epsilon_a} - \Gamma^2} . \quad (1.23)$$

Therefore, the LSPR frequency is dependent on the NP shape and the dielectric constant of the surrounding medium [122,125,127] in the quasistatic approximation. The size of the NP can also influence the resonance frequency when the quasistatic approximation does not apply [86]. Larger NPs usually result in a lower LSPR energy. When the particle size is comparable with the wavelength of the exciting light or the shape of NP does not

have elliptical symmetry (e.g., Ag/Si(100) islands have cubic or triangular symmetry), the LSPR is usually determined by simulations because no simple solutions are available to describe the particle's plasmonic properties.

#### **1.3.4 Applications of localized surface plasmon resonance.**

The renewed interest in the surface plasmon is due to recent advances in the investigation of the optical properties of metallic NPs. The most attractive aspect of the localized surface plasmon is that it concentrates light in a considerably smaller region than the optical wavelength, ranging from sub-10 nm to hundreds of nm depending on the particle size. Exploiting the confined intense electromagnetic energy, metallic NPs have been employed to enhance QD luminescence [128], as well as photovoltaic [129], photodiode [130] and chemical sensing [131] efficiencies. Since our project is about improving the PL efficiency of Ge QDs, various theoretical and experimental investigations regarding the application of LSPR in QD luminescence will be discussed in detail.

The enhancement of QD luminescence efficiency by metallic NPs has been theoretically investigated over the last decade [30,132 – 134]. Basically, three fundamental factors are critical to predicting the PL enhancement factor: (i) an increase in absorption by field enhancement, (ii) a higher radiative recombination rate induced by the LSP and (iii) an increased nonradiative energy transfer near the metal NPs.

An illustration of the PL enhancement process, based on the enhancement-to-absorption rate, radiative emission and nonradiative decay, is shown in fig. 1.11 (a) which was revised from a figure in ref. [132]. Without a metal NP in the vicinity, the QD is typically excited by absorbing photons from a focused laser beam. When a metal NP is

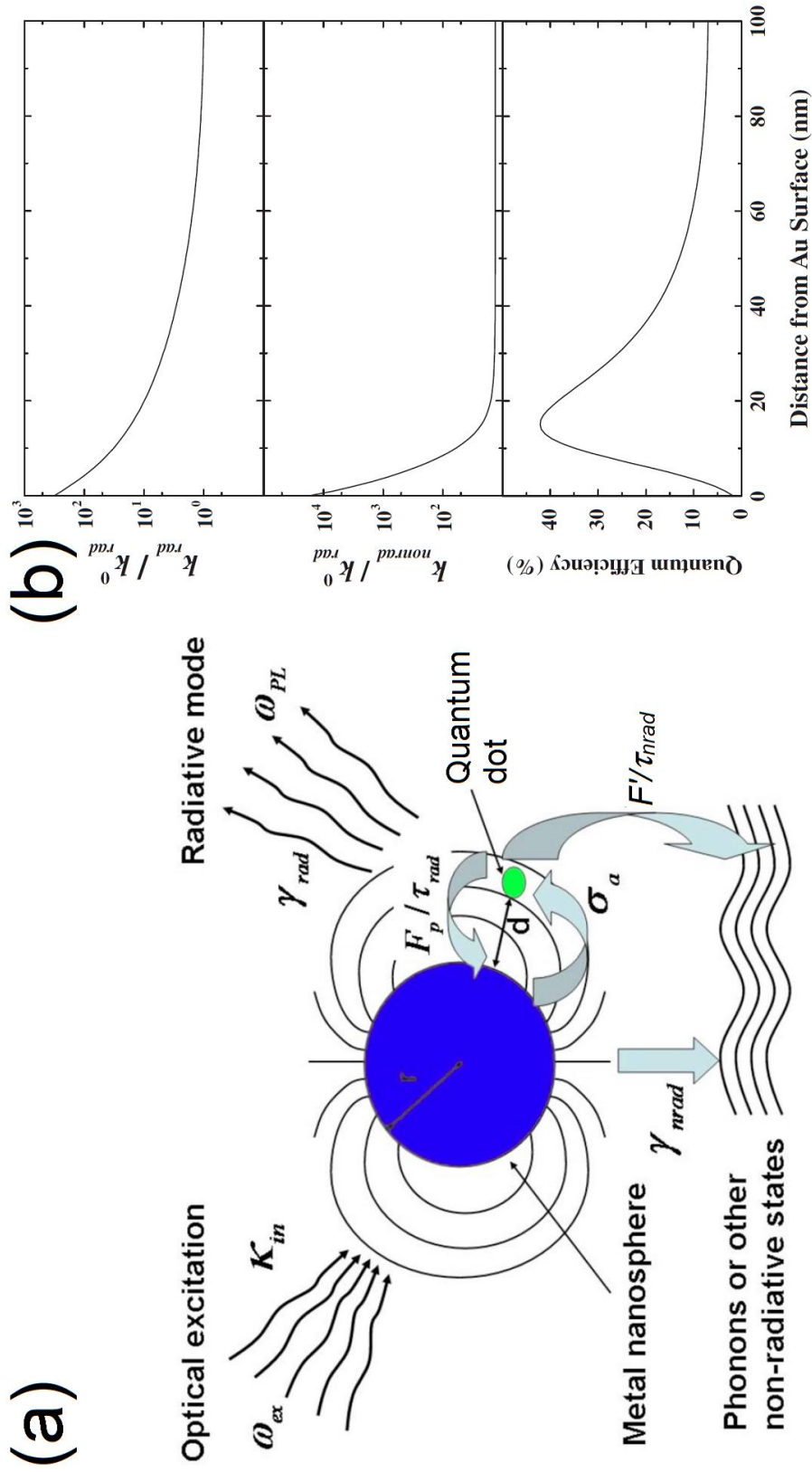


Figure 1.11. (a) Illustration of PL enhancement by the LSPR of a metal NP is shown (adapted from fig. 1 of ref. [132]). (b) shows how the enhancement factor to radiative emission (top), nonradiative decay (middle) and to the quantum efficiency (bottom) depend on the distance between a CdS QD and an Au NP. They are adapted from ref. [134]

placed near the QD, the light is also coupled via the intensely confined LSP modes of the metal NP, which enhances the electromagnetic energy density around the NP. Exposing the QD to highly concentrated electromagnetic fields results in a higher absorption rate. The same LSP modes can also enhance the radiative recombination rate through the Purcell effect [135]. The Purcell effect states that the spontaneous emission rate of atoms can be enhanced by placing them in a matched resonant cavity.

By assuming LSPR has no effect on the rate of nonradiative decay, Sun et al. [132] examined the dependence of the total enhancement factor on the size of the metal NP, as well as on the relationship between these three frequencies, as shown in fig. 1.11 (a) (excitation light  $\omega_{\text{ex}}$ , LSPR of metal NP  $\omega_0$  and emission of QD  $\omega_{\text{PL}}$ ). They found that optimum enhancement occurs when  $\omega_{\text{ex}} \sim \omega_0 \sim \omega_{\text{PL}}$  and the metal sphere is  $\sim 20$  nm in radius. They use the example of InGaN QD separated from Ag NP embedded in a GaN matrix by 5 nm to claim that the total maximum enhancement factor, defined as the multiplication of the absorption enhancement factor and the radiative recombination enhancement factor, could be as large as  $8 \times 10^4$ .

The predicted enhancement factor can be significantly reduced by considering the influence of LSP modes on the nonradiative decay rate of the QD, because LSP modes can enhance both the radiative recombination rate and the nonradiative decay rate of the QD [134]. The enhancement to both radiative and nonradiative processes sensitively depends on the distance between the metal NP and the QD, but in different manners as shown in fig. 1.11(b). This figure clearly shows that enhancement of nonradiative decay is dominant at small distances, which quenches the PL efficiency of the QD. The QD can't feel the LSPR of the metal NP if they are too far apart. As shown in the bottom plot

in fig 1.11(b), there is an optimum distance (~20 nm) that maximizes the quantum efficiency of the QD. The example used in ref. [134] is the Au NP and CdS QD system. Therefore, the enhancement of QD PL can be optimized by tuning the size of the metal NP, adjusting the distance between NP and QD and tuning the LSPR energy to be as close as possible to the QD emission energy.

It has been reported that epitaxial Ag NPs grown on GaAs enhances the PL emission of InAs QD significantly [128]. Similar enhancement behavior has been reported for the CdS QD and Au NP systems [136], as well as the CdTe QD and Ag NP systems [137]. Experimental observations of quenching due to LSPR of metal NPs have also been reported [138,139]. These investigations provide a baseline to investigate the effects of epitaxial Ag NP on the PL of Ge/Si(100) QD.

## CHAPTER 2

### EXPERIMENTAL METHODS

In this chapter, I will discuss the experimental techniques and procedures employed in my research project in detail. My project is to enhance the photoluminescence efficiency of Ge quantum dots (QD) with the localized surface plasmon resonance (LSPR) of Ag nanoparticles (NPs). This project includes 3 parts, Ag NP growth on the Si(100) surface, tuning the LSPR energy of Ag NPs and growing heterostructures incorporating Ge QDs and Ag NPs. Samples in the first part were grown in a home-built small molecular beam epitaxy (MBE) system for epitaxially growing Ag NPs on the Si(100) surface, and the growth in the other two parts is performed in a Group IV MBE system manufactured by SVTA, Inc. As described below, the prep/buffer chamber of this system was modified to incorporate an Ag deposition station.

The surface quality and dot/NP morphology of the samples were characterized with *ex-situ* techniques, such as atomic force microscopy (AFM), scanning electron microscopy (SEM) and transmission electron microscopy (TEM). The Si deposition rate was calibrated with Rutherford back scattering spectrometry (RBS). RBS was also used to measure the coverage of Ag and Ge for each sample. The optical properties were investigated using spectroscopic ellipsometry (SE) and photoluminescence spectroscopy (PL). The average strain and the amount of Ge that segregated to the surface of the Si cap layer grown atop the Ge dots were characterized using Raman spectroscopy and X-ray photoelectron spectroscopy (XPS). The components of the MBE systems, the growth procedures and the *ex-situ* characterization techniques will be described in the following sections of this chapter.

## **2.1 Introduction**

### **2.1.1 Molecular beam epitaxy systems.**

We used a MBE system to grow the self-assembled Ge/Si(100) quantum dots, the thin Si cap layer and the epitaxial Ag NPs. MBE is a technique for epitaxially growing thin or ultrathin films via the interaction of one or several molecular or atomic beams on a heated single crystalline substrate. It is popular in both research and industry due to its capability for producing high quality crystals with atomic level control. MBE was first investigated in the late 60's [140], and then rapid progress was made in growing III-V compounds and in group IV semiconductors.

The molecular or atomic beams are usually created by heating solid sources until they evaporate. There are several methods commonly employed to heat the solid sources. We employed a Knudsen effusion cell for Ag growth and electron beam sources for deposition of Si and Ge. The Knudsen cell includes a crucible, a resistive heater, and thermal shields. The crucible is used for confining the source material. The designed shape and dimensions of the crucible can ensure the required angular distribution of the source beam. The electron beam evaporator bombards the source with high energy electrons (several to 15 keV) to partially heat it to evaporation. The high energy electron beam is generated by applying high voltage to a tungsten filament, and then the electron beam is guided to the source by a magnetic field. The electron beam evaporator is especially useful for the materials that require higher temperature to evaporate than Knudsen cells can provide.

The solid source MBE operates at ultra high vacuum (UHV) (pressure <  $10^{-9}$  torr) to provide a very clean ambient for high quality growth, since a better vacuum level



usually provides better thin film quality. To achieve good and reliable vacuum, the MBE is usually equipped different vacuum pumps for different part of the system. The group IV MBE employed in this project is equipped with a cryo pump for growth chamber, an ion pump for the preparation chamber, and a turbo molecular pump for the load lock. Growth parameters such as substrate temperature can be monitored with a thermocouple and the deposition rate can be monitored using a quartz crystal thickness monitor. Additional instrumentation, e.g., reflection high electron energy diffraction (RHEED) and residual gas analyzer (RGA), can also be incorporated into the MBE for *in-situ* analysis and diagnostic purposes.

Two different MBE systems are used for different parts of this project. The growth of Ag islands on Si(100) is investigated in a home-built small MBE system, because it allows us to grow samples more efficiently than the big MBE system. The big SVTA MBE system is used to grow Ge QDs, the Si cap layer, Ag islands and the amorphous Si ( $\alpha$ -Si) layer. The components in each MBE system and growth procedures will be discussed in detail in the following sections.

### **2.1.2 Sample characterization.**

Several analysis techniques were employed to investigate the properties of the samples. The morphologies of Ag islands and Ge dots were characterized with AFM in tapping mode and SEM. The SEM we employed is housed in Center for Solid State Electronic Research (CSSER). From digital AFM and SEM micrographs, the size, shape and volume of Ag islands and Ge dots were studied with offline analysis software. AFM, was also used to measure the surface quality of both the Si buffer layer and the Si cap layer. We employed a Bruker Dimension AFM that is housed in the Center for Solid

State Science (CSSS). RBS is an accurate and convenient technique to determine the coverage of deposited material. So we exploited the RBS capability within CSSS to calibrate the Si deposition rate measured with our *in-situ* crystal monitor, and to measure the actual coverage of Ge and Ag in this project. The structure of capped Ge dots and Ag islands was also characterized with cross section TEM. A JEOL 4000EX TEM housed in CSSS was employed for characterizing the structure of our samples.

The goal of this project is to enhance the PL of Ge dots using the localized surface plasmon of Ag islands, so the optical properties of Ge dots and Ag islands were studied. The localized surface plasmons of the Ag islands were studied using a spectroscopic ellipsometer manufactured by J. A. Woollam Co (SE) in collaboration with Professor Jose Menendez. The PL of the Ge dots, including the effect of Ag surface plasmon was characterized using a laser spectroscopy apparatus housed in the Department of Physics Laser Facility. XPS was used to determine the amount of Ge segregated to the surface of Si cap layer, and the XPS is a facility that housed in CSSS. Raman spectroscopy was used to characterize the average strain on the surface of the Si cap layer grown atop the Ge dots, and Raman spectroscopy apparatus, a laser facility in Department of Physics, is maintained by Christian Poweliet.

## **2.2 Small Molecular Beam Epitaxy and Calibrations**

### **2.2.1 Small molecular beam epitaxy system.**

To efficiently study epitaxial Ag island growth on the Si(100) surface, we built a small MBE system. This small MBE system incorporated a load lock and growth chamber all sealed with conflat flanges. Its schematic is shown in fig. 2.1.

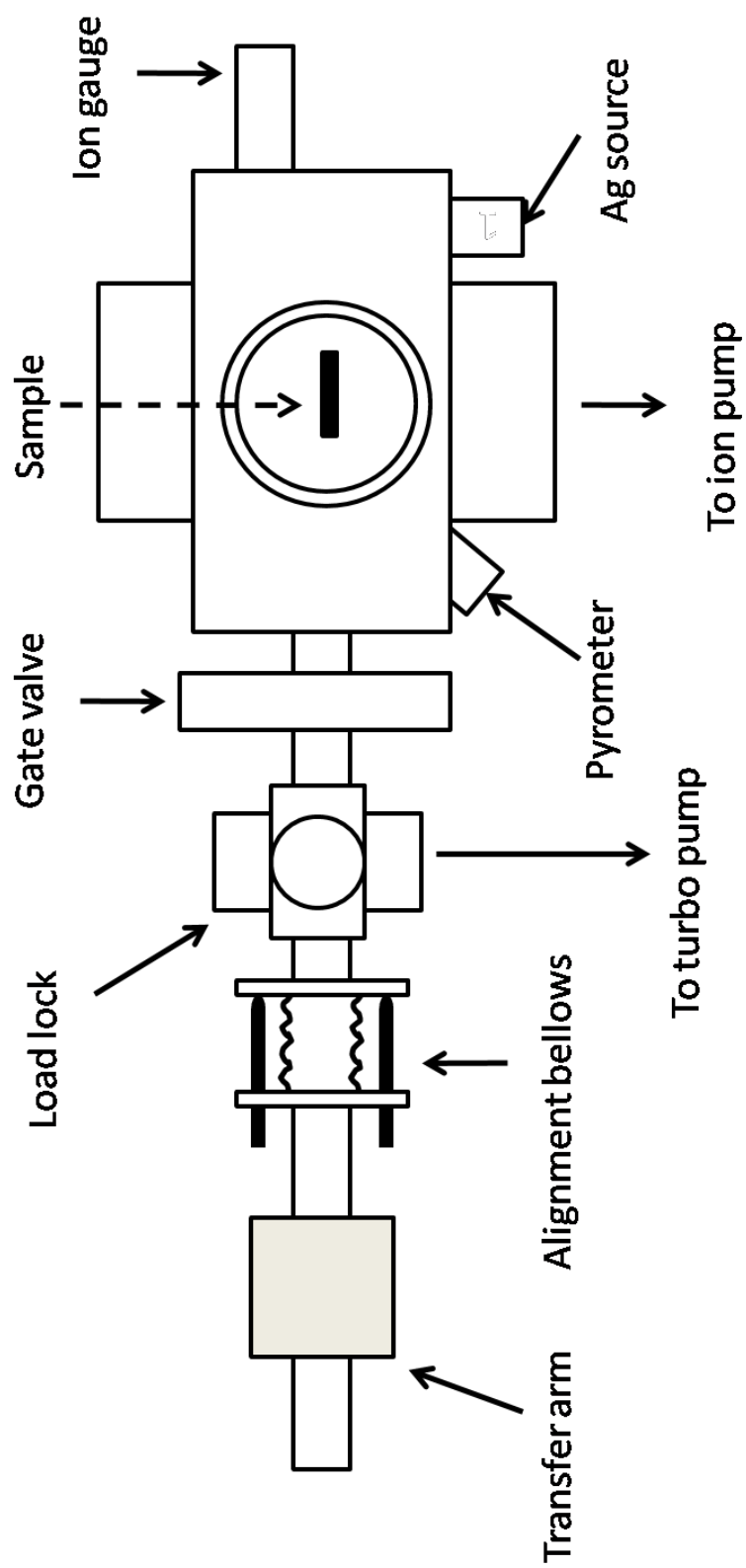


Figure 2.1. Schematic of the small MBE system employed for Ag deposition. The base pressure in growth chamber is about  $2 \times 10^{-10}$  torr.

A magnetically coupled linear/rotary motion drive enables sample transfer between the load lock and the growth chamber under vacuum. The sample holder can be easily attached to the end of the transfer rod so it can be transported between the load lock and growth chamber. The bellows-sealed alignment mechanism enables us to precisely align the transfer arm so that the sample holder can be directly transferred into or out of the sample dock mounted in the growth chamber.

The load lock in our Ag deposition system provides a convenient method for transferring samples in and out of the deposition chamber without breaking vacuum. It is isolated from the growth chamber by a manually operated 2 ¾ inch gate valve, so that the growth chamber vacuum will not be affected when the load lock is vented to exchange samples. A 2 ¾ inch quick access door allows the sample holder to be easily loaded into or out of the load lock. The quick access door is sealed with a viton-o-ring, and is hinged and fitted with a swing-away hand knob locking mechanism. The load lock is pumped with a turbo molecular pump backed with a Varian mechanical pump. After 2 hours of pumping, the pressure in load lock is in the low  $10^{-6}$  torr range, so the load lock was usually pumped for at least 2 hours before transferring the sample to the growth chamber. The gate valve is closed immediately once the sample transfer is complete.

The growth chamber is designed for Ag island growth on the Si(100) surface under UHV conditions. It is pumped by a Varian starcell ion pump with a pumping speed of 300 L/s. The base pressure is about  $2 \times 10^{-10}$  torr after baking out. The growth chamber incorporates three components. These are the sample dock, the Ag deposition source and an ion gauge, as shown in fig. 2.1. The sample dock supports the sample holder and

provides electrical contact for DC resistive heating. The substrate temperature is measured by an IR pyrometer through a 2 ¾ inch viewport.

Ag is deposited from a home-built Knudsen cell. Ag is loaded into a pyrolytic boron nitride crucible. The crucible is resistively heated by a tungsten wire insulated by alumina tubing. The crucible surrounded by the tungsten wire heater is inserted into a pyrolytic boron nitride cylinder to reduce heat dissipation. Several layers of tantalum sheet metal are used for radiation shielding. There is a C-type thermocouple about 3 mm below the crucible mounted between two tantalum strips to monitor the temperature of the crucible. A manually-operated shutter is installed on the Knudsen cell flange to precisely control the deposition time. The growth chamber pressure is monitored by an ionization gauge.

### **2.2.2 Bake out procedure for the small molecular beam epitaxy system.**

It is necessary to bake out the MBE system to obtain an ultra-clean UHV ambient. To bake out the system, heating tapes are wrapped around the chamber. During the bakeout, the chamber is heated to 200 °C. At this temperature water molecules and other contaminants adsorbed on the inner surface of the chamber or other components desorb and are pumped.

The bake out procedure includes 3 steps. The first step is to wrap the heating tapes around the growth chamber and the ion pump. It is important that the heating tapes do not touch themselves or one another to avoid melting their insulation. Then the whole system is covered with aluminum foil to minimize convective heat loss during the bakeout. The second step is to pump the whole system only with turbo pump while slowly ramping up bake-out temperature. During this stage of bake out, the pressure of the system was kept

below  $5 \times 10^{-5}$  torr by regulating the temperature, since higher pressure may cause problems for the turbo pump. After about 2 days of bake out in this stage, the temperature of the system is already at about 150 °C. It is time to move to the third stage when we turn on the ion pump and close the gate valve between load lock and growth chamber. After doing so, the load lock and growth chamber were being pumped by the turbo pump and ion pump, respectively. Since the ion pump is more efficient than the turbo pump in this pressure range, we are able to ramp the bake-out temperature further till the final point of about 200 °C. The temperature is maintained at 200 °C until the pressure stabilizes at its lowest value near  $8 \times 10^{-8}$  torr. This usually occurs after about 24 hours pumping with ion pump at the bake-out temperature of 200 °C. Then the bake is terminated. After the bake out, the base pressure is about  $2 \times 10^{-10}$  torr, and the system is ready for degassing and Ag deposition.

### **2.2.3 Calibrations and sample preparation.**

In this section, the sample temperature calibration, source rate calibration and sample preparation procedures will be described. The sample temperature calibration is conducted before the system is baked out. The sample temperature was monitored through a 2 ¾ inch viewport with an Omega infrared pyrometer. The pyrometer was calibrated to a k-type thermocouple which was attached to the backside of a calibration sample. The thermocouple wire was bent so that the junction was in contact with the Si substrate.

The Omega pyrometer can be operated in either of 2 modes: 1-color mode or 2-color mode. In fig. 2.2, the temperature readings from the pyrometer are compared to the thermocouple temperature in the range of 400 °C~800 °C. 1-color mode measures the

temperature based on the absolute intensity at a specific wavelength. The emissivity setting ( $\epsilon$ ) of the pyrometer was adjusted until the pyrometer temperature reading matches that of the thermocouple. By setting the emissivity to 0.59, the pyrometer reading in 1 color mode matched that of the thermocouple at 500 °C. In 2-color mode, the pyrometer measures the temperature based on the ratio of intensities at two different wavelengths. Since the silicon substrate is a gray body, the slope of the pyrometer in 2-color mode is set to 1. From fig. 2.2, we can see the readings of pyrometer in both modes agree with the thermocouple reading within 10 °C.

The Ag source deposition rate was calibrated using RBS so that the coverage of deposited Ag could be precisely controlled. By heating the Ag Knudsen cell to a specific temperature measured by the C-type thermocouple, depositing Ag for a specific time and measuring the coverage using RBS, we were able to calibrate Ag deposition rate vs. Knudsen cell temperature. The results are shown in fig. 2.3, which plots Ag deposition rate vs. C-type thermocouple temperature. The deposition rate is measured in monolayers (ML) per minute. One ML on Si(100) is  $6.78 \times 10^{14}$  atoms/cm<sup>2</sup>.

0.5 cm by 4 cm Si strips were cleaved from boron-doped 4 inch wafers with a resistivity of 0.05  $\Omega$ -cm. Once the substrate is loaded into growth chamber through the load lock, the sample was degassed at 650 °C for at least 2 hours. The degassing procedure is necessary to desorb hydrocarbons and other impurities on the surface. After the substrate is well degassed, it is cleaned by flash desorption of the native oxide. The substrate temperature is rapidly increased up to 1200 °C and then down to  $T < 100$  °C. This process is repeated several times until the integrated time at  $T = 1200$  °C is about 20 sec.

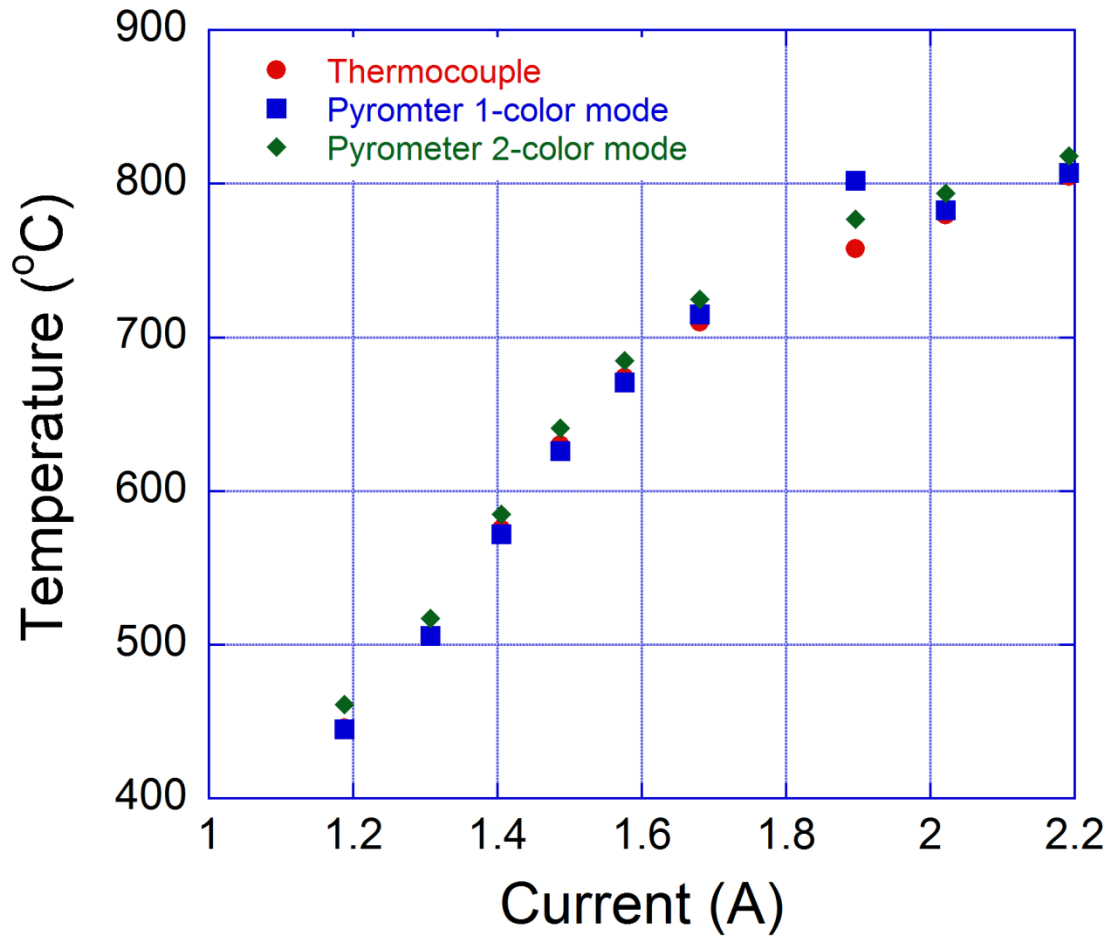


*Figure 2.2.* Temperature vs. sample current measured using a k-type thermocouple bonded to the back side of the resistively heated Si substrate and an infrared pyrometer in both 1-color and 2-color mode. The emissivity setting of the pyrometer was set at 0.59 so that the pyrometer reading matched that of the thermocouple. The 3 temperature readings agree to within about 10 °C.



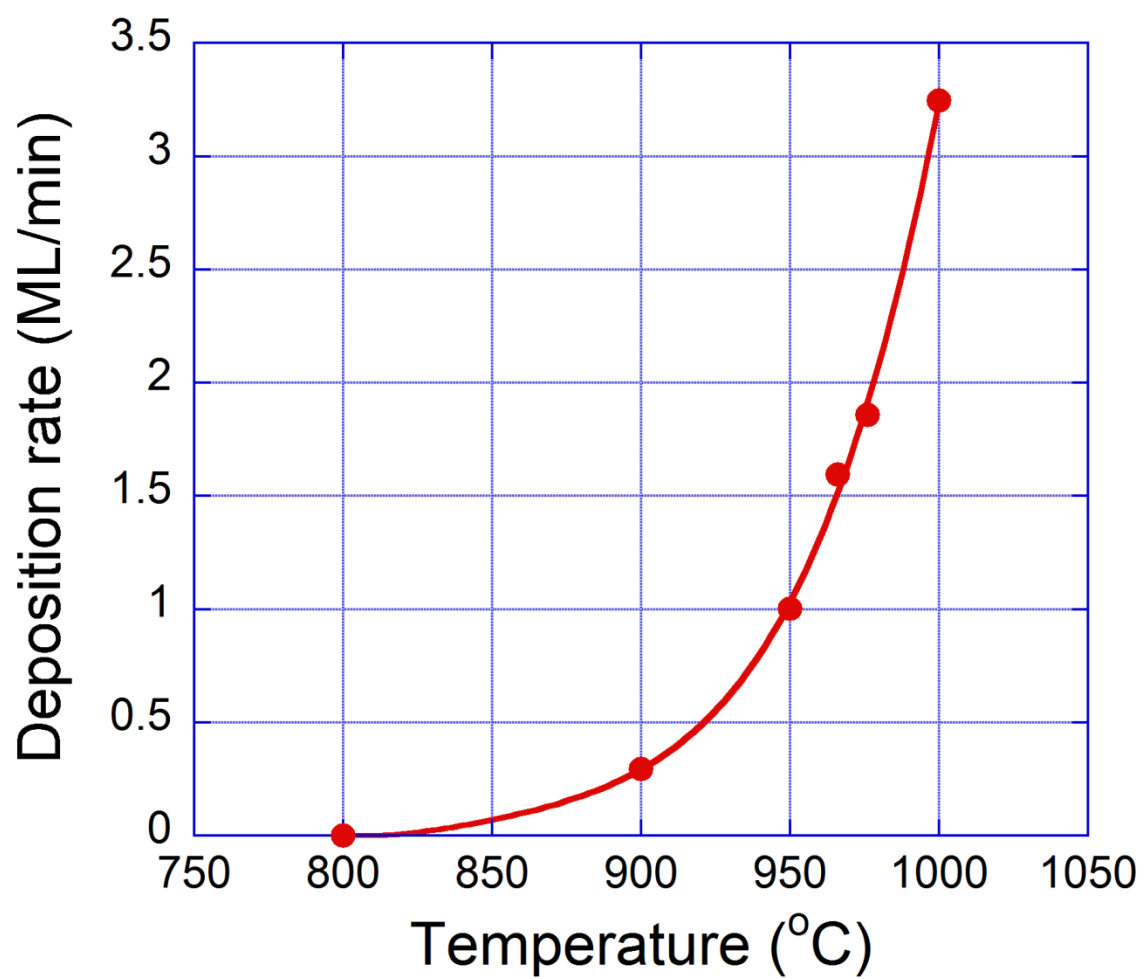


*Figure 2.3.* Ag deposition rate vs. C-type thermocouple temperature. The Ag coverage was determined by RBS. The deposition rate monotonically increases with temperature. The curve is a fourth order polynomial fit to the experimental data points.

In this way, the native oxide layer and any contaminants are rapidly removed from the surface, resulting in a clean and atomically flat Si(100) surface. The pressure in growth chamber should not rise to higher than the low  $10^{-8}$  torr range during flashing or the surface may roughen unacceptably.

After flashing, the Ag source temperature is increased so that the desired deposition rate is obtained and the sample is heated up to the deposition temperature (from 300 °C to 600 °C). Ag islands were grown by depositing 5.3 ML Ag on this freshly prepared Si(100) surface. During growth, the pressure rose to  $\sim 2 \times 10^{-9}$  torr. The dependence of Ag island size, density and morphology on the deposition temperature and post-growth annealing time was systematically studied. *Ex-situ* analysis techniques including AFM, SEM and RBS, were employed to characterize the Ag islands grown on Si(100) surface.

## **2.3 SVTA MBE System and Components**

### **2.3.1 SVTA MBE system.**

We modified the MBE system manufactured by SVTA, Inc. to incorporate an Ag deposition system. The modified MBE system is shown in fig. 2.4. It is a 3-chamber MBE system including a load lock chamber, prep/Ag deposition chamber and growth chamber. This MBE system is designed for 4" wafers. In the following subsections, the functions and components in each chamber will be described in detail.

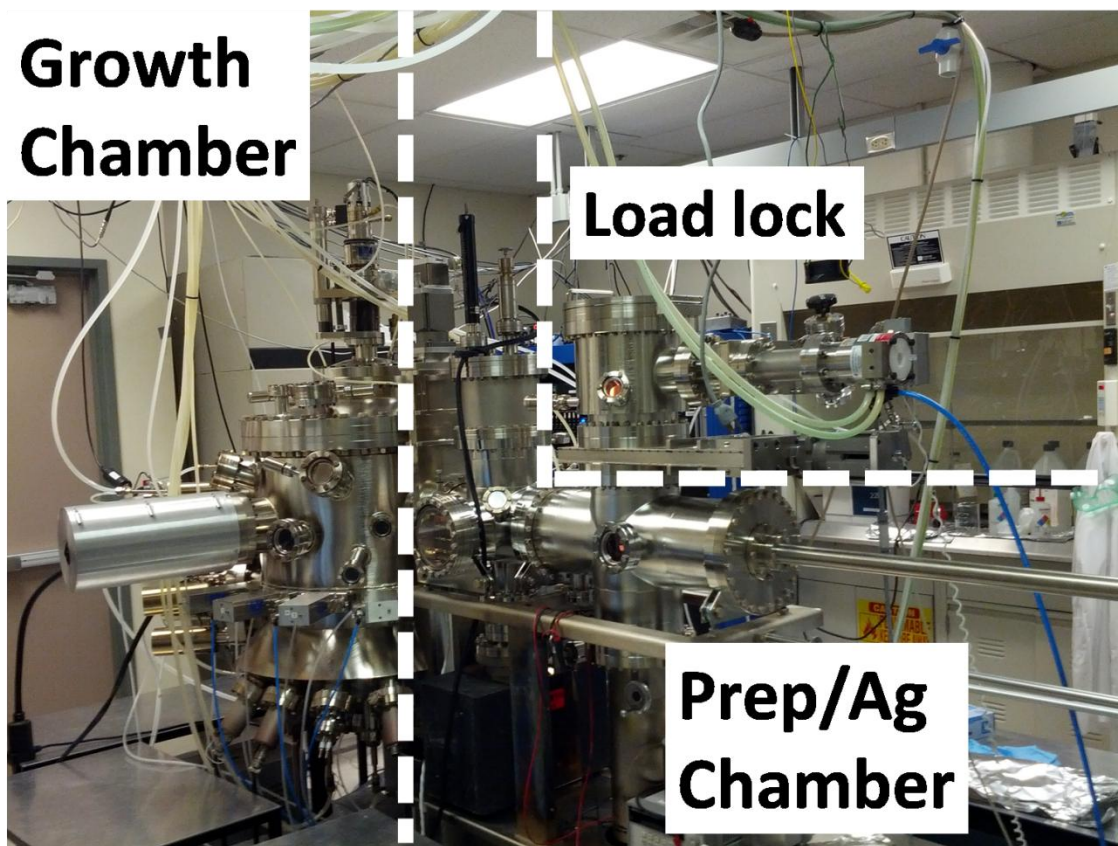


*Figure 2.4.* MBE system used for heterostructure growth.

### ***2.3.1.1 Load lock chamber.***

The load lock chamber is for rapidly exchanging samples between vacuum and atmosphere, for transferring samples among chambers without breaking vacuum, and also for venting the whole MBE system. The load lock chamber is shown below in fig 2.5. As shown in fig 2.5, the load lock is isolated from the prep/Ag chamber by a gate valve, and is pumped with a turbo pump backed with a diaphragm pump. There is also a gate valve between the turbo pump and the load lock, which enables us to vent the load lock and turbo pump separately. The turbo pump can pump the load lock chamber from atmosphere to  $\sim 6 \times 10^{-8}$  torr in 12 hours. Once the pressure in load lock is lower than  $6 \times 10^{-8}$  torr, we are able to transfer the wafer cassette between the load lock and the prep/Ag chamber with the help of a manually operated elevator housed in the prep/Ag chamber. The wafer cassette is for stocking 4 inch wafers, and up to 6 wafers/samples can be stocked simultaneously.

The top port of the load lock chamber has a quick access door, through which the wafer cassette can be loaded. The quick access door is hinged and sealed by a single Kalrez O-ring. On the opposite side of the hinge, there is a latch mechanism to help with opening and sealing the door. The base port is a 10" conflat flange, which is attached to the gate valve between load lock and prep/Ag chamber. The load lock chamber is equipped with several ports. The turbo molecular pump is mounted on a 4.5" port. A view port, an ion gauge, a convectron gauge, a vent valve and a linear motion drive are mounted on 2.75" ports. The linear motion drive is used for actuation the wafer cassette docking mechanism. The wafer cassette docking mechanism is inside the load lock

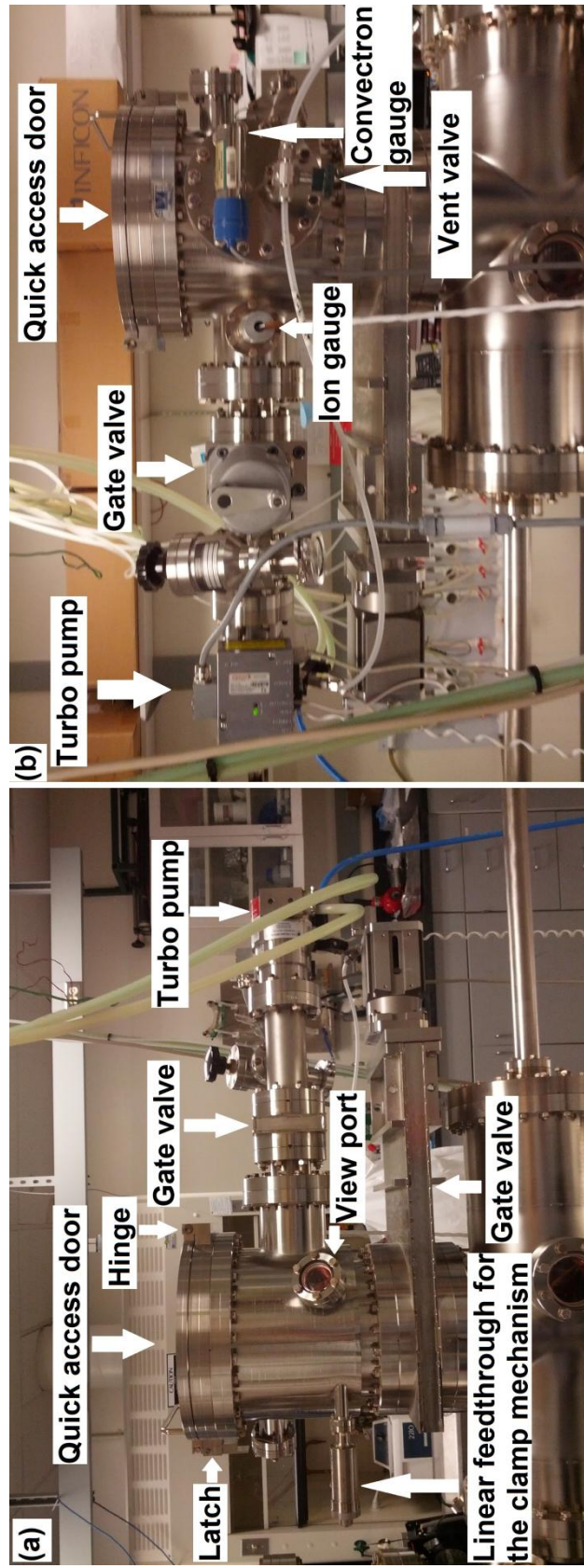


Figure 2.5. Opposing views of the MBE loadlock with various components labeled.

chamber, and there are 3 fingers attached to a clamping mechanism, which can be actuated by the linear feedthrough. When the docking mechanism is clamped, these 3 fingers fit into 3 slots at the bottom of the cassette to secure it. While the docking mechanism is unclamped, 3 fingers move out of the way so that the cassette can be transferred to prep/Ag chamber.

#### ***2.3.1.2 Prep/Ag chamber and components.***

The prep/Ag chamber separates the growth chamber from the load lock chamber, so the growth chamber only is exposed to UHV when wafers are transferred to the growth chamber. The prep/Ag chamber was initially for storing the wafer cassette. For this research project an Ag deposition capability was added to the prep chamber. The vacuum of this chamber was initially provided by a differential diode ion pump with a pumping speed of 120 l/s, manufactured by Physical Electronics. With this pump, the base pressure of the prep chamber was in the low  $10^{-9}$  torr range. To achieve better vacuum and to handle the additional gas load during Ag deposition, we replaced this ion pump with a Starcell ion pump manufactured by Varian. The nominal pumping speed of the Starcell ion pump is 300 l/s, and the vacuum is improved by an order of magnitude to the low  $10^{-10}$  torr range.

There are two mechanisms in the prep/Ag chamber that facilitate sample transfer between different chambers. The first is the elevator for vertical transfer of the wafer cassette between the load lock and the prep/Ag chamber. The second is a magnetically coupled linear transport mechanism for transferring a single wafer horizontally between the growth chamber and prep/Ag chamber. There is a platen at the vacuum end of the transfer arm, which can hold a single Mo wafer block.



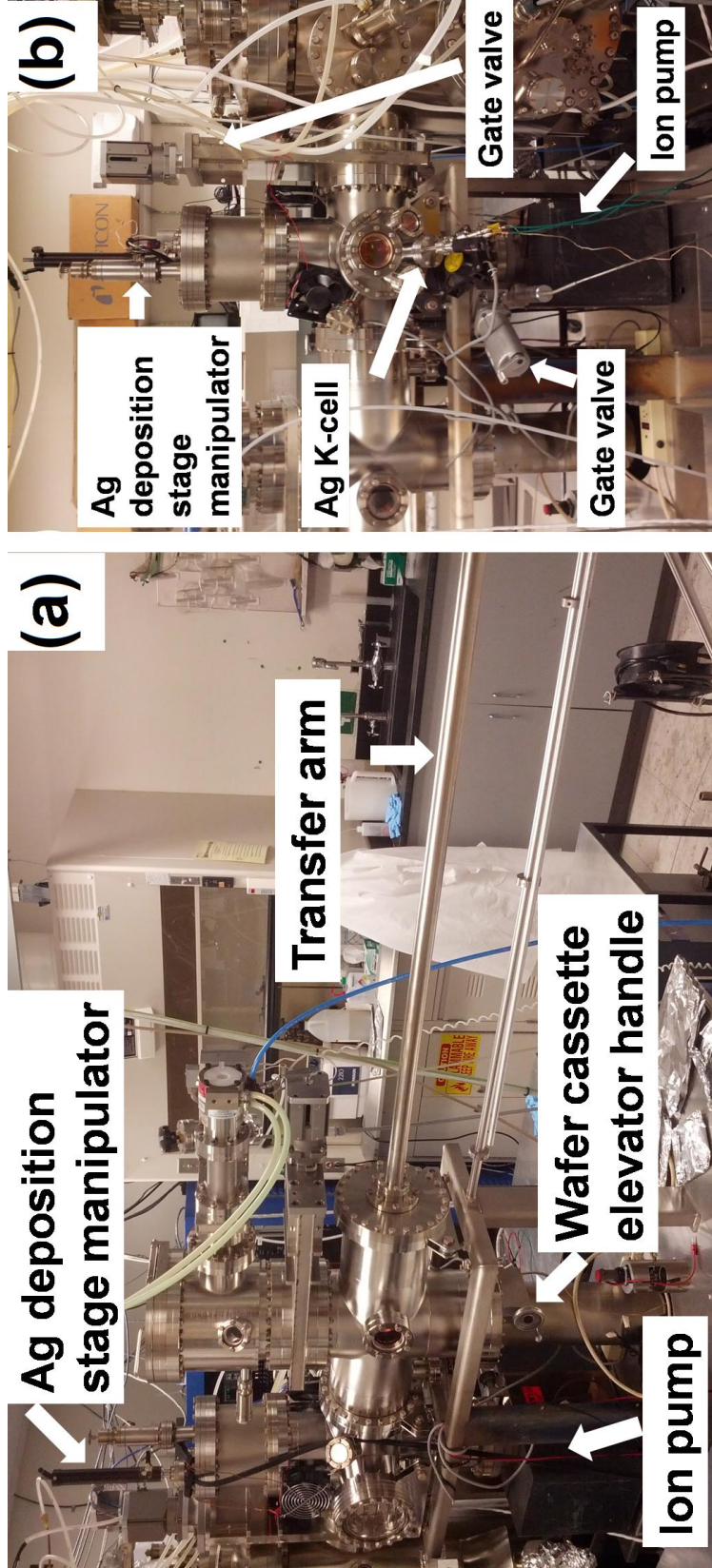


Figure 2.6. Different views of the prep/Ag chamber with various components labeled.

Each wafer block can hold one wafer with the polished side facing down.

The newly installed Ag deposition station includes an Ag Knudsen cell similar to the one discussed in section 2.2.1, a sample heater and a vertical transfer mechanism. A schematic of the stage manipulator is shown in fig 2.7. The manipulator was removed from a VG 100 MBE system and was modified to accept 4” wafers instead of the 3” wafers that it was originally designed for. The modifications to the VG manipulator and fabrication of the vertical transfer mechanism were done by the Physics machine shop to meet our specifications.

The vertical transfer mechanism incorporates a C-ring wafer block support, which is used for transporting the wafer between the platen of the transfer arm and the VG manipulator. Vertical motion of the C-ring is accomplished using a rack-and-pinion linear motion drive. 4 claws that are equally distributed at the bottom of the VG manipulator engage notches in a modified Mo wafer block. The VG manipulator is rotated and the wafer block is supported by these claws during Ag deposition. Stage rotation is actuated by a rotary motion drive, which can be driven by a DC motor. The stage can be rotated during Ag deposition to ensure uniformity of wafer temperature and Ag coverage.

The wafers are radiatively heated by a Ta strip heater that is immediately above the sample. Wafer temperature is sensed by a thermocouple mounted above the heater. Sample temperature is feedback controlled by a Eurotherm controller. The thermocouple temperature is carefully calibrated with an IR pyrometer in the range of 300 °C-500 °C. To ensure that Ag is not deposited onto the Mo wafer block, a stainless steel evaporation shield with a 1” diameter hole at its center is supported about 0.5 cm below the wafer by the C-ring of the vertical transport mechanism during Ag deposition.



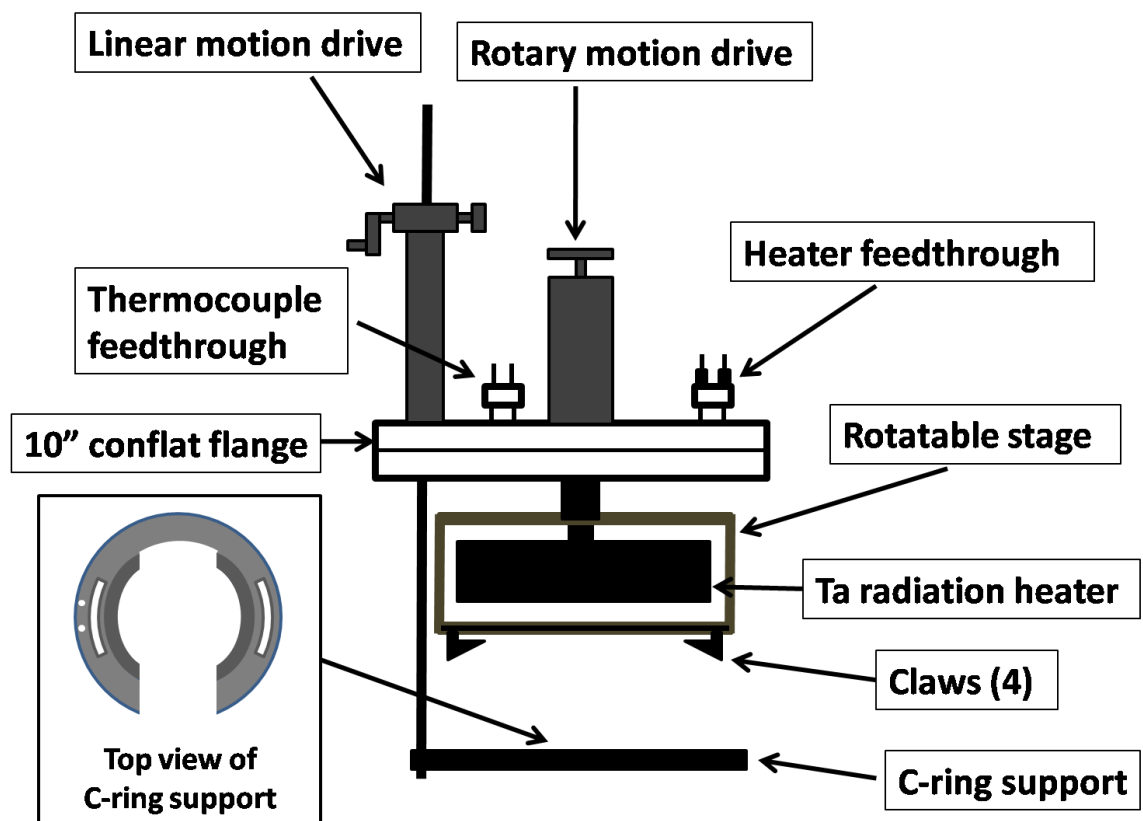


*Figure 2.7.* Schematic of prep/Ag chamber stage showing detail of C-ring support that accepts Mo wafer blocks.

### ***2.3.1.3 Growth chamber and components.***

The growth chamber is employed for Si and Ge deposition in this research project. It is shown below in fig. 2.8. In addition to the Si and Ge sources, the growth chamber also includes dopant and other sources, a sample stage and in-situ characterization instruments. The growth chamber is pumped by a Cryo-Plex 8 cryo pump manufactured by Oxford Instrument inc. It maintains a cold-head temperature of 15K using an Austin Scientific 125W 2-stage closed-cycle He compressor. Its pumping speed is 1500 liters/sec for air and 4000 liters/sec for water vapor. There is a pneumatically controlled gate valve between the growth chamber and the cryo pump. It is necessary to regenerate the cryo pump about twice a year, since the cold head becomes saturated with absorbed gases. Regenerating the cryo pump desorbs the trapped gas from the cold head and exhausts the gas from vacuum. The gate valve between the growth chamber and the cryo pump is first closed, and then the compressor is switched off to warm up the cryo pump. A turbo pump is immediately connected to an accessory port located on the backside of the cryo pump. A metal sealed valve isolates the cryo pump from atmosphere. Overnight pumping with the turbo pump is enough for cryo pump regeneration. The growth chamber has a water-cooled jacket and a cryo panel at the bottom. These features minimize heat-induced degassing and vacuum degradation during long growths. After a complete bake out, the base pressure in the growth chamber can be as low as  $1 \times 10^{-11}$  torr.

Si and Ge are both deposited using electron beam evaporators. There are two Si sources and one Ge source. The 2-pocket Si e-beam source is shown in fig. 2.9. The Ge source is in a single pocket e-gun assembly. These e-guns are manufactured by Temescal,

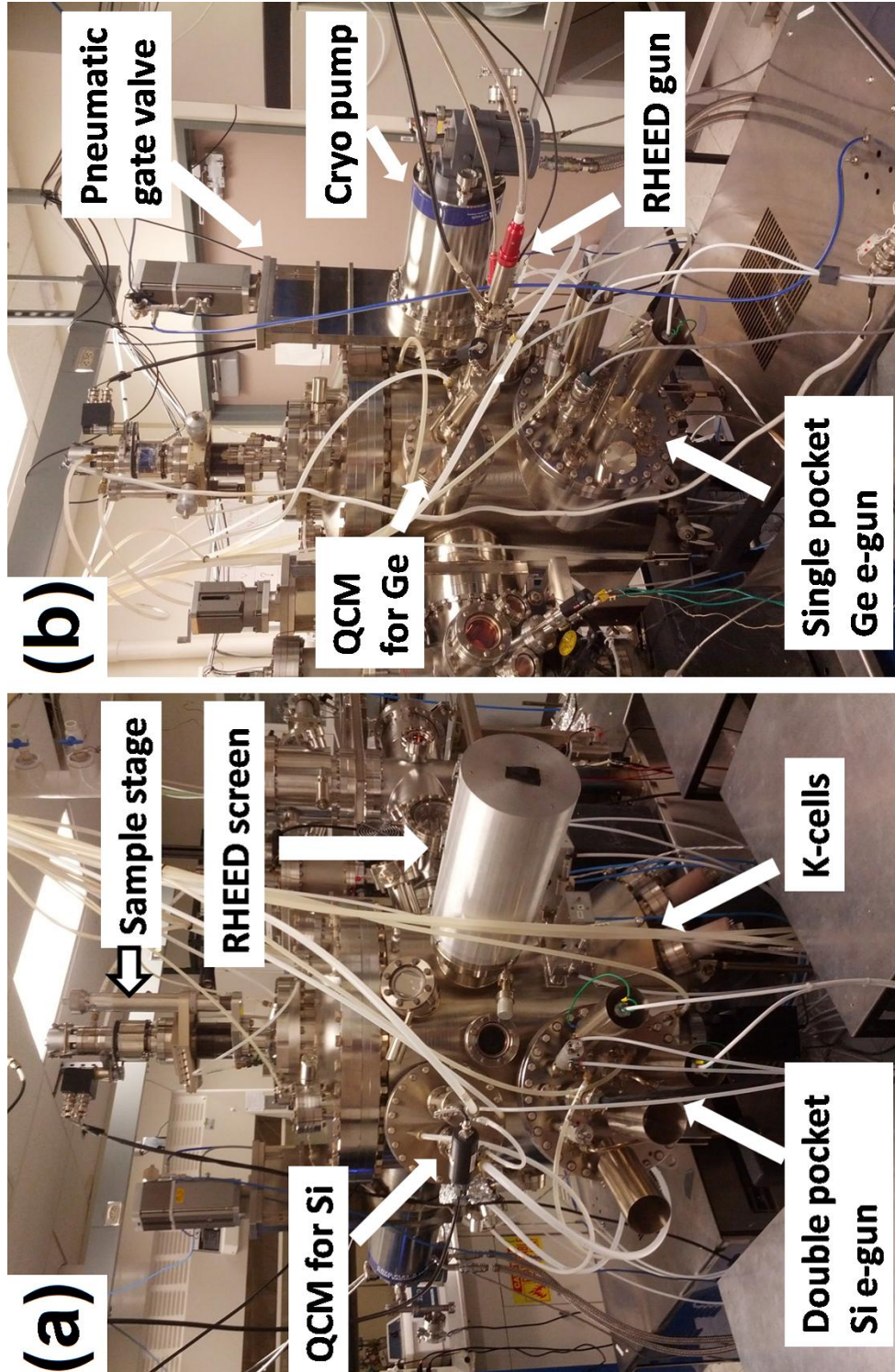


Figure 2.8. Views of the growth chamber with various components labeled.

and are capable of melting any known material. Basically, the e-gun creates an intense, concentrated high energy electron beam and directs it at the target material so that a pool of molten material is formed on the surface. The electron beam emitter is operated at a potential of -7500 Volts with respect to the evaporant material which is earth-grounded. The accelerating potential is supplied by a SEB-15 high voltage power supply manufactured by Thermionic Laboratory Inc. It can supply a maximum output of 10k Volts and 15k Watts. We typically employ only 7.5k Volts.

Electrons are thermionically emitted from a resistively heated tungsten filament in the emitter assembly. The emitted electrons are formed into an electron beam by a beam former assembly. This electron beam is accelerated by the high voltage and deflected to the evaporant material by magnetic fields created by permanent magnets.

The electron beam can be swept across the target material by pairs of electromagnets that are driven by a sweep control unit. The sweep can be independently controlled in the lateral (perpendicular to egun flange) and horizontal (parallel to egun flange) directions. By adjusting the DC sweep coil excitation, the beam can be translated to any position on the surface of the evaporant charge. In addition to DC excitation, AC excitation of the sweep coils can be used for precise control of effective beam shape and current density through variation of the amplitudes and frequency. The XYS sweep control units, which are also manufactured by Thermionic Laboratory inc., can either be controlled at their front panel or by a hand held remote controller. Remote control enables observation of the electron beam as we are adjusting its position, as well as the sweep amplitude and frequency.

The e-gun assembly includes a water cooled copper hearth, incorporating a pocket that can accommodate up to 40 cc of material. The copper hearth provides an effective heat barrier at the molten material interface. We employ shaped Si charges acquired from Vacuum Engineering and Materials of 99.999% purity. Si lumps acquired from Alfa-Aesar of similar purity are used to replenish the shaped Si charge until it is no longer useable. 99.999% purity Ge lumps acquired from Alfa-Aesar are used for the Ge source. Prior to loading evaporant material into the copper pocket, a copper oxide barrier, which is critical for the heat barrier and for ensuring that the evaporant does not bond to the copper, is formed by ‘painting’ the pocket with 30%  $\text{H}_2\text{O}_2$ .

The sweep coils are located above the emitter assembly on either the front side of hearth (farther from the e-gun flange) or the back side (closer to the e-gun flange). The copper hearth is cooled with flowing water. The main permanent magnet is located between the base plate and heat sink, and the magnetic pole pieces are attached on the inner vertical side wall of the copper hearth. Pneumatically controlled source shutters are mounted on the top of hearth, which are used to precisely control the source flux exposure time. The Si and Ge fluxes are controlled and monitored by quartz crystal microbalances (QCM). The sensor head of the QCM can always ‘see’ the source whether the shutter is open or closed, which enables stabilization of the beam fluxes prior to deposition.

A QCM can accurately measure very small mass changes by sensing changes in the resonant frequency of the piezoelectric quartz crystal. These mass changes can correspond to film thicknesses in the Angstrom range. The quartz crystal is driven at its resonant frequency by oscillating electric potentials applied between Au or Ag electrodes deposited directly on its faces. The QCM in our MBE system comprises a gold-coated



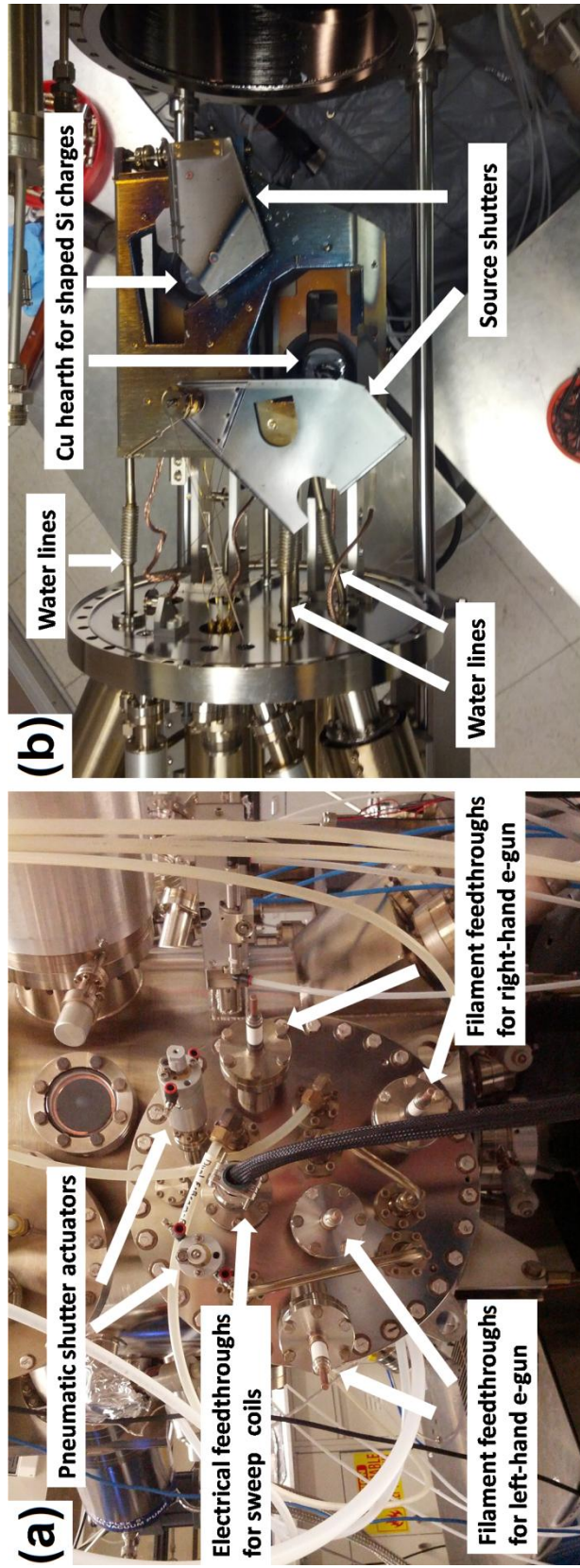


Figure 2.9. Two-pocket e-gun employed for Si deposition. (a) external view. (b) shows the two-pocket e-gun removed from the chamber for maintenance with various components labeled.

quartz crystal, which is installed into a sensor incorporated at the end of the vacuum feedthrough. The oscillator and control electronics are external to the vacuum system. The resonant frequency of a brand new quartz crystal is near 6 MHz. The resonant frequency decreases as material is deposited on the quartz crystal. We usually change the quartz crystal when it has consumed 10-20% of its 'lifetime', following the manufacturer's recommendation.

The QCM is controlled by a XTC/2 thin film deposition controller manufactured by Inficon inc. The controller has an easily readable LCD display, which continuously shows the deposition related parameters, and a control panel which can be used to easily program the film deposition recipes. The XTC/2 controller can also be computer controlled using the RoboMBE software provided by SVTA. Both the Si and Ge deposition rates can be feedback controlled by the XTC/2. The controller is capable of adjusting the e-gun power to match the deposition rate the set point. The deposition rate measured by the QCM must be calibrated so that it corresponds to an actual film thickness. For this purpose, we employed RBS. A schematic of the crystal monitor assembly is shown in fig. 2.10.

The sample stage is mounted on the top flange of the growth chamber as shown in fig 2.8. The stage can move the sample stage along the x, y and z directions, which allows us to align the stage with the platen that carries the wafers at the end of the transfer arm to facilitate wafer transfer. The stage can also rotate the wafer about its vertical axis, so that uniform wafer temperature and coverage of deposited material can be achieved during growth. Stage rotation is achieved by driving a magnetically coupled

rotary drive with a DC stepper motor. The main features of the stage are shown in fig 2.11.

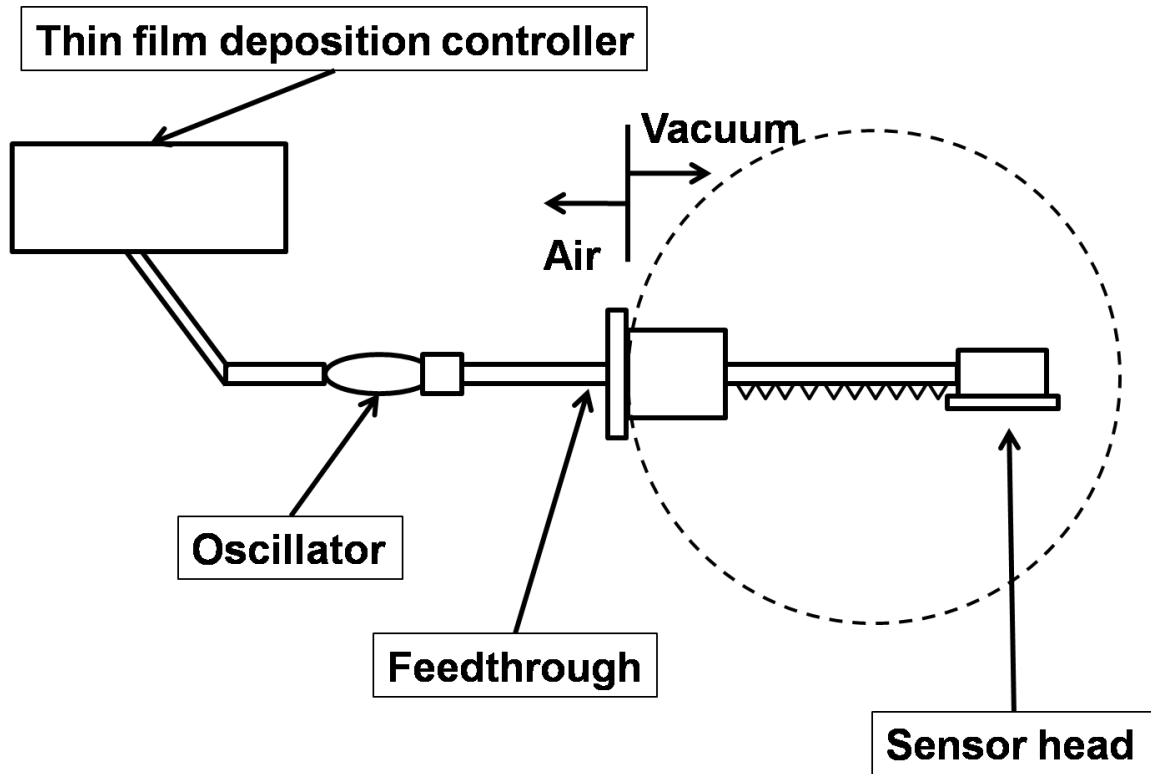


*Figure 2.10.* Schematic of quartz crystal microbalance (QCM) assembly.

There is a manually controlled master shutter at bottom of the stage manipulator at a fixed vertical distance from a C-ring wafer block support. This C-ring support in the growth chamber is similar to the one in prep/Ag chamber in fig 2.7. The C-ring support is for securely holding a wafer block with a substrate. The substrate can be heated up to 1000 °C by a radiation heater made of graphite which is immediately above the substrate. The substrate temperature is monitored by a C-type thermocouple which contacts the last stage of the Ta radiation shielding above the heater. Previous investigators carefully



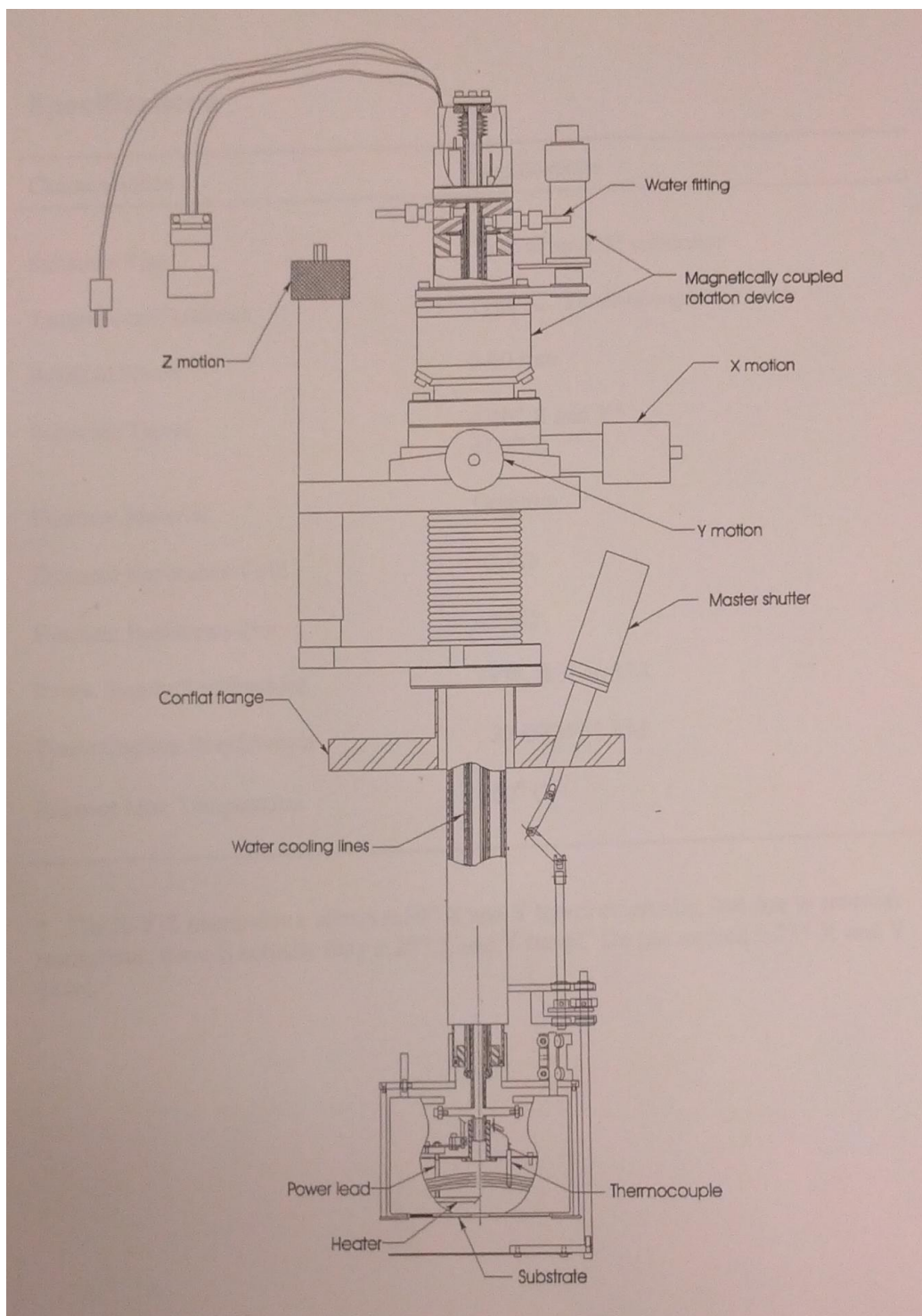


*Figure 2.11.* Main features of the sample stage. Adapted from SVTA operation manual.

calibrated the thermocouple temperature with the temperature reading from pyrometer provided by SVTA, and the agreement between thermocouple reading and pyrometer was within  $\pm 25$  °C. The manipulator is cooled with constantly flowing water to minimize thermal expansion and to protect parts that cannot tolerate the high temperatures encountered during heating the wafer to  $T > 800$  °C. Both stage rotation and substrate temperature can be computer controlled using RoboMBE.

Once the stage is aligned with the platen, we are able to transfer samples from the platen at the end of the transfer arm to the stage. The opening of C-ring support must also be aligned to accept the platen. To load a sample into the sample stage, the stage heater assembly must be raised above the C-ring support by flipping a lever located at the top of the manipulator. After raising the heater, the platen can insert the wafer and wafer block into and above the C-ring. Subsequently, the stage is raised using the manipulator z-motion so that the wafer block rises above the platen and the platen can be retracted from the growth chamber. If the wafer block with a sample sits on the C-ring support perfectly, the heater should lower easily and securely retain the wafer block. This is achieved by flipping back the lever at the top of the manipulator.

### **2.3.2 Bake out procedure and degassing.**

To achieve UHV conditions and an ultra-clean environment required for high-quality growth, the MBE system must be baked out. Contaminants are introduced into the growth chamber whenever it is vented for maintenance or repair. Without a proper bakeout, these contaminants desorb very slowly from the chamber walls and limit the base pressure of the system to the  $10^{-9}$  torr range, which is unsuitable for high quality

material growth. By heating the system up to 200 °C, these contaminants are desorbed from the chamber walls and internal components and are efficiently pumped.

Bake out equipment includes heating elements, a control unit and an insulating tent. There are 6 24” strip heaters mounted under the growth chamber (zone 1), and 8 9” strip heaters and 2 U-shaped heaters mounted under the prep/Ag chamber (zone 2). In each zone, there is a thermocouple mounted on the chamber so that the control unit can monitor and control the bake out temperature. There is a timer in the bake-out control unit, which is used to control the bake out duration. The control unit interrupts the heating current if the pressure exceeds a user-selected setpoint or if the temperature exceeds the selected bakeout temperature. We typically selected a pressure setpoint of  $5 \times 10^{-6}$  torr and temperature setpoints of 180 °C and 160 °C for zone 1 and 2, respectively. Fans in both zones provide efficient air circulation during the bakeout duration to ensure even heating of the entire chamber.

In preparation for the bakeout, all temperature sensitive equipment must be removed from the system or protected to avoid damage by high temperature. All of the PVC water cooling and air supply tubing must be removed from the system. All of the view ports have to be covered with aluminum foil to avoid thermal shock due to the inhomogeneous heat distribution. All of the shutters should be closed and shutter actuators removed. A bake-out wafer should be loaded into the stage, since it will be heated up to 300 °C during the bake out. The DC motor and magnet assemblies on the growth chamber and transfer arm should be removed.

Once these heat intolerant components have been removed from the system, the insulating tent is installed. The gate valve between the cryo pump and growth chamber is

partially closed to reduce the heat load to the cryo pump. The growth chamber stage, prep/Ag chamber stage and the Ag K-cell are heated up to 300 °C to prevent desorbed contaminants from adsorbing on these items during the bake. Once the bake out starts, it usually lasts for 5 days. The bake is manually terminated when the pressure stabilizes at its minimum value for several hours.

After the bake out, all of the system components removed in preparation for the bake must be reinstalled. In addition, all of the deposition sources, stages and shutters need to be degassed before any actual growth. To degas the stages and sources, they are heated up to temperatures higher than those employed for normal deposition. Ag K-cell degassing is accomplished by slowly ramping up the temperature to ~1000 °C while maintaining the pressure below  $5 \times 10^{-7}$  torr. The Ag deposition stage is heated up to 500 °C slowly with the stainless steel shield right below the substrate while maintaining the pressure below  $5 \times 10^{-7}$  torr. Both the Si and Ge e-guns are degassed by slowly ramping up their power up to 72% and 42%, respectively. The stage in growth chamber is degassed up to 650 °C with the master shutter closed. All pneumatically controlled shutters are degassed by exercising them through 30-50 open/close cycles with RoboMBE.

### **2.3.3 Calibration of sources.**

The deposition rates of Si, Ge and Ag are carefully calibrated in order to precisely control the coverage of deposited materials. Both the Si and Ge deposition rates are monitored with QCMs and the detected frequency shifts are proportional to the amount of material deposited. To calibrate these frequency shifts to the amount of deposited material, we used RBS. By performing these measurements at a series of source powers, the dependence of deposition rate on source power was calibrated.

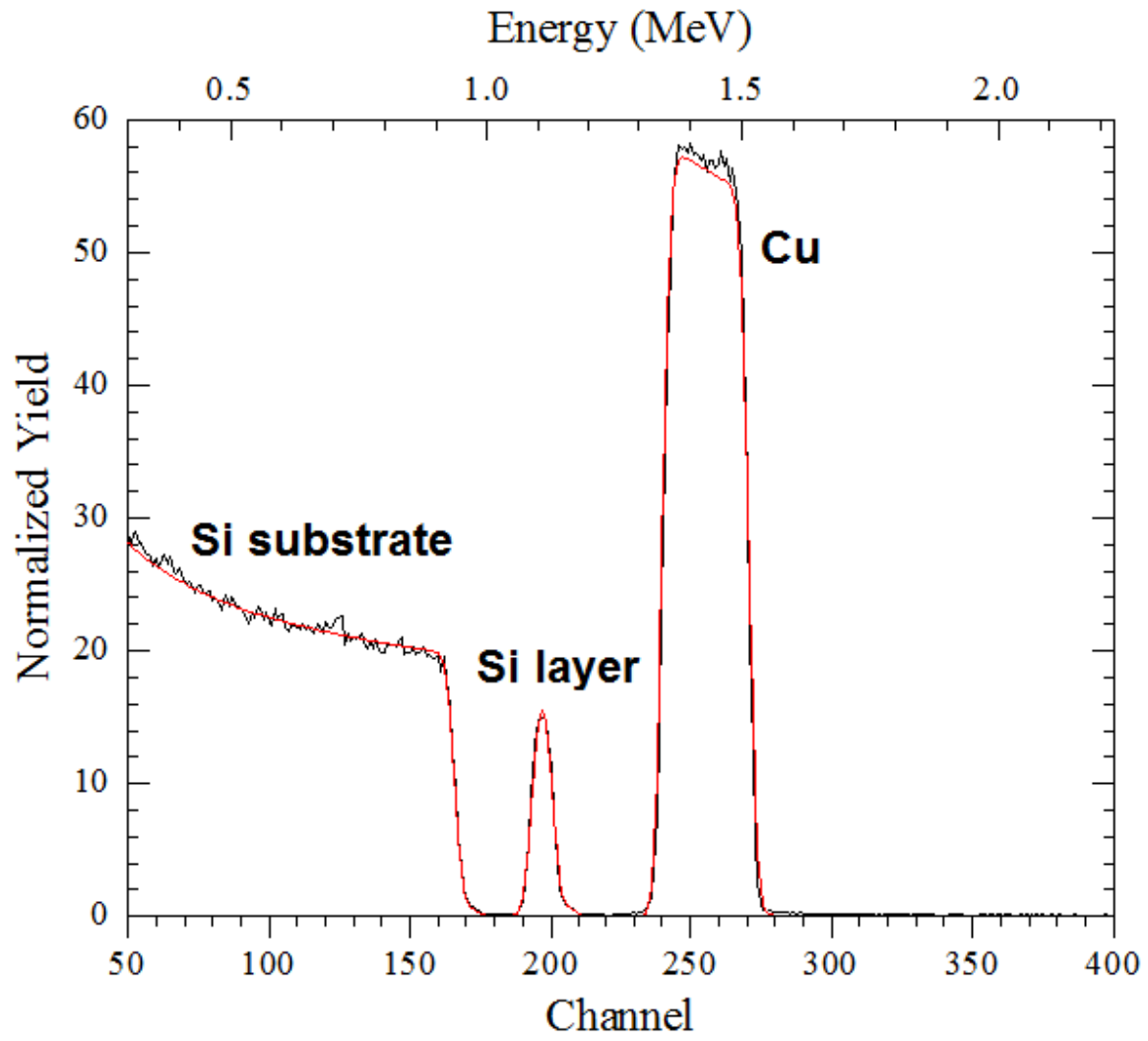


*Figure 2.12.* The normalized RBS spectrum for a Si/Cu film deposited onto Si used for calibrating the Si e-gun deposition rate. The black curve is the raw RBS data and the red curve is the RUMP simulation. The best match was obtained for a Si layer 92.6 nm-thick atop a Cu layer 150 nm-thick.

Since the atomic mass of Ge is sufficiently large compared to that of Si, the Ge peak in a RBS spectrum is well separated from that of the Si substrate. As a consequence,, the Ge deposition rate can be calibrated by simply depositing Ge on the Si surface under normal growth conditions. At least 3 samples were used for Ge rate calibration in order to assess the rate stability. During growth, the Ge deposition rate is feedback-controlled by the QCM and XTC/2. Typically, a growth rate of 2.7 ML/min was used.

It is more challenging to calibrate the Si deposition rate using RBS since the signal of the newly deposited Si cannot be distinguished from that of the substrate. The strategy we used to separate the RBS peak of the newly deposited Si from that of the Si substrate was to sputter a ~150 nm-thick Cu layer atop the Si substrate. The Cu film is thick enough to reduce the energy incoming and backscattered alpha particles as they traverse the film. As a consequence the Si signal associated with the substrate appears at lower energy than that of the newly deposited Si layer, as shown in fig. 2.12. We maintained the sample at room temperature during the Si source calibration to avoid Cu film agglomeration or silicide formation. Following this strategy, the Si egun power and QCM frequency shifts could be calibrated to the actual amount of deposited Si.

The Ag Knudsen cell deposition rate was also calibrated using RBS. This Knudsen cell is different than the one employed in the small MBE, which was discussed in section 2.2.3. At a heating current of 7.10 A, the Ag deposition rate was found to be 3.2 ML/min.

## **2.4 Growth Procedure of Epitaxial Heterostructure**

A complete heterostructure growth begins with wet chemical wafer cleaning and results in a typical sample shown in fig. 2.13. Intermediate steps include overnight degassing, Si buffer layer growth, Ge dot growth, Si cap layer growth, Ag island growth and  $\alpha$ -Si cap layer growth. Si and Ge deposition was carried out in the MBE growth chamber, and Ag deposition was performed in the MBE prep/Ag chamber. Each step of the growth procedure will be discussed in detail in this section.

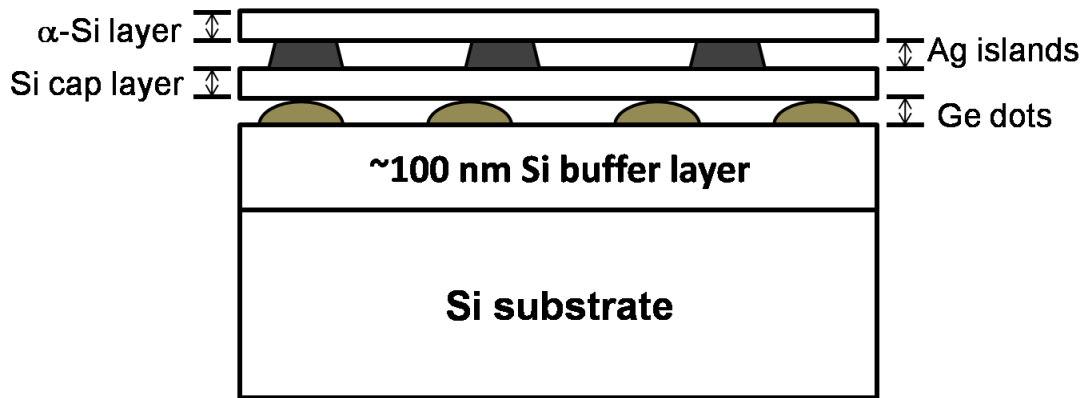


*Figure 2.13.* Schematic of a typical heterostructure showing the buffer layer, Ge dot layer, epitaxial Si cap layer, Ag island layer and  $\alpha$ -Si layer.

#### 2.4.1 Wafer cleaning.

A clean and flat Si surface is crucial for successful epitaxial growth. However, the surface of Si wafers as received from the manufacturer always has a ~10-15 nm thick native oxide layer. On top of this native oxide, contaminants such as hydrocarbons, metals or organic impurities, could exist in the form of particles or films. There are several methods that can be used to clean wafers. These include wet chemical, dry physical or vapor phase methods [141]. To prepare the Si surface for high quality epitaxy, we have found wet chemical methods to be advantageous for two reasons. The first

reason is that wet chemical methods can remove contaminants without damaging the surface or introducing new contaminants. The other reason is that this wet chemical cleaning method removes the native oxide layer and re-grows a less stable wet chemical oxide layer that protects the surface and is easily removed using vacuum processing techniques.

The wet chemical cleaning method employed is a modified RCA process. It uses 3 solutions, SC1 for removing organic, metallic and other impurities from the oxide layer, HF for removing the oxide layer and SC2 for reoxidation. The SC1 solution is made up of DI water,  $\text{NH}_4\text{OH}$  and  $\text{H}_2\text{O}_2$  in the volume ratio of 4:1:1. The SC2 solution is made up of DI water,  $\text{HCl}$  and  $\text{H}_2\text{O}_2$  in the same volume ratio. The HF solution is made by diluting semiconductor grade HF with DI water in the volume ratio of 2:98.

The wafer cleaning process is performed using an acid wet bench equipped with 2 heaters in the ‘class 100’ clean room housed in the Center for Solid State Electronics Research. We use two 4L glass beakers for the SC1 and SC2 solutions, one 4L Teflon beaker for the dilute HF solution, 2 graduated cylinders (1L and 100mL), a Teflon wafer dipper, Teflon tweezers and 2 thermometers. At the beginning of the wafer cleaning, all of the tools and containers are well cleaned with hot SC1 solution (at 80 °C) and DI water. Once these tools and containers are cleaned, we start cleaning wafers by following the modified RCA recipe. Both the SC1 and SC2 solutions are heated to 80 °C. Since the wafer cassette inserted into the MBE system can accommodate 6 wafers, we clean 7 wafers simultaneously. The wafer cleaning process is now detailed [142].

*Step 1-Metallic and organic contaminants removal*



Once the SC1 solution is at 80 °C, we immerse the wafers in the hot SC1 solution for 10 min. The mixture of alkaline  $\text{NH}_4\text{OH}$  and  $\text{H}_2\text{O}_2$  in the SC1 solution is very efficient in removing metals and organic contaminants on the surface. After removal from the SC1 solution, the wafers are immediately rinsed in a flowing DI water bath for 5 min.

*Step 2-Stripping native Si oxide layer*

After 5 min of DI water rinsing, the wafers are immersed in a dilute HF solution for 2 min, which strips the native oxide layer. The HF solution is always held at room temperature. The wafers are rinsed in the flowing DI water bath for 5 min once they are removed from the HF solution.

*Step 3- Repeat step 1 and 2*

Repeating steps 1 and 2 one more time ensures that the Si surface is free of any contaminants or native oxide layer.

*Step 4- Controlled chemical oxide layer re-growth*

After finishing step 3 the wafers are dipped in to 80 °C SC2 solution for 10 min. However, care must be taken so that the SC2 solution is not held at  $T = 80\text{ °C}$  for too long since HCl preferentially evaporates at this high temperature. This hot acidic  $\text{H}_2\text{O}_2$  solution oxidizes the Si surface forming a chemical oxide layer [142]. After the wafers are removed from the SC2 solution, they are rinsed in the flowing DI water bath for 5 min

*Step 5- Stripping the chemical oxide layer*

By immersing the wafers in the dilute HF solution, the chemical oxide layer is removed. This step can reduce the roughness of the Si surface and remove any impurities

trapped underneath the chemical oxide layer. The wafers are next rinsed in the flowing DI water bath for 5 min.

*Step 6- Final growth of chemical oxide layer*

Step 4 is repeated again to grow the final chemical oxide layer on the Si surface. This chemically-formed oxide layer protects the surface, since exposing bare Si to atmosphere can contaminate the surface immediately.

*Step 7- Drying*

Once the wafers have been rinsed in the flowing DI water bath, we carefully dry each of wafers with pressurized nitrogen. The dry N<sub>2</sub> is supplied from a filtered dry nitrogen gun. The freshly cleaned wafers are loaded in the load lock chamber of the MBE system within 30 min.

**2.4.2 Substrate degassing and growth preparation.**

After the wafers are loaded into Mo wafer blocks and the wafer blocks are loaded into the wafer cassette, they are placed into the load lock. After pumping with the turbo pump for 12 hours, the loadlock pressure reaches the mid  $10^{-8}$  torr range and the wafers can be transferred to the prep chamber. During this transfer, the prep chamber pressure can rise from its base value in the mid  $10^{-10}$  torr range to  $\sim 6 \times 10^{-9}$  torr. About 5 hours is required for the prep chamber pressure to fall back to base pressure, at which point it is safe to transfer a wafer to the growth chamber.

A wafer is transferred to the growth chamber on the day before performing a growth. The newly transferred wafer is ready for pre-growth degassing. We have a standard degassing recipe, which includes 3 steps: 1. ramping the substrate temperature from room temperature to 300 °C in 60 min and dwelling at 300 °C for 30 min; 2.

ramping the temperature up from 300 °C to 600 °C in 60 min and dwelling at 600 °C for 30 min; 3. Ramping the temperature up from 600 °C to 650 °C in 30 min and dwelling at 650 °C overnight until the start of the growth. The substrate temperature is automatically controlled by a Eurotherm temperature controller, which is programmed via computer using the RoboMBE software. Degassing the wafer desorbs any trace contaminants on top of the freshly grown chemical oxide layer introduced during atmospheric exposure. Since the chemical oxide layer is stable up to about 800 °C, it is not damaged during the degassing process. During the degassing, the pressure in growth chamber and the substrate temperature are written to a log files stored on the MBE control computer hard drive by the RoboMBE software.

Before initiating growth, the regulator that controls the pressure to the pneumatic valves for the shutters needs to be adjusted to 40 psi. The electron gun sweep control units need to be powered on and the high voltage should be switched on and slowly ramped to 7.5 kV. The Z height of sample stage in the growth chamber should be adjusted to Z=7.6 cm, which is the optimum height for recording RHEED patterns. The EMG-14 RHEED e-gun is manufactured by Kimball Physics inc. The EMPS-14 RHEED e-gun power supply should be powered on and the accelerating voltage should be slowly ramped up to 10 kV. The e-gun filament current should be increased to 3 A to achieve electron emission. Under normal RHEED gun operation, the emission current is about 3 mA. At this point, the MBE system is prepared for growth. During growth, several growth parameters are written to log files that are stored on the control computer hard drive. Parameters logged include the pressure in the growth chamber, substrate temperature and the Si and Ge e-gun power.

### 2.4.3 Si buffer layer, Ge quantum dot and Si cap layer growth.

A growth timing diagram for deposition of the Si buffer layer, Ge QD and Si cap layer is shown in fig 2.14 (a). In fig. 2.14(b), a plot of the actual growth parameters obtained from log files generated by RoboMBE is shown. The similarity between fig 2.14 (a) and fig 2.14 (b) shows that we have good control over those critical growth parameters.

Growing a ~100 nm-thick Si buffer layer on the Si substrate can generate an atomically flat surface and eliminate the influence of any contaminants on the subsequent growth of Ge quantum dots or of Ag islands. To grow the buffer layer, the Si e-gun power is first ramped up to 60% in 40 min while the substrate temperature remains at 650 °C. Next the substrate temperature is ramped up to 700 °C in 10 min while the Si e-gun power remains at 60%. The Si source shutter and master shutter are opened when the substrate temperature starts ramping to 850 °C. While the substrate temperature is ramping up to 850 °C and then down to 600 °C, the Si e-gun power is ramping up to 70% in 30 min. Heating the substrate up to 850 °C will desorb the chemical oxide layer, which begins to desorb at around  $T = 800$  °C. The  $2 \times 1$  Si(100) surface reconstruction can be clearly observed in the RHEED pattern as the substrate temperature reaches 850 °C. We have found that it is critical to supply low Si flux ( $\sim 0.7$  Å/s) to the substrate while desorbing the chemical oxide layer. If this Si flux is not supplied, the surface roughens. If the Si flux is too high, the chemical oxide may be trapped.

After desorbing the oxide, when the substrate temperature is at 600 °C, the Si deposition rate is 2.6 nm/min. To reach a Si buffer layer thickness near 100 nm, about 40

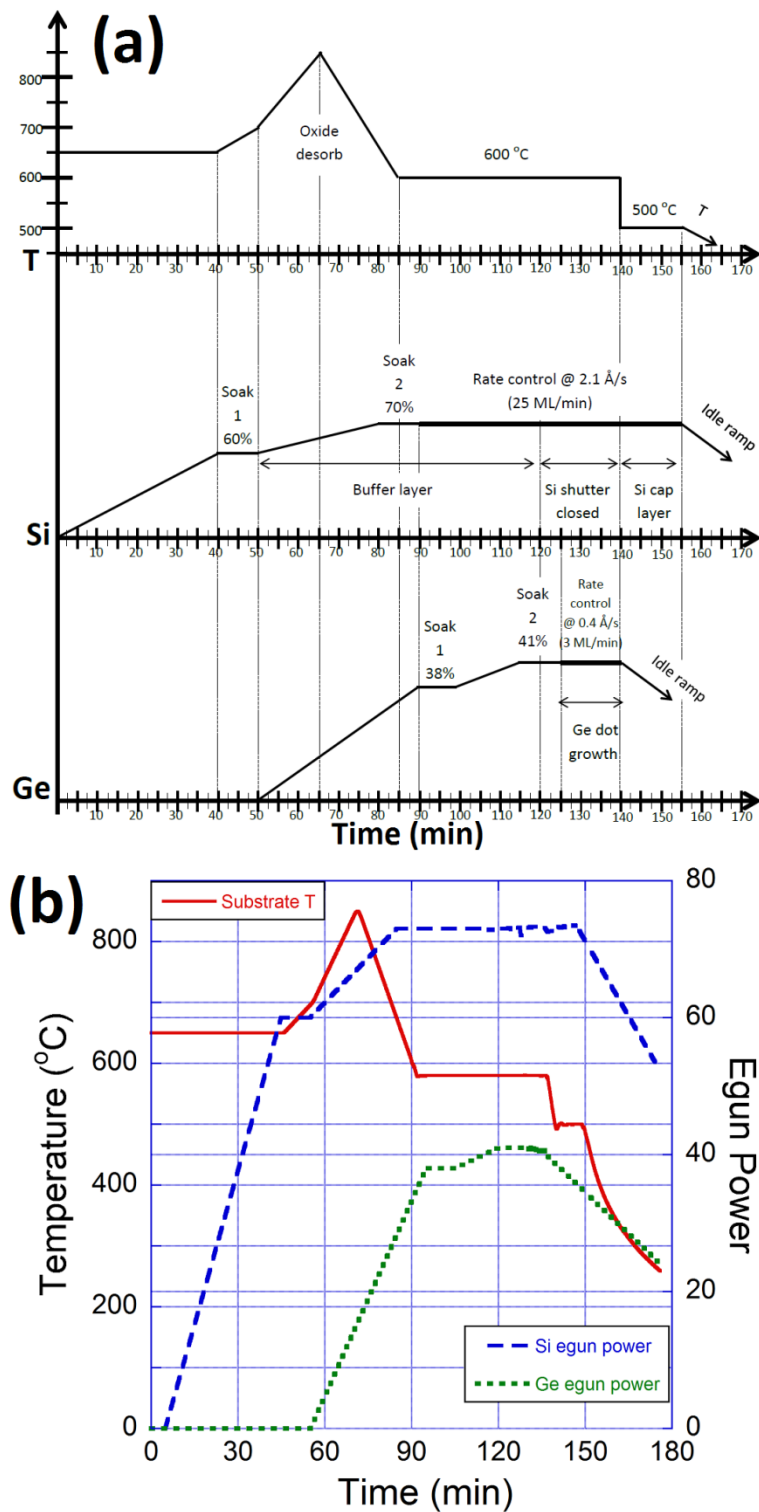


Figure 2.14. (a) Growth timing diagram for a typical sample. T is the substrate temperature, and Si (Ge) represents Si (Ge) e-gun power. (b) plots log files generated by Robo MBE corresponding to the timing diagrams in (a).

min of deposition at this rate is required. During buffer layer growth, the Si egun rate is controlled by the XTC/2 and QCM.

As shown in fig. 2.14, the Ge source begins ramping to its deposition power at the same time the Si source begins its increase from 60% to 70%. The Ge source reaches its deposition power of 41% just 5 min before completion of the Si buffer layer. As a consequence, the Ge deposition can be initiated 3 min after completion of the Si buffer layer. Ge deposition is also performed at a substrate temperature of 600 °C. During Ge dot growth, the Ge deposition rate is controlled by the XTC/2 and QCM at a rate of 2.7 ML/min. We deposit either 6.8 ML or 5.6 ML Ge in order to get significantly different densities of Ge domes. The morphology of Ge quantum dots has already been discussed in chapter 1.

During Ge dot growth, the Si source is kept under rate control with the Si source shutter closed. Growth of the Si cap layer atop the Ge dots is initiated by simultaneously closing the Ge source shutter and opening the Si source shutter. We employed two temperature profiles during growth of the Si cap layer. One of these profiles maintained the substrate temperature at 600 °C during growth of the entire cap layer growth. The second profile ramped down the temperature of substrate from 600 °C to 500 °C as quickly as possible after completing Ge dot growth.

Using cross-section TEM, we found that growing the Si cap layer while holding the substrate temperature at 600 °C almost completely flattens the Ge dots, resulting in a Ge quantum well rather than Si capped Ge quantum dots. In contrast, growing the cap layer almost completely at a substrate temperature of  $T = 500\text{ }^{\circ}\text{C}$  more faithfully preserves the shape of the Ge dome clusters. Once the Si cap layer growth is done, we

immediately ramp the substrate temperature down to room temperature and ramp the Si source power down to zero. The thickness of Si cap layer was varied between 10 nm and 30 nm in order to determine the optimum thickness for PL enhancement.

#### **2.4.4 Ag island growth.**

We transfer the sample to the prep/Ag chamber for Ag island growth about 90 min after the Si cap layer growth is done. The sample heater in Ag chamber is already ramped up to the Ag island growth temperature and the Ag source is ramped up to ~500 °C when transferring the sample from growth chamber to prep/Ag chamber. Ag island growth is initialized by opening Ag source shutter 35 min after the sample is loaded onto the heater stage. About 9.6 ML Ag is deposited atop the Si cap layer. The substrate temperature during Ag island growth was varied from 350 °C to 450 °C to achieve the desired Ag island size and density.

#### **2.4.5 Amorphous Si layer growth.**

For some samples, we grew a 30 nm-thick  $\alpha$ -Si layer on top of the Ag islands. Theory suggests that the surface plasmon resonance of Ag islands can be redshifted to the near IR range by encapsulating the Ag islands in  $\alpha$ -Si. To grow this  $\alpha$ -Si layer, the sample is transferred back to growth chamber about 30 min after the Ag island growth is done. The Si source is ramped up to the Si deposition condition with the same recipe discussed in section 2.4. About 30 nm of Si is deposited onto the wafer, which is maintained at room temperature. When the growth is done, the sample is removed from the MBE for *ex-situ* characterization.

### **2.5 Sample Characterization**

Various characterization tools and techniques were employed in this research project to measure the morphology and optical properties of samples. These characterization techniques will be briefly discussed in this section.

### **2.5.1 Atomic force microscopy.**

AFM is a useful technique to image the surface morphology of MBE-grown samples. The basic principle of AFM is to extract surface morphology information utilizing the interactions between a sharp tip and the sample surface. Based on the types of interactions, there are several types of force microscopes, including magnetic force, electrostatic force and atomic force. We have employed atomic force microscopy for our measurements, so we will focus on this type of microscope.

The physics of AFM is based on the Lennard-Jones potential, therefore, this type of microscope is capable of converting the magnitude of the interatomic force to the distance between the tip and the sample surface. A schematic of a typical AFM is shown in Fig 2.15. A typical AFM includes a cantilever with a sharp tip at one end, a diode laser, a quadranted photodiode and a mechanical scanning system. The beam from the laser diode is reflected off the back of the cantilever onto the photodiodes. As the tip scans the sample surface, the cantilever is deflected and the intensity sensed by the different quadrants of the photodiode changes. These intensity variations are converted into cantilever deflection, producing a map of surface topography as the tip is raster scanned over the surface.

There are two main operation modes for AFM, contact mode and tapping mode. We used tapping mode for all of our measurements, because tapping mode is better in reducing artifacts and in protecting both tip and sample. In tapping mode, the cantilever



oscillates at its resonant frequency and the oscillation amplitude is maintained at a constant value as the tip is rastered over the sample surface. As the tip encounters a feature on the surface, the oscillation amplitude changes and the z-actuator has to be adjusted so that the amplitude regains the set point. Height information can be extracted by tracking the z-actuator adjustment. The amplitude change can also be recorded to produce an image. These amplitude images appear to be similar to derivatives of the height image. The AFMs used in this project are housed in the LeRoy Eyring Center for Solid State Science (LE-CSSS) at ASU.

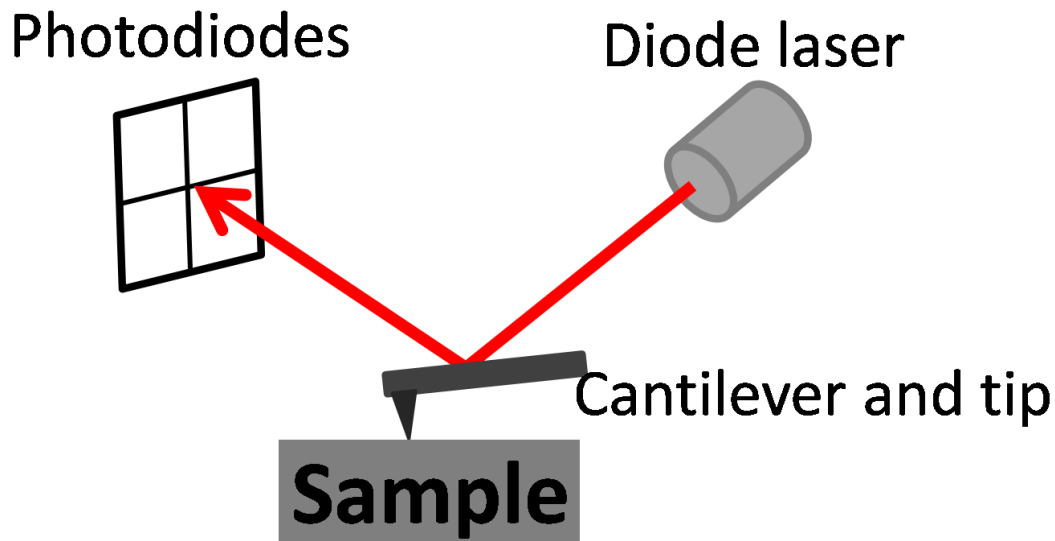


*Figure 2.15.* A schematic showing the basic components of a standard AFM.

### **2.5.2 Rutherford back scattering.**

RBS is an excellent technique for quantitatively determining the areal density of elements on surfaces. The depth distribution of an individual element in the depth range of  $1\mu\text{m}$ - $5\mu\text{m}$  can be determined since the incident ions inelastically scatter and lose energy for films in this thickness range. For elements heavier than the substrate elements,

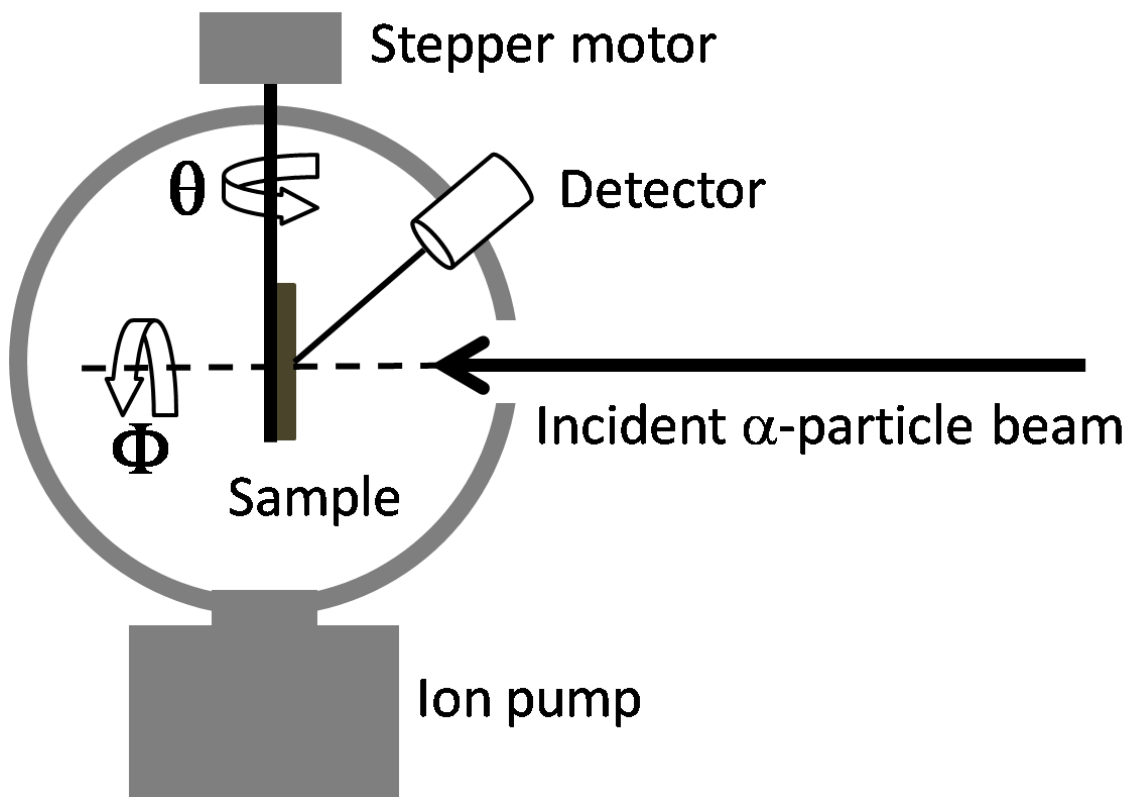


*Figure 2.16.* Schematic of RBS main chamber.  $\alpha$  particles are scattered from the sample and are collected by detector. By analyzing the energy loss of the scattered particles, the mass spectrum of the target material can be easily generated.

RBS provides up to 0.1 monolayer sensitivity, which makes RBS an excellent technique for characterizing our samples (Ag or Ge on a Si substrate). The basic principle of RBS lies classical particle scattering theory. After the interaction between an incident high energy ion and the target, the energy loss of the back scattered particle provides elemental information about the surface of target.

RBS has been extensively used to determine the areal Ag and Ge coverage. And as previously discussed, this information is used to calibrate the Ge, Si and Ag deposition rates. Fig. 2.16 shows the schematic of the RBS instrument. RBS spectra were acquired

under high vacuum condition in the ASU Ion Beam analysis facility in LE-CSSS. A 3 mm by 3 mm  $\alpha$ -particle ( $\text{He}^{++}$  ion) beam is incident at 2 MeV. The sample is mounted on a goniometer that can rotate the sample about 2 different axes, as shown in fig. 2.16. To prevent ion channeling, the sample is randomly rotated about the ' $\Phi$ ' axis in the range of 5 degrees during spectrum acquisition. Once the acquisition is complete, the elemental composition of the sample surface can be deduced in terms of atoms/cm<sup>2</sup> by using the analytical software package RUMP. Fig. 2.13 shows a typical RBS spectrum of a sample with 56 nm Si and 150 nm Cu on a Si substrate.

### **2.5.3 Scanning electron microscopy.**

Besides AFM, we have also used SEM to obtain morphological and statistical information about Ag islands and Ge quantum dots. When the height information of surface features is not that crucial, SEM is a more efficient characterization technique than AFM, especially for imaging large areas. The instrument model is a Hitachi S-4700-II field emission SEM. This microscope is housed in the Center for Solid State Electronics Research. Different sample holders enable imaging in either plan-view or cross-sectional mode. We used plan-view mode to study the shape and size distribution of Ag islands and Ge quantum dots. In cross-sectional mode, information about island height can be acquired.

A SEM image is acquired by scanning the high energy primary electron beam (5~30 keV) over the sample surface and collecting the low energy secondary electrons (<50 eV) emitted from the sample surface created by the interaction with the primary beam. Fig. 2.17 shows the geometry of a typical SEM column, which is adapted from ref. [143]. SEM image acquisition is performed under high vacuum condition, since this

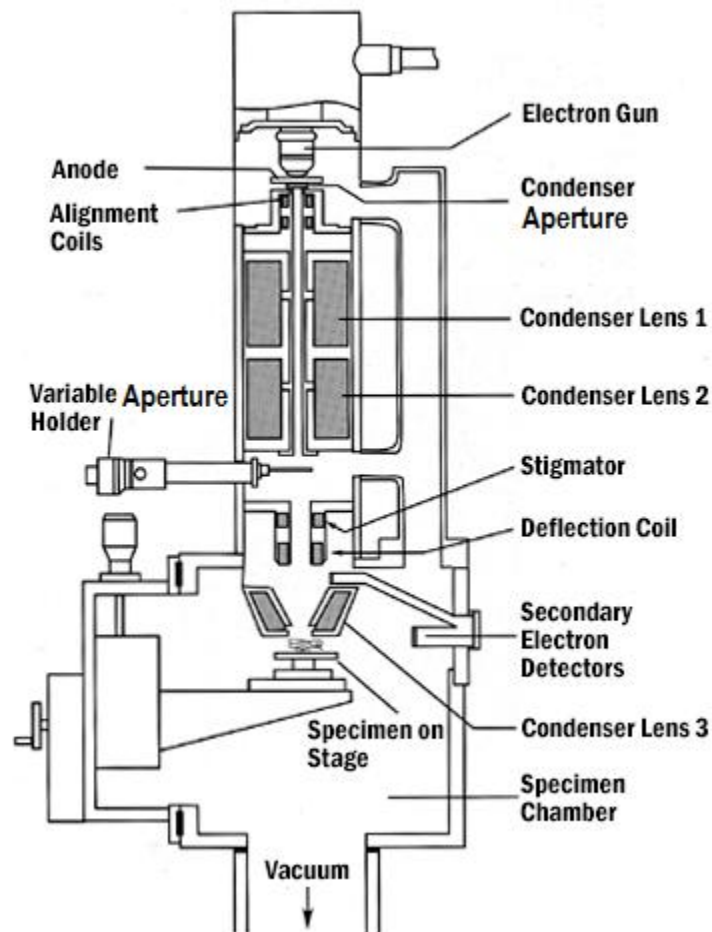


*Figure 2.17.* Schematic of a typical SEM column. This diagram is adapted from ref [143].

can prevent electrical discharge of the egun assembly and beam scattering caused by gas-electron collisions. The electron beam is first generated by applying an extraction voltage of 5 kV to a sharp W tip from which electrons are field emitted. The electron beam then passes through a condenser aperture and two condenser lenses. The condenser aperture skims off high angle electrons, and the condenser lenses control the convergence angle to prepare the beam for focusing on the sample. The beam then passes through the objective

aperture, which limits the beam current and partially controls the beam spot size. The beam becomes uneven and elliptical due to imperfections of the condenser lenses and apertures. Passing the beam through quadrupole stigmators can correct these aberrations, producing a circular beam. Finally, the objective lens focuses the beam on the sample and the deflector coil enables the beam to raster on the sample.

The quality of a SEM image can be optimized by adjusting the accelerating voltage, working distance and aperture diameter. For most of our measurements with SEM, we used a 15 kV accelerating voltage and a working distance of 6 mm.

#### **2.5.4 Transmission electron microscopy.**

TEM is a useful and powerful characterization technique for analyzing the internal structure of samples, e. g. the morphology of embedded nanoparticles, defects, interfaces of thin films and chemical compositions. TEM uses a parallel electron beam to illuminate electron-transparent samples (sample thickness  $<100$  nm) and images the sample by collecting electrons transmitted through the sample. The incident electron beam energy is usually between 100 keV and 400 keV, which can provide the spatial resolution of Angstroms. Cross-sectional TEM (XTEM) has been used to analyze the Ag islands and Ge quantum dots that have been encapsulated in a Si matrix. All TEM measurements presented in this dissertation have been acquired through collaboration with Prof. David Smith and his group.

#### **2.5.5 Photoluminescence.**

Photoluminescence (PL) is a widely used characterization technique to characterize the optical properties of materials. For semiconductors, PL can provide information about electronic properties such as the bandgap, defects, dopant ionization

energies, band edge offsets and quantum efficiency. The basic principle of PL characterization of semiconductors involves two steps. Step 1 is photoexcitation of the sample using light at energies greater than the excitation to be characterized. Step 2 is to spectroscopically detect the radiative electron-hole recombination. We performed PL measurements to characterize the luminescence of the Ge quantum dots and the effect of the Ag localized surface plasmon resonance on the Ge PL intensity.

Fig. 2.18 shows a schematic of the PL apparatus employed in this work. It is maintained by Dr. Christian Poweleit and is located in the Physics Laser Facility. This PL system includes an excitation source, a cryostat, a collection system and detection system. The excitation source we employed is a laser. Both Si and Ge are indirect bandgap semiconductors, so the radiative recombination rate is low resulting in low signal-to-noise ratio PL spectra. The signal-to-noise ratio can be increased by cooling the sample to 10 K, which can reduce much of the thermal degradation of the PL process. The cryostat is a necessary component for our PL measurements. The collection system consists of lenses, mirrors, filters and a spectrometer. The detection system includes detector and a lock-in amplifier. Data acquisition is computer controlled.

The laser we used as the excitation source is either a Nd: YAG green laser (532 nm) or HeCd blue laser (468 nm). The incident laser beam passes through an optical chopper which enables detection using standard lock-in amplifier techniques. The initial laser beam size is in the mm range, so lenses are used to focus the beam onto the sample which is mounted on sample stage in cryostat. The final spot size at the sample was varied from 500  $\mu\text{m}$  to 5 mm, which enabled excitation intensity effects on the PL to be investigated.

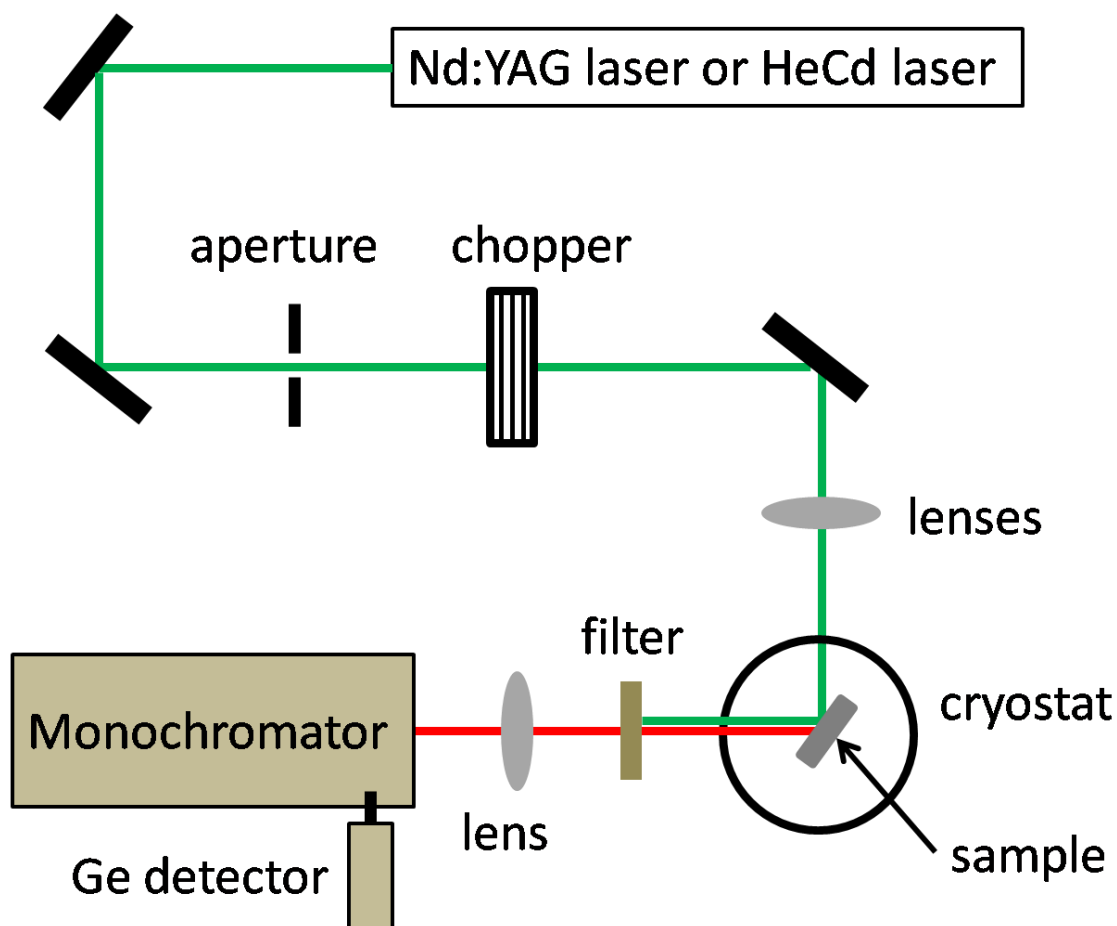


*Figure 2.18.* Schematic of PL system. Most PL spectra were acquired using the Nd:YAG laser. Some were acquired using the HeCd laser to determine the effect of excitation energy on the PL spectra of our samples.

A mechanical pump is used to pump the cryostat for at least 1 hour before cooling the sample down, and can be isolated from the cryostat by a valve once cooling is started. The sample can be cooled down to 10 K using a water-cooled closed-cycle helium refrigerator. After the excitation from the focused laser beam, the emission from the sample is focused by a lens onto the entrance slits of a spectrometer. The reflected laser beam is blocked from entering the spectrometer by an 850 nm filter. The detector is a liquid nitrogen cooled Ge detector with a spectral response window of 600 nm-1700 nm.

For most of our measurements, we used a laser power of 70 mW,. Most spectra were acquired using a dwell time of 9 seconds per data point with a 5 nm step through a spectral window of 900 nm to 1600 nm. The sensitivity was set to 20 mV during acquisition.

#### **2.5.6 Spectroscopic ellipsometry.**

Spectroscopic ellipsometry (SE) is a sensitive technique to determine the optical properties of surfaces by performing standard ellipsometry at a varying wavelength. SE measures the change in the polarization state between linearly polarized incident and reflected light. A schematic of a spectroscopic ellipsometer is shown in fig. 2.19. Because the reflection coefficients for the two orthogonal polarizations are different, the reflected light becomes elliptically polarized. SE simultaneously measures both the amplitude ratio  $\Psi$  ( $\tan(\Psi)=E_p/E_s$  where  $E_p$  and  $E_s$  are p- and s-components of the electric field, respectively) and the phase difference  $\Delta$  of these orthogonally polarized components. The dielectric function of a surface can be extracted from these measurements. For a thin film system, the ‘pseudodielectric’ function can be extracted. The pseudodielectric response can be modeled to obtain parameters such as film thickness for uniform films. For island films, the situation is much more complicated and more sophisticated modeling is required.

The pseudodielectric response of Ag/Si(100) islands was compared to results of a simulation employing the thin island film model that was developed by Bedeaux and Vlieger [144]. The SE measurements were carried out at room temperature using a variable-angle ellipsometer of VASE 18 from J. A. Woollam Co., in collaboration with the group of Professor Jose Menendez. The spectroscopic energy range for our



measurements varies from 0.6 eV to 4.8 eV, and the incident angle was set to 70 °, which is close the Brewster angle of Si.

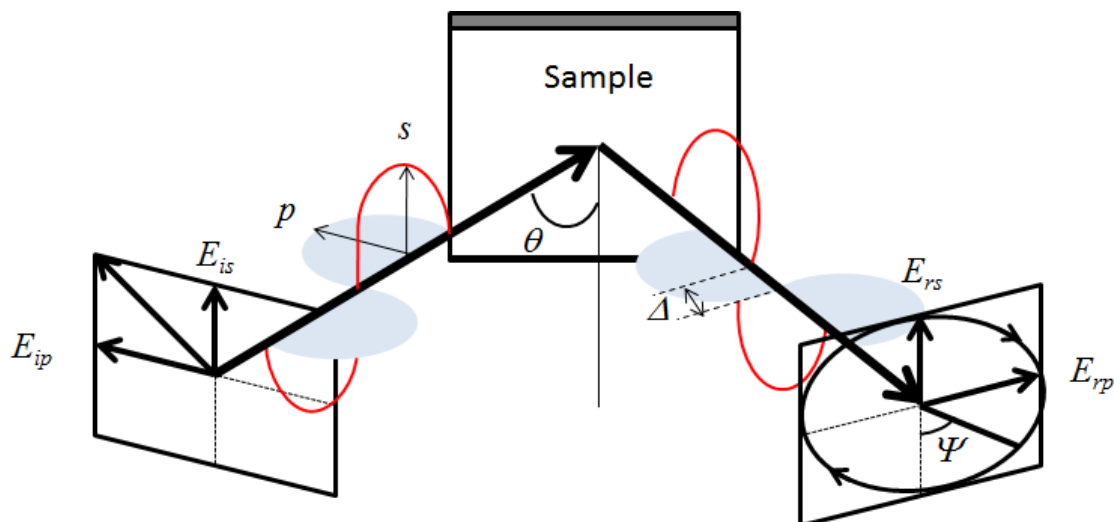


Figure 2.19. Schematic of ellipsometry measurement geometry.

### 2.5.7 X-ray photoelectron spectroscopy.

XPS is a sensitive technique for probing the elemental composition and associated chemical bonding states of the sample near surface region. The basic principle of XPS is to excite the near surface atoms with X-rays, and then the secondary electrons emitted from the sample surface are spectrally analyzed. The penetration depth of X-rays could be up to 1  $\mu\text{m}$  or so, but only photo-emitted electrons from near surface atoms can actually escape and be detected. Photoelectrons can undergo inelastic collision, they can be recaptured, they can excite the sample, and they can recombine or be trapped in excited states. All of these processes contribute to an exponential decrease in escape probability as the depth of the photoexcitation event increases. As a consequence, photoelectron spectroscopy is very surface sensitive. XPS is typically sensitive to the 3

nm - 5 nm region nearest the surface. The acquired photoelectron spectrum provides the information about the composition and bonding of surface atoms. The energy resolution of XPS is good enough so that subtle shifts in elemental photoelectron energies can be correlated with chemical bonding. XPS can have a composition sensitivity of 0.1 – 1 percent (for Li or heavier atoms).

We used XPS to determine the relative compositions of Si and Ge at the surface of the Si cap layer grown atop the Ge quantum dots. These measurements were performed to assess the degree of Ge surface segregation during Si cap layer growth for different Si cap layer thicknesses. The XPS measurements were performed by Timothy Karcher, a research scientist in LE-CSSS. He employed an Al K $\alpha$  line at 1486 eV and his electron spectrometer is capable of an energy resolution of 0.7 eV. The X-ray spot size on the sample can be as large as 500  $\mu$ m in diameter.

#### **2.5.8 Raman spectroscopy.**

Raman spectroscopy is a non-destructive spectroscopic technique to probe vibrational, rotational and other low-frequency modes in a system. Raman spectroscopy relies on the inelastic scattering of incident laser light from the sample. The interactions between incident laser light and low-energy excitations of the sample, such as phonons, result in the energy of scattered photons being shifted up (anti Stokes shift) or down (Stokes shift). The energy shift of scattered laser photons contains information about sample, e.g., the vibrational modes of the sample. Analysis of the energy and intensity of these vibrational modes allows us to determine the phase present or to investigate the strain field in the sample.

We used Raman spectroscopy to investigate the average strain in the of Si cap layer. The Raman spectroscopy system we employed is maintained by Dr. Christian Poweleit and it is housed in the Physics Laser Facility. The Raman measurements were performed using laser excitation at a wavelength of 532 nm or 364 nm with an incident power of 1 mW. An optical microscope focuses the laser beam on the sample to a circular spot with 1  $\mu\text{m}$  diameter and collects the scattered light. The elastically scattered light is filtered by a notch filter. The Raman scattering signal is dispersed by a 0.5 m Acton spectrometer and then detected by a Princeton Instruments back-thinned Si CCD camera with a 2  $\text{cm}^{-1}$  FWHM resolution.

## CHAPTER 3

### RESULTS AND DISCUSSION

In this chapter, the results of the investigation into the effect of the localized surface plasmon resonance of the epitaxial Ag islands on the photoluminescence (PL) of Ge quantum dots (QDs) will be presented. The systematic investigation of Ag/Si(100) island growth will be discussed first. These results establish a baseline for comparison to the Ag islands grown on Si cap layers. Two types of Ag islands were observed, and the evolution of each type of Ag islands with the growth temperature and growth-temperature annealing will be discussed in the first section.

In the second section, the plasmonic properties of epitaxial Ag/Si(100) islands will be discussed in detail. The research project seeks to enhance the PL of Ge QDs by utilizing the localized surface plasmon resonance (LSPR) of Ag islands grown on Si(100), so the investigation of the plasmonic properties of Ag islands grown on Si(100) could be useful for us to optimize the plasmonic enhancement. Spectroscopic ellipsometry was employed to study the plasmonic properties of Ag islands grown on Si. From these measurements, the pseudodielectric function of the Ag island / Si(100) system was determined. It is difficult to identify the plasmonic features of Ag islands due to the variation of the Si dielectric function in the spectral range of interest, so we used thin island film (TIF) theory to simulate the pseudodielectric functions in order to assist in associating spectral features with the LSPR of the Ag islands.

In the third section, the growth of our final heterostructure will be discussed step by step. An atomically flat Si buffer layer is critical for the growth of complete heterostructure, so the buffer layer quality will be discussed first. Next, Ge QD growth

results are presented. The epitaxial Si cap layer growth process has a significant effect on the morphology and PL of the Ge dots. The relationship between the cap layer growth process and the properties of the Ge dots will be discussed. Finally, the growth of Ag islands on the Si cap layers is discussed. Our investigation shows that the density of Ag islands depends significantly on the thickness of the Si cap layer, and the physical factors that may contribute to this dependence are discussed.

In the last section, the effect of the Ag LSPR on the Ge QD PL will be presented in detail. The results of the investigation into optimizing the Ge dot-related PL will be discussed first. An understanding of the PL spectra of Ge dots in the absence of Ag islands is required to assess any Ag LSPR-related alterations to the spectra. The plasmonic effect of Ag islands capped with 30 nm amorphous Si ( $\alpha$ -Si) layer on the Ge dot-related PL peaks and Si band-gap peak will then be discussed. The effect of LSPR of bare Ag islands on the Ge dot-related PL peaks and Si band-gap peak was also investigated, and the results of our investigation will be discussed next. The LSPR of bare Ag islands can either reduce or enhance the PL intensity of Ge QDs, depending on the doping level of the Si wafers and on the methods of controlling growth temperature. The present findings provide a feasible process to fabricate epitaxial Ag nanoparticles (NPs) into sophisticated Si-based optoelectronic devices, which could enhance the optical performance of the devices by exploiting the LSPR.

### **3.1 Ag/Si(100) Epitaxial Island Growth**

Epitaxial Ag island growth on Si(100) was systematically investigated, the results are discussed now. As-grown samples will be discussed first, followed the discussion of samples annealed at their growth temperature. Two types of Ag islands were observed.

The differences in each of these Ag island types as growth conditions were varied will be discussed in detail in this section.

Ag was deposited onto Si(100) surfaces heated to  $300^{\circ}\text{C} < T < 500^{\circ}\text{C}$ , and we systematically investigated island ensemble morphology as a function of growth and annealing conditions. We found that there are two distinct types of 3D islands formed atop a planar S-K wetting layer. The first, which we will call “big islands” for brevity, have basal dimensions in the few hundred nm to  $\mu\text{m}$  range, are well-faceted with their bases aligned crystallographically to the substrate and form in a variety of shapes. The second type, which we will call “small islands” are not obviously faceted in either atomic force or scanning electron micrographs and have basal dimensions in the few 10s of nm range. These two types of Ag islands behave differently as the growth temperature and the amount of annealing time change, which indicates that the big and small islands form via different mechanisms.

In this section, I will first discuss the island ensemble morphologies and densities observed for as-grown samples, which were rapidly quenched to room temperature immediately after terminating the Ag flux. Next, I will discuss the evolution of island size and density during anneals at the growth temperature. The shape evolution of Ag islands during growth temperature annealing will also be discussed.

### **3.1.1 As-grown Ag/Si(100) islands.**

As mentioned earlier, samples were grown in an ion-pumped ultra high vacuum (UHV) chamber with a base pressure of  $2.0 \times 10^{-10}$  torr. 0.5cm by 4cm strips were cleaved from 4 inch diameter B-doped Si(100) wafers with resistivity  $\rho = 0.01\text{-}0.02 \Omega \text{ cm}$ . The

long axis of the cleaved strips is always parallel to the  $\langle 110 \rangle$  direction, which is used to determine the crystallographic orientation of the elongated axis of big Ag islands.

Fig. 3.1 displays two scanning electron micrographs of Ag islands formed by depositing 5.3 ML (1 ML =  $6.78 \times 10^{14}$  atoms/cm<sup>2</sup>) of Ag onto Si(100) heated to 300 °C. As shown in the higher resolution micrograph of fig. 3.1(a), we observe two distinct families of islands. The first are the big islands, which have basal dimensions in the several hundred nm to  $\mu\text{m}$  range, are clearly faceted and have their bases aligned along  $\langle 110 \rangle$  - type directions.

The second are the small islands, with diameters in the 10s of nm range and are not clearly faceted. Note that there is a region surrounding each big island for which no small islands form and that the width of this denuded zone is comparable to the average spacing between the small islands. Fig. 3.1(b) is a lower resolution scanning electron microscope (SEM) image showing that the big islands form in a variety of shapes. We distinguish the big islands by the shape of their bases: square, rectangular, triangular or irregularly-shaped. The higher resolution images of all these typical island shapes are displayed below fig. 3.1(b). Big islands with triangular bases can also form with truncated triangular bases. Square islands have basal aspect ratios,  $l/w$  (length to width)  $\leq 1.5$  while rectangular islands have  $l/w > 1.5$ . Big islands with irregularly-shaped bases have been observed previously by Li, et al. [117], who called them bamboo-like islands. Fig. 3.2 displays height profiles of islands from the same sample depicted in fig. 3.1. The height profiles were obtained from typical islands along the indicated lines shown in the inset atomic force microscope (AFM) images. The AFM image and linescan in fig. 3.2(a) also shows that the small islands are not clearly faceted and appear mound-like.

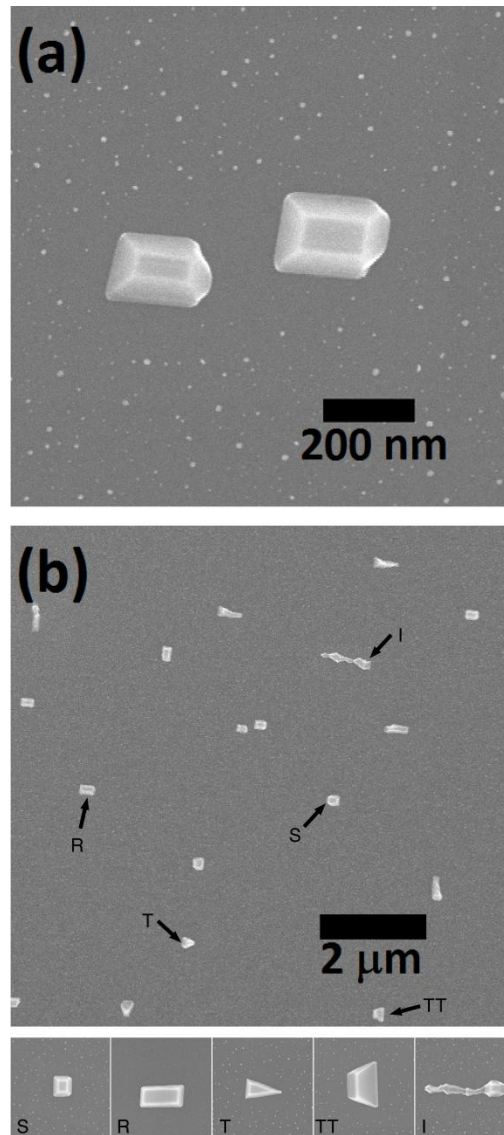


*Figure 3.1.* Scanning electron micrographs of Ag islands formed by depositing 5.3 ML Ag at 2.1 ML/min onto Si(100) heated to 300 °C. (a) clearly shows two distinct classes of islands. The big islands are clearly faceted and their bases are aligned along  $\langle 110 \rangle$ . The big islands shown have rectangular bases. The small islands are not clearly faceted. Note the zone surrounding the big islands that is denuded of small islands. The width of this denuded zone is comparable to the average spacing between the small islands. (b) shows that the big islands form with a variety of basal shapes. The five distinct shapes are identified in the image: S (square), R (rectangular), T (triangular), TT (truncated triangular) and I (irregular). Individual higher resolution ( $1\ \mu\text{m} \times 1\ \mu\text{m}$ ) images of examples of each of these island types are shown below fig. 1(b).



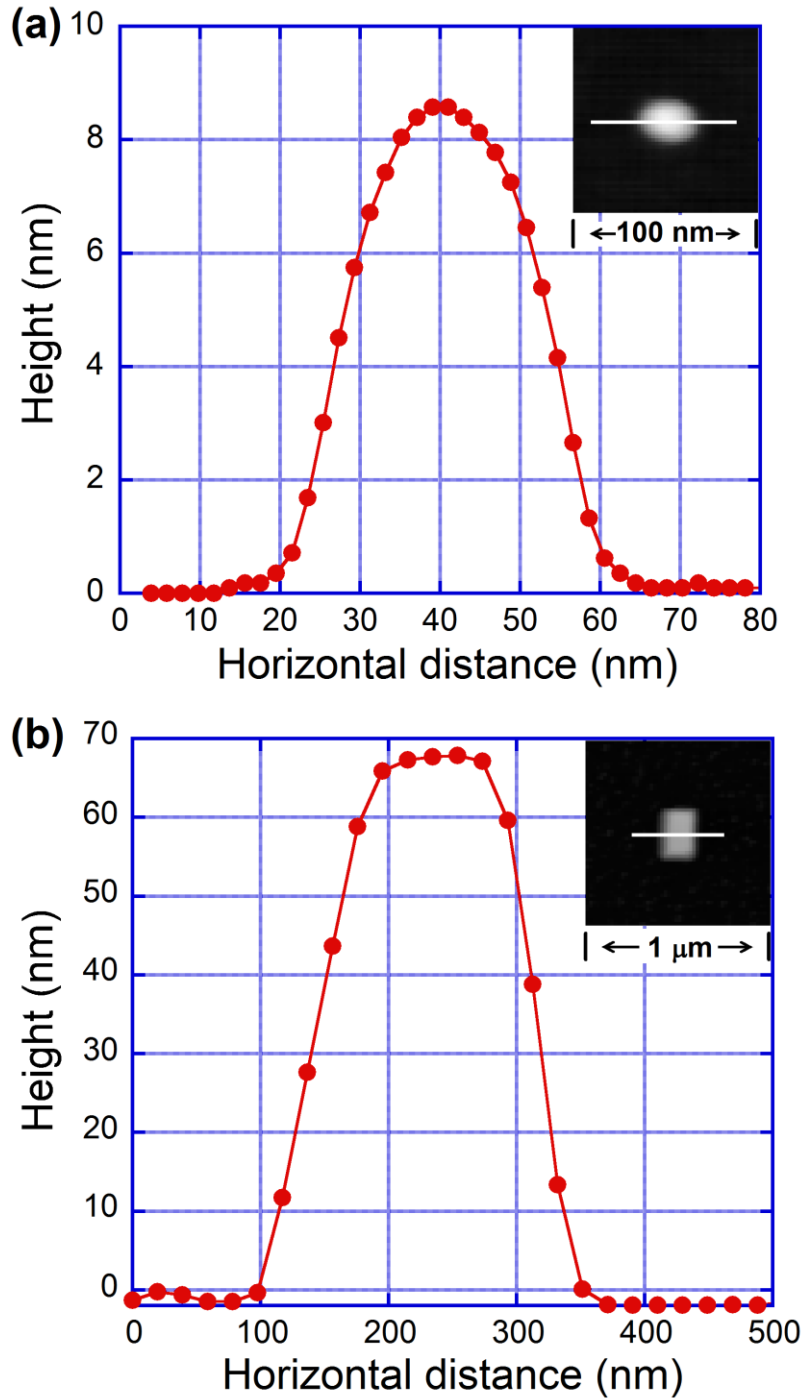


*Figure 3.2.* Height profiles of small (a) and big (b) islands obtained from typical islands along the indicated lines in the inset AFM images. These islands are from the same sample depicted in fig. 1. The small islands are not clearly faceted and appear mound-like while the big island is clearly faceted. These morphologies are typical of big and small islands for the range of growth and annealing conditions investigated.

Similar linescans of small islands indicate that their aspect ratio,  $d/h \sim 5$  (diameter to height) is nearly constant and independent of small island diameter, regardless of growth or annealing conditions. Fig. 3.2(b) displays similar data for a typical rectangular big island. This island is clearly faceted, in agreement with the SEM image shown in fig. 3.1(a). Typically, the aspect ratio of rectangular or square big islands,  $w/h$  (width to height) is in the range 3 to 4, as in fig. 3.2(b). The height of the rectangular big islands can sometimes vary slightly along the long dimension. For triangular or truncated triangular big islands, the height almost always varies along the direction of the island taper, decreasing toward the pointed end.

We examined the effect of growth temperature on the size and areal density of the big islands. A series of samples were grown by depositing 5.3 ML Ag at 2.1 ML/min onto Si(100) heated to temperatures in the 300 - 500 °C range. We scrutinized these samples using SEM and analyzed the images to produce the island size distributions shown in fig. 3.3. These island size distributions were obtained by measuring at least 300 big islands on each sample. The size plotted on the horizontal axis is the square root of the island area measured in the SEM images. Note that the vertical scale changes at higher growth temperatures to facilitate quantitative comparison between the different growth conditions. The average island size, which is roughly the peak in the size distribution at each growth temperature, increases as the growth temperature rises throughout the range we investigated. This is expected for islands form via conventional nucleation and growth mechanisms.

By integrating the area under the peaks for each curve displayed in fig. 3.3, we obtain the areal density of big islands, which is plotted vs. inverse temperature in fig. 3.4.

We estimate that the error bars on our density measurements to be about the size of the plot symbols. The big island density decreases as substrate temperature increases throughout the range of substrate temperatures that we investigated, which would be expected for islands that formed via nucleation and growth. As described in the introduction chapter 1.3.2, the island density depends on the growth temperatures as a function of  $\exp(E_n/kT)$ . By performing linear fit to the plot of the logarithm of density vs  $1/kT$  which is known as an Arrhenius plot, we are able to extract the information about the nucleation energy. From the Arrhenius plot of fig. 3.4, we obtain a nucleation energy of 0.73 eV for the big islands (red solid circles). The excellent linear fit to our nucleation density data suggest that the same kinetic processes contribute to nucleation of Ag islands for the relatively narrow range of temperatures that we investigated.

Although Ag desorption becomes measurable at  $T=500\text{ }^{\circ}\text{C}$ , we believe that the 0.4 ML/hr desorption rate measured using Rutherford back scattering (RBS) only becomes important for the annealing experiments as discussed below. For the 2.5 min duration of the depositions, only about 0.017 ML Ag desorbs, which is not even measurable from RBS. The nucleation energy extracted from our areal density measurements is half the value of 1.45eV found by M. Hanb ücken, et al. [102]. This discrepancy could be attributed to several factors that may include systematic differences in temperature measurements between the two experiments or to different surface preparation procedures. In addition, their growths occurred predominantly at the higher end of the temperature range that they explored ( $T=600\text{ }^{\circ}\text{C}$ ) where Ag desorption becomes increasingly important. A high Ag desorption rate would decrease the nucleation density and increase the nucleation energy.

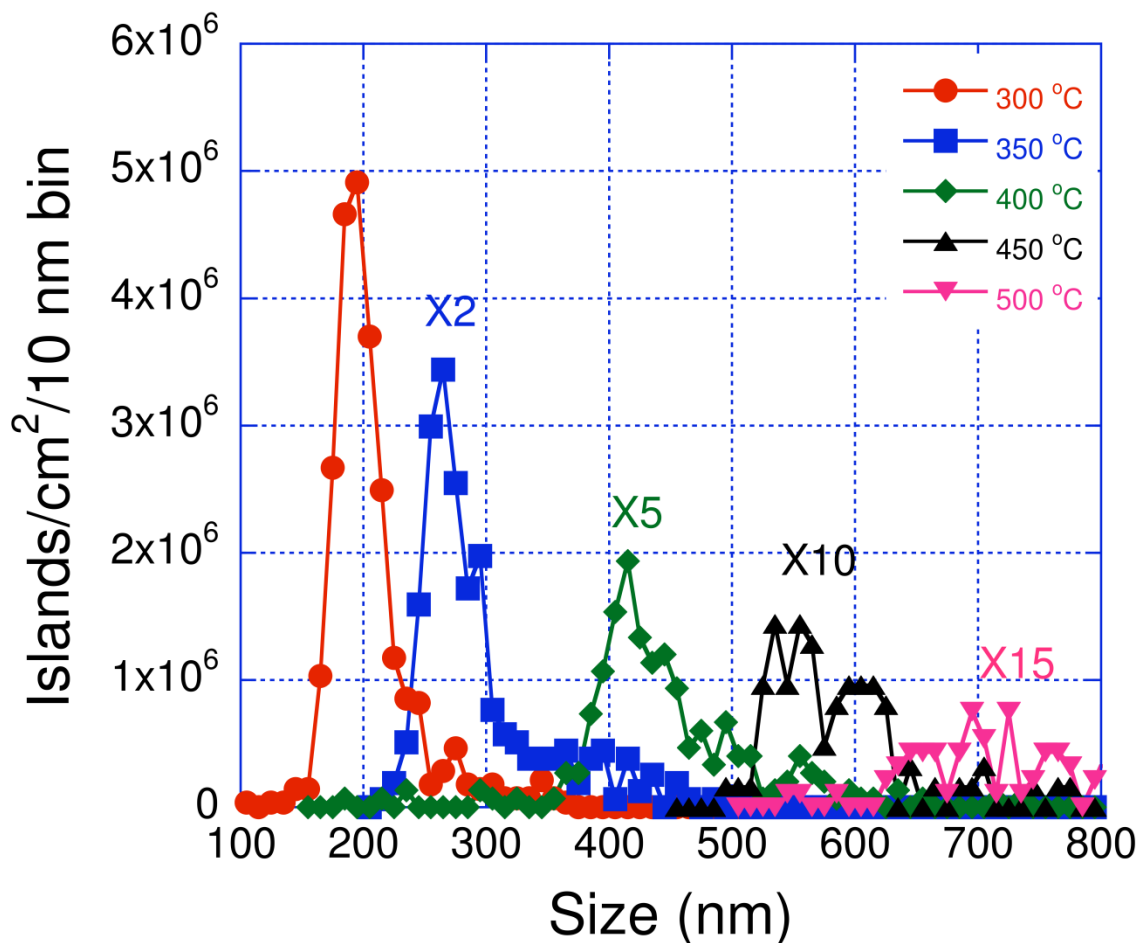
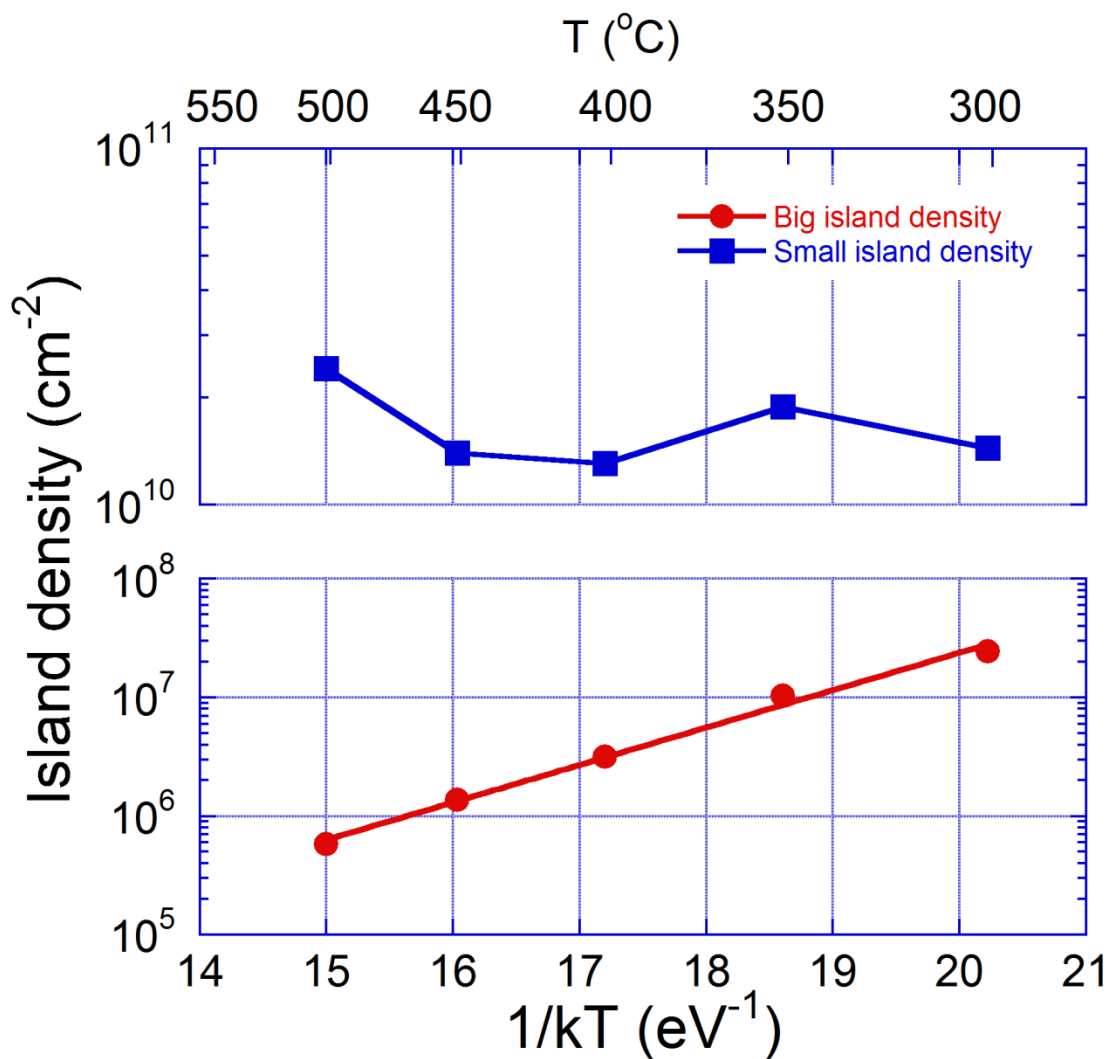


Figure 3.3. Island size distributions for big islands formed via deposition of 5.3 ML Ag at 2.1 ML/min onto Si(100) heated to the indicated temperatures. Note the vertical scale change at  $T \geq 350^\circ\text{C}$ . At these higher growth temperatures, the data have been multiplied by the indicated factors. For example, the maximum in the areal density for  $T=350^\circ\text{C}$  is  $1.8 \times 10^6$  islands/cm<sup>2</sup>. The increase in average size as growth temperature increases is expected for islands formed via nucleation and growth. The size plotted on the horizontal axis is the square root of the island area measured from SEM images. The vertical axis plots the island areal density in islands/cm<sup>2</sup> using 10 nm wide bins.



*Figure 3.4.* Areal density for both big and small islands vs. inverse temperature. The linear dependence of the big island density in the semilogarithmic Arrhenius plot indicates that the big islands form via a nucleation and growth mechanism with a nucleation energy of 0.73 eV. The small island density does not vary systematically over the 300 – 500 °C range, suggesting that they form via some alternate mechanism. The error bar is about the size of the plot symbols.

We now turn our attention to the small islands that are shown in figs. 3.1(a) and 3.2(a). Similar islands have been observed previously by Li, et al., [117] who did not systematically investigate their origin. The small island density for samples grown at the indicated temperatures with  $\theta_{\text{Ag}} = 5.3$  ML using a deposition rate of 2.1 ML/min is also plotted in fig. 3.4. This figure confirms that the small island density is orders of magnitude greater than that of the big islands, as can be seen in the SEM images shown in fig. 3.1(a). Note also that the small island density does not vary systematically and is relatively constant when compared to the big island density that varies by  $\sim 2$  orders of magnitude through the 300-500 °C range. This observation is quantified by the small island size distributions shown in fig. 3.5. Fig. 3.5 shows small island size distributions obtained from AFM images acquired from the same samples for which the density data of fig. 3.4 were obtained. The similar size distributions of small islands in fig. 3.5 confirm that the small island density is relatively constant through the 300-500 °C range. From these observations, we conclude that the formation mechanism of small islands is same for the temperature range of 300-500 °C.

Based on these observations, and those of our annealing experiments that are discussed below, we hypothesized that these small islands are formed via precipitation of Ag that is incorporated into a planar layer in between the big islands. We believe that this planar layer may exceed the  $\frac{1}{4}$  ML thickness of the S-K layer at elevated temperatures [102,105] and the Ag in excess of this thickness precipitates to form the small islands when the sample is quenched from the growth temperature. In order to more fully investigate this peculiar behavior and test our hypothesis, we conceived a series of experiments designed to elucidate the formation mechanism of the small islands.

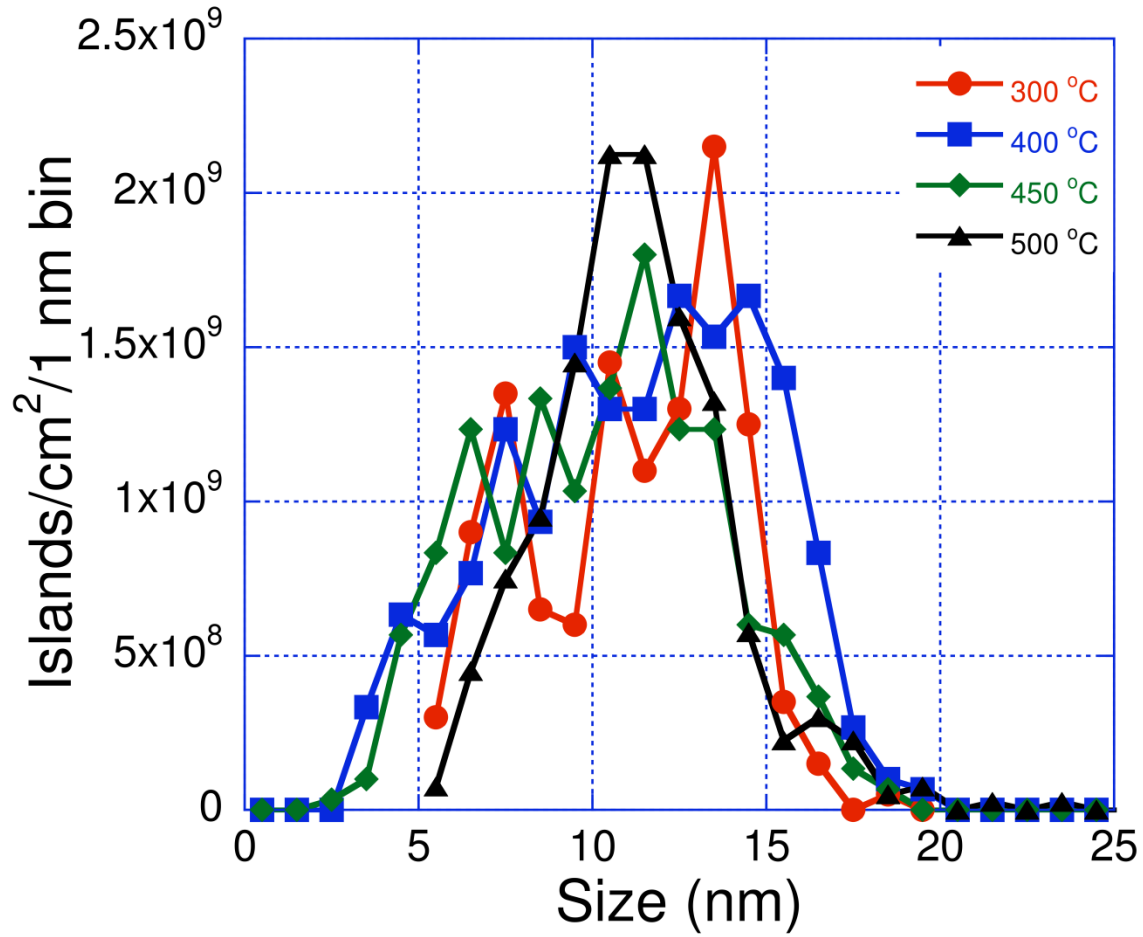


Figure 3.5. Size distributions for small islands grown by depositing 5.3 ML Ag at 2.1 ML/min onto Si(100) heated to the indicated temperatures. The size plotted on the horizontal axis is the cube root of the island volume measured from AFM images.

Using AFM, we carefully examined sample morphologies obtained for Ag deposition to different values of  $\theta_{\text{Ag}}$  for the substrate temperature of 500 °C. We chose 4 different  $\theta_{\text{Ag}}$  values. One was slightly less than the  $\sim 1/4$  ML thickness [102,105] of the S-K layer, 0.22 ML. For this value of  $\theta_{\text{Ag}}$ , we observed no islands. At higher values of  $\theta_{\text{Ag}}$ , 0.6 ML and 0.75ML, we observed small islands, but no big islands. The fourth, and highest value of

$\theta_{\text{Ag}}=0.88$  ML yielded both big and small islands. These observations are summarized in TABLE I.

TABLE I. Existing island types on samples grown to the indicated coverages on Si(100) heated to 500 °C. N = no islands; S = small islands only; B, S = big and small islands

$\theta_{\text{Ag}}$ (ML)	0.22	0.6	0.75	0.88
Existing islands	N	S	S	B, S

The results of these experiments support our hypothesis. That is, the small islands do not exist at the growth temperature and only form as the sample is cooled from the growth temperature. For deposition onto heated Si(100) to  $\theta_{\text{Ag}} < \frac{1}{4}$  ML, all Ag is incorporated into the S-K layer. For deposition to  $\frac{1}{4} < \theta_{\text{Ag}} < 0.8$  ML, no big islands form. Since the small islands that form at these coverages have nearly identical densities and sizes independent of deposition temperature (see figs. 3.4 and 3.5), they clearly do not form via nucleation and growth during Ag deposition. For Ag deposition onto heated Si(100) to  $\theta_{\text{Ag}} > 0.8$  ML, both big islands and small islands form. This scenario can be explained if big islands form atop a  $\sim 3/4$  ML-thick planar layer that is stable at the growth temperature but is not stable at some lower temperature that is passed as the sample cools to room temperature. As the sample cools, additional Ag becomes available for island formation as the planar layer that has grown to a thickness in excess of the  $\frac{1}{4}$  ML – thick S-K layer decays. Since the sample is at a lower temperature than the one at



which the big islands formed, the Ag diffusion length is shorter and the small island density is much larger than the big island density.

### **3.1.2 Growth temperature annealing.**

Some samples prepared identically to those discussed above were annealed at their growth temperature for 1 or 2 hours in order to investigate island ensemble stability and to further elucidate the small island formation mechanism. From these experiments, we are able to conclude that the big islands undergo peculiar anti-coarsening behavior, their density increases and their average size decreases as annealing time increases. This anti-coarsening behavior is opposite to Ostwald ripening as described in introduction chapter. We also find that their shapes evolve. It is more difficult to identify systematic behavior of the small islands during growth temperature annealing. However, we believe that their ‘stability’ during prolonged annealing at their growth temperature is further support for our hypothesis that they do not exist at the elevated growth or annealing temperature and only form as the samples are cooled to room temperature.

We first discuss the behavior of small islands during growth temperature annealing. Fig. 3.6 displays the evolution of both the big and small island areal densities during growth temperature annealing at 300 and 400 °C for up to 2 hours. The island densities were determined by analyzing a total area of  $\sim 10 \mu\text{m}^2$  from SEM images. Fig. 3.7 displays the average size of small islands vs. annealing time at 400 °C measured by AFM. First, we note that the small islands ‘survive’ growth temperature anneals for up to 2 hours. This observation further supports our hypothesis that the small islands do not exist at growth or annealing temperatures in the 300-500 °C range. That is, if the big and

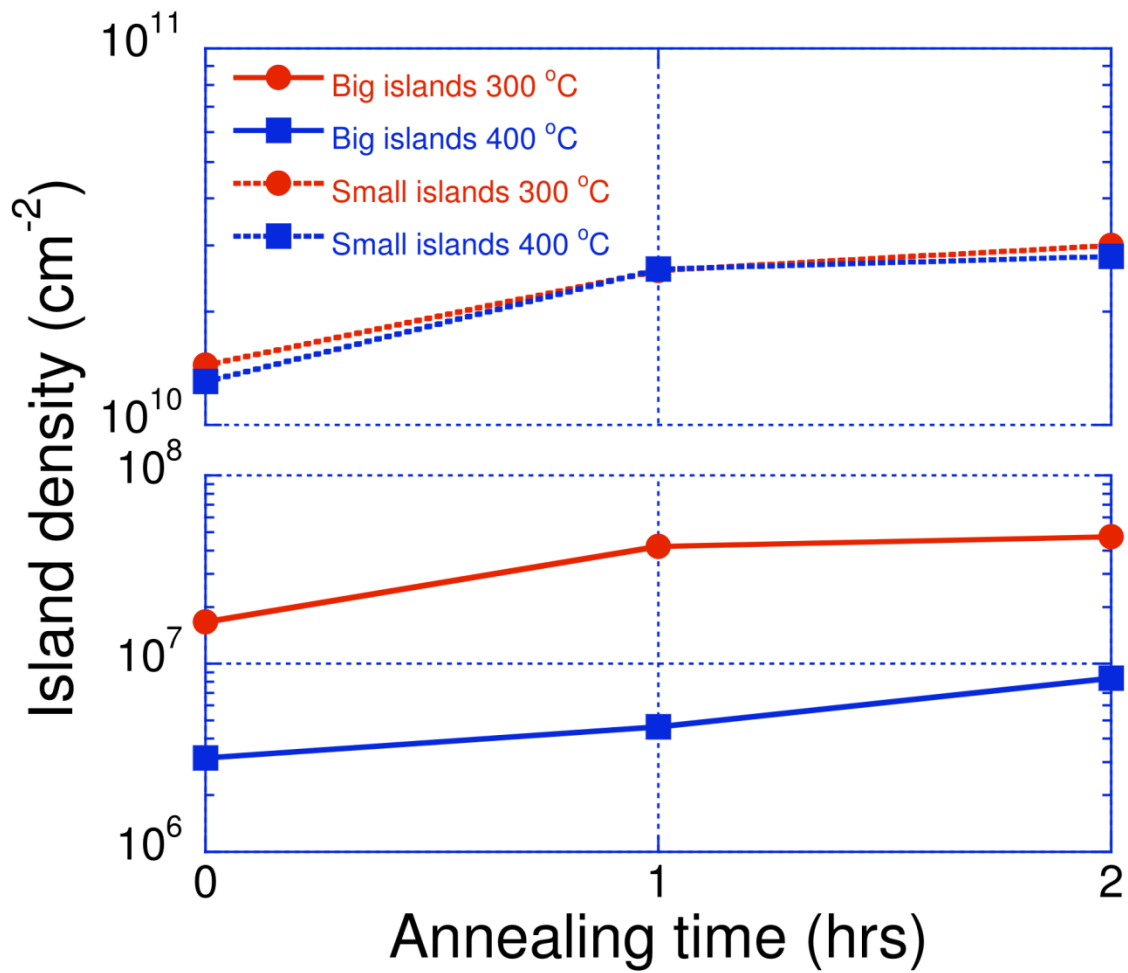


*Figure 3.6.* Areal density of big and small islands vs. anneal time for both big and small islands. The apparent increase in small island density with anneal time is within the scatter of small island densities observed in as-grown samples. The big island density increases with increasing anneal time.

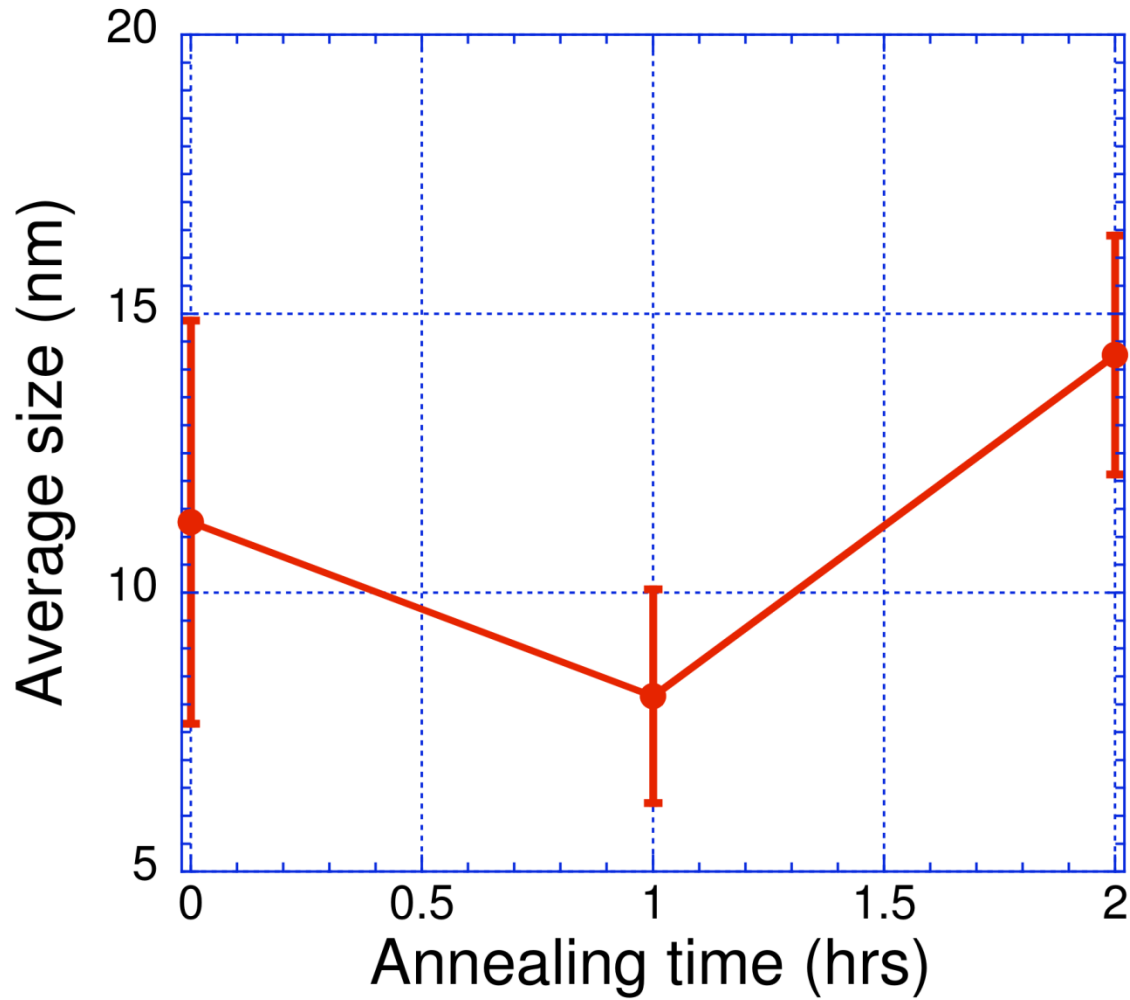


*Figure 3.7.* Average size of small islands vs. anneal time for 5.3 ML Ag deposited at 2.1 ML/min onto Si(100) heated to 400 °C and annealed for the indicated times. The small island density does not vary monotonically with anneal time. The error bars are 1 standard deviation long. The size was calculated using the cube root of island volume measured from AFM images.

small islands coexisted at elevated temperature, it is reasonable to expect that the small islands would likely be consumed by the big islands due to Ostwald ripening.

Second, while fig. 3.6 indicates that the small island density increases with increasing annealing time, the change of small island densities displayed in fig. 3.6 is within the scatter of small island densities observed for the various growth temperatures plotted in fig. 3.4. Moreover, fig. 3.7 indicates that the average small island size does not systematically depend on annealing time. It is difficult to identify mechanisms responsible for the small island behavior based on figs. 3.6 and 3.7. The non-monotonic dependence of the average island size on annealing time at 400 °C and the relatively small variation in areal density that is within the scatter observed for as-grown samples suggests that the small islands are relatively unaffected by annealing, which would only be reasonable if they did not exist at elevated temperature and only formed as the samples were cooled to room temperature.

In contrast to the small islands, the big island size and areal density both depend systematically on annealing time. Fig. 3.6 shows that the big island areal density monotonically increases as the annealing time increases. Fig. 3.8, which displays the size distributions for big islands annealed at their growth temperatures of 300 and 400 °C, shows that their sizes decrease as annealing time increases. Clearly, figs. 3.6 and 3.8 indicate that the big islands undergo unusual anti-coarsening behavior: their areal density increases and their sizes decrease as the annealing time increases.

In an attempt to better understand this peculiar anti-coarsening behavior, we analyzed the evolution of big island shapes as a function of annealing time at 300 °C. This analysis is shown in fig. 3.9. We chose 3 annealing times: 1 hour, 2 hours and 8

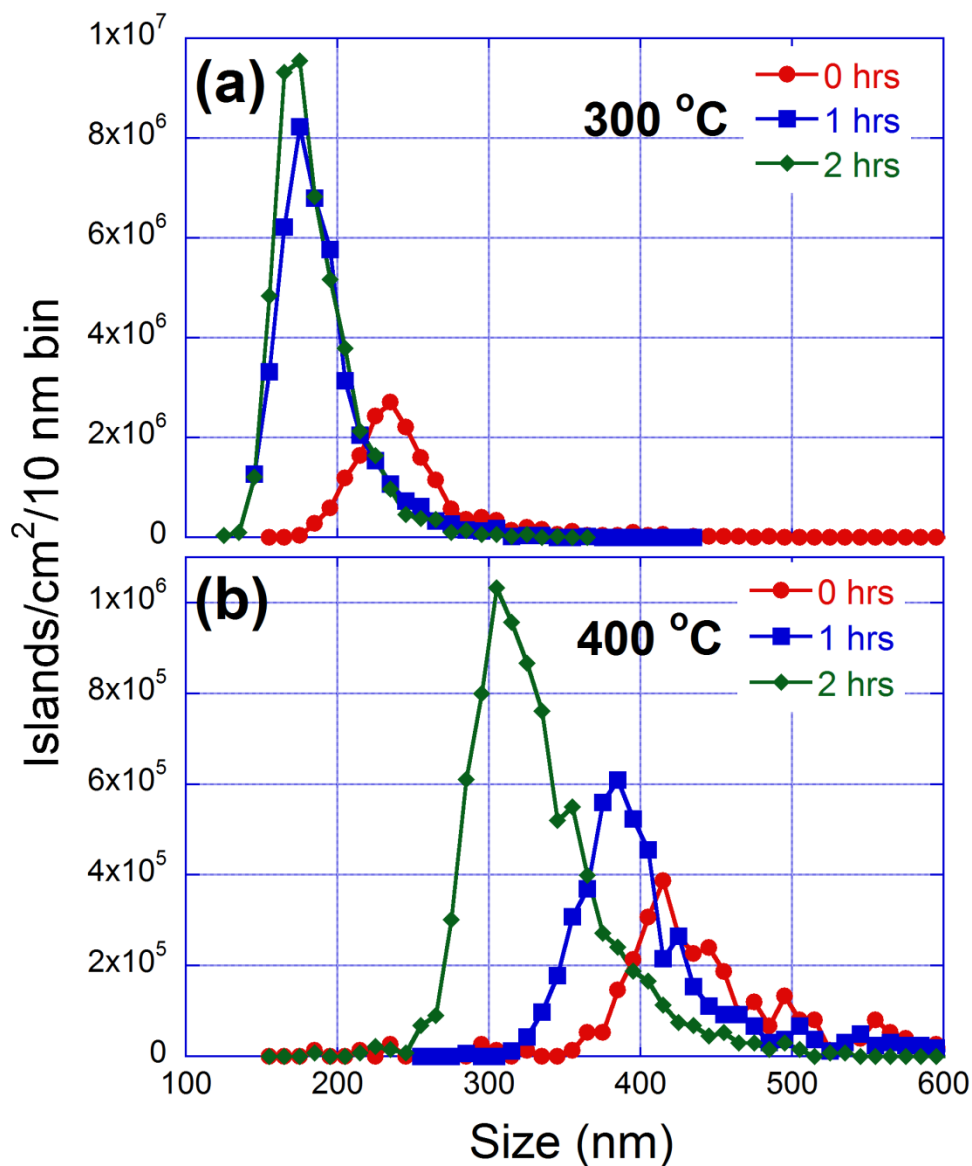


*Figure 3.8.* Size distributions for big islands grown by depositing 5.3 ML of Ag at 2.1 ML/min onto Si(100) heated to 300 °C (a) and 400 °C (b) and annealed for the indicated times at the growth temperatures. The average island sizes decrease and the island areal density increases with increasing anneal time.

hours. As shown in fig. 3.9, the evolution of all five island families stops after 2 hours of annealing. First, we found that the islands with irregular bases are completely absent in the samples that had been annealed at their growth temperature for 1 hour, as shown in fig. 3.9. In as-grown samples, about 10% of the total island population had irregular bases. This observation is consistent with the results reported by Li, et al. [117]. They used low-energy electron microscopy (LEEM) to observe the decomposition of irregular islands (their ‘bamboo-like islands’) into several smaller fragments after 32min annealing at 570 °C. They attributed this behavior to the defects contained in the irregular islands, like stacking faults and microtwins.

We also find that the population of the other 4 types of big islands varies as the anneal progresses, as shown in fig. 3.9. While square islands are the most populous shape in the as-grown sample, their fraction decreases from about 40% to about 35% after 1 hour of annealing. In as-grown samples, truncated triangular islands were the second most populous family at about 30% and increased to become about as populous as square islands after 1 hour of annealing. Both triangular (5 to 10%) and rectangular (10 to 20%) islands increase their fractions throughout the course of the 2-hour duration anneal.

The shape evolution for the remaining island shapes: square, rectangular, triangular and truncated triangular is shown in fig. 3.10. We find that the trend is toward a more elongated shape as the anneal progress. Fig. 3.10 (a), (b), (c) and (d) are double y-axis plots with annealing time plotted along the x axis for square, rectangular, triangular and truncated triangular, respectively. The average length  $\langle L \rangle$  and average width  $\langle W \rangle$  of the rectangular bounding box of islands are plotted on the right y axis, and the aspect ratio  $\langle L \rangle / \langle W \rangle$  is plotted on the left y axis. The width of all of these islands decreases as

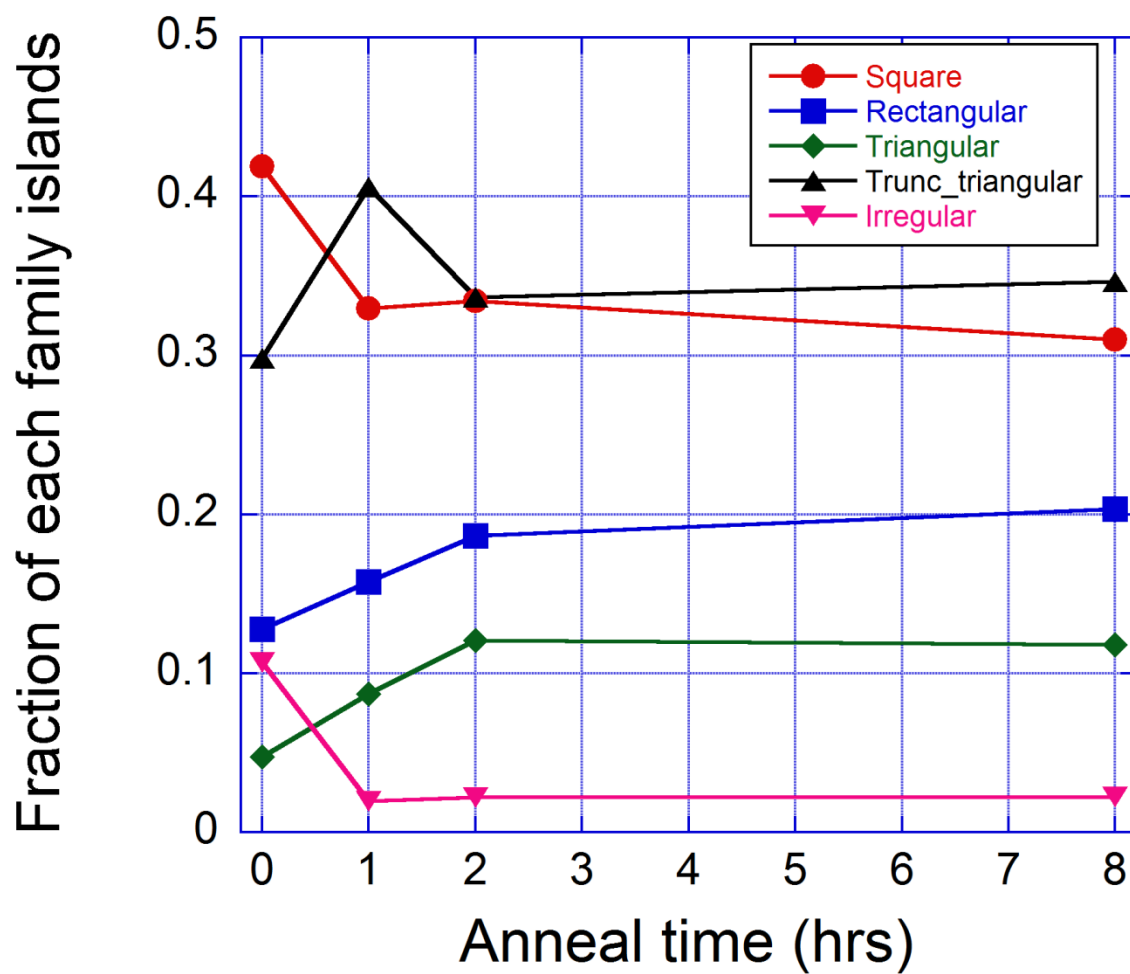


Figure 3.9. The shape evolution of all 5 families of big Ag islands is shown here. It shows that the fraction of each family islands varies as the anneal progresses.

the anneal time increases and, except for triangular islands, the length also decreases. For triangular islands as shown in fig 3.10(c), their average length increases and their average width decreases, resulting an increase of their aspect ratio.

For square islands, both width and length decrease at the same rate to keep aspect ratio constant, near 1.2 as shown in fig. 3.10 (a), but their fraction of the total island population decreases during the anneal. For the shape evolution of rectangular islands (in fig. 3.9(b)) and of truncated triangular islands (in fig. 3.9(c)), the rate of decrease of their average width is larger than that of their average length, which also results in elongation of these islands.

Our observation that the islands increase their aspect ratio (length / width) during growth temperature annealing is consistent with the observation of very elongated Ag islands by other investigators [108,110]. However, further work is required to understand the unusual anti-coarsening behavior that we observe. It is possible that a mechanism similar to that observed in the LEEM work of Li may play a role.

Other investigators have found that a large fraction of Ag/Si(100) islands are multiply twinned [114], which could lead to the island decomposition found by Li. It could be possible that multiply twinned islands do decompose during annealing to produce the higher densities that we observe. However, we very infrequently observe groups of islands that might be expected from decomposition of a larger island into smaller fragments, since this process would require mobility of quite large Ag islands at temperatures of 300-400 °C. Moreover, the incidence of island groups we find that could be the result of island decomposition is too small to account for the areal density increase



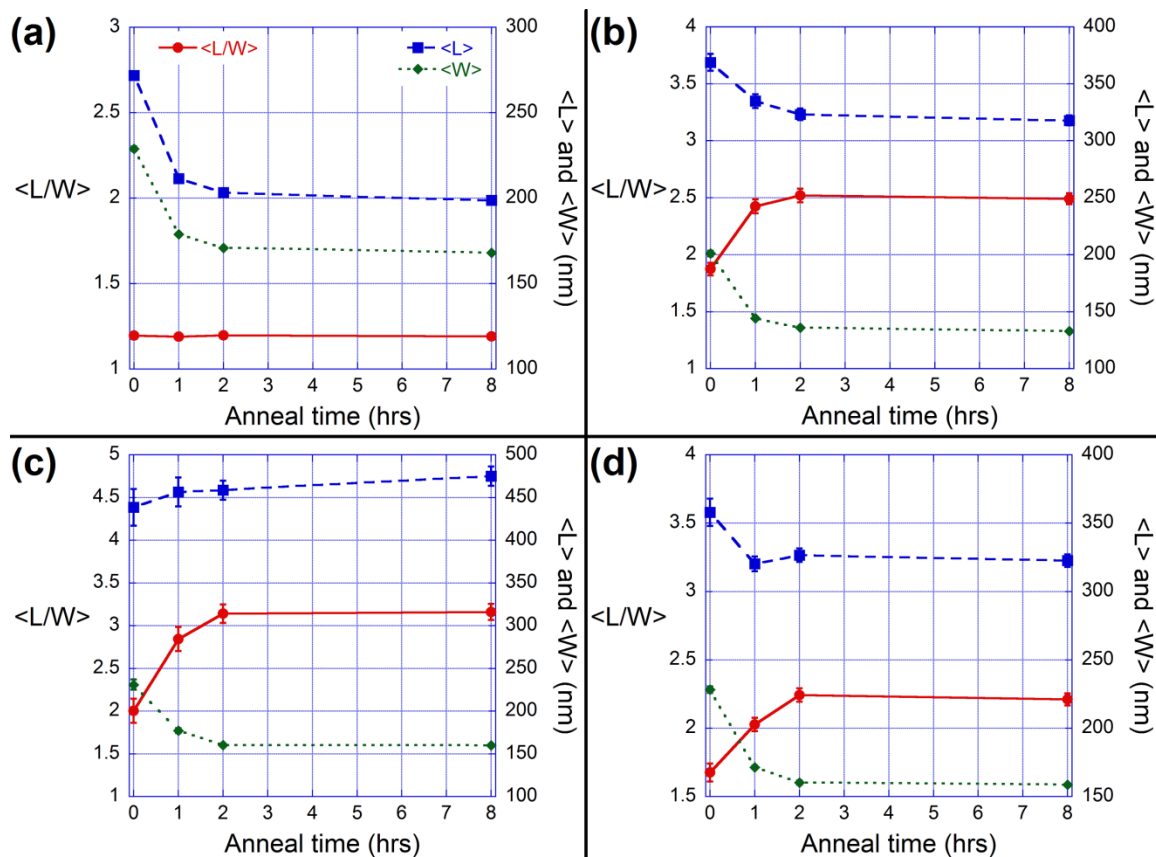


Figure 3.10. These figures are double y-axis plots with annealing time as  $x$  axis. The average length  $\langle L \rangle$  and width  $\langle W \rangle$  are plotted on the right  $y$  axis, and the average aspect ratio  $\langle L/W \rangle$  is plotted on the left  $y$  axis. Irregular islands essentially disappear after one hour of annealing, so their shape evolution could not be investigated over the same time scale as for the other islands. (a), (b), (c) and (d) show the shape evolution of square, rectangular, triangular and truncated triangular islands, respectively. The legend for all panels of this figure is shown in (a).

that we measure. Clearly further work is required to determine the origin of the anti-coarsening behavior reported here.

### **3.2 Tuning the Localized Surface Plasmon of Ag/Si(100) Islands**

In order to optimize the plasmonic enhancement of Ag islands on the PL of Ge QDs, the LSPR energy of Ag islands may need to be tuned to the emission energy of Ge QDs, because this could optimize the spontaneous emission rate based on the Purcell effect. It has been discussed in section 1.3.3 that the LSPR energy of metal nanoparticles (NP) depends on the particle size, shape, and dielectric environment.

We employed spectroscopic ellipsometry to study the plasmonic properties of Ag islands grown on Si(100) by varying the size and morphology of the Ag islands. The pseudodielectric functions of samples with Ag islands on Si(100) were derived from the measurements. Some features in the pseudodielectric functions with Ag islands qualitatively behave as predicted from Mie theory calculation for a Ag prolate spheroid. Calculated LSPR energies of ‘best-fit’ Ag prolate spheroids from Mie theory seem to match features observed in experimental pseudodielectric functions. It is difficult to conclusively associate these Ag-related features with plasmon resonances of Ag islands due to the variation of the Si dielectric function in the spectral range of interest. Therefore, we developed a more realistic method to study the experimental pseudodielectric function by simulating the pseudodielectric function with Abeles methods and the thin island film (TIF) theory. In the simulation, an ensemble of Ag islands with average size of  $\sim 25$  nm was modeled as oblate spheroids. Based on this more realistic model, some features in the experimental pseudodielectric functions can be clearly associated with the perpendicular mode. Further investigation is required to

conclusively associate other features in the experimental pseudodielectric functions with in-plane modes. The investigation results for the plasmonic properties of bare Ag islands on Si(100) will be discussed in detail.

The ambient dielectric around Ag islands is changed by capping the Ag islands with a 30 nm thick  $\alpha$ -Si layer, so as to tune the LSPR of the Ag islands. One plasmon-related peak was identified by simply comparing the pseudodielectric function in the presence of Ag islands with the one in which Ag islands are absent. A detailed discussion about the LSPR of Ag islands capped with an  $\alpha$ -Si layer will be considered after the discussion of bare Ag islands.

### **3.2.1 Bare Ag/Si(100) islands.**

#### ***3.2.1.1 The Mie theory.***

As discussed in section 1.3.3, the LSPR energy of Ag NPs is in the UV range, while the PL emission energy of Ge QDs is at  $\sim 0.8$  eV. Plasmonic enhancement of the spontaneous emission rate of Ge QDs by Ag NPs should be improved by decreasing the energy difference between the Ag LSPR and the PL energy of the Ge QDs. An investigation into tuning the LSPR of Ag NPs is necessary for optimizing the plasmonic enhancement of Ge QD PL with Ag NPs.

As discussed in section 3.1, Ag islands grown on Si(100) are elongated, with their long axis parallel to the substrate. By simply approximating these Ag islands as prolate spheroids, the LSPR of Ag islands can be calculated from Mie theory. The schematic of a prolate spheroid is shown in the inset of fig. 3.11, where  $a > b = c$ . Its shape can be described by its aspect ratio ( $AR$ ), which is defined as the ratio of its semi-major axis ( $a$ ) to its semi-minor axis ( $b$ ).  $AR = a/b$ .

For prolate spheroids, the depolarization factors in eq. 1.21 become

$$f_x = \frac{1-e^2}{2e^3} \left( \ln \frac{1+e}{1-e} - 2e \right), \text{ and } f_y = f_z = \frac{1-f_x}{2}, \quad (3.3)$$

where  $e$  is the eccentricity defined as  $e = \sqrt{1 - \frac{b^2}{a^2}} = \sqrt{1 - \frac{1}{AR^2}}$ . The LSPR energy can be calculated by substituting eq. 3.3 into eq. 1.23. The result shows that the LSPR energy of Ag islands can be tuned by varying the aspect ratio of prolate spheroids. Additional flexibility for tuning the resonance energy is available by varying the dielectric environment of the Ag islands.

Fig. 3.11 shows the calculated LSPR for a Ag prolate spheroid versus its aspect ratio ( $AR=a/b$ ). Solid curves are for the Ag prolate spheroid in vacuum, and dotted curves are for the Ag prolate spheroid embedded in Si. Blue indicates the LSPR associated with the short axis modes ( $y$  or  $z$  axes), and red indicates the LSPR associated with the long axis modes ( $x$  axis).

For a Ag prolate spheroid in vacuum, the LSPR associated with the elongated  $x$  axis (red solid curves) redshifts as the aspect ratio of the prolate spheroid increases, while the LSPR associated with the short  $z$  or  $y$  axis (blue solid curve) slightly blueshifts with increasing aspect ratio. As the aspect ratio increases from 1 to 5, the LSPR of the long-axis ( $x$ ) mode redshifts by  $\sim 1.5$  eV, and the LSPR of the short-axis ( $z$  or  $y$ ) mode blueshifts by only  $\sim 0.2$  eV.

For a Ag prolate spheroid embedded in a Si matrix ( $\epsilon_{Si}=11.9$ ), the Ag LSPR are plotted with dotted curves in fig. 3.11. The dotted curves also show that the LSPR associated with the elongated X-axis mode redshifts and that the plasmon mode

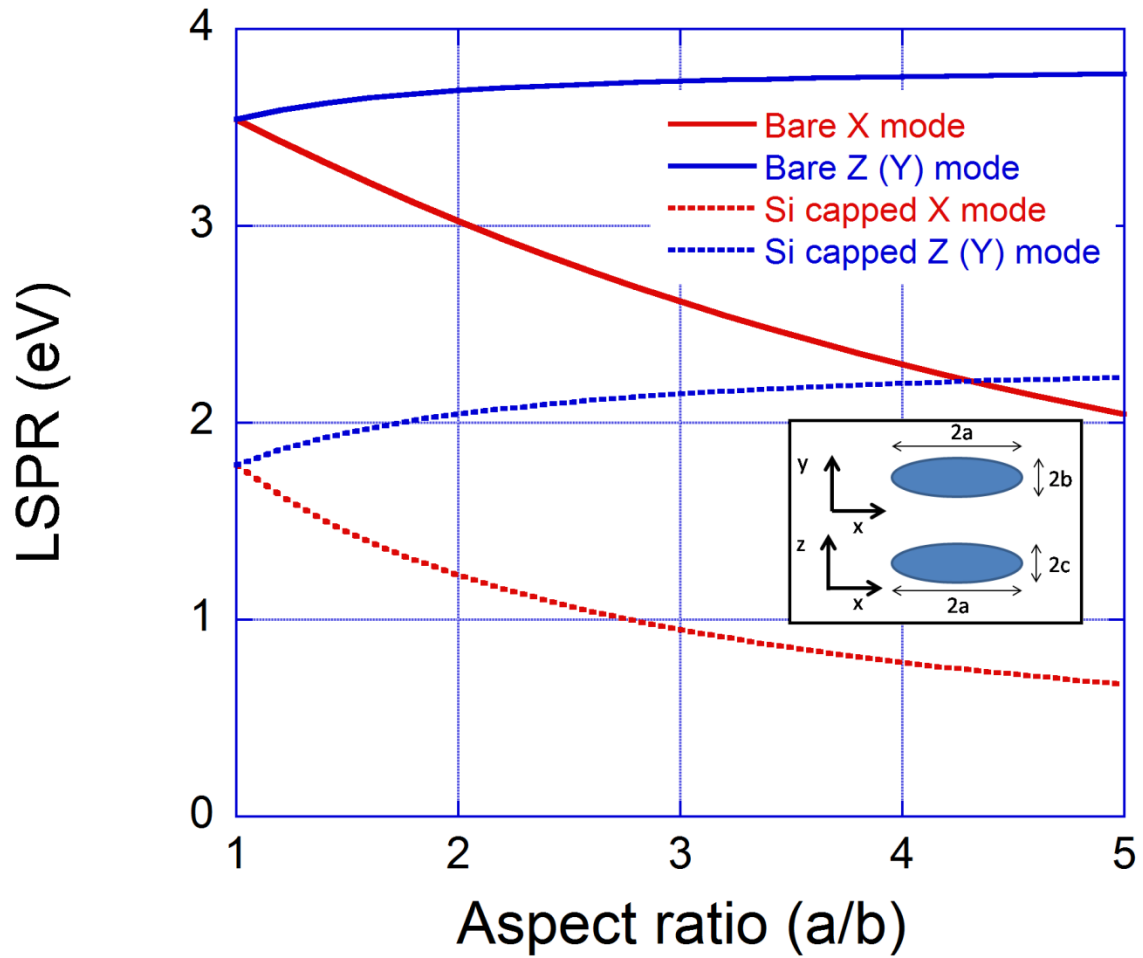


*Figure 3.11.* The calculated LSPRs of a prolate spheroid from Mie theory are plotted against the aspect ratio, defined as  $a/b$ . The LSPRs of the prolate spheroid in vacuum are plotted as solid curves, and the LSPRs of the prolate spheroid embedded in Si are plotted as dotted curves. Blue indicates the plasmon mode associated with short axes ( $z$  or  $y$ ), and red indicates the plasmon mode associated with long axis ( $x$ ). The schematic of a prolate spheroid is shown in the inset figure.

associated with the short axis blueshifts when the aspect ratio of the Ag prolate spheroid increases. Comparing the dotted curves with solid ones of the same color indicates that both the long-axis ( $x$ ) and short-axis ( $z$  or  $y$ ) mode LSPR energies are redshifted by almost  $\sim 1.6$  eV due to embedding in Si. For instance, the long-axis ( $x$ ) mode LSPR of a bare Ag prolate spheroid with  $AR=2$  is at  $\sim 3.0$  eV in the UV range, and the same LSPR mode of the same prolate spheroid embedded in a Si matrix is at  $\sim 1.2$  eV in the IR range.

As discussed in section 3.1, the shape of Ag islands grown on Si(100) can be tuned by varying the growth and annealing conditions. Two growth conditions were selected to produce ensembles of Ag islands with different shapes and sizes. 9.6 ML of Ag was deposited on both samples at the same rate of 3.2 ML/min. The growth temperatures for the Ag island ensembles shown in fig. 3.12 are 430 °C for (a) and 450 °C for (b).

Scanning electron micrographs of these two ensembles of Ag/Si(100) islands are shown in fig. 3.12. The ensemble of Ag islands shown in fig. 3.12 (a) has an average size of 25 nm. The Ag island ensemble shown in fig. 3.12 (b) has an average size of 100 nm. These sizes were calculated by averaging the square root of the island areas for over one hundred islands in scanning electron micrographs. The Ag islands shown in fig. 3.12 (a) are termed as smaller big (SB) islands in order to distinguish them from the small islands discussed in section 3.1. The islands shown in fig. 3.12 (b) are called bigger big (BB) islands.

From the SEM micrographs, we measured the average length ( $L$ ) and average width ( $W$ ) of Ag islands. The measured geometry of the BB Ag islands is  $L=147.0\pm39.0$  nm and  $W=70.5\pm12.5$  nm, and the average aspect ratio ( $a/b$ ) of the best-fit ellipses for

BB Ag islands is 2.46. AFM measurement shows that the average width-to-height ratio is  $\sim 3$ . The measured geometry of the SB Ag islands from SEM is  $L=37.5 \pm 10.6$  nm and  $W=27.2 \pm 4.6$  nm, and the average aspect ratio ( $a/b$ ) of best-fit ellipses for SB Ag islands is 1.45. It is difficult to get accurate height information for SB Ag islands from AFM measurement due to the high density of SB islands, but rough analysis of AFM data for SB Ag islands shows that the average width-to-height ratio from SB Ag islands could also be  $\sim 3$ .

For a Ag prolate spheroid with the same aspect ratio as SB Ag islands, 1.45, simple calculation from Mie theory suggests that the LSPR mode associated with the long axis ( $x$ ) is expected to be at 3.3 eV, and that the LSPR mode associated with the short axis ( $z$  or  $y$ ) is expected to be at 3.6 eV. For SB Ag islands, two plasmon modes with different energies,  $\sim 3.3$  eV and  $\sim 3.6$  eV, are expected to appear. For a prolate spheroid with the same aspect ratio as BB Ag islands, 2.46, the LSPR associated with the long axis ( $x$ ) is expected to be at 2.8 eV, and that associated with the short axis ( $z$  or  $y$ ) is expected to be at 3.7 eV. We employed spectroscopic ellipsometry to experimentally determine the plasmonic features of Ag/Si(100) islands.

Fig. 3.13 (a) and (b) show the real and the imaginary parts of the pseudodielectric functions of the samples shown in fig. 3.12 measured using spectroscopic ellipsometry. As discussed in section 2.5.6, the quantities measured directly from ellipsometry are  $\Delta$  and  $\Psi$ . They are related to the reflection coefficients of the  $p$ - ( $R_p$ ) and  $s$ - ( $R_s$ ) components by the following equation,

$$\rho = \frac{R_p}{R_s} = \tan(\Psi)e^{-i\Delta}. \quad (3.1)$$

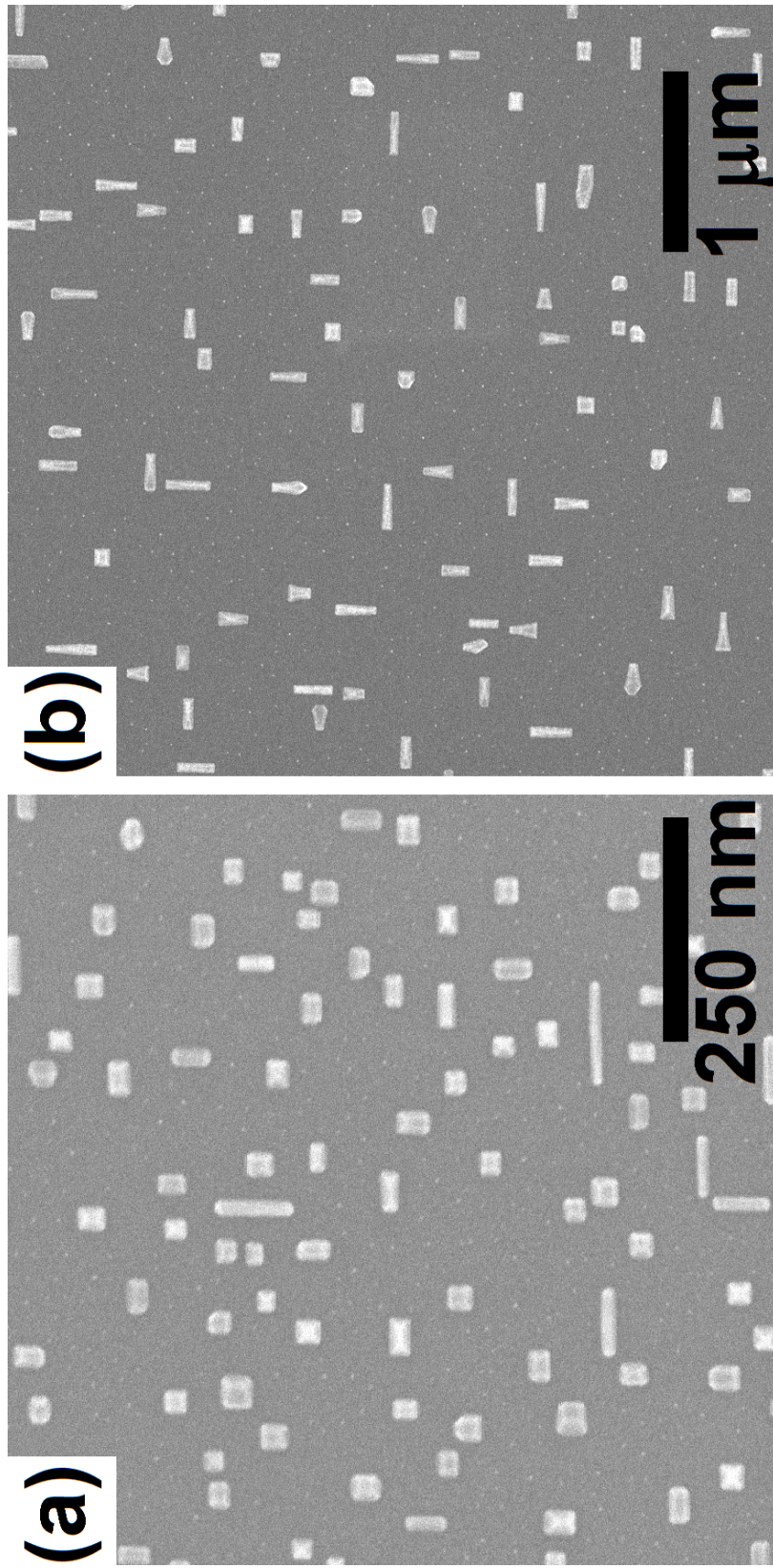


*Figure 3.12* (a) shows a scanning electron micrograph of Ag islands with an average size of 25 nm, which are called smaller big (SB) islands. (b) shows a SEM image of Ag islands with an average size of 100 nm, which are called bigger big (BB) islands.



By assuming the sample has a sharp interface with air, Snell's law and the Fresnel equations can be applied to this two-medium system. Therefore, a relation connecting the dielectric functions of the two media can be derived

$$\langle \varepsilon \rangle = \varepsilon_0 \sin^2(\theta_0) + \frac{(1 - \rho^2)(\sin^2 \theta_0)(\tan^2 \theta_0)}{(1 + \rho^2)}, \quad (3.2)$$

where  $\langle \varepsilon \rangle$  is called the pseudodielectric function of the sample [145]. For our spectroscopic ellipsometry measurement, the sample interfaces with air, so  $\varepsilon_0=1$  in eq.

3.2. The incident angle,  $\theta_0$  is  $70^\circ$ . In fig. 3.13 (a) and (b), the red curves show the actual dielectric function of the Si substrate. The blue curves show the pseudodielectric function of the sample with SB Ag islands on Si, and the green ones show that of the sample with BB Ag islands on Si.

Qualitative examination of the curves suggests that two features on each spectrum with Ag islands may be associated with the LSPR of Ag islands, as indicated in fig. 3.13 (a) and (b). Comparing the spectra from the sample having SB Ag islands on Si (blue) with those of Si (red) in fig. 3.13, two features related to the SB Ag islands can be located at  $\sim 3.1$  eV and  $\sim 3.9$  eV. Comparing the green pseudodielectric function curves from the sample having BB Ag islands on Si with the red one in fig. 3.13, two features of the BB Ag islands can also be determined; one located at  $\sim 2.8$  eV and the other at  $\sim 3.9$  eV. However, it is difficult to identify their physical meaning conclusively, due to the variation of the Si dielectric constant over the spectral region of interest.

The comparison between experimental Ag-related features determined from fig. 3.13 and the simple calculation from Mie theory is shown in fig. 3.14 (a). In fig. 3.14 (a), the solid red curve shows the calculated LSPR modes associated with the long axis ( $x$ ) as

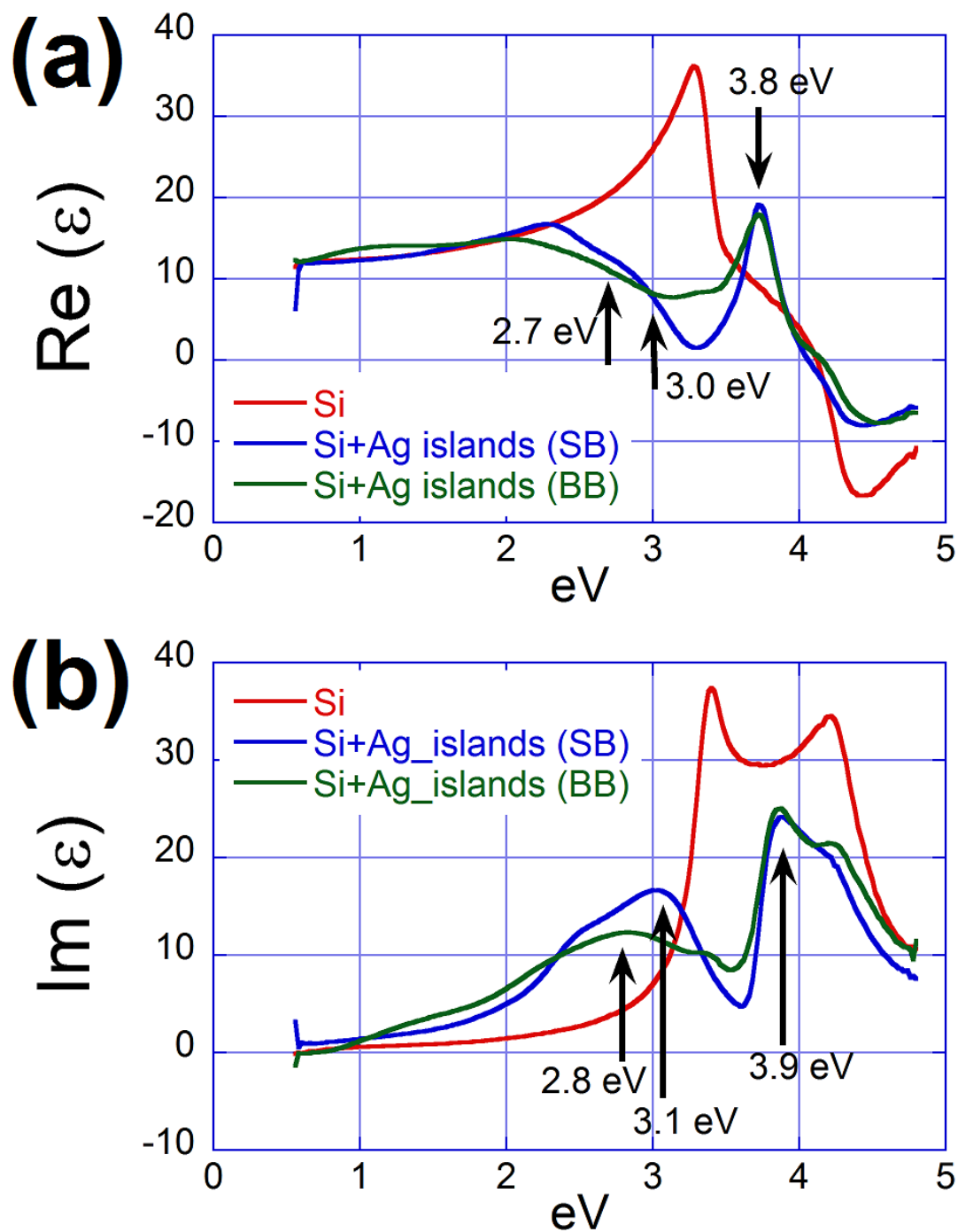


Figure 3.13. (a) and (b) show the real and imaginary parts of the pseudodielectric functions measured using spectroscopic ellipsometry. The red curves are the dielectric function of the Si substrate. The blue curves are the measured pseudodielectric functions of SB Ag islands on Si. The green curves are the measured pseudodielectric functions of BB Ag islands on Si. The incident angle used for measurement is  $70^\circ$ .

a function of the aspect ratio ( $a/b$ ), and the solid blue curve shows the calculated plasmon modes associated with the short axis ( $z$  or  $y$ ) as a function of the aspect ratio ( $a/b$ ). These solid curves in fig. 3.14 (a) are exactly same as those solid curves in fig. 3.11. The scattered plot symbols in fig. 3.14 (a) are the experimental data for SB and BB island ensembles indicated in fig. 3.13. Circular plot symbols represent features in the experimental pseudodielectric functions with SB Ag islands that may be related to the Ag LSPR. Square plot symbols represent features in the experimental pseudodielectric functions with BB islands that may be related to the Ag LSPR. As discussed above, the average aspect ratio of the best-fit ellipses for BB islands in SEM images is 2.46, and that for SB islands in SEM images is 1.45. The features at the lower energy side for each island ensemble are plotted in red, and those at the high energy side are plotted in blue.

Schematics of a Ag prolate spheroid on a Si substrate is shown in fig. 3.14 (b). The Si substrate surface lies in the  $x$ - $y$  plane, and the  $z$  direction is perpendicular to the substrate surface. The major axis of the Ag prolate spheroid is along the  $x$  direction, and the minor axis is along the  $z$  or  $y$  direction. The length of the semi-major axis is  $a$ , and the length of the semi-minor axis is  $b$  or  $c$  ( $b=c$  for prolate spheroids).

Comparison of the experimental data with the rough theoretical calculation in fig. 3.14 (a) suggest that the LSPR features at  $\sim 3.1$  eV for SB Ag islands (2.8 eV for BB Ag islands) may be associated with the in-plane long axis ( $x$ ) mode, and that the feature at 3.9 eV may be associated with the perpendicular short axis ( $z$ ) mode. The red data points follow the trend of the long-axis ( $x$ ) mode plasmon with aspect ratio, which is the long-axis mode of the LSPR redshifts with increasing aspect ratio. The calculation shows that the short-axis mode of the LSPR is much less sensitive to aspect ratio, and the blue data

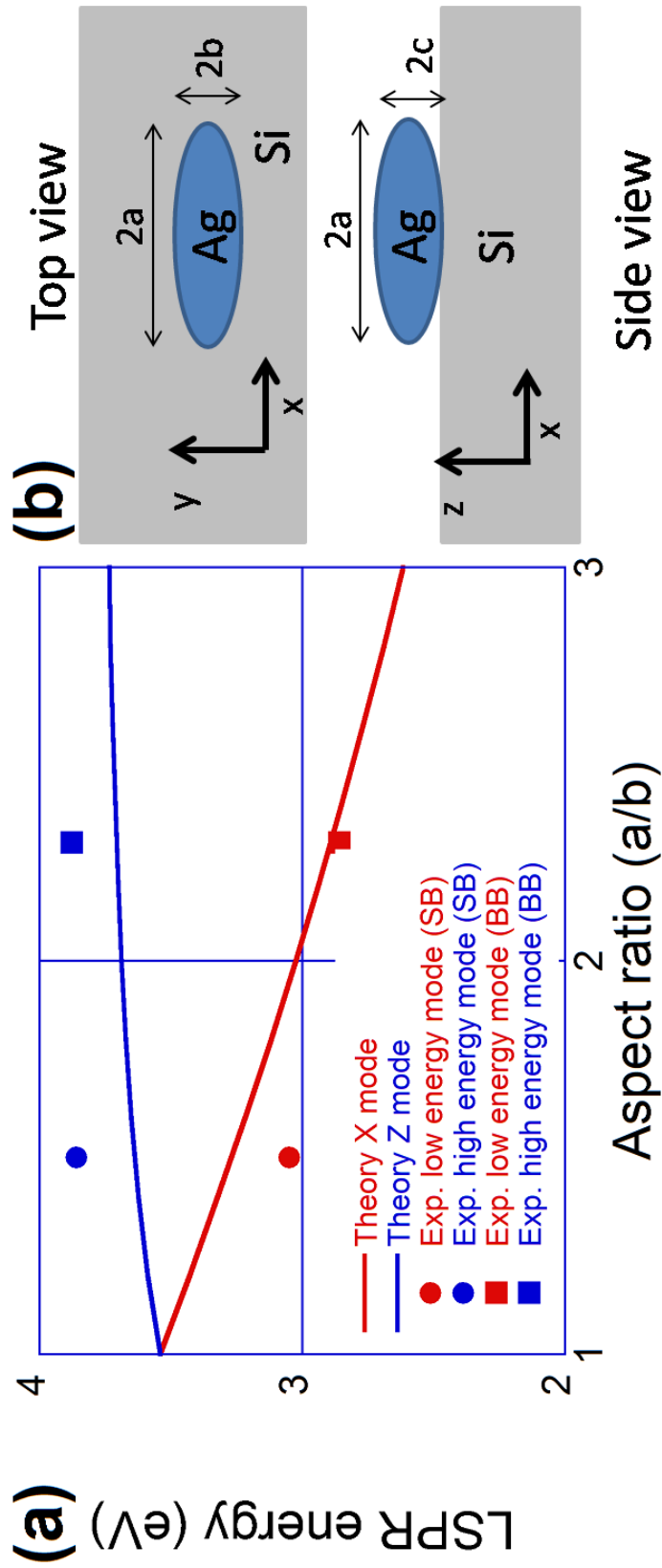


Figure 3.14 (a) shows the comparison between experimental Ag-related features (dots) and theoretical calculation from Mie theory by approximating Ag islands as prolate spheroids. (b) shows the schematic of a Ag prolate spheroid on top of Si. The experimental Ag plasmon features are determined by simply comparing the pseudodielectric functions of samples having Ag islands on Si with that of Si the substrate, and these plasmonic features are indicated in fig. 3.13.

points indicate the same trend. The actual island height ( $\sim 2c$ ) is about  $\sim 1/3$  of the island width ( $\sim 2b$ ), so that the approximation of taking  $c=b$  results in the redshifts of the theoretical calculated energy, which explains why the blue experimental data points associated with the short-axis plasmon modes are above the blue line.

This semi-quantitative comparison between the experimental data and the simple calculation are not enough to conclude that the lower energy features are associated with the long-axis ( $x$ ) mode, or that the higher energy features are associated with the perpendicular short-axis ( $z$ ) mode of LSPR, because the variation of the dielectric function of Si complicates the experimental spectra in the spectral range of interest. A more realistic method, using the TIF theory and Abeles method to simulate the pseudodielectric function, was developed to interpret the complicated experimental spectra.

### **3.2.1.2 *Thin island film theory.***

In order to quantitatively investigate the LSPR of Ag islands, the pseudodielectric function of the sample with SB Ag islands on Si was simulated using the Abel's method [146,147]. This method treats each layer as a  $2 \times 2$  matrix, and the product of all layers provides the final transfer matrix, from which the pseudodielectric properties of thin films and stratified media can be determined. The Abel's method will be briefly discussed first, and then the incorporation of the TIF model into the simulation will be examined.

In the simulation, the Ag island layer is treated using the TIF model developed by Bedeaux and Vlieger [148]. SB Ag islands are simulated since they are better approximated as spheroids with their rotational axes normal to the substrate, which is the

situation treated by the TIF model, than are BB Ag islands. As discussed above, the ratio of the in-plane major axis to the in-plane minor axis for SB Ag islands is 1.45, which is closer to 1 than that ratio of 2.46 for BB islands. The average width-to-height ratio for both BB and SB Ag islands is  $\sim 3$ . Therefore, SB Ag islands can be reasonably approximated as oblate spheroids (short and fat). The schematic of an oblate spheroid is shown in fig. 3.15 (a) with  $a=b>c$ . For oblate spheroids, the aspect ratio is defined as diameter to height,  $2b/2c=b/c$ , which describes the shape of oblate spheroids. The shape of SB Ag islands affects their LSPR, and the width-to-height ratio of SB Ag islands is not a constant. Therefore, the size distribution of SB islands needs to be considered in the simulation.

The Abel's method uses two types of matrices to describe the interaction between a thin film and light. One is the interface matrix that describes the transition from film  $m$  to film  $m+1$ , which is defined as

$$I_{m,m+1} = \frac{1}{t_{m,m+1}} \begin{pmatrix} 1 & r_{m,m+1} \\ r_{m,m+1} & 1 \end{pmatrix}. \quad (3.4)$$

$r_{m,m+1}$  and  $t_{m,m+1}$  are the usual Fresnel reflection and transmission coefficients, respectively. The Fresnel reflection coefficients are

$$r_{m,m+1}^p = \frac{n_{m+1} \cos \theta_m - n_m \cos \theta_{m+1}}{n_{m+1} \cos \theta_m + n_m \cos \theta_{m+1}}, \quad (3.5a)$$

and

$$r_{m,m+1}^s = \frac{n_m \cos \theta_m - n_{m+1} \cos \theta_{m+1}}{n_m \cos \theta_m + n_{m+1} \cos \theta_{m+1}}. \quad (3.5b)$$

The Fresnel transmission coefficients are

$$t_{m,m+1}^p = \frac{2n_m \cos \theta_m}{n_{m+1} \cos \theta_m + n_m \cos \theta_{m+1}}, \quad (3.5c)$$

and

$$t_{m,m+1}^s = \frac{2n_m \cos \theta_m}{n_m \cos \theta_m + n_{m+1} \cos \theta_{m+1}}. \quad (3.5d)$$

In the above four equations, the superscripts  $p$  and  $s$  indicate parallel and perpendicular polarization, respectively.  $n_m$  is the refractive index of the  $m^{\text{th}}$  layer, and  $\theta_m$  denotes the incident angle of light inside the  $m^{\text{th}}$  layer. The incident angles of light inside the  $m^{\text{th}}$  and  $(m+1)^{\text{th}}$  layers are related by Snell's law ( $n_m \sin \theta_m = n_{m+1} \sin \theta_{m+1}$ ).

The other type of layer matrix describes the passage of light through the layer, so it only involves the phase factor.

$$L_m = \begin{pmatrix} e^{-i\Delta_m} & 0 \\ 0 & e^{i\Delta_m} \end{pmatrix}. \quad (3.6)$$

$\Delta_m = (2\pi d_m / \lambda) n_m \cos \theta_m$ ,  $\lambda$  is the wavelength of light in vacuum and  $d_m$  is the thickness of layer  $m$ . For a system consisting of 3 layers, the final transition matrix is defined as

$$A = I_{1,2} L_2 I_{2,3} L_3. \quad (3.7)$$

The overall reflection coefficient is calculated from  $R = A_{21}/A_{11}$ . For both the parallel and perpendicular polarizations, the reflection coefficients  $R_p$  and  $R_s$  can be obtained by inserting the appropriate Fresnel coefficients (eqs. 3.5) in eq. 3.4. For our samples with bare Ag islands on a Si substrate, 3 layers should be included in the simulation: air (layer 1), the Ag island layer (layer 2), and the Si substrate (layer 3), as shown in fig. 3.15 (b).

As discussed above, it is reasonable to approximate each SB Ag island has as an oblate spheroid with  $a=b>c$ , as shown in fig. 3.15 (a). The dimensions of each oblate spheroid are acquired from the actual morphological measurements of its corresponding

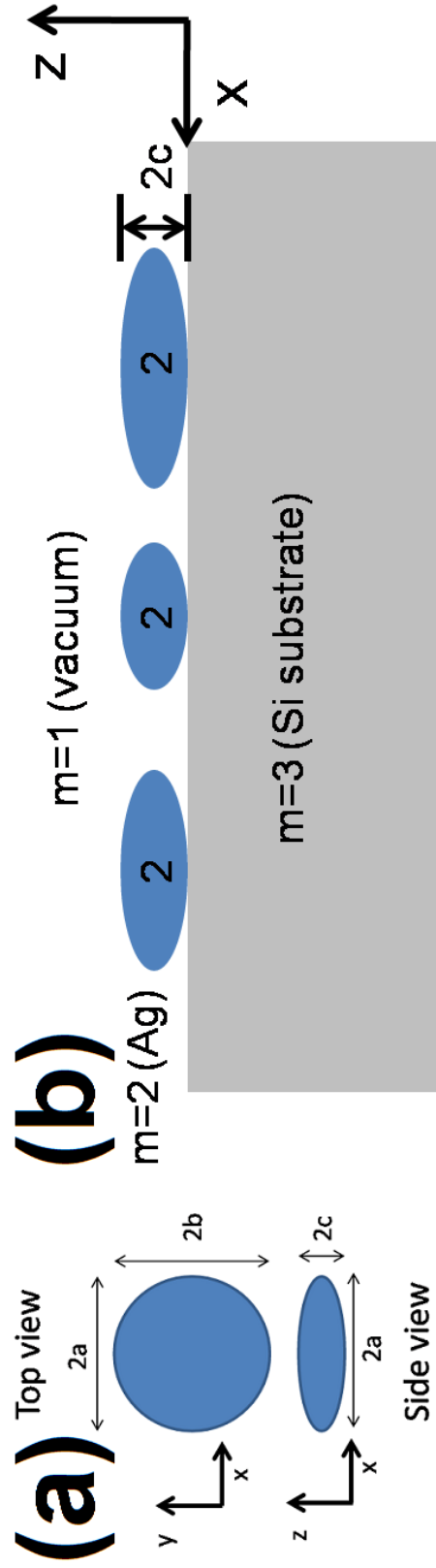


Figure 3.15. (a) shows the schematic of an oblate spheroid. The surface of the Si substrate is in the  $x$ - $y$  plane, and the  $z$  direction is perpendicular to the substrate. (b) shows the schematic of the 3 simulated films.



island, e.g.,  $c$  is 1/2 of the maximum island height and  $a$  ( $b$ ) is 1/2 of the island width. As discussed in the introduction chapter, the LSPR is shape-dependent, so the distribution of aspect ratios,  $b/c$ , needs to be incorporated into the simulation of the pseudodielectric function. In the simulation, the parameter  $c$  is set as a constant, and  $b$  is varied according to the distribution measured using SEM. The fraction of the substrate area covered by islands with widths in the range from  $b$  to  $b+db$  is defined as

$$d\Phi = N(b)A(b)db = \phi(b), \quad (3.8)$$

where  $N(b)db$  is the number of islands with width in the range from  $b$  to  $b+db$ , and  $A(b)$  is the substrate area covered by islands with width  $2b$ . For oblate ellipsoids,  $A(b) = \pi b^2$ .

The width distribution of SB Ag islands can be well fitted with a parabola

$$N(b) = C(b_{max} - b)(b - b_{min}), \quad (3.9)$$

where  $C$  is a normalization factor that can be determined by equating the integral of eq. 3.8 from  $b_{min}$  to  $b_{max}$  with the fraction of substrate area covered by Ag islands ( $\phi_{exp} = 0.2$ ) as measured using SEM.

$$C = \frac{60\phi_{exp}}{\pi(b_{max} - b_{min})^3[3(b_{max} - b_{min})^2 + 10b_{max}b_{min}]}. \quad (3.10)$$

The Ag island layer is modeled using the TIF theory, which is, in principle, a multipole expansion for solving the electromagnetic problem of the response of identical particles to incident electromagnetic radiation. We use the spheroidal dipole approximation in our simulation, because Bobbert and Vlieger showed that the dipole approximation already gives a quite good result [149]. For the oblate spheroids with radii in the range from  $b$  to  $b+db$ , the collective optical response to an electromagnetic field is

expressed by the excess dipole strength parallel ( $\gamma$ ) and normal ( $\beta$ ) to the substrate, respectively

$$\gamma_{12} = \phi(b) \frac{8\pi c \varepsilon_1}{3\lambda} \frac{\delta \varepsilon_{12}}{1 + f_p \delta \varepsilon_{12}}, \quad (3.11)$$

$$\beta_{12} = \phi(b) \frac{8\pi c}{3\lambda \varepsilon_1} \frac{\delta \varepsilon_{12}}{1 + f_z \delta \varepsilon_{12}}, \quad (3.12)$$

where  $\delta \varepsilon_{12} = (\varepsilon_2 - \varepsilon_1)/\varepsilon_1$ , and  $c$  is the semi-axis of the spheroid along the  $z$  direction.

The parameters of  $f_p$  in eq. 3.11 and  $f_z$  in eq. 3.12 are the depolarization factors,  $\varepsilon_1$  is the dielectric function of layer 1 (air), and  $\varepsilon_2$  is the frequency-dependent dielectric function of the Ag islands. The schematic of our system with 3 layers is shown in fig. 3.15 (b). For an isolated oblate spheroid in vacuum, the in-plane ( $x$ - $y$  plane) depolarization factor  $f_p^0$  and perpendicular depolarization factor  $f_z^0$  can be analytically calculated from eq. 1.21,

$$f_z^0 = (1 + \xi^2) \left[ 1 - \xi \tan^{-1} \left( \frac{1}{\xi} \right) \right], \quad (3.13)$$

$$f_p^0 = \frac{1}{2}(1 - f_z^0), \quad (3.14)$$

where  $\xi = \frac{1}{\sqrt{(b/c)^2 - 1}}$ . Because Ag islands are on top of the Si substrate, the effect of the

Si substrate on the depolarization factors can be modeled as the interaction of a point dipole with its own image-dipole in the Si substrate [150]. The dressed depolarization factors for an oblate spheroid on a Si substrate are calculated in the spheroidal dipole approximation by Valamanesh et al. [150],

$$f_p^* = f_p^0 - \frac{1}{2}B_{13}(1 + \xi^2) \left[ \left( \frac{3}{2} + \xi^2 \right) \xi^2 \ln \left( 1 + \frac{1}{\xi^2} \right) - \xi \tan^{-1} \left( \frac{1}{\xi} \right) - \xi^2 \right], \quad (3.15)$$

$$f_z^* = f_z^0 - B_{13}(1 + \xi^2) \left[ \left( \frac{3}{2} + \xi^2 \right) \xi^2 \ln \left( 1 + \frac{1}{\xi^2} \right) - \xi \tan^{-1} \left( \frac{1}{\xi} \right) - \xi^2 \right], \quad (3.16)$$

where  $B_{13} = (\varepsilon_1 - \varepsilon_3)/(\varepsilon_1 + \varepsilon_3)$ .  $\varepsilon_3$  is the frequency dependent dielectric function of layer 3, the Si substrate.

The polarization-dependent reflection and transmission coefficients for a film of Ag oblate spheroids are given in [146],

$$r_{12}^s = \frac{X^s}{1-X^s}, \quad (3.17a)$$

$$t_{12}^s = \frac{1}{1-X^s}, \quad (3.17b)$$

$$r_{12}^p = \frac{X^p}{1-X^p} - \frac{Y^p}{1-Y^p}, \quad (3.17c)$$

$$t_{12}^p = 1 + \frac{X^p + Y^p - 2X^p Y^p}{(1-X^p)(1-Y^p)}, \quad (3.17d)$$

where the parameters  $X$  and  $Y$  are

$$X_{12}^s = \frac{i}{2n_1 \cos \theta_1} \gamma_{12}, \quad (3.18a)$$

$$X_{12}^p = \frac{in_1^3 \sin^2 \theta_1}{2 \cos \theta_1} \beta_{12}, \quad (3.18b)$$

$$Y_{12}^p = \frac{i \cos \theta_1}{2n_1} \gamma_{12}, \quad (3.18c)$$

where  $n_1$  is the refractive index of layer 1 (air) and  $\theta_1$  is the incident angle of light in layer 1, for which  $70^\circ$  was used in the measurements.

The Abelés matrix of the thin island film can be expressed in terms of these reflection and transmission coefficients. For the  $s$ -polarized component, the Abelés transition matrix is

$$F_{12}^s = \frac{1}{t_{12}^s} \begin{pmatrix} 1 & -r_{12}^s \\ r_{12}^s & (t_{12}^s)^2 - (r_{12}^s)^2 \end{pmatrix}. \quad (3.19a)$$

For the  $p$ -polarized component, the Abelés transition matrix is

$$F_{12}^p = \frac{1}{t_{12}^p} \begin{pmatrix} 1 & -r_{12}^p \\ r_{12}^p & (t_{12}^p)^2 - (r_{12}^p)^2 \end{pmatrix}. \quad (3.19b)$$

The Abelés matrix for light passing through the Ag island film is same as eq. 3.6, but with a different expression for the phase-factor,

$$L_f = \begin{pmatrix} e^{-i\Delta} & 0 \\ 0 & e^{i\Delta} \end{pmatrix}, \quad (3.20)$$

where  $\Delta = (2\pi/\lambda)cn_1 \cos \theta_1$ . Here, the parameter  $c$  is half of the oblate height. For Ag oblate spheroids in vacuum that are in intimate contact with the Si substrate, the  $p$ -reflectivity can be found from

$$A^p = F_{12}^p L_f I_{13}^p, \quad (3.21a)$$

and the  $s$ -reflectivity can be found from

$$A^s = F_{12}^s L_f I_{13}^s, \quad (3.21b)$$

using the equations  $R^p = A_{21}^p/A_{11}^p$  and  $R^s = A_{21}^s/A_{11}^s$ .

With the calculated reflectivity, the pseudodielectric function can be simulated from eq. 3.1 and 3.2. For the simulation, the dielectric function of the Ag island film in [150] is used

$$\varepsilon_2 = \varepsilon_b + \frac{\omega_p^2}{\omega(\omega + i\tau_b^{-1})} - \frac{\omega_p^2}{\omega(\omega + i\tau_j^{-1})}, \quad (3.22)$$

where  $\varepsilon_b$  is the frequency dependent dielectric function of bulk Ag,  $\omega_p$  is the Ag bulk plasmon frequency ( $1.72 \times 10^{16}$  rad/s),  $\tau_b$  is the relaxation time of the bulk plasmon ( $3.1 \times 10^{-14}$  s), and  $\tau_j$  is the relaxation time of surface plasmons in the Ag islands ( $3.6 \times 10^{-15}$  s).

The simulated pseudodielectric functions are shown in fig. 3.16, where the frequency-dependent dielectric function of Si is plotted as red solid lines. The purpose of

fig. 3.16 (a) and (b) is to identify the LSPR modes associated with Ag-related features associated with in-plane and out-of plane plasmon modes. In fig. 3.16 (a) and (b), the pseudodielectric function of Ag oblate spheroids on a Si substrate with the parallel in-plane plasmon modes turned off is shown in blue, and that with the perpendicular plasmon modes turned off is shown in green. The parallel or perpendicular plasmon modes are ‘turned off’ by setting  $\gamma$  or  $\beta$  (eqs. 3.11 or 3.12) to zero in the simulation.

In this part of the simulation, the semi-axis of the oblate spheroids in the  $z$  direction is set to 4.14 nm and the radius of the oblate spheroids,  $b$ , ranges from 10 to 20 nm. The number of bins for the radius,  $b$ , is 4, because using a small number of wide bins in the simulation results in pseudodielectric functions showing clearly separated, discrete plasmon modes.

In fig. 3.16 (a), the sequence of features shown around 2 eV in the green spectrum that plots the pseudodielectric function with the perpendicular modes turned off correspond to different aspect ratios ( $b/c$ ). The peak at lowest energy has the largest aspect ratio of 4.8, and the peak at highest energy has the smallest aspect ratio of 2.4, which indicates that the parallel in-plane plasmon mode redshifts as the aspect ratio of  $b/c$  increases. For the blue spectrum that plots the pseudodielectric function with the parallel in-plane modes turned off in fig. 3.16 (a) and (b), we don’t observe clearly separated features associated with the the high-energy plasmonic feature, which indicates that the perpendicular plasmon mode barely depends on the change of aspect ratio ( $b/c$ ). The observations are consistent with the results shown in fig. 3.14 (a).

By comparing the spectrum without perpendicular plasmon modes to the Si dielectric function, we can see that turning off the perpendicular plasmon modes makes

the pseudodielectric function at higher energy match that of the Si substrate. Fig. 3.16 (a) and (b) clearly suggest that the feature at  $\sim 3.9$  eV in the experimental pseudodielectric functions for SB Ag islands on Si, as shown in fig. 3.13, is associated with the perpendicular plasmon modes ( $z$  direction).

From fig. 3.16 (a) and (b), we can see that the pseudodielectric function with Ag islands on Si (blue) at energy range  $<2.5$  eV fits the dielectric function of a Si substrate (red) when the parallel in-plane plasmon modes are turned off. Even though the spectrum (blue) without parallel plasmon modes in fig. 3.16 (b) does not overlap with that of Si at energy range  $<2.5$  eV, the peak-like features at the low energy side of the blue spectrum disappear. Thus, we believe that the peak-like features appearing near 2 eV in the simulated pseudodielectric functions are associated with the in-plane plasmon modes of the Ag islands. However, if we use the actual size distribution of SB islands in the simulation, turning off the in-plane plasmon modes does not change the spectrum at all. This simulation work is ongoing, and more work needs to be done in order to determine if the features at  $\sim 3.0$  eV in experimental pseudodielectric functions with SB Ag islands are associated with the parallel in-plane plasmon modes ( $x$  or  $y$  direction).

Fig. 3.16 (c) and (d) show the comparison between the experimental pseudodielectric function (green) and the best fit from the simulation (blue). As stated above, the red curves represent the dielectric function of the Si substrate. The simulation curve that fits the experimental pseudodielectric function best requires the parameter,  $c$ , to be 8.18 nm, which doubles the actual SB Ag island height (4.18 nm), and the diameter of the oblate spheroids,  $b$ , varies from 10 to 20 nm. The number of bins for the diameter of  $b$  is set to 20. Several reasons can be attributed to the requirement of doubling the

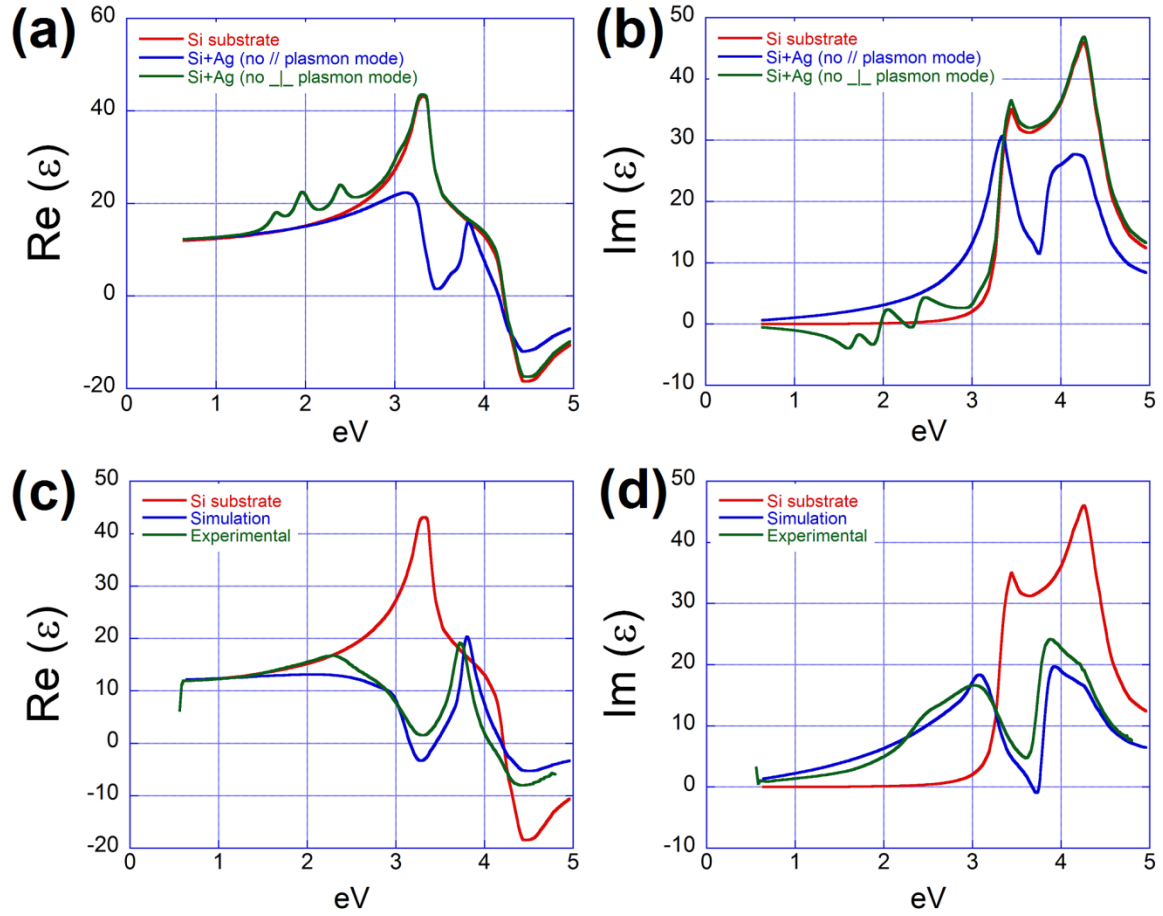


*Figure 3.16.* (a) and (b) show the real and imaginary part of the simulated pseudodielectric functions, respectively. The red curves are for the Si substrate. The blue curves are simulated with the in-plane parallel plasmon modes turned off. The green curves are simulated with perpendicular plasmon modes turned off. (c) and (d) compare the real and imaginary part of the experimentally measured and best-fit simulated pseudodielectric function. The simulated pseudodielectric functions are plotted in blue, experimentally measured are plotted in green and the Si dielectric function is plotted in red.

island height in order to fit the experimental pseudodielectric function. First, it is possible that the height information for SB islands roughly determined from AFM data is smaller than their actual height because AFM tip may not be able to reach the Si surface due to very high density of SB Ag islands. Secondly, the approximation of actual island morphology to oblate spheroidal shapes is probably too rough. Thirdly, the oxidization of Si could increase the actual spacing between the plasmonic dipole and pure Si. The final reason could be that sharp corners of Ag islands introduce higher multipolar plasmons, resulting in that the dipolar approximation in the simulation is not good enough.

### **3.2.2 Ag/Si(100) islands capped with an $\alpha$ -Si layer.**

The effect of the Si dielectric medium on the LSPR of Ag islands was also investigated, and the results are discussed in this section. As shown in fig. 3.11, embedding Ag islands in a Si matrix could redshift the LSPR of Ag islands. On top of two selected ensembles of Ag islands, we deposited  $\sim 30$  nm of  $\alpha$ -Si. The plasmonic properties of capped Ag/Si(100) islands were measured using spectroscopic ellipsometry. The effect of the  $\alpha$ -Si cap layer on the LSPR of Ag islands is determined by comparing the ellipsometry spectra of  $\alpha$ -Si capped samples to those with bare Ag islands.

Fig. 3.17 (a) and (b) show SEM images of  $\alpha$ -Si capped SB and BB Ag islands, respectively. The growth conditions for the Ag islands shown in fig. 3.17 (a) is exactly same as those for the islands shown in fig. 3.12 (a), and the growth conditions for the islands shown in fig. 3.17 (b) is exactly same as those for the islands shown in fig. 3.12 (b). Figs. 3.17 (c) and (d) show the imaginary part of the frequency-dependent pseudodielectric functions for  $\alpha$ -Si capped SB and BB Ag islands on Si, respectively. In both fig. 3.17 (c) and (d), the red solid curves are for samples without an  $\alpha$ -Si cap layer,



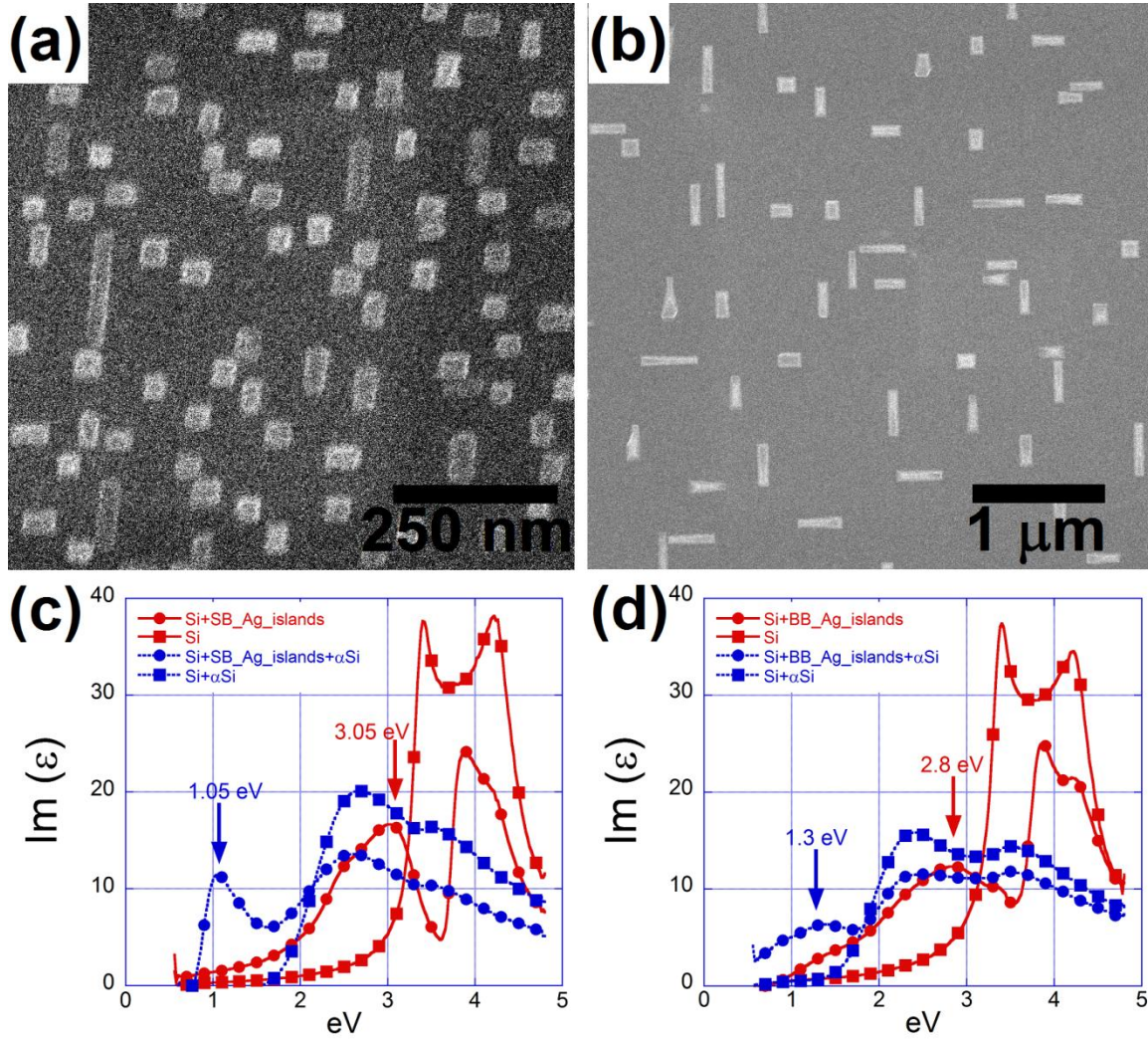


*Figure 3.17.* (a) and (b) show SEM images of SB and BB Ag islands capped with 30 nm thick  $\alpha$ -Si layer. (c) and (d) show the imaginary part of experimental pseudodielectric functions for samples with SB Ag islands and BB Ag islands, respectively. In both (c) and (d), the red curves with circular markers are for bare Ag islands on Si, the red curves with square markers are for the Si substrate, the blue curves with circular markers are for the  $\alpha$ -Si capped Ag islands on Si, and the blue curves with square markers are for the  $\alpha$ -Si capped layer on Si.

and the blue curves are for samples with a 30 nm thick  $\alpha$ -Si cap layers. Curves with solid circular markers refer to the samples with Ag NPs, and curves with solid square markers are for samples without Ag NPs.

From the discussion in section 3.2.1, the two plasmon modes, the parallel in-plane mode at the lower energy side and the perpendicular mode at the higher energy side, may contribute to the features in experimental pseudodielectric functions with bare Ag/Si(100) islands (red curves). By comparing the two blue spectra in fig. 3.17 (c), a plasmon feature related to the  $\alpha$ -Si capped SB Ag islands can be found at  $\sim 1.05$  eV. A similar plasmon-related feature for  $\alpha$ -Si capped BB Ag islands can also be found at  $\sim 1.3$  eV by comparing the two blue curves in fig. 3.17 (d). The plasmon-related peaks in the IR range are redshifted from the plasmons for bare Ag islands due to the dielectric screening effect of the  $\alpha$ -Si cap layer, but it is difficult to identify from which plasmon modes the LSPR of  $\alpha$ -Si capped Ag islands are originated without detailed simulation. Even though it is not clear which plasmon modes contribute to the LSPR feature associated with  $\alpha$ -Si capped Ag islands, a clear conclusion can still be made that the  $\alpha$ -Si cap layer dramatically redshifts the LSPR of Ag islands from the UV to the IR range.

### **3.3 Ag Growth on Si-capped Ge/Si(100) Dots**

In this section, results of the investigation into determining the optimum heterostructure growth conditions will be discussed. This heterostructure is schematically depicted in fig. 2.13. The Ge/Si(100) QD growth will be treated first. Next, the surface quality of the Si cap layer will be discussed. The change of dot morphology during growth of the Si cap layer will then be considered. It will be shown that different Si cap layer-growth recipes produce different morphologies for the buried Ge dots. Finally, we

will describe Ag island growth on the Si cap layers and the effect of cap layer thickness on Ag island nucleation.

### 3.3.1 Ge/Si(100) quantum dot growth.

As pointed out in the earlier discussion of Ge/Si(100) QDs, there are several different distinct dot morphologies: huts/pyramids, coherent domes, and dislocated domes. Any specific dot morphology with distinct density can be achieved by tuning the growth parameters [151]. A series of experiments were performed to determine the optimum growth conditions for the desired dot morphologies and densities. These parameters can be controlled by varying the Ge deposition rate, Ge coverage, and substrate temperature. Based on the work of previous researchers in our group, we were led to explore one deposition rate of 2.7 ML/min, and two growth temperatures, 550 and 600 °C. Ge coverage was tuned to obtain island ensembles containing solely huts, solely coherent domes, or a mixture of both.

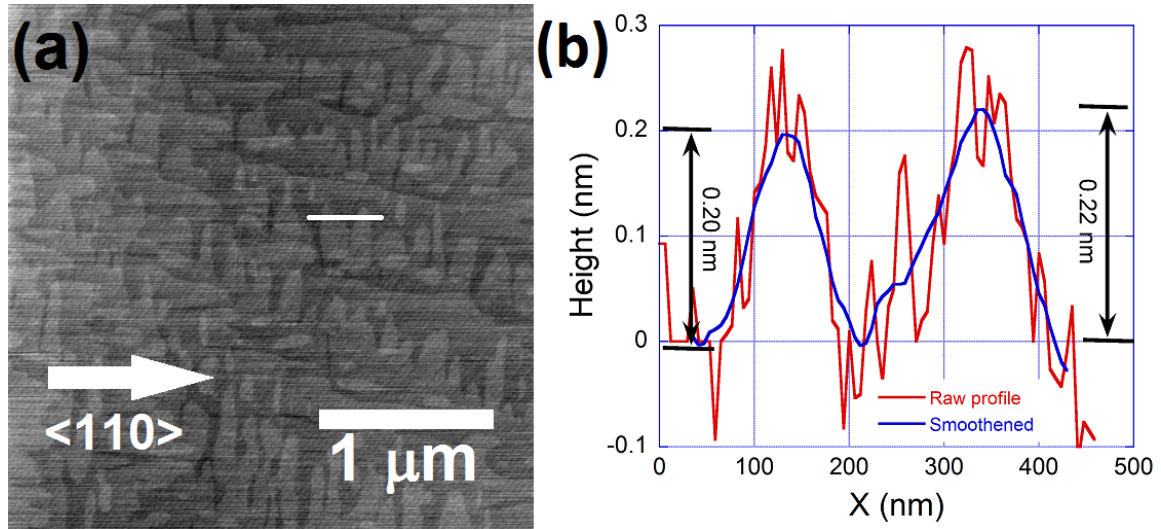


*Figure 3.18.* An AFM image of a Si buffer layer is shown in (a), which is a 3 μm by μm scan. The crystallographic orientation of the AFM image is indicated in (a). The height profile of the white line as indicated in (a) is shown in (b). It clearly shows the step height is ~0.2 nm.

A standard growth recipe for a ~100 nm buffer layer was employed to obtain an atomically flat surface, which is critical for successful dot growth. The surface quality of the Si buffer layer was investigated using AFM. From the AFM image shown in fig. 3.18 (a), single-atomic-layer steps can clearly be seen. The height profile plot of the line scan indicated in fig. 3.18 (a) is shown in fig. 3.18 (b). In fig. 3.18(b), the red curve shows the raw height profile, and the smoothened raw height profile is shown in blue. This height profile clearly shows the step height to be about 0.2 nm, as indicated in fig. 3.18(b).

A series of samples were grown at 550 °C with different Ge coverages in order to determine the optimum coverage that produces ensembles with huts/pyramids only. AFM images of these samples are shown in fig. 3.19. The Ge coverage corresponding to fig. 3.19 (a), (b), (c), and (d) are 5.6 ML, 5.9 ML, 6.3 ML, and 6.8 ML, respectively. The Ge dots in fig. 3.19 (a) and (b) are solely huts/pyramids, and we can see that the density of the Ge huts/pyramids increases as the Ge coverage increases from 5.6 to 5.9 ML. When the Ge coverage is above 6.0 ML, both huts and coherent domes coexist, as shown in fig. 3.19 (c) and (d). Simple morphology analysis shows that the bright dots with circular bases in both fig. 3.19 (c) and (d) are coherent domes, and that those with square or rectangular bases are huts/pyramids. As the Ge coverage increases from 6.3 to 6.8 ML, the density of Ge coherent domes is not affected, while the density of Ge huts/pyramids increases drastically. The Ge coverage for each of these samples was determined from RBS. By varying the Ge coverage at the same growth temperature, both dot morphology and density can be tuned. The quantitative analysis of Ge dot density will be given in the following discussion.

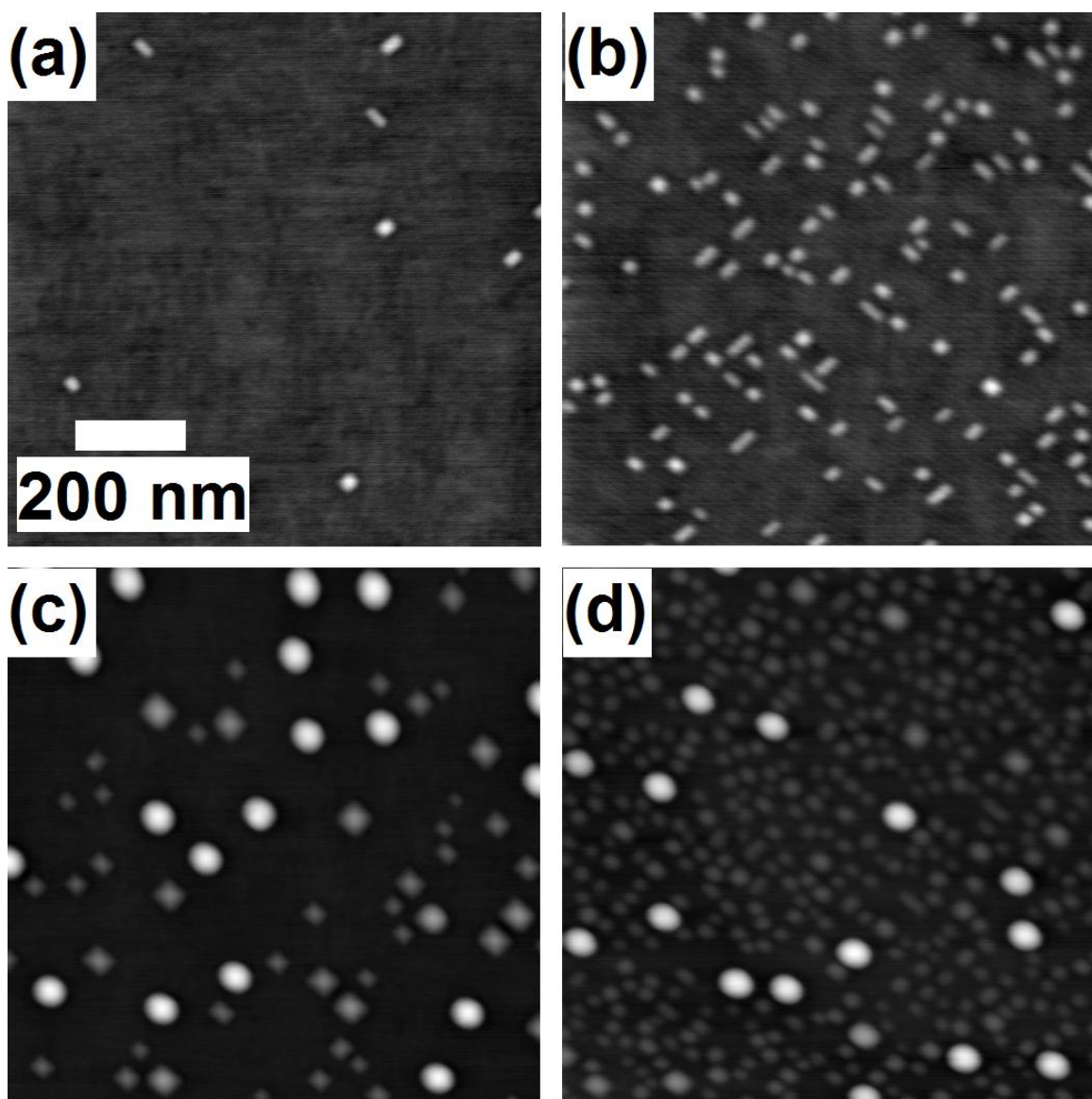


*Figure 3.19.* The AFM images of a series of samples grown at 550 °C under identical deposition rate of 2.7 ML/min. All of these 4 images have the same size, and the scale bar is shown in (a). The Ge coverage corresponding to (a), (b), (c) and (d) are 5.6 ML, 5.9 ML, 6.3 ML and 6.8 ML, respectively.

Below 6.0 ML, the dot ensemble contains solely huts/pyramids, as shown in fig 3.19 (a) and (b). However, the increase of Ge coverage from 5.6 ML to 5.9 ML results in an increase of the dot density from  $3.7 \times 10^8 / \text{cm}^2$  to  $1.2 \times 10^{10} / \text{cm}^2$ , as shown in fig. 3.19 (a) and (b). The average size of huts/pyramids, defined as the square root of the island basal area, is in the range of ~30–40 nm.

With the Ge coverage in the 6–7 ML range, as shown in fig. 3.19 (c) and (d), both huts/pyramids and coherent domes co-exist for as-grown samples at 550 °C. For the sample with 6.3 ML, as shown in fig. 3.19 (c), the density of coherent domes is  $1.7 \times 10^9 / \text{cm}^2$ , and that of huts/pyramids is  $4.8 \times 10^9 / \text{cm}^2$ . For the Ge coverage of 6.8 ML, as in fig. 3.19 (d), the density of domes is  $1.8 \times 10^9 / \text{cm}^2$ , but the density of huts/pyramids is  $3.9 \times 10^{10} / \text{cm}^2$ . Note that the density of domes is not affected when Ge coverage increases from 6.3 ML to 6.8 ML, while the density of huts/pyramids increases by an order of magnitude, so the additional 0.5 ML contributes to the huts/pyramids growth.

From this series of samples grown at 550 °C at a rate of 2.7 ML/min, we are able to produce Ge dot ensembles comprised solely of huts/pyramids if the Ge coverage is between 5.1 ML and 6.0 ML. Fig. 3.19 (a) and (b) suggest that any density of huts/pyramids can be achieved by varying the Ge coverage between 5.1 ML and 6.0 ML.

Another series of samples were grown at 600 °C to determine the optimum growth conditions for domes-only ensembles. These samples were grown with identical deposition rates but different Ge coverage. AFM images of these samples are shown in fig. 3.20. The Ge coverage corresponding to fig. 3.20 (a), (b), (c), and (d) is 5.6 ML, 5.8 ML, 6.2 ML, and 6.6 ML, respectively. Each of the four images is 1  $\mu\text{m}$  by 1  $\mu\text{m}$ , so they share the same scale bar that is shown in fig. 3.20 (a). Both (a) and (b) in fig. 3.20 display



domes-only ensembles. These domes have diameters of  $\sim 70$  nm and heights of  $\sim 15$  nm. The areal density of domes in fig. 3.20 (b) is higher than that in (a). Fig. 3.20 (c) exhibits a mixture of coherent domes and huts/pyramids. Analyzing the morphology of the shorter (darker) dots indicates that their bounding facets make contact at an angle of  $11^\circ$  with the substrate. Similar analysis of the higher (brighter) dots indicates that their bounding facets contact the substrate at an angle of  $25^\circ$ . Fig. 3.20 (d) shows that the majority of Ge dots are coherent domes and that huts/pyramids are almost negligible. At the fixed growth temperature of  $600^\circ\text{C}$ , the morphology and density of Ge dots can be tuned by varying Ge coverage.

Fig. 3.20 (a) shows the sample with 5.6 ML Ge; the density of domes in this sample is  $9 \times 10^7 / \text{cm}^2$ . The sample with 5.8 ML Ge is shown in fig. 3.20 (b), from which the density of domes is determined to be  $1.1 \times 10^9 / \text{cm}^2$ . When the coverage is between 6.0 ML and 7.0 ML, samples grown at  $600^\circ\text{C}$  contain a mixture of domes and huts. Fig. 3.20 (c) shows the sample with Ge coverage of 6.2 ML; by analyzing fig. 3.20 (c), the density of domes is determined to be  $1.8 \times 10^9 / \text{cm}^2$  and the density of huts  $3.9 \times 10^9 / \text{cm}^2$ . As the Ge coverage increases to 6.6 ML, the density of domes becomes  $3.5 \times 10^9 / \text{cm}^2$  and that of huts decreases to  $6 \times 10^8 / \text{cm}^2$ , as shown in fig. 3.20 (d). Compared with fig. 3.19 (c) and (d), we can conclude that domes and huts co-exist at both growth temperatures of  $550^\circ\text{C}$  and  $600^\circ\text{C}$  if the Ge coverage is in the range of 6.0–6.8 ML. However, the fraction of domes grown at  $600^\circ\text{C}$  is higher than those grown at  $550^\circ\text{C}$ .

It is interesting to note that growing at  $550^\circ\text{C}$  produces ensembles with huts/pyramids only, and growing at  $600^\circ\text{C}$  leads to ensembles with coherent domes only when the Ge coverage is below 6.0 ML. We also noted that dislocated domes start to

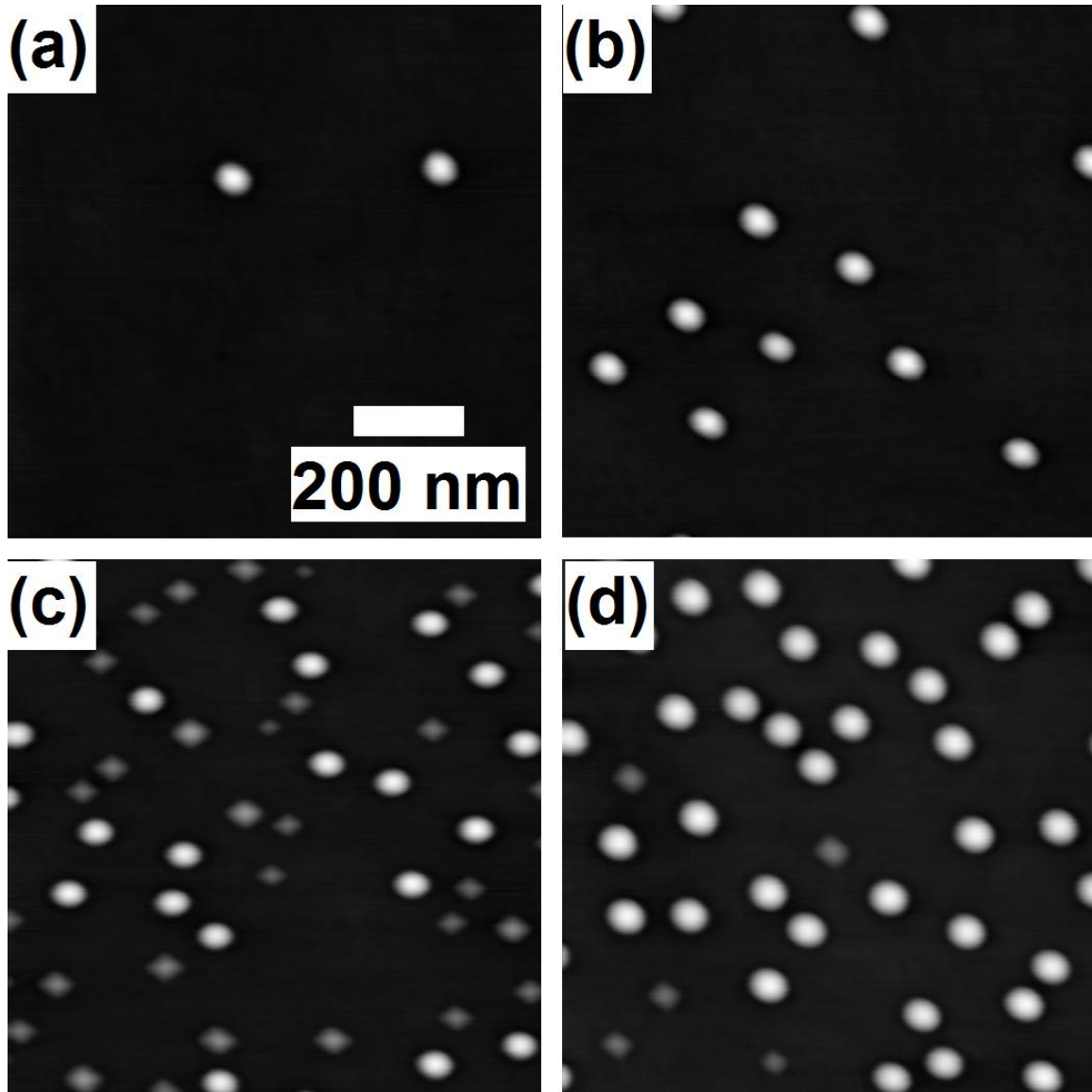


*Figure 3.20.* AFM images of a series of samples grown at 600 °C with an identical deposition rate of 2.7 ML/min. All of these images are 1  $\mu\text{m}$  by 1  $\mu\text{m}$ . The scale bar is shown in (a). The Ge coverage corresponding to (a), (b), (c) and (d) are 5.6 ML, 5.8 ML, 6.2 ML and 6.6 ML, respectively.

appear if the Ge coverage is above 6.8 ML at the growth temperature of 600 °C. Based on the results from fig. 3.20 (a) and (b), any density of Ge domes can also be obtained by varying Ge coverage. We employed two ensembles of Ge domes with different densities



to investigate the optical properties of Ge QD:  $\sim 9 \times 10^7 / \text{cm}^2$  and  $\sim 3.5 \times 10^9 / \text{cm}^2$ . The reason we did not investigate the optical properties of ensembles with huts/pyramids only is that they are very likely to be flattened out during Si capping. This process will be discussed further in the next sub-section.

### 3.3.2 Si capping of Ge quantum dots.

In order to investigate the optical or electronic properties of Ge/Si(100) QDs, or to incorporate them into devices, it is critical to cap these dots with Si. The results of our investigation with regard to Si capping of Ge QD will be discussed in this sub-section. Two growth recipes for cap layers were employed in our investigation. As described in the introduction, the Ge dot morphology will be affected during Si cap layer growth, so the evolution of dot morphology will be addressed here. Another issue is the roughness of the cap layer surface, so the dependence of the cap layer roughness on the cap layer thickness will be discussed. The minimum cap layer thickness yielding an atomically flat surface is also determined. This information provides a starting point for us to grow Ag islands atop this surface.

The first growth recipe for the Si cap layer consisted of growing the cap layer at the same temperature as that of Ge QD. Four AFM images of samples grown according to the first recipe are shown in fig 3.21. Fig. 3.21 (a) and (c) show Ge huts-only ensembles (the coverage of Ge,  $\theta_{\text{Ge}}$ , is 5.8 ML) capped with 10 nm and 15 nm thick Si layers, respectively, that were grown at 550 °C. The surface quality of the 10 nm and 15 nm thick Si cap layers on Ge domes-only dot ensembles ( $\theta_{\text{Ge}}=6.8$  ML) grown at 600 °C are shown in fig. 3.21 (b) and (d). Each of these four AFM images shares the same scale bar, which is indicated in fig. 3.21 (a). Fig. 3.21 (a) shows that the 10 nm Si cap layer on

hut/pyramids is already atomically flat, except for a low density of shallow pits that are indicated in the figure. For a 10 nm Si cap layer on coherent domes, as shown in fig. 3.21 (b), the surface is rougher than that in (a) due to the existence of larger and deeper pits. This could be attributed to the fact that coherent domes have larger heights ( $\sim 15$  nm) than huts/pyramids ( $\sim 3$  nm), as shown in fig. 1.3. Pits in both fig. 3.21 (a) and (b) are correlated with Ge QD [152].

During Si capping, Ge dots undergo flattening. Ge atoms on the surface of Ge dots vertically flip position with deposited Si adatoms on the dot surface. [153] These Ge atoms then diffuse to the substrate surface to rejoin the dots at their perimeter. As discussed in section 1.2.2, this intermixing between the Si cap layer and the Ge dots reduces the misfit. This misfit reduction drives shape evolution of the Ge dots, given that the critical dot volume for the hut to dome shape transition is proportional to  $1/\epsilon^6$ . This flattening process is believed to stop when the first layer of Si adatoms on the dot surface is capped by the second layer at the growth temperatures we investigated. The dot flattening rate depends on the Si cap layer growth rate and on the substrate temperature.

By increasing the Si cap layer thickness to 15 nm for huts/pyramids and to 20 nm for coherent domes, we obtained atomically flat surfaces for both dot ensembles, as shown in fig. 3.21 (c) and (d). Note that no pits are evident in either fig. 3.21 (c) or (d), so the minimum Si cap layer thickness required to achieve an atomically flat surface (i.e., without any pits on the cap layer surface) is 15 nm for the huts/pyramids ensemble and 20 nm for the coherent domes ensemble. According to the literature, the maximum Si cap layer thickness, under which the cap layer surface still retains enough strain to modulate the growth of the next Ge QD layer, is  $\sim 80$  nm [54,62], so the strain field on the surface

of the  $\sim 20$  nm cap layer may play a role in templating Ag island growth or affect Ag nucleation.

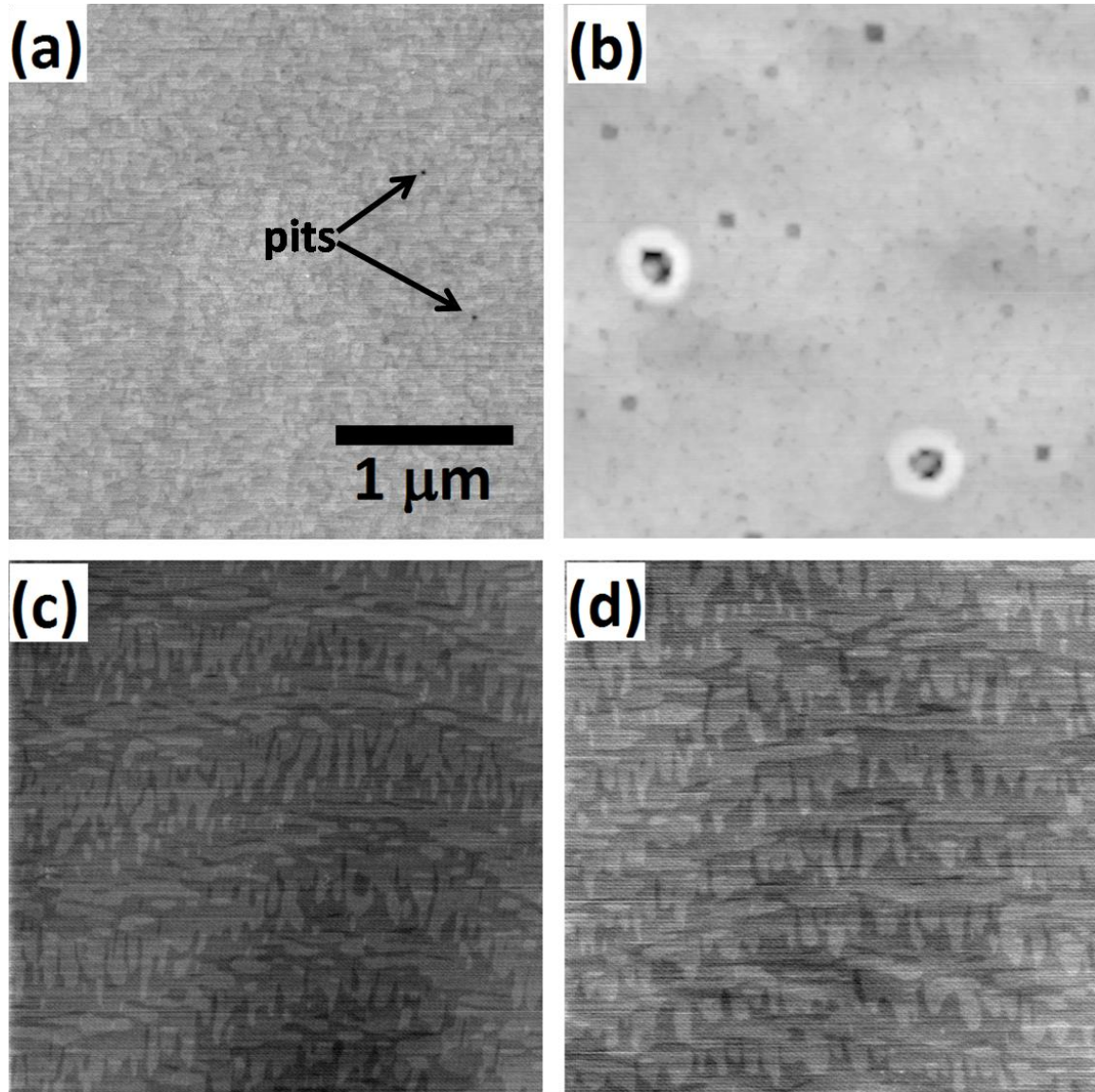


*Figure 3.21.* The AFM images of Si cap layer grown at 550 and 600 °C are shown here. (a) and (c) show 10 nm and 15 nm capping for huts only ensembles grown at 550 °C, respectively. (b) and (d) show 10 nm and 20 nm Si cap layer on domes only ensembles grown at 600 °C, respectively. They share the same scale bar as shown in (a).

From PL measurements, as discussed in section 3.4, we noticed that there is no Ge dot-related peak for the samples grown with the first recipe for the Si cap layer, so we performed cross-section transition electron microscopy (XTEM) measurements for one of these samples. The sample characterized by using XTEM had a domes-only dot ensemble ( $\theta_{\text{Ge}}=6.6$  ML) capped with a  $\sim 30$  nm Si layer at  $600^\circ\text{C}$ . The density of domes before capping with Si for this sample was  $3.5 \times 10^9 / \text{cm}^2$ , with an average spacing of  $\sim 180$  nm. We examined a relatively large area of the sample with an integrated length of  $\sim 5 \mu\text{m}$  along the Ge layer, but no Ge dots were observed in the XTEM image shown in fig. 3.22 (a). The same result was observed for another sample grown under identical conditions, but with a 20 nm thick Si cap layer. So we can conclude that all Ge coherent domes are flattened out when they are capped by Si at  $600^\circ\text{C}$ . Because huts/pyramids have a much smaller height-to-width ratio than coherent domes, it is reasonable to expect that they disappear more easily than coherent domes during Si capping. Therefore, a new growth recipe for the Si cap layer was developed.

Apparently, the first recipe for growing the Si cap layer at the same temperature as that of Ge dots does not work well, so we developed a new recipe for growing the Si cap layer that would preserve the dot morphology. As discussed previously, the dot-flattening rate is dependent on two parameters: growth temperature and the growth rate of the Si cap layer. Increasing the Si deposition rate requires higher Si e-gun power, which is likely to cause physical problems, e.g., arcing, higher growth pressure, and reduction in the lifetime of the e-gun filament. Therefore, the new recipe involved decreasing the growth temperature of the Si cap layer without introducing any growth interruption. The typical growth recipe is shown in fig. 2.14 (a), which indicates that the substrate

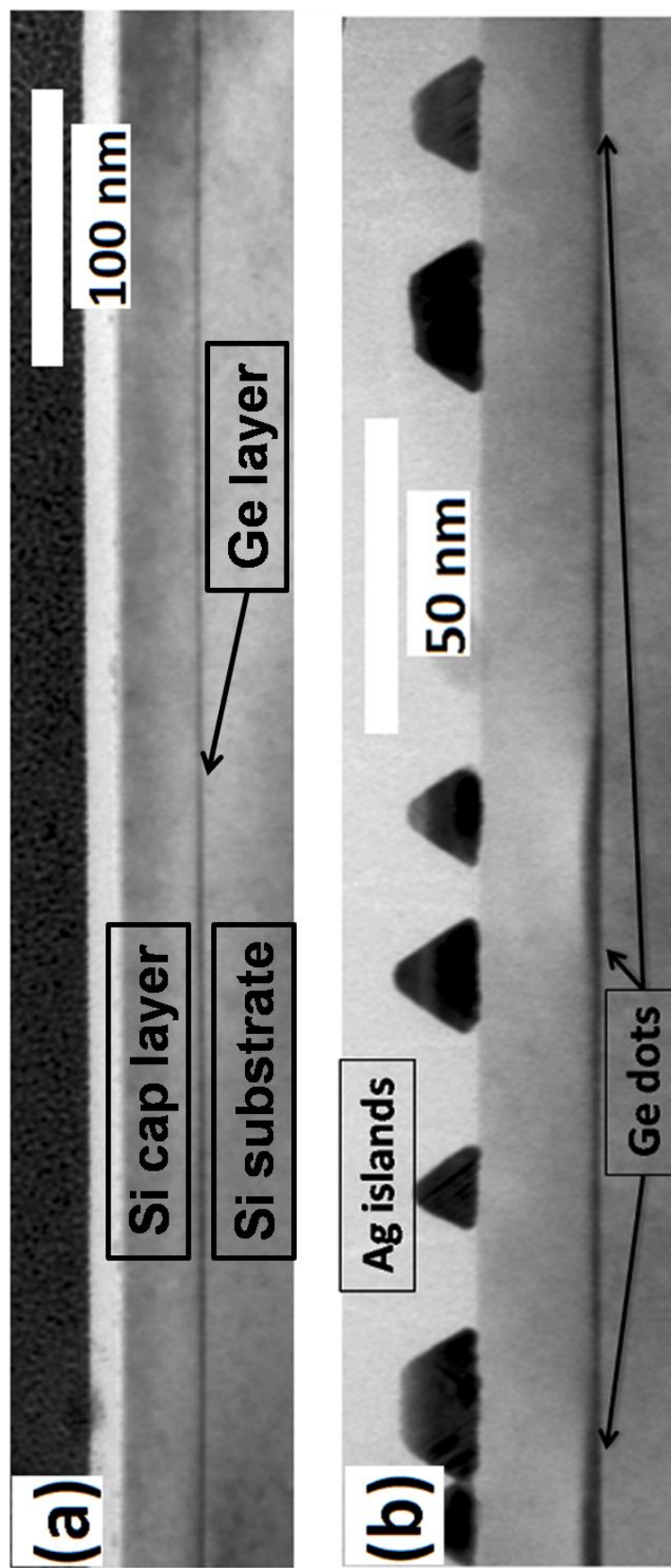
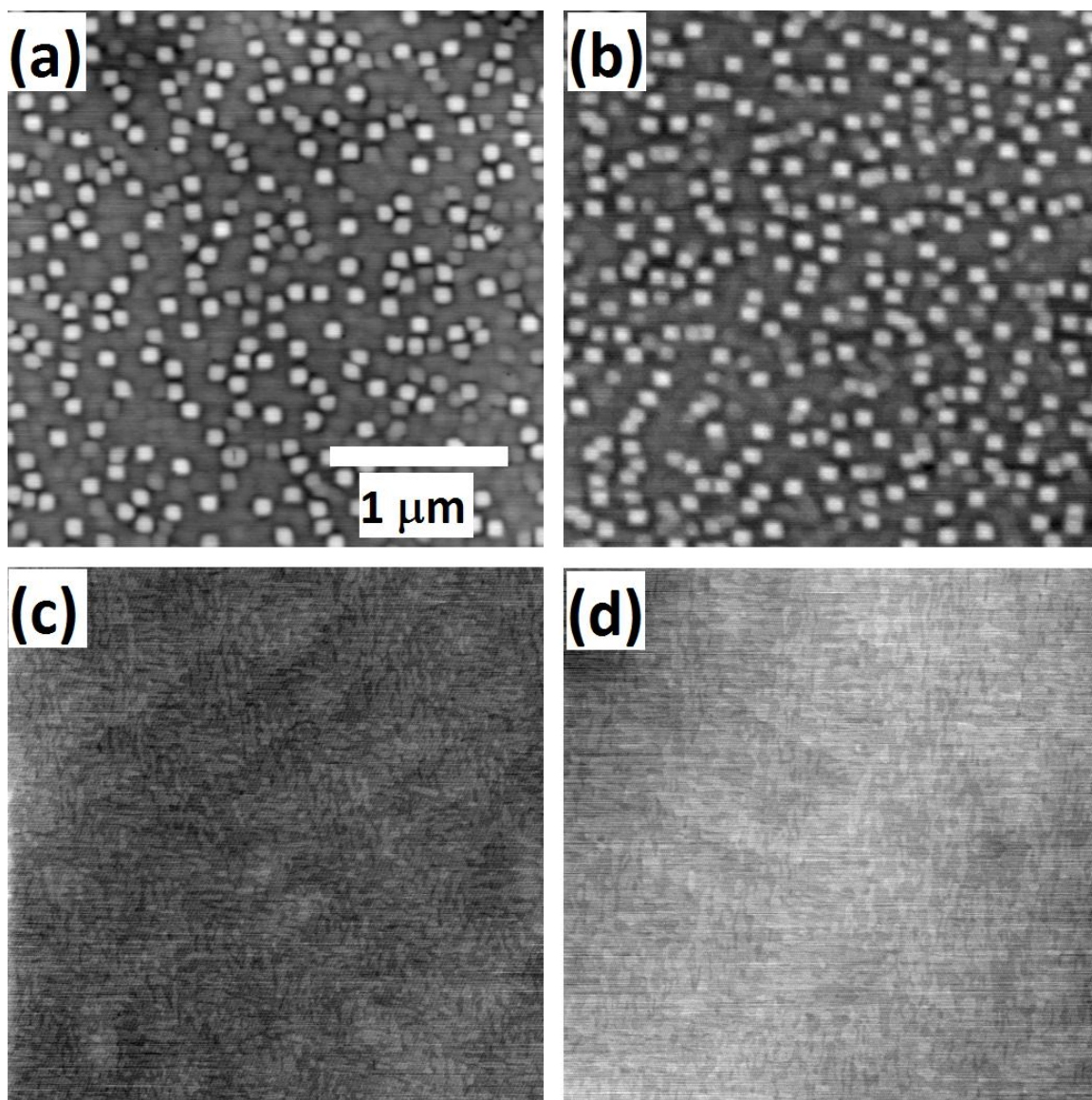


Figure 3.22. Both (a) and (b) show cross sectional TEM images. (a) is a TEM image of a sample comprised solely of domes ( $1.1 \times 10^9 / \text{cm}^2$ ) before capping with 30 nm of Si grown at 600 °C. There are no domes remaining after capping using this recipe. (b) displays the structure of a domes-only sample ( $1.1 \times 10^9 / \text{cm}^2$ ) capped with 20 nm of Si grown using the second cap layer growth recipe. During Si cap layer growth, sample temperature was dropped from 600 to 500 °C as quickly as possible. Domes are still evident after cap layer growth.

temperature is dropped from 600 to 500 °C as quickly as possible at the moment Ge flux is terminated and Si deposition is simultaneously initiated. The Eurotherm controller was retuned at several different substrate temperatures so that the substrate temperature could be dropped from 600 to 500 °C as rapidly as possible. With the optimized Si cap layer growth recipe, the substrate temperature drops to 500 °C in 3 min and overshoots only 4 °C below 500 °C. A XTEM image of the sample grown using the second recipe is shown in fig. 3.22 (b), from which we can clearly see the Ge dot morphology. The Ge dot growth condition for the sample shown in fig. 3.22 (b) is exactly the same as the one in fig. 3.22 (a), but with different growth recipes for the Si cap layer. We continued to use the second recipe for growing Si cap layers for the optical properties investigation.

The surface quality of Si cap layers grown according to the second recipe has been investigated using AFM. A series of samples with different Si cap layer thicknesses have been grown with the second recipe. AFM images of these samples are shown in fig. 3.23. The surface morphology of 5 nm, 10 nm, 15 nm, and 20 nm thick Si cap layers is shown in fig. 3.23 (a), (b), (c), and (d), respectively. 6.6 ML of Ge was deposited at 600 °C for all four of these samples, which produced domes-only dot ensembles. When the thickness of the cap layer is below 15 nm, an atomically flat surface cannot be achieved. By comparing fig. 3.23 (a) and fig. 3.21 (b), it is interesting to notice that growing a 10 nm Si cap layer by means of the second recipe forms only mountains, but without any pits, as shown in fig. 3.23 (a). This can be explained by the fact that lowering the growth temperature for the Si cap layer from 600 to 500 °C significantly reduces the interdiffusion between Ge dots and the cap layer. Mountains are correlated to Ge dots





*Figure 3.23.* AFM images of Si cap layers with a series of thicknesses, 5 nm in (a), 10 nm in (b), 15 nm in (c) and 20 nm in (d). These AFM images share the same scale bar as shown in (a). The Si cap layer was grown with the new recipe, which is to drop the substrate temperature from 600 to 500 °C as quickly as possible. The minimum cap layer thickness that produces an atomically flat surface is 15 nm.

because, as shown in fig. 3.22 (b), the height of capped Ge dots is 3 nm, which is similar to that of mountains, as shown in fig. 3.23 (a). From this series of samples, the minimum thickness of the Si cap layer that produces an atomically flat surface has been determined to be 15 nm for the second recipe, which is 5 nm thinner than that for the first recipe. By reducing the value of minimum thickness, stronger strain modulation at the cap layer surface can be achieved, which may facilitate the templating of Ag islands directly on top of Ge dots.

### **3.3.3 Ag island growth on the Si cap layer.**

In this section, the investigation of Ag islands growth on Si cap layers will be discussed. Our results show that the density of Ag islands strongly depends on the thickness of the Si cap layer. To identify possible factors that may contribute to the change in Ag island density, the average strain of the Si cap layer has been analyzed using Raman spectroscopy and the composition of the Si cap layer has been characterized using X-ray photoelectron spectroscopy (XPS). The results of these measurements will also be discussed.

A series of samples was grown in order to determine the effect of the strained Si cap layer on templating Ag island growth. Si cap layers with various thicknesses were grown according to the second recipe, i.e., the substrate temperature was ramped from 600 to 500 °C as quickly as possible during the cap layer growth. The selected Si cap layer thicknesses were 5, 10, 15, and 20 nm, the surface morphologies of which are shown in fig. 3.23. For each of the samples with these Si cap layer thicknesses, the Ge dot layer was grown by depositing 6.6 ML of Ge at 600 °C at rate of 2.7 ML/min. These Ge deposition conditions yield dome-only dot ensembles. Subsequent to the cap layer



deposition at 500 °C, 9.6 ML of Ag was deposited at a rate of 3.2 ML/min on the Si cap layer surface at 450 °C. By analyzing this series of samples, the effect of the Si cap layer thickness on the growth of Ag islands can be determined.

SEM images of Ag islands grown on top of the Si cap layers are shown in fig. 3.24, and they all share the same scale bar as shown in (a). The thickness of the Si cap layer corresponding to figs. 3.24 (a), (b), (c), and (d) is 20, 15, 10, and 5 nm, respectively. Fig. 3.24 shows that the density of the Ag islands monotonically decreases as the thickness of the Si cap layer decreases from 20 to 10 nm. When the thickness of the Si cap layer decreases from 10 to 5 nm, the density of the Ag islands increases by almost a factor of 2, as shown in fig. 3.24 (c) and (d). The quantitative dependence of Ag island density on the thickness of the Si cap layer is shown in fig. 3.27 (a).

There are several factors that may contribute to this effect, among them being average strain in the Si cap layer, the Ge concentration on the surface of the Si cap layer, and surface roughness. As discussed in section 1.2.4, strain can propagate to the Si cap layer surface from the buried Ge dots. It has been observed that strain can template the growth of the next Ge dot layer, which ensures that dots in the new layer grow atop those underneath the Si cap layer [57,59,62]. The strain at the surface of the Si cap layer is dependent on its thickness [59]. The strain at the cap layer surface could influence the density of Ag islands.

As discussed in section 1.2.4, Ge surface segregation may occur during Si capping of Ge QDs when the substrate temperature is above 300 °C due to the lower Ge surface energy [55]. In our recipe for growing the Si cap layer, the temperature of the substrate is decreased as rapidly as possible from 600 to 500 °C, which is well above 300

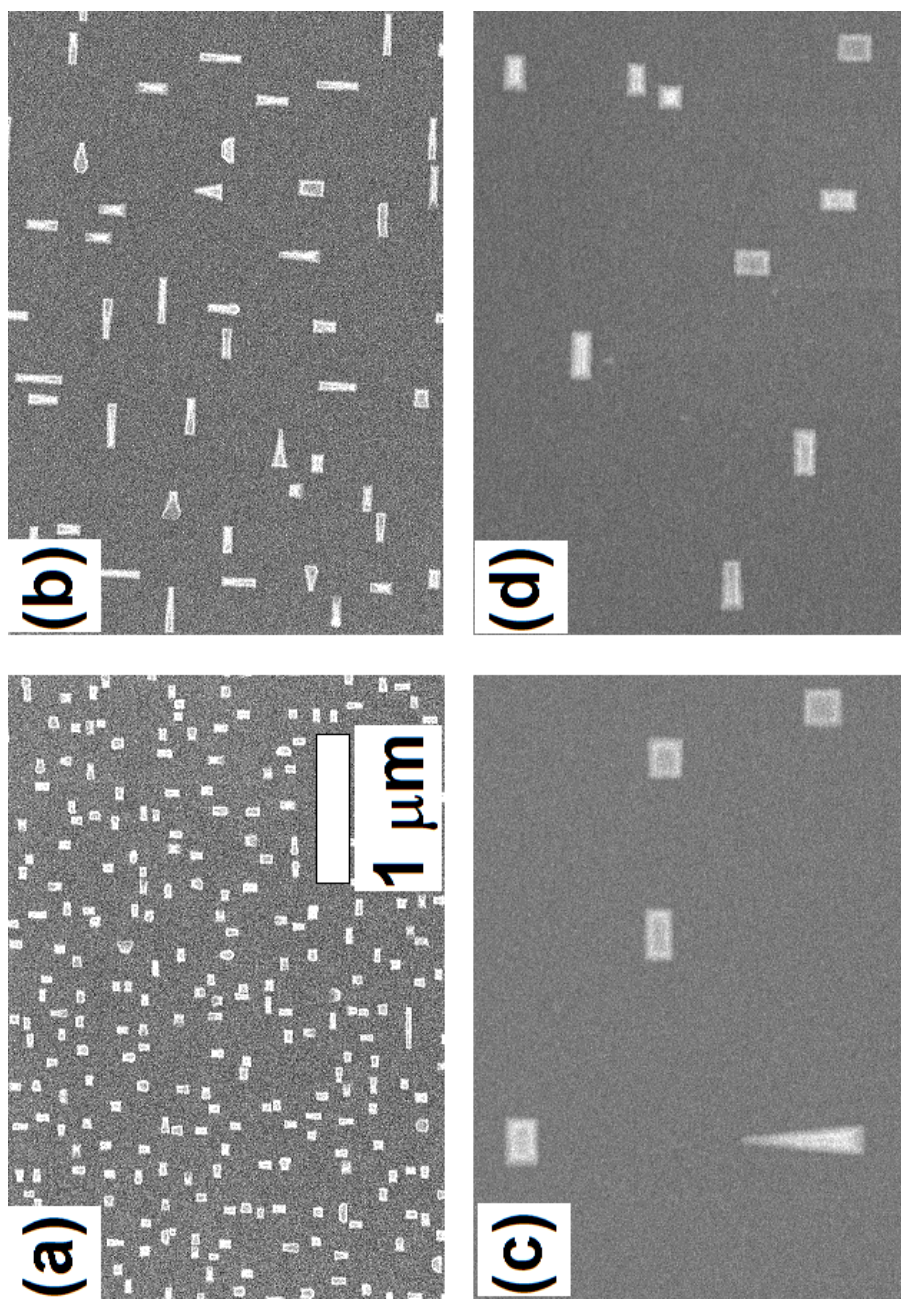


*Figure 3.24.* SEM images of Ag islands grown on top of the Si cap layer are shown here. These 4 SEM images share the same scale bar as shown in (a). The Ag island growth conditions for the samples corresponding to these 4 SEM images is identical. 9.6 ML of Ag was deposited on the Si cap layer at 450 °C. For each sample, the Ge dots were grown identically. 6.6 ML of Ge was deposited at 600 °C. The thickness of the Si cap layer corresponding to (a), (b), (c) and (d) is 20, 15, 10 and 5 nm, respectively.

°C, so there is a possibility that Ge atoms segregate to the surface. Ge at the surface of the Si cap layer may also influence Ag island growth. As shown in fig. 3.23, the Si cap layer surface is rough for thicknesses less than 15 nm, which may affect Ag island nucleation on the Si cap layer.

The average strain of the Si cap layer is determined from UV Raman spectroscopy. The reason we use UV Raman spectroscopy is that the penetration depth of UV light in semiconductor materials is typically on the order of a few nanometers, which allows us to investigate the average strain of the Si cap layer (from a thickness of 10 nm to 20 nm) on top of Ge dots. A typical UV Raman spectrum is shown in fig. 3.25 for the sample with a 10 nm thick Si cap layer. The red spots in fig. 3.25 are the experimental Raman spectrum, and the blue solid curve is the best fit Lorentzian to the experimental data. The peak located at  $\sim 525 \text{ cm}^{-1}$  is from Si-Si bonding. Tsang et al. [154] have noted that the Si-Si vibration peak can be shifted by the concentration of Ge ( $x$ ) and the strain field ( $\varepsilon$ ) for a bulk alloy of Si and Ge, as described by the following equation [154]

$$\Delta\omega_{\text{Si-Si}} = 520.2 - 62x - 815\varepsilon . \quad (3.23)$$

With this equation, the concentration of Ge and the average strain of the Si-Ge layer can be determined. The study by Tsang et al. showed that the accuracy of Raman measurements is comparable with those from other techniques, i.e., X-ray diffraction measurements. Other investigators reported relationships similar to eq. 3.23 [155–158].

The center frequency of the Si-Si peak,  $\omega_c$ , can be determined by the Lorentzian fit:

$$y(\omega) = y_o + \left( \frac{2A}{\pi} \right) \left( \frac{\Gamma}{4(\omega - \omega_c)^2 + \Gamma^2} \right), \quad (3.24)$$

where  $y_o$ ,  $A$ ,  $\Gamma$ , and  $\omega_c$  are fitting parameters. The function  $y(\omega)$  in eq. 3.24 represents the frequency-dependent photon counts, with  $\Delta\omega_{Si-Si} = \omega - \omega_c$  as given in eq. 3.23. The fitting parameters for the blue solid curve in fig. 3.25 are,  $y_o = 421.5$ ,  $A = 66583.2$ ,  $\Gamma = 4.6$ , and  $\omega_c = 525.3$ . The shift of the center frequency of the Si-Si vibration peak can be determined by comparing the value of  $\omega_c$  from the Lorentzian fit with the peak center for pure unstrained Si. Based on equation 3.23, the average strain in the Si cap layer can be calculated using  $\varepsilon = \frac{\Delta\omega_{Si-Si}}{-815}$ . When applying eq. 3.23, the Ge concentration of the Si cap layer is assumed to be negligible, as in our case, which is confirmed from XPS measurements. The determined average strain is plotted against the thickness of the Si cap layer in fig. 3.27 (b).

The second factor that could influence the density of Ag islands grown atop the Si cap layer is the segregation of Ge to the surface. A typical XPS spectrum acquired from the sample with a 10 nm thick Si cap layer is shown in fig. 3.26. The sample used for the XPS measurement is the same as the one used for the UV Raman measurement. The relative elemental composition can be determined by analyzing the integrated peak areas of all elements by using the commercial Casa XPS software package. The background has to be subtracted from each peak by using the Shirley algorithm before integrating the peak area [159]. The carbon (C) and oxygen (O) signals result from atmospheric exposure. By comparing the integrated areas of the Ge 2p and Si 2p peaks, the Ge fraction on the surface of the Si cap layer can be determined. The measured Ge concentration is plotted against the thickness of the Si cap layer in fig. 3.27 (c).

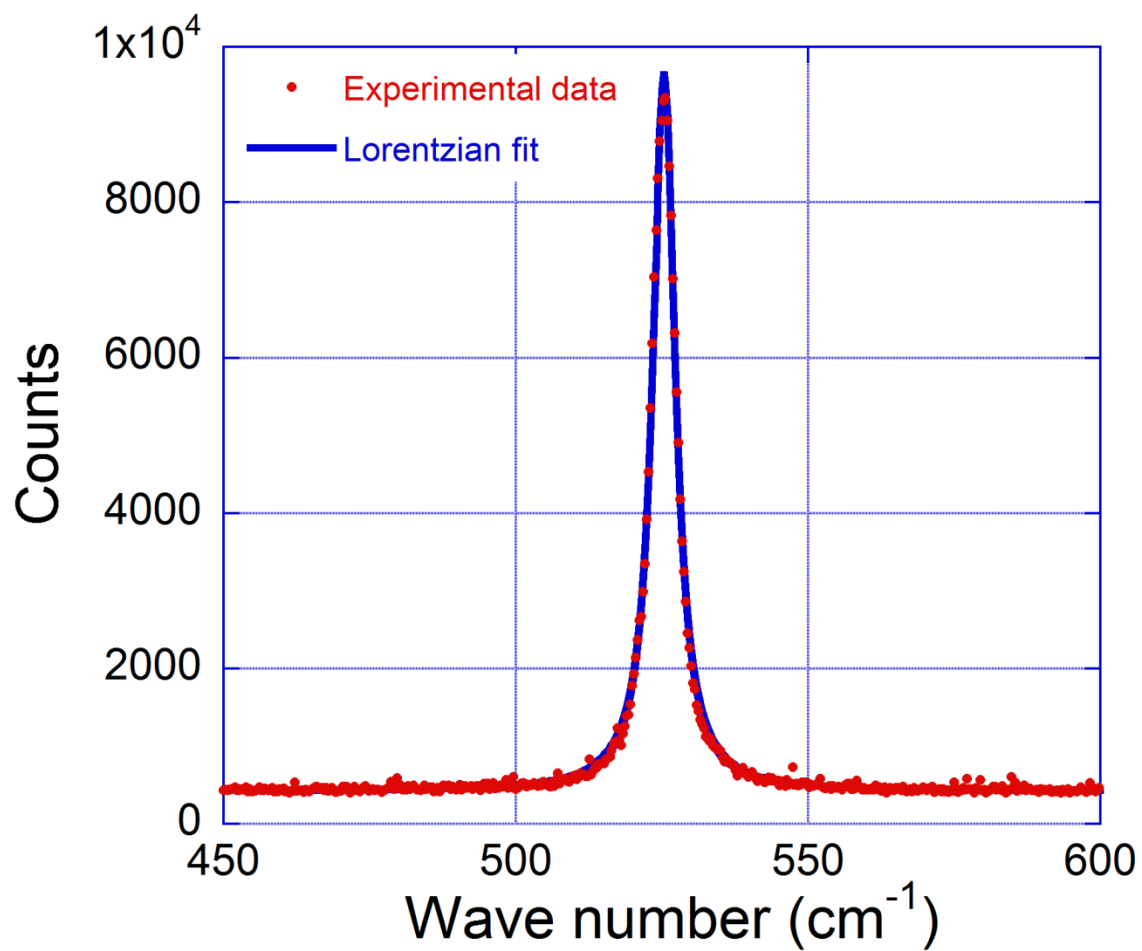


*Figure 3.25.* Typical UV Raman spectrum acquired from the sample with a 10 nm thick Si cap layer grown with new lower temperature recipe. The blue curve is the best fit Lorentzian to the experimental data.

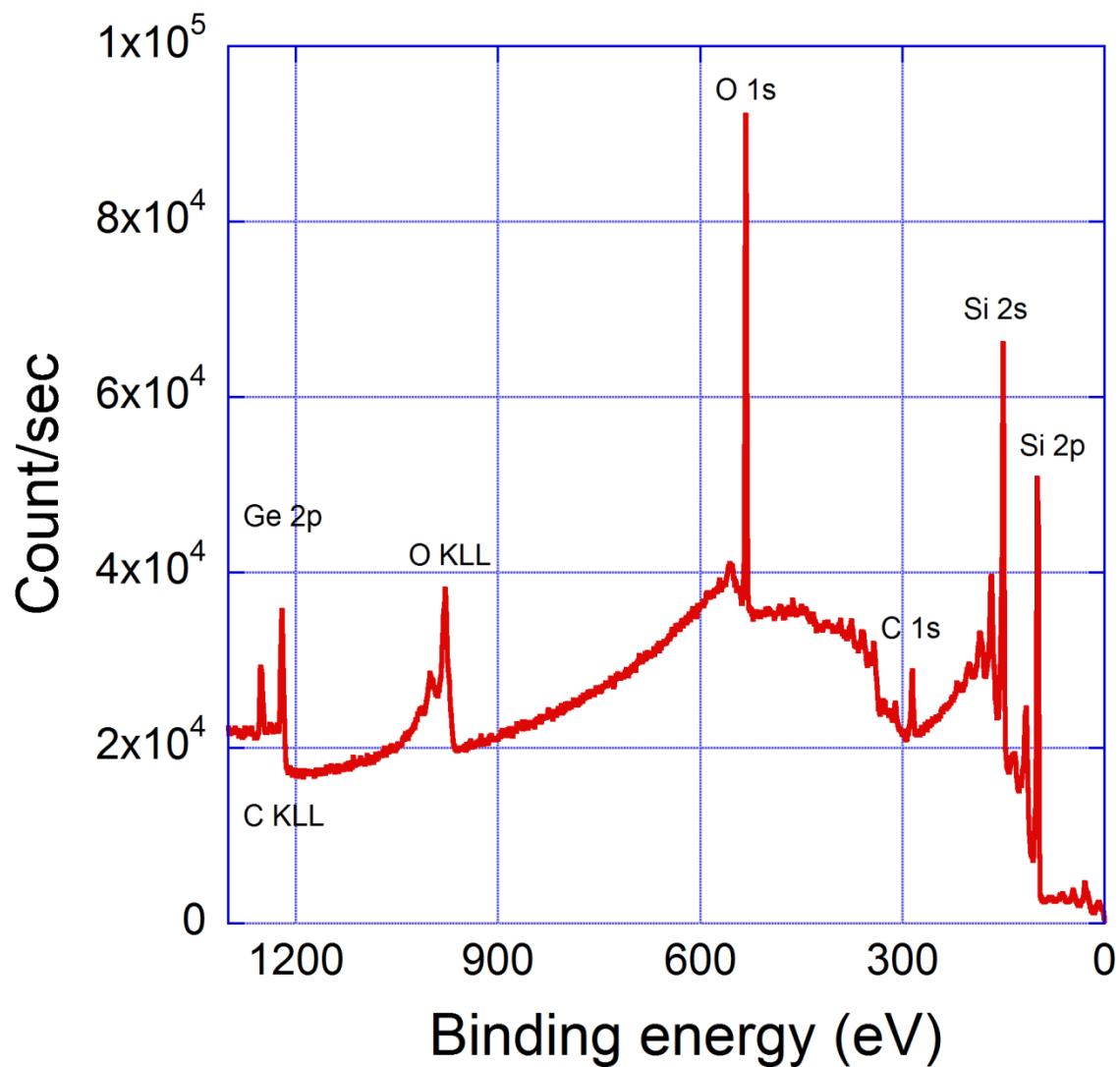


*Figure 3.26.* XPS spectrum acquired from the sample with a 10 nm thick Si cap layer grown using the new lower temperature recipe. The elemental peaks are indicated in the figure. The carbon and oxygen peaks appear due to exposure of our sample to air.

Fig. 3.27 summarizes the dependence of Ag island density, average strain, and the Ge concentration on the thickness of the Si cap layer. Fig. 3.27 (a) and (b) show the correlation between the average strain in the Si cap layer and the Ag island density. Fig. 3.27 (a) and (c) show the correlation between the Ge concentration at the surface of the Si cap layer and the Ag island density. These correlations will be discussed below.

By comparing figs. 3.27 (a) and (b), a correlation between Ag island density and the average strain can be found. The average strain monotonically increases and the density of Ag islands monotonically decreases as the thickness of the Si cap layer decreases from 20 to 10 nm. This correlation between Ag island density and the average strain seems indicate that the average strain may play a role in affecting the diffusion energy of Ag atoms on Si cap layer.

As indicated in fig. 3.27 (b), the average strain decreases when the Si cap layer thickness decreases from 10 to 5 nm. As discussed above, the penetration depth of UV Raman is only a few nm, so it is possible that the Si substrate is measured for the sample with 5 nm thick Si cap layer. Since Si substrate is not strained, the measured average strain drops to  $\sim 0$  when the thickness of Si cap layer changes from 10 to 5 nm.

The dependence of Ge concentration at the surface of the Si cap layer on its thickness is plotted in fig. 3.27 (c). It shows that the Ge concentration monotonically decreases as the Si cap layer thickness increases, as expected, because it will be more difficult for Ge atoms to segregate to the cap layer surface as the layer becomes thicker. Even though the fraction of Ge on the surface is low ( $< 3.5\%$ ), the formation of a Si-Ge alloy on the surface of the Si cap layer still could affect Ag surface diffusion and influence the nucleation density. The increase of Ge concentration on Si cap layer surface

may cause smaller Ag surface diffusion activation energy, which results in faster Ag surface diffusion. In consequence, larger Ag islands with smaller densities will be formed. It is shown in fig. 3.27 (c) that the concentration of Ge on the Si cap layer surface depends on the thickness of the cap layer, which relates the density of Ag islands to the cap layer thickness.

As shown in fig. 3.23, the surface of the Si cap layer becomes rough at a thickness  $< 15$  nm. Surface roughness could also affect Ag surface diffusion and therefore the density of Ag islands. Thus, there are at least three factors that could affect the density of Ag islands grown on the Si cap layer: average strain, Ge fraction, and surface roughness.

The increase of surface roughness is usually associated with slower diffusion rates, which would result in higher Ag island density. However, the density of Ag islands decreases by almost an order of magnitude as the thickness of the Si cap layer decreases from 15 to 10 nm, even though the RMS surface roughness increases from its value for an atomically flat surface (0.1 nm) to  $\sim 0.7$  nm (as measured from a  $3\ \mu\text{m} \times 3\ \mu\text{m}$  AFM micrograph in height mode). The effect of surface roughness on the Ag nucleation is negligible in the range of our investigation ( $\leq 0.7$  nm) compared with the other two factors; therefore, the factor of surface roughness will be omitted in the following discussion.

The dependence of Ag island density on the thickness of the Si cap layer, as shown in fig. 3.27 (a), can possibly be explained by considering the thickness-dependent strain and the Ge concentration on the surface. The density of Ag islands decreases by two orders of magnitude as the thickness of the Si cap layer decreases from 20 to 10 nm, which could be due to the change in the Ag diffusion coefficient on the Si cap layer.



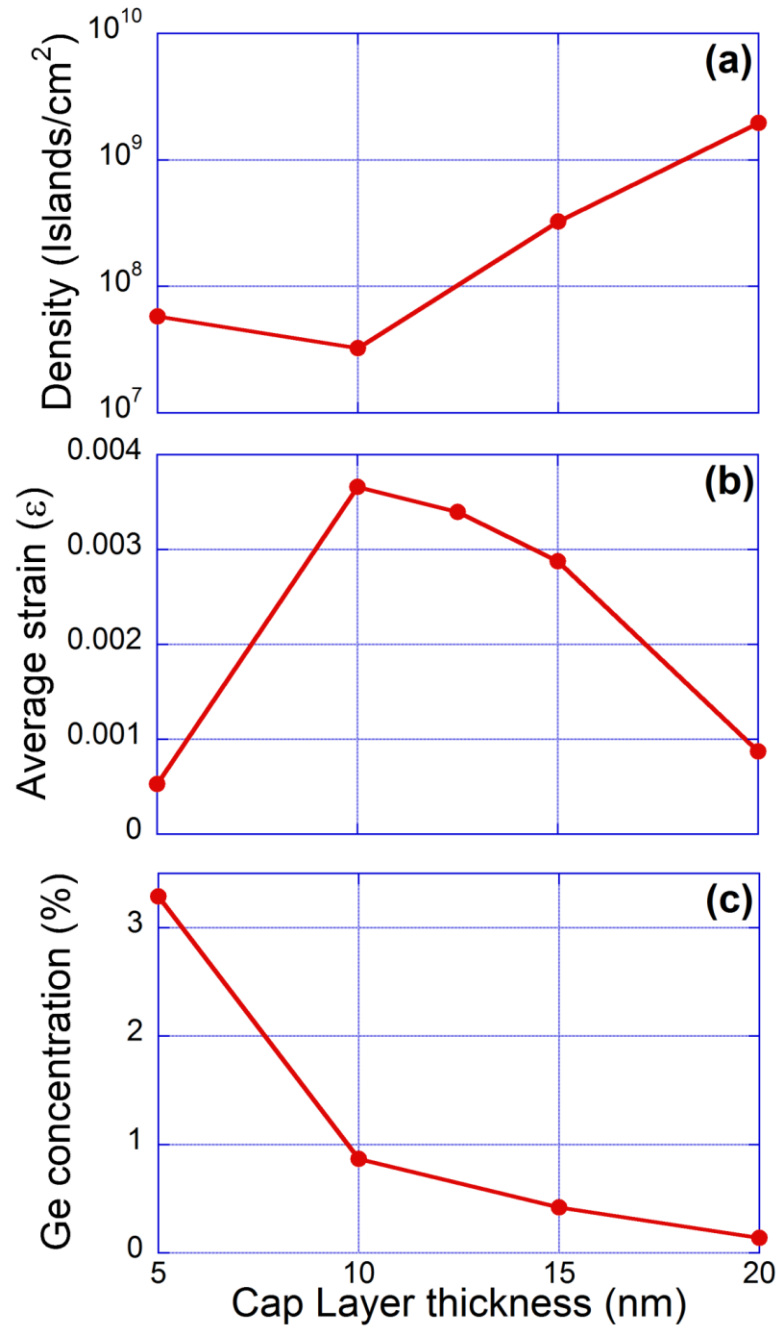


Figure 3.27. The dependence of Ag island density on the thickness of Si cap layer is plotted in (a). (b) is the plot of average strain, determined from UV Raman spectroscopy, against the cap layer thickness. (c) shows the concentration of Ge on the surface of the Si cap layer is a function of cap layer thickness.

Raman measurements show that the average strain in the Si cap layer monotonically increases as the thickness of the Si cap layer decreases from 20 to 10 nm. XPS results show that the Ge concentration on the Si cap layer monotonically increases with the decrease of Si cap layer thickness. This correlation between the change of Ag island density and the change of the average strain and Ge concentration on the Si cap layer indicates that the increase of strain and Ge concentration may decrease the diffusion activation energy of Ag atoms on the surface of the Si cap layer.

When the Si cap layer decreases from 10 to 5 nm thick, the density of Ag islands only increases by a relatively small factor of  $\sim 2$ . Even though the Ge concentration on the Si cap layer surface continues to increase when the cap layer thickness drops from 10 to 5 nm, the measured average strain for 5 nm thick Si cap layer is not reliable anymore because it is possible that UV Raman is measuring the unstrained substrate due to the comparable penetration depth of UV Raman. It is possible that the actual average strain on the surface of 5 nm thick Si cap layer is saturated at 4, and that the increase of surface roughness causes the small change of Ag island density when the average strain on the surface of the Si cap layer with thickness  $<10$  nm is saturated. Growing Ag islands on Ge would be helpful to identify the effect of Ge concentration on Ag island nucleation.

### **3.4 Effect of the Ag Localized Surface Plasmon on the Photoluminescence of Ge Dots**

This project aims to enhance the PL of Ge/Si(100) QDs by exploiting the LSPR of Ag islands epitaxially grown atop the Ge QDs. To investigate the effect of the Ag LSPR on the PL of the Ge dots, Ag islands are grown on part of the Si cap layer surface, allowing us to compare the PL spectra directly from areas with no Ag coverage to those

from areas with Ag island coverage. In this section, PL intensity optimization for Ge QDs will first be discussed, followed by a discussion about the effect of capped Ag islands on the PL of Ge QD. The LSPR energy was tuned to the IR range by capping Ag islands with 30 nm of  $\alpha$ -Si. This brings the LSPR of Ag islands close to the luminescence energy of Ge QD, which may enhance the PL efficiency of Ge QD based on the Purcell effect. Finally, the effect of bare Ag islands on the PL of Ge QD will be given.

### **3.4.1 Photoluminescence of Ge/Si(100) quantum dots.**

It is critical for the goal of this project to successfully grow samples with Si-capped Ge QDs that exhibit relatively strong Ge-related PL. Investigations of PL signal optimization from Ge QDs will be considered in this sub-section. As described in section 1.2.4, the morphology of capped Ge dots is sensitively dependent on the growth recipe of the Si cap layer, so the effect of the Si cap layer growth recipe will be discussed. The uniformity of the PL spectrum across the whole 4" sample was investigated, because, to investigate the effect of Ag LSPR on the PL of Ge dots, the spectra acquired from the area covered with Ag islands must be compared directly with those obtained from areas without Ag coverage on the same sample.

#### ***3.4.1.1 Photoluminescence of Ge quantum wells.***

From the discussion in section 3.3.2, we learned that growing the Si cap layer at the same temperature as Ge the QDs causes all of the coherent dots to completely flatten out, resulting in a uniform planar Ge layer, as shown in fig. 3.22 (a). We will refer to these samples with uniform Ge planar layers, which resulted from the growth of the Si cap layer, as Ge quantum well (QW) structures. RBS measurements show that the Ge coverage is uniform across the whole 4" wafer, so it is not surprising to see that the PL

intensity is uniform across the wafer, as discussed below. We did not intend to form this Ge QW structure; it resulted from growing the Si cap layer and the Ge QDs at the same growth temperature. As discussed in the introduction section of 1.2.5.2, the PL lines of the Ge WL are between 0.9 and 1.0 eV, and the Ge dot-related PL peak has lower energy than that of the WL.

We first investigated the optical properties of samples with Ge QW structures, i.e., samples with both the Si cap layer and Ge QDs grown at the same temperature. The PL spectra of samples with Ge QWs are shown in fig. 3.28 (a). In fig. 3.28 (a), the red spectrum is for a Ge QW resulting from the flattening of a dot ensemble with coherent domes only capped with a 30 nm Si cap layer. The blue spectrum was acquired from a Ge QW resulting from the flattening of a dot ensemble with huts only capped with a 15 nm Si cap layer. The green spectrum in fig. 3.28 (a) was taken from a reference sample which was grown under identical conditions to those of the capped domes-only sample, but without Ge deposition. All three of these spectra were acquired under the same conditions at 10 K. The excitation source was a 532 nm, 34-mW laser beam focused to a spot with a diameter of 500  $\mu\text{m}$ , and the detector sensitivity was set to 2 mV.

We first investigated the optical properties of samples with Ge QW structures, i.e., samples with both the Si cap layer and Ge QDs grown at the same temperature. The PL spectra of samples with Ge QWs are shown in fig. 3.28 (a). In fig. 3.28 (a), the red spectrum is for a Ge QW resulting from the flattening of a dot ensemble with coherent domes only capped with a 30 nm Si cap layer. The blue spectrum was acquired from a Ge QW resulting from the flattening of a dot ensemble with huts only capped with a 15 nm Si cap layer. The green spectrum in fig. 3.28 (a) was taken from a reference sample

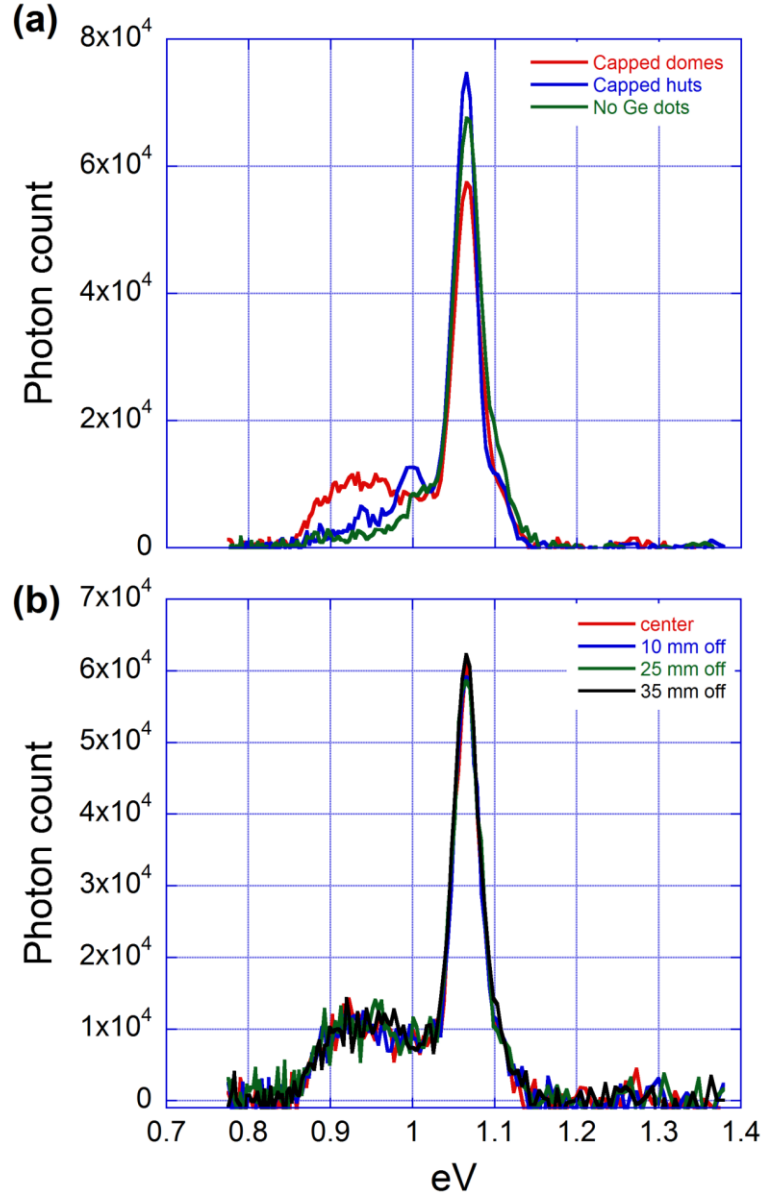


*Figure 3.28.* All PL spectra in this figure were acquired with 34 mW excitation from a 532 nm laser. The samples were at 10 K during acquisition at 9 s per data point with 2 mV sensitivity. (a) shows spectra from a series of Ge QWs resulting from Si capping of Ge QDs at the dot-growth temperature. In (a) the red spectrum is for a sample with a Ge QW that resulted from Ge domes capped with 30 nm Si at 600 °C. The blue spectrum was acquired from a sample with a Ge QW that formed due to hut flattening during 15 nm Si cap layer growth at 550 °C. The green spectrum was acquired from a reference sample grown without Ge deposition. The uniformity of the PL spectra from the sample of completely flattened domes is shown in (b). These spectra were acquired at the indicated distance from the center of the 4" diameter wafer.

which was grown under identical conditions to those of the capped domes-only sample, but without Ge deposition. All three of these spectra were acquired under the same conditions at 10 K. The excitation source was a 532 nm, 34-mW laser beam focused to a spot with a diameter of 500  $\mu\text{m}$ , and the detector sensitivity was set to 2 mV. The spectrum acquisition parameters were 9 sec per data point for a total of 140 data points.

By comparing the spectrum for the sample with QW from the flattening of huts (blue) with the one from the reference sample without Ge (green) in fig. 3.28 (a), there is one additional peak at  $\sim 1$  eV in the blue spectrum, besides their identical Si PL peaks at  $\sim 1.06$  eV. As discussed above, the Ge WL-related PL is usually between 0.9 and 1 eV, so the observed peak at  $\sim 1$  eV in the blue spectrum for the sample with QW is from the planar Ge layer. The Ge dot-related PL peak has lower energy than that of the WL. At spectral range of  $< 1$  eV, there is no other obvious peak in the blue spectrum from the sample with QW structure. This indicates that all huts are completely flattened out during Si capping at 550  $^{\circ}\text{C}$ , resulting in the disappearance of hut-related PL.

Because Ge huts/pyramids are bound by shallower facets (making contact angle of only  $\sim 11^{\circ}$  with the substrate surface) than facets of domes (making a contact angle of  $25^{\circ}$ ), huts/pyramids are easier to flatten out than coherent domes during Si capping. Therefore, the Ge dot ensemble comprised solely of coherent domes was used for this project to investigate the effect of Ag LSPR on the PL of Ge QD.

By comparing the spectrum for the sample with QW from the flattening of coherent domes (red) with the one from the reference sample without Ge (green), only one relatively broad peak between 0.9 and 1.0 eV shows up in the red spectrum, besides the identical Si PL peak at  $\sim 1.06$  eV as the one from the reference sample. As discussed

above, the Ge WL-related PL is usually between 0.9 and 1 eV, so the broad peak between 0.9 eV and 1.0 eV in the red spectrum is related with the Ge QW due to domes flattening. There is no other peak observed below 0.9 eV for the sample with capped domes, as indicated in fig. 3.28 (a). Therefore, it is reasonable to conclude that coherent domes are also completely flattened out during Si capping at 600 °C, explaining the absence of dot-related PL peaks. This conclusion is confirmed by the XTEM image shown in fig. 3.22 (a) for which no Ge dots are evident after Si capping at 600 °C.

All three spectra in fig. 3.28 (a) have the Si band-gap transition peaks located at the same energy, ~1.06 eV. The PL peak (blue) associated with the Ge QW resulting from the flattening of huts is at ~ 1 eV, and the PL peak (red) associated with the Ge QW resulting from the flattening of domes is at ~ 0.95 eV. The PL peak of Ge QW from the flattening of huts/pyramids is at a higher energy than that from domes flattening by ~ 50 meV. This can be explained by noting that the Ge QW that results from the flattening of huts/pyramids (5.8 ML) is thinner than that resulting from flattening of domes (6.6ML). The reason that we don't resolve separate non-phonon assisted (NPA) and transverse-optical (TO) PL lines from the Ge planar layer, as shown in fig. 1.7, is because the energy resolution of the PL setup that we employed is low.

The uniformity of the PL spectra across the 4" sample was investigated for the sample with the QW that resulted from the flattening of domes. The substrate is rotated during growth, so only the radial uniformity requires investigation. Fig. 3.28 (b) shows four PL spectra taken from 4 different spots, as indicated in the figure legend. The red spectrum was taken from the center of the sample, and the rest were taken from spots at the indicated radial distances from the center. The acquisition conditions for the spectra

displayed in fig. 3.28 (b) is exactly the same as those for the spectra displayed in fig. 3.28 (a). Fig. 3.28 (b) indicates good uniformity for the PL spectra across the sample, which is expected. Because the Ge dots are completely flattened out, resulting in a uniform planar Ge layer, the PL spectra measured from different positions are the same. RBS results show that the Ge coverage across the whole wafer is uniform.

#### ***3.4.1.2 Photoluminescence of flattened Ge coherent domes.***

Apparently, capping the Ge dots at the growth temperature causes them to be flattened out, resulting in a uniform planar layer. In order to obtain dot-related PL peaks, we developed a new recipe to grow the Si cap layer. For the reasons stated in section 3.3.2, the new recipe for growing the Si cap layer calls for the decrease in the substrate temperature from 600 to 500 °C to occur as quickly as possible at the moment the growth of Ge QDs has finished. Once the growth of Ge QDs is complete, the Ge source shutter is closed and the Si source shutter is opened simultaneously, so that no interruption is introduced between the growth of the Ge QD and that of the Si cap layer. Fig. 3.22 (b) shows that the new recipe for growing the Si cap layer preserves the dot morphology. The morphology of Ge coherent domes capped by means of the new recipe is ~ 120 nm in width and ~ 3 nm in height, which is shorter and fatter than the uncapped Ge domes (~ 75 nm in diameter and ~ 15 nm in height). To distinguish the capped domes grown with the new recipe for the Si cap layer from the uncapped Ge domes, we refer to the capped domes as flattened domes.

The PL spectra of flattened domes capped with 20 nm Si layers are shown in fig. 3.29. These spectra were taken from different spots on the same sample. The acquisition parameters for these spectra are indicated in the figure caption. The peak located at ~ 1.1



eV is the TO peak from the Si substrate and cap layer. The Ge-related PL peaks are replotted in the inset of fig. 3.29 to show their features clearly. The inset of fig. 3.29 clearly shows that the PL energy peak of the Ge WL (at  $\sim 0.97$  eV) is well-separated from the broad peak related to Ge flattened domes (at  $\sim 0.88$  eV). Only one PL peak emanating from the Ge WL is observed in our spectra, due to the low energy resolution of the PL setup used. The broad peak of the Ge flattened domes is similar to that in fig. 1.7. As discussed in section of 1.2.5.2, this broad peak from Ge flattened domes can be deconvolved into two Gaussian-shaped peaks, which are attributed to the NPA and TO transitions in Ge flattened domes. The new recipe for growing Si cap layers provides well-defined PL lines from the WL and flattened QD.

The uniformity of the PL spectra across the sample can also be analyzed from fig. 3.29, because these four spectra were taken from different spots on the same sample. The radial distance of each spot from the sample center is indicated in the legend of fig. 3.29. It can be seen that the Si peak increases and that the intensity of the Ge dot-related peak decreases as the acquisition location moves farther away from the sample center.

To understand this variation in dome-related PL intensity, we performed SEM measurements on uncapped dots grown at the same conditions. The SEM data show that the density of Ge coherent domes is fairly uniform, and that dislocated domes are barely observed in the area with radius  $r < 15$  mm. It also shows that the density of coherent domes decreases by  $\sim 20\%$ , and that many more dislocated domes appear, as  $r$  increases from 15 to 40 mm. The variation of Ge dome density may be caused by a non-uniform radial temperature distribution across the wafer during growth. The non-uniform

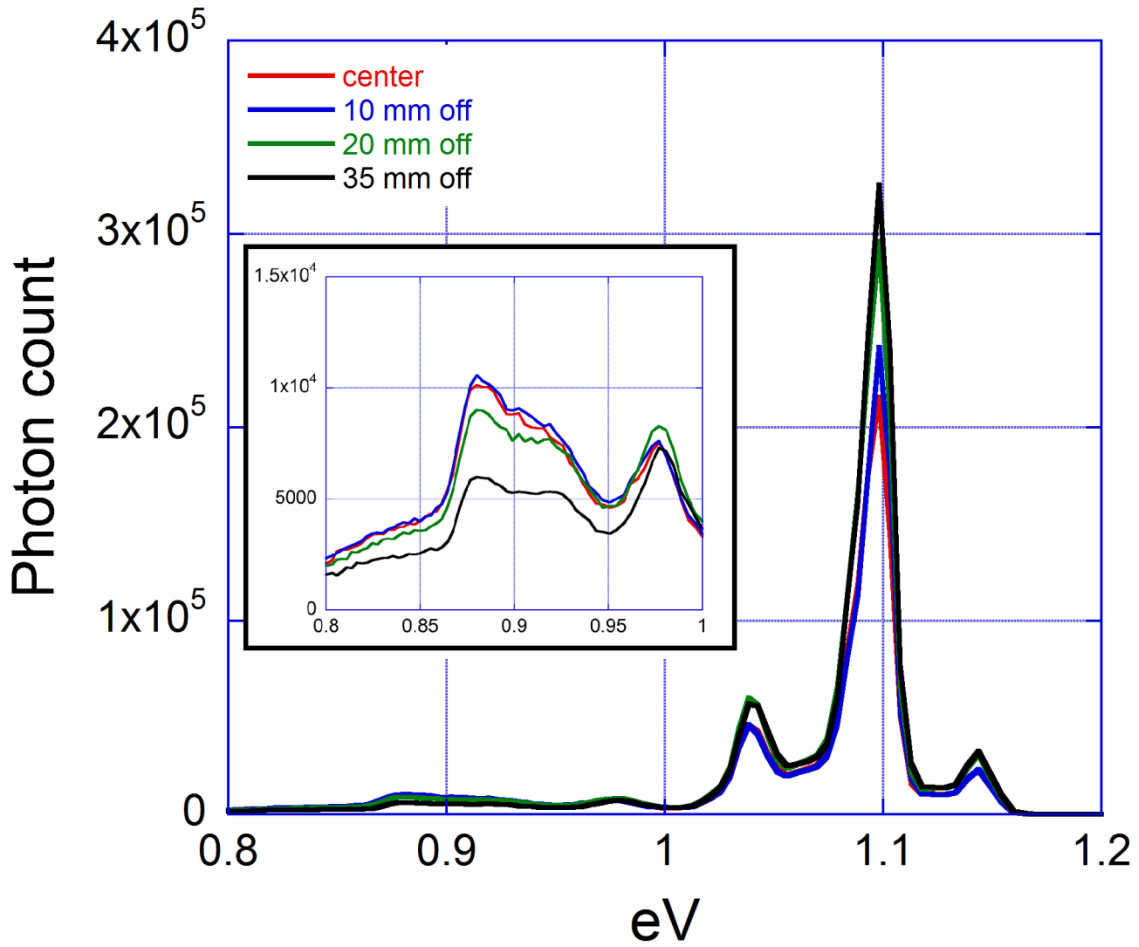


*Figure 3.29.* These spectra were taken from different spots on the same sample, at the radial distances from the center indicated in the legend. 6.6 ML Ge was deposited on the substrate at 600 °C, which generates only coherent domes. A 20 nm thick Si cap layer was grown at 500 °C. The spectra were acquired using a 532 nm, 39 mW laser.

temperature distribution is evident as a non-uniform glowing intensity distribution across the wafer. The wafer glows more brightly at its perimeter than at its center.

The variation of the PL spectra can be attributed to the variation of coherent dome density across the sample. The PL peak for Ge flattened domes decreases as the density of Ge domes decreases, because fewer dots contribute to the dot-related recombination, resulting in a smaller PL peak intensity related to Ge flattened domes. Fewer electron-

hole recombinations in Ge flattened dots may result in an increase of recombinations from Si, which could contribute to the increase in the Si PL peak, as shown in fig. 3.29.

#### ***3.4.1.3 Solving the non-uniform photoluminescence intensity problem.***

To address the non-uniformity in PL intensity across the sample, a new strategy of depositing Ag islands was developed. The strategy is to load a molybdenum (Mo) shield ~500  $\mu\text{m}$  below the sample surface during Ag deposition, using the linear motion drive shown in fig. 2.7. In this way, the boundary between the region covered with Ag islands and that without Ag is very sharp ( $<50\text{ }\mu\text{m}$ ), and both regions are in the area with uniform Ge dot density ( $r < 15\text{ mm}$ ).

Fig. 3.30 (a) shows a SEM image detailing the boundary between the regions with and without Ag. From this SEM image, it is possible to determine the boundary width, which is measured to be ~10  $\mu\text{m}$ . This new method of growing Ag islands provides an area with uniform Ag island density, the dimensions of which are ~ 6 mm x 12 mm. This area is more than enough for us to perform PL measurements.

The PL will be measured at two spots in the region with uniform Ag island density and at two spots in the region with no Ag. These four spots are separated from each other by 5 mm. The diagram in fig. 3.30 (b) illustrates the new strategy. Taking two spectra in each region allowed us to verify the PL uniformity. If the two spectra acquired in each region are the same, we can conclude that the PL signal is uniform in an area of 5 mm x 5 mm. The effect of Ag islands on the PL of Ge QD can be extracted by directly comparing spectra acquired from the two spots with Ag to those acquired from the two locations with no Ag, as indicated in fig. 3.30 (b). All discussions of the PL measurements that follow assume that the new Ag deposition method has been used.

Even though the SEM data in fig. 3.30 (a) show that the boundary between the area covered with Ag islands and that without Ag islands is  $\sim 10\ \mu\text{m}$ , Ag may diffuse beyond the boundary without forming 3D islands. Energy-dispersive X-ray spectroscopy (EDX) equipped in the SEM was utilized to detect Ag atoms that diffused out of the boundary. The EDX spectra were acquired from a  $\sim 10\ \mu\text{m} \times 10\ \mu\text{m}$  area with incident electron beam energy of 7 keV. The incident electron beam was set to 20  $\mu\text{A}$ , and the time constant was set to 35  $\mu\text{s}$ . These settings resulted in a dead time of  $\sim 30\%$ . The total integration time for each acquisition was 500 seconds.

Fig. 3.30 (c) shows two EDX spectra taken from two spots indicated in fig. 3.30 (a). The red spectrum was taken from spot 1,  $\sim 20\ \mu\text{m}$  from the boundary toward the region with Ag. The blue spectrum was taken from spot 2,  $20\ \mu\text{m}$  into the region without Ag. Two major peaks are identified in fig. 3.30 (c): Si K $\alpha$  at  $\sim 1750\ \text{eV}$  and Ag L $\alpha$  at  $\sim 2980\ \text{eV}$ . There is a small peak in both spectra located at  $\sim 3500\ \text{eV}$ , which is the sum of the peaks of Si K $\alpha$ . This is a kind of spectral artifact. The sum of the peaks occurs as two Si K $\alpha$  photons reach the detector almost simultaneously, and the pulse processor erroneously records the sum of their energies rather than individual photon energy. The Ag L $\alpha$  peak (at 2980 eV) appears in the red spectrum for spot 1 but not in the blue spectrum for spot 2, which indicates that the Ag coverage in spot 2 is below the detection limit of EDX.

The sensitivity of EDX can be determined simply, based on the signal-to-noise ratio of the Ag L $\alpha$  peak in fig. 3.30 (c), which is  $\sim 3$  for 9.6 ML of Ag on the Si surface. The height of the Ag L $\alpha$  peak is proportional to the amount of Ag on the Si substrate, so

the Ag  $L\alpha$  peak will not be distinguished from noise if the amount of Ag drops by a factor of 3. With the acquisition time fixed at 500 sec, the required sensitivity of EDX to

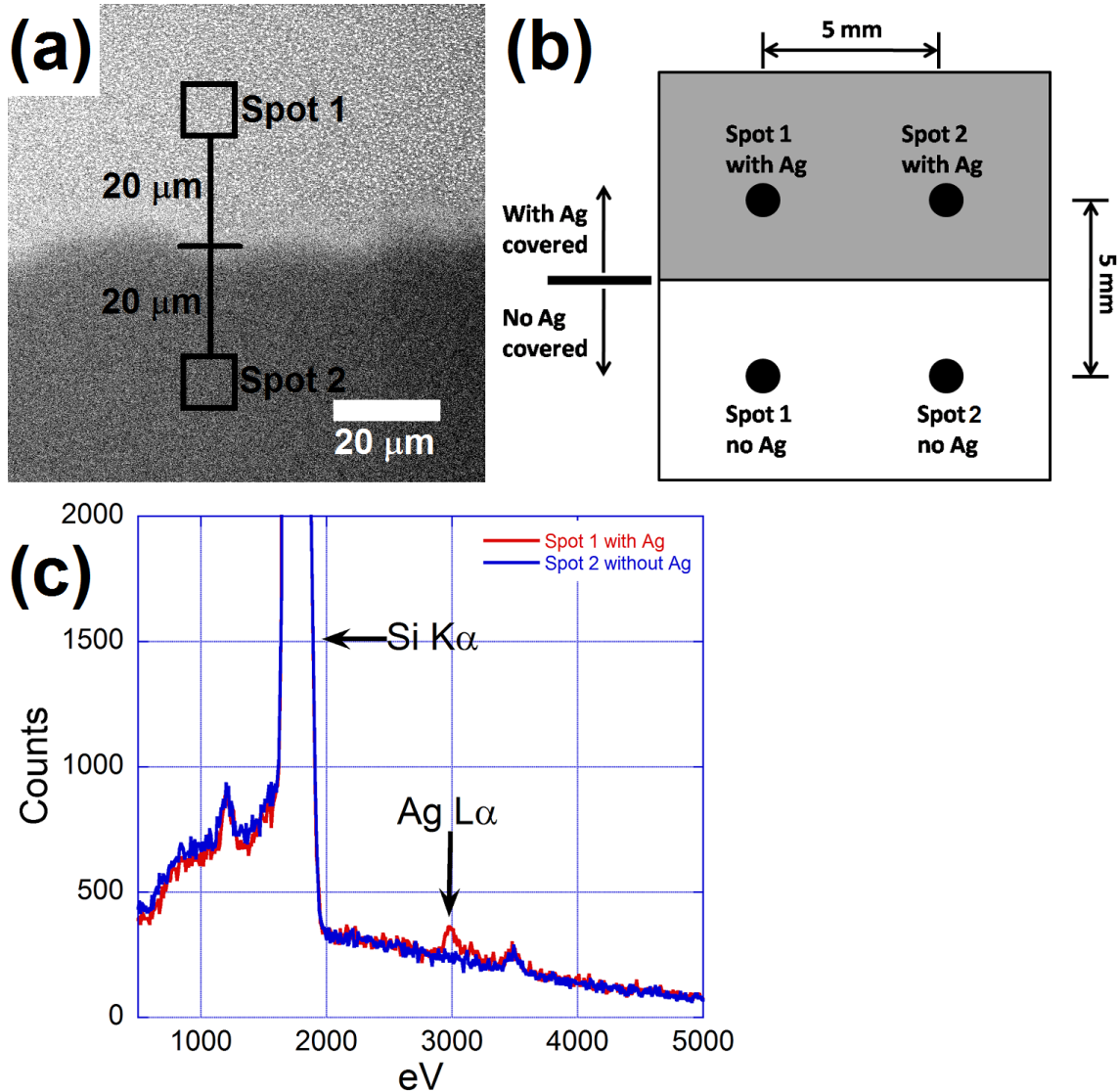


*Figure 3.30.* (a) shows a SEM micrograph of the boundary between the region covered with Ag islands and that with no Ag coverage. The schematic of our strategy to solve non-uniform PL intensity problem is illustrated in (b). PL spectra will be taken from those 4 spots as indicated in (b), and they will be horizontally compared to identify if the PL intensity is uniform in 5 mm by 5 mm region. (c) shows two EDX spectra taken from two spots as indicated in (a). The red spectrum was acquired from spot 1 as indicated in (a), and the blue spectrum was acquired from spot 2 as labeled in (a). Si  $K\alpha$  is at 1739 eV, and Ag  $L\alpha$  is at 2980 eV. The small peak at 3500 eV is the sum of Si  $K\alpha$  peak due to the detection of two photons.

detect the Ag L $\alpha$  signal is  $\sim 3.3$  ML. Because high-resolution SEM images provide much better sensitivity for detecting Ag than does EDX, Ag island features will show up once the coverage of Ag is  $> 0.3$  ML [116]. No Ag island features were observed in the high-resolution SEM image taken from spot 2. Combining the EDX and SEM measurements, we are confident in concluding that the actual boundary between the region with Ag islands and that with no Ag is  $< 20$   $\mu\text{m}$ .

### **3.4.2 Effect of localized surface plasmons of capped Ag islands.**

The emission energy of a Ge flattened QD is at  $\sim 0.85$  eV, while the LSPR of a Ag island in vacuum is  $\sim 3.5$  eV in the UV range. This large energetic gap may limit the enhancement factor, because the Purcell effect states that the spontaneous emission rate of atoms can be optimized if the excitation light is at the resonant condition with the emission energy of those atoms. Based on the discussion in section 3.2.2, the LSPR energy of Ag islands can be tuned from the UV range to the IR range by capping them with a 30 nm  $\alpha$ -Si layer. The effect of Ag islands capped with  $\alpha$ -Si on the PL of Ge flattened QDs will be discussed in this section.

Fig. 3.31 shows four PL spectra taken from different samples at 10 K, with the excitation source having 35 mW of power and consisting of a focused 532-nm laser beam. The acquisition parameters for all of these spectra are 9 sec per data point, with detector sensitivity of 20 mV. They are plotted in the same color code, which is red for spectra from areas covered with Ag islands and blue for those from areas with no Ag coverage. These two samples only contain flattened domes in the dot ensembles, and have the Si cap layer grown by means of the new recipe. The sample corresponding to fig. 3.31 (a) has a high Ge coherent dome density of  $3.5 \times 10^9 / \text{cm}^2$ , capped with a 20 nm

epitaxial Si cap layer. The other sample, corresponding to fig. 3.31 (b), has a low Ge dome density of  $9 \times 10^7 / \text{cm}^2$ , and is also capped with a 20 nm epitaxial Si cap layer. The growth conditions for Ag and 30 nm  $\alpha$ -Si are identical. Ag islands were grown by depositing 9.6 ML of Ag on a Si cap layer at 450 °C, and a 30 nm  $\alpha$ -Si cap layer was subsequently grown at room temperature. SEM measurements show that the density of Ag islands in the sample corresponding to fig. 3.31 (a) is  $1.6 \times 10^9 / \text{cm}^2$ , and that the density of Ag islands in the sample for fig. 3.31 (b) is  $1.9 \times 10^9 / \text{cm}^2$ . The difference in the density of Ag islands for these two samples is  $\sim 15\%$ , which is negligible for affecting the PL spectra.

The only difference between the samples from which the spectra displayed in fig. 3.31 (a) and (b) is the density of Ge QDs,  $3.5 \times 10^9 / \text{cm}^2$  for fig. 3.31 (a) and  $9 \times 10^7 / \text{cm}^2$  for fig. 3.31 (b). By comparing fig. 3.31 (a) with (b), one can clearly see that the Ge dot-related PL intensity does not scale with the dot density. The Ge dot-related peak height for the sample with low dot density in fig. 3.31 (b) is  $4 \times 10^4$  counts, and that for the sample with high dot density in fig. 3.31 (a) is  $3 \times 10^4$  counts. Two possible factors may contribute to this. For the sample with high dot density, potential defects may form because flattened domes touch or merge with their neighboring dots, and so reduce the flattened dot density due to dot merging.

As discussed earlier, Ge domes become shorter and fatter after Si capping. High resolution TEM results show that Ge domes capped with Si have basal widths of  $\sim 120$  nm and heights of 3 nm. For samples with high dot densities, the average dot spacing is  $\sim 180$  nm, which is comparable with the basal width of capped Ge dots, so some dots overlap or touch with their neighbors during Si capping, potentially resulting in the

formation of defects. These defects enhance the non-radiative recombination rate, and as a consequence reduce the radiative recombination rate. Due to the high density of Ge domes, flattened domes may merge with others to form larger dots during Si capping, resulting in a density of isolated flattened dots that is smaller than the density of uncapped Ge domes. The reduced density of isolated flattened dots may also cause the PL intensity for flattened Ge dots (fig. 3.31 (a)), which is smaller than the PL intensity for flattened dots (fig. 3.31 (b)).

For samples with low Ge dot density, because they are far apart (with an average spacing of  $\sim 600$  nm), the incidence of defect formation or dot merging is much lower than in the sample with high dot density. Because the samples with low Ge dot density provide more pronounced dot-related PL peaks than the samples with high density, we will use the recipe for growing the sample with low Ge dot density to investigate the effect of Ag LSPR on the PL of Ge QD.

By comparing the spectrum from the Ag-covered area (red) with the one from the area without Ag coverage (blue) in each plot of fig. 3.31, it suggests that the LSPR of capped Ag islands with an  $\alpha$ -Si layer significantly decreases the peak intensity of the Si band-gap transition at 1.1 eV by  $\sim 25\%$ . This is because the incident laser intensity on Si is reduced by the Ag island layer due to the absorption and reflection by the Ag islands, which we call the attenuation effect of the Ag island layer on the incident laser intensity. The attenuation effect is dependent on the LSPR energy of the Ag islands. From the general optics, the incident light passes through the Ag island layer if the incident light energy is smaller than the plasmon resonance energy of the Ag islands. If the light energy is larger than the plasmon resonance energy of the Ag islands, then the incident light is



reflected. The reduced intensity of the laser beam that penetrates into the Si and Ge creates fewer electron-hole pairs, which results in a decrease in the Si band-gap PL peak. However, the Ge dot-related PL peaks are not significantly affected by the LSPR of Si-capped Ag islands. The inset plots in fig. 3.31 (a) show that the Ge dot-related peak for the sample with high dot density is reduced by  $\sim 10\%$ . The inset plots in fig. 3.31 (b) show that the Ge dot-related peak for the sample with low dot density is not affected at all. This can be explained by considering the origin of electron-hole pairs in Ge QDs.

The majority of electron-hole pairs confined in Ge QD are not really originated from dots, and they are excited in Si (either the epitaxial layer or substrate) and then thermally diffuse to Ge QD. Fig. 1.6 shows the band alignment of Ge/Si QD. As discussed in section 1.2.5.1, electrons are confined to the tensile-strained Si region adjacent to the dots, where the conduction band is bent toward a lower energy by the strain, and holes are confined inside Ge QD. Note that only  $\sim 6$  electrons can be confined in one Ge coherent dome [70], so the electronic states in a Ge QD are very limited. The electron confinement in Ge QD is spatially separated from the hole confinement, so the probability for wave functions of electrons overlapping with those of holes is low. This results in a long lifetime of electron-hole pairs in Ge QDs. Therefore, it is still possible that excited electrons in Si saturate the occupancy of electronic states of Ge QD, even though electron-hole pairs excited in Si are reduced because the Ag island layer reduces the incident laser intensity. This is why Ge dot-related peaks are affected differently from the Si band-gap transition peaks by the incident laser intensity, which is identical for each measurement. The density of Ge dots for the sample corresponding to fig. 3.31 (a) is about two orders of magnitude higher than that for fig. 3.31 (b), so more electron-hole

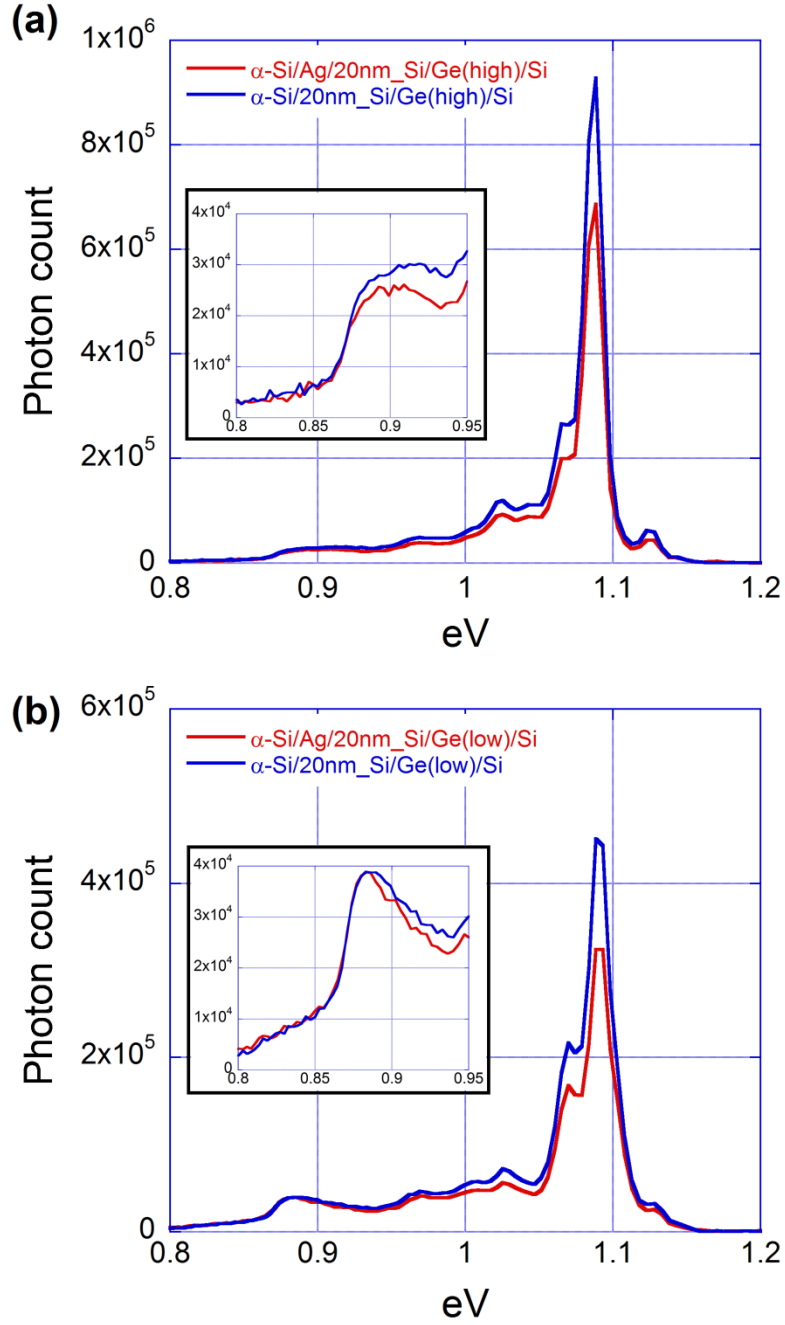


*Figure 3.31.* PL spectra of samples with different Ge dome densities are shown. The legend in each figure describes the sample structure corresponding to each spectrum. (a) shows PL spectra of samples with a high Ge dot density of  $3.5 \times 10^9 / \text{cm}^2$ . The inset figure in (a) details the Ge dot-related PL. (b) plots the PL spectra of samples with a low Ge dot density of  $9 \times 10^7 / \text{cm}^2$ . The inset figure in (b) details the dot related PL. These spectra were acquired at 10 K using 35 mW of 532 nm laser excitation, 20 mV detector sensitivity, and 9 sec per data point.

pairs are needed to saturate the electronic states in Ge dots for the sample with high density than for the sample with low dot density. A reduction of ~25% in the Si electron-hole pairs reduces the Ge dot-related peak for the high density sample by ~ 10%, but does not affect the Ge dot-related peak for the low dot density sample.

As discussed in the introduction, the plasmonic effect of metal nanoparticles on the PL of QD depends on the size of the metal particles [132] and the distance between the QD and the metal particles [133]. For the heterostructure shown in fig. 2.13, the distance between the Ag islands and Ge QD can be varied by changing the thickness of the epitaxial Si cap layer. The size and density of Ag islands grown on top of the epitaxial Si cap layer can be tuned by varying the deposition temperature.

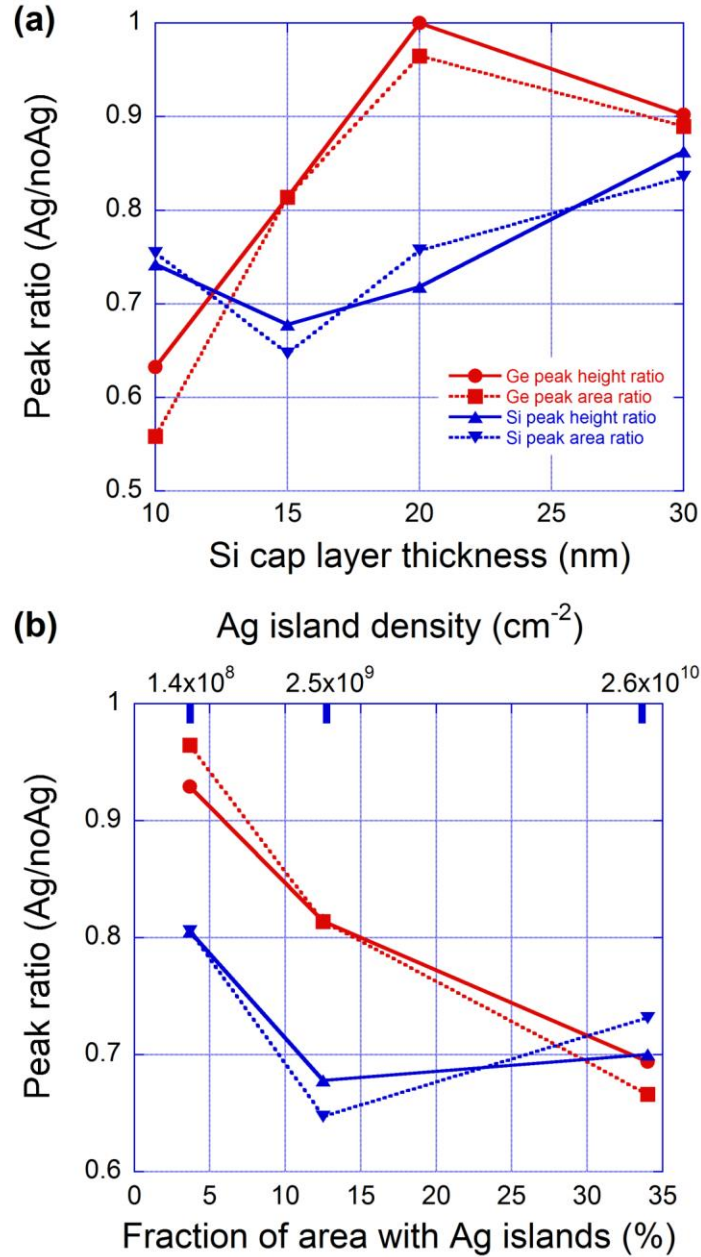
Fig. 3.32 shows how the plasmonic effect of Ag islands capped with  $\alpha$ -Si on the PL of Ge flattened dots depends on the thickness of the epitaxial Si cap layer in (a) and on the fraction of area covered with Ag islands in (b). Instead of using the average size of Ag islands in fig. 3.32 (b), we use the fraction of area covered by Ag islands, defined as the sum of all Ag island areas divided by the total investigated area from SEM micrographs. This is because this quantity is more useful than the average size of Ag islands for investigating the attenuation effect of the Ag island layer as the incident light passes through this layer. In fig. 3.32 (b), the thickness of the epitaxial Si cap layer is kept constant at 15 nm in order to investigate the effect of the area fraction of Ag islands on the PL of Ge QD.

Fig. 3.32 (a) shares the same legend as (b), and the y-axis in both figures indicates the peak ratio which is defined as the PL peak from spectra with Ag islands divided by the same peak from spectra without Ag. Red solid curves with circular marks are for the

Ge dot-related peak height ratio, and red dotted curves with square marks are for the integrated area ratio of Ge dot-related peaks. Blue solid curves with upward triangular marks are for Si band-gap peak height ratio, and blue dotted curves with downward triangular marks are for the integrated area ratio of Si band-gap peaks.

The dependence of peak ratios on the thickness of epitaxial Si layers is plotted in fig. 3.32 (a). The peak integrated area ratio follows the change in peak height ratio for both Si and Ge. Both red curves relate to the peak ratio for Ge dots. Fig. 3.32 (a) shows that the Ge dot-related peak ratio increases from  $\sim 0.6$  to 0.95 as the epitaxial Si cap layer varies from 10 to 20 nm. The drop from 0.95 to 0.90 is in the range of error, so the Ge dot-related peak ratio is saturated at  $\sim 0.9$  when the thickness of the Si cap layer increases from 20 to 30 nm. The Ge dot-related peak ratios in fig. 3.32 (a) indicate that the Ge dot-related PL is reduced by the LSPR of the  $\alpha$ -Si capped Ag islands when the epitaxial Si cap layer is below 20 nm. When the thickness of the Si cap layer increases from 20 to 30 nm, the peak ratio associated with the flattened Ge dots is barely changed (the change from 0.95 to 0.90 is in the range of scatter) by LSPR of the  $\alpha$ -Si capped Ag islands. This indicates that the LSPR of  $\alpha$ -Si capped Ag islands does not affect the PL intensity of Ge dot-related peaks when the thickness of the Si cap layer is above 20 nm.

When the Si cap layer is at 10 nm, the LSPR of the  $\alpha$ -Si capped Ag islands reduces the PL peak intensity of flattened Ge dots by 40%. For the sample with a 15 nm Si cap layer, this percentage decreases to  $\sim 20\%$ . For samples with 20 and 30 nm Si cap layers, this percentage drops to and saturates at 10%. The amount of reduction in the Ge dot-related PL intensity by the LSPR of  $\alpha$ -Si capped Ag islands decreases with the increase of Si cap layer thickness. As discussed in section 1.3.4, the PL of a QD will be



*Figure 3.32.* The peak ratio is defined as the height (area) PL peak from the spectra with Ag island divided by that of the same peak from spectra without Ag. The PL peak ratios of Ge dots and Si band-gap transition are plot against the thickness of epitaxial Si cap layer in (a), and against the fraction of Ag island area in (b). The fraction of area with Ag islands in (b) is calculated from SEM micrographs, by taking the summation of Ag island areas divided by the total investigation area. (b) share the same legend as (a). Solid curves with circular (red) and upward triangular (blue) marks are peak height ratio for Ge dot related peak and Si band-gap peak, respectively. Dotted curves with square (red) and downward triangular (blue) marks are the peak area ratio for Ge dot related peak and Si band-gap peak, respectively.

quenched by the LSPR of metal particles if they are too close to each other. The quenching effect decreases as the distance between the QD and the metal particle increases, and the quenching effect turns to enhancement at some critical distance. For our situation, it seems that 20 nm of Si cap layer is the magic thickness where the reducing effect on the Ge dot-related PL by the LSPR of  $\alpha$ -Si capped Ag islands disappears. However, the LSPR of  $\alpha$ -Si capped Ag islands does not enhance the PL of Ge flattened dots when the thickness of the Si cap layer is above 20 nm.

Blue curves associated with Si PL peak ratios in fig. 3.32 (a) show that the peak ratio of the Si band-gap transition does not monotonically change with the thickness of the epitaxial Si cap layer, and that the data points scatter between 0.65 and 0.85, with an average at 0.75. As discussed above, the Si band-gap PL drops by 25% due to the attenuation effect of the Ag island layer as the incident light passes through it. The observation that the average peak ratio associated with the Si band-gap transition is at 0.75 in fig. 3.32 (a) confirms the above explanation.

Fig. 3.32 (b) shows how the plasmonic effect of Ag islands capped with  $\alpha$ -Si depends on the fraction of the area covered with Ag islands, keeping the epitaxial Si cap layer at 15 nm. The density of Ag islands is labeled on the top  $x$ -axis. The red curve in fig. 3.32 (b) shows that the peak ratio of the Ge dot-related PL decreases from 0.95 to 0.7 with the increase of the area fraction of Ag islands from 4% to 33%. The increase in the area fraction covered by Ag islands results from the increase in the Ag island density. As the density of Ag islands increases, there are more Ag islands getting close to the Ge QD, resulting in an increase of electromagnetic energy density around the Ge QD. As discussed above, the LSPR of  $\alpha$ -Si capped Ag islands reduces the PL intensity of Ge

flattened dots when the thickness of the Si cap layer is  $< 20$  nm. The increase of electromagnetic energy density around Ge flattened dots, which results from the increase of Ag island density, can also be obtained by decreasing the distance between flattened Ge QDs and Ag islands. Therefore, the effect of increasing Ag island density on the Ge dot-related PL intensity is the same as decreasing the average distance between the Ge flattened dots and Ag islands. As discussed in section 1.3.4, the quenching effect of metal particles on the PL of QDs increases as the distance between metal particles and QDs decreases in the range of the distance smaller than the critical distance.

The triangular data points of the Si band-gap transition peak ratio in fig. 3.32 (b) again scatter in the range of 0.65-0.8, with the average at  $\sim 0.75$ . The total coverage of Ag on each sample is the same ( $\sim 9.6$  ML). An increase in the Ag island area fraction results in a decrease in the Ag island layer thickness. The attenuation effect of the Ag island layer on the incident laser power intensity is enhanced by an increase in the area covered with Ag islands, and is reduced by a decrease in the layer thickness, so the combination of these factors keeps the attenuation effect unaffected in our investigation with 9.6 ML of Ag coverage.

In summary, the reducing effect of Ag islands capped with  $\alpha$ -Si layers on the Ge dot-related PL peak has been discussed in this section. The dependence of this reducing effect on the thickness of the epitaxial Si cap layer and on the fraction of area covered with Ag islands was investigated. The result shows that the LSPR of capped Ag islands reduces the PL of Ge QD. The amount of reduction decreases with an increase in the epitaxial Si cap layer thickness, and saturates at  $\sim 0.1$ , when the Si cap layer reaches 20

nm. The amount of reduction in Ge dot-related PL peaks increases with an increase in the area fraction covered by Ag islands.

### **3.4.3 Effect of localized surface plasmons of bare Ag islands.**

The LSPR of Ag islands capped with a 30 nm  $\alpha$ -Si layer reduces the PL intensity of Ge dots, as discussed in section 3.4.2. However, the LSPR of bare Ag islands may play a different role from that of Si-capped Ag islands. Even though the LSPR of bare Ag islands is in the UV range, much higher than the emission energy of Ge QD, the excited LSPR of bare Ag islands may contribute to excitation of the electron-hole pairs in Si, and thus increase the local density of electron-hole pairs, which could enhance the PL intensity of Ge dots. The investigation results regarding the effect of the LSPR for bare Ag islands will be discussed in this section.

As for the Si-capped Ag islands, the plasmonic effect of bare Ag islands also depends on the thickness of the epitaxial Si cap layer and on the fraction of area covered by Ag islands. Fig. 3.33 shows how the PL intensity of Ge QD is affected by the LSPR of bare Ag islands; how the effect depends on the thickness of the epitaxial Si cap layer is shown in (a), and how the effect depends on the area fraction of the Ag islands is shown in (b). The meaning of the y-axis quantity and of the legend in fig. 3.33 is the same as for those items in fig. 3.32, and the definition of the area fraction covered with Ag islands is also the same as in fig. 3.32.

The blue curves with triangular marks in both fig. 3.33 (a) and (b) show that the peak ratios associated with Si band-gap transitions are constant at  $\sim 0.90$ , even with changing Si cap layer thickness and the area fraction covered by Ag islands. The drop in Si band-gap PL peak is due to the attenuation effect of the Ag island layer when the



incident light passes through it. As discussed in section 3.4.2, the attenuation effect of the Ag island layer does not depend on the thickness of the epitaxial Si layer, nor on the fraction of surface area covered by Ag islands. The peak ratio for the Si band-gap peak in fig. 3.33 is at  $\sim 0.90$ , higher than the value of 0.75 in fig. 3.32. This is because the 30 nm  $\alpha$ -Si layer redshifts the LSPR energy of Ag islands from the UV to the IR range, resulting in an increase in reflection by the capped Ag island layer. The excitation laser has a wavelength of 532 nm in the visible range, which is greater than the LSPR energy of the Si-capped Ag islands, and less than the LSPR energy of bare Ag islands, so the Si-capped Ag island layer has a greater reflection coefficient to the 532 nm light than does the bare Ag island layer. This is why the Ag island layer capped with  $\alpha$ -Si layer reduces the incident laser beam power more when the light passes through it.

The solid red curve with circular marks in fig. 3.33 (a) shows how the peak height ratio of the Ge dot-related PL peak changes with the thickness of the epitaxial Si cap layer. In fig. 3.33 (a), the dotted curve with square marks shows how the peak area ratio of the Ge dot-related PL peak depends on the thickness of the epitaxial Si cap layer. Both these curves follow the same trend. The peak ratio definition is the same as in section 3.4.2. When the thickness of the epitaxial Si cap layer increases from 15 to 25 nm, the peak ratio of the Ge dot-related PL increases from 0.1 to 1.0. This indicates that the Ag islands significantly reduce the Ge dot PL in the range of a 15 to 25 nm Si cap layer. For a Si cap layer with a thickness of 15 nm, the LSPR of bare Ag islands almost completely extinguishes the PL signal of Ge QDs. The effect of reducing the Ge dot-related PL decreases as the thickness of the Si cap layer increases. This is because the plasmonic energy density around Ge QDs decreases as Ag islands are separated further from them

by the increase in Si cap layer thickness. Therefore, the quenching effect of the LSPR of bare Ag islands decreases as the Si cap layer becomes thicker. As the Si cap layer increases from 25 to 30 nm, the peak ratio drops slightly from 1.04 to  $\sim 1.0$ , which is in the range of the error bar. The quenching effect of the Ag LSPR saturates at a Si cap layer thickness of 25 nm.

The red curves (solid with circular marks for peak height ratio and dotted with square marks for peak area ratio) in fig. 3.33 (b) show the dependence of Ge dot PL peak ratio on the fraction of area covered with Ag islands for a Si cap layer of 25 nm thickness. They show that the PL peak ratio of Ge QD decreases with the increase in the area fraction covered by Ag islands. This indicates that the plasmonic reduction effect increases as the area fraction covered by Ag islands increases. As discussed in section 3.4.2, the increase of area fraction covered by Ag islands results from the increase of Ag island density, which causes the number of Ag islands around each Ge dot to increase on average. Therefore, the intensity of plasmons around Ge QD is greater, resulting in the plasmonic (quenching) effect increasing with the increase in area fraction covered with Ag islands. The amount by which the Ge dot peak ratio decreases from the increase in the area fraction covered with Ag islands is smaller in fig. 3.33 (b) than in fig. 3.32 (b). This is because the thickness of the epitaxial Si cap layer corresponding to fig. 3.33 (b) is 25 nm, which is 10 nm greater than that for fig. 3.32 (b).

The plasmonic enhancement of the PL of Ge QD by bare Ag islands was observed. Fig. 3.34 (a) shows the spectra of the largest enhancement that we observed. The red spectrum in fig. 3.34 (b) was taken from the region covered with Ag, and the blue spectrum was taken from the region without Ag coverage.

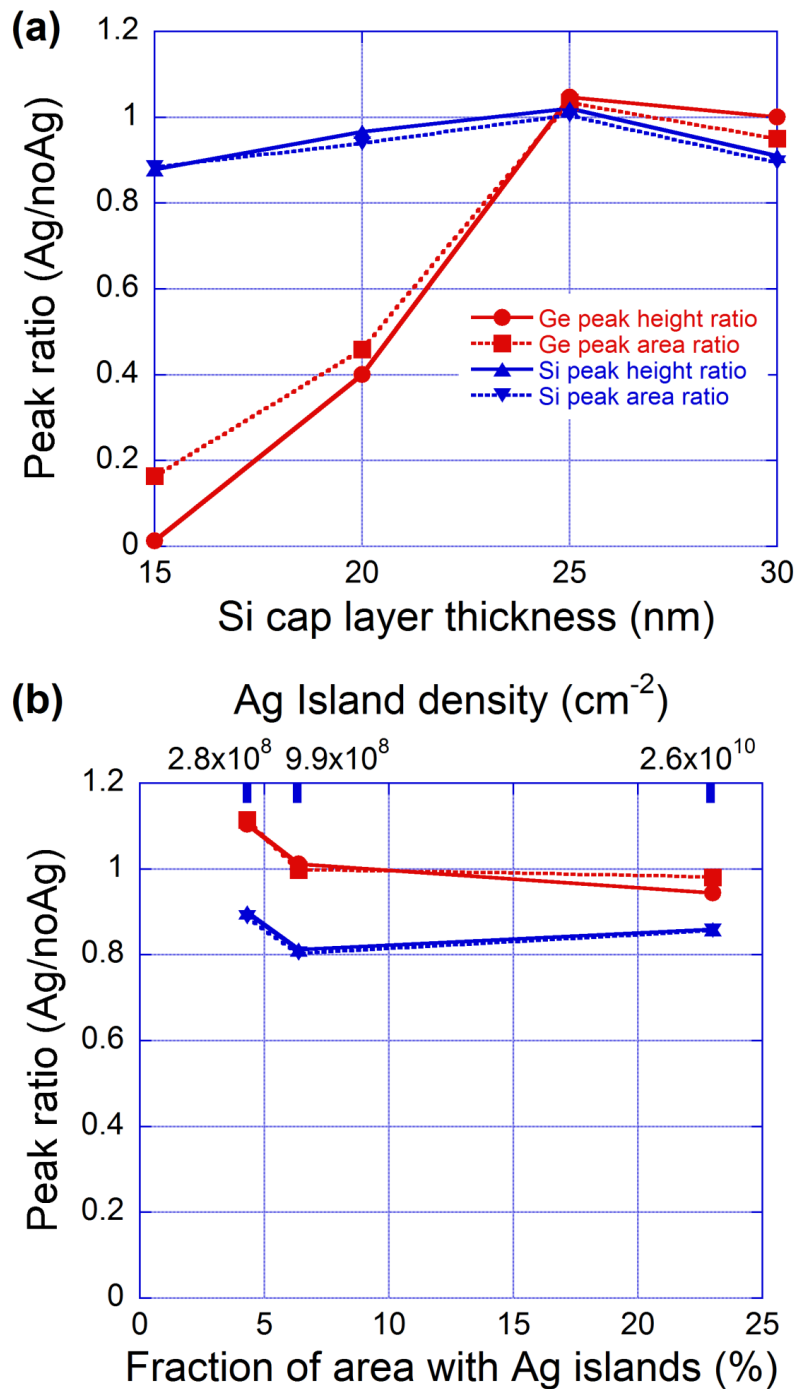


Figure 3.33. This figure is to show how the effect of the LSPR of bare Ag islands depends on the thickness of epitaxial Si cap layer and on the fraction of area with Ag islands. The definitions of peak ratio and fraction of area with Ag islands are same as that in fig. 3.32. The legend is also same as that in fig. 3.32.

The sample corresponding to fig. 3.34 (a) has the low density of Ge QD ( $9 \times 10^7$  /cm<sup>2</sup>) and 15 nm of epitaxial Si cap layer. A  $\sim 6$  mm x 12 mm region of the sample was deposited with Ag, and the boundary between the part with Ag and the part with no Ag was  $\sim 20$   $\mu$ m. By comparing these two spectra, the Si band-gap transition peak is seen to decrease by 10% due to the attenuation effect by the Ag island layer, while the Ge dot-related PL peak height was enhanced by  $\sim 40\%$  due to the LSPR effect of the bare Ag islands.

Fig. 3.34 (b) shows the dependence of Ge and Si peak ratios on the fraction of the area covered with Ag islands. These samples have the same thickness of epitaxial Si cap layer (15 nm). The solid blue curve with triangular marks in fig. 3.34 (b) shows that the Si band-gap transition peak ratio is almost a constant at  $\sim 0.9$ , which is same as the blue curves in fig. 3.33 (b). In fig. 3.34 (b), the solid red curve with circular marks is the peak height ratio of Ge QD, and the dotted red curve with square marks shows the peak area ratio of Ge QD. The peak ratio has the same definition as for previous graphs.

Both red curves associated with Ge dot-related peak ratios show that the peak ratio monotonically increases with the fraction of surface area covered by Ag islands, which means the plasmonic effect of Ag islands on Ge dot-related PL increases with the area fraction of Ag islands. The density of Ag islands corresponding to each area fraction of Ag islands is indicated on the top  $x$ -axis in fig. 3.34 (b). The same argument applies to explain the change in the red curves of fig. 3.34 (b), which have the higher density of Ag islands. This results in more Ag islands around each Ge dot, on average. Therefore, the energy intensity of plasmons around Ge QDs increases, and as a consequence the

plasmonic effect of Ag islands on the PL of Ge QDs increases with the fraction of area covered by Ag islands.

The observed maximum enhancement of the Ge dot-related PL intensity by the LSPR of bare Ag islands is  $\sim 40\%$ , which is much smaller than the enhancement predicted from the theory ( $8 \times 10^4$  at optimum conditions). This can be explained by considering the possibility for a Ag island growing right atop of one flattened Ge QD. From our investigations, there is no clear correlation between Ag islands and capped Ge QDs. The possibility for Ag islands aligned with Ge QDs can be roughly calculated by multiplying the fraction of substrate surface covered by flattened Ge domes with the surface fraction covered by Ag islands. The fraction of the substrate surface covered by flattened Ge domes is  $\sim 1.3\%$ , and the highest fraction of the substrate surface covered by Ag islands, as shown in fig. 3.34 (b), is  $\sim 7.5\%$ . The possibility for Ag islands growing right atop of Ge QDs is  $\sim 1 \times 10^{-3}$ . This could be the reason why our observed enhancement factor is much smaller than the theoretically predicted enhancement.

Fig. 3.33 shows that the LSPR of bare Ag islands significantly reduces the PL of Ge QDs, while fig. 3.34 shows the opposite. The results shown in fig. 3.34 are conditional, because they are not reproducible with different batches of wafers. The wafers used for the results shown in fig. 3.34 are highly p-doped with Boron, at a concentration of  $6 \times 10^{19} / \text{cm}^3$ , while the doping level of wafers used for the results shown in fig. 3.34 is four orders of magnitude lower, at a Boron concentration of  $7 \times 10^{15} / \text{cm}^3$ . Schottky barrier formed at the interface between Ag islands and p-type Si could be attributed to the different observations for high doping wafers and low doping wafers.

Schottky barrier may form at the interface when a metal is in contact with a semiconductor, depending on the work functions of the metal and the semiconductor. Work function is defined as the minimum energy needed to remove an electron from a solid to vacuum. The work function of Ag(110) surface is 4.52 eV [160]. The work function of Si depends on types of dopants and the doping level [161]. The work function for p-type Si with Boron doping level of  $6 \times 10^{19} / \text{cm}^3$  is 5.27 eV, and that for p-type Si with Boron doping level of  $7 \times 10^{15} / \text{cm}^3$  is 5.02 eV. The Schottky barrier height, which is roughly the difference between the work function of Ag and Si, has been experimentally determined as 0.55 eV by Smith and Rhoderick [162].

The work function of Ag is lower than that of Si, so electrons in Ag flow to Si till equilibrium is established, leaving positive ionized particles at the interface. A depletion region of charge carrier is formed in Si, and there is electric field established in the depletion region. The width of the depletion region is inversely proportional to the square root of the dopant concentration. For high doping Si wafers, the calculated depletion width is  $\sim 3$  nm, which is smaller than the employed thinnest Si cap layer 10 nm. For low doping Si wafers, the depletion width is  $\sim 500$  nm, which is much larger than the employed thickest Si cap layer, 30 nm. Ge dot layer is in the depletion region for low doping wafers, so the electric field in depletion region for low doping wafers may contribute to the observation that the LSPR of Ag islands reduces the PL of Ge QDs.

Another difference between the results in fig. 3.33 and those in fig. 3.34 arises from the temperature control methods. Samples for fig. 3.34 were grown using a thermocouple to measure the substrate temperature, whereas samples for fig. 3.33 were grown using a pyrometer to measure the temperature. Even though an effort was made to

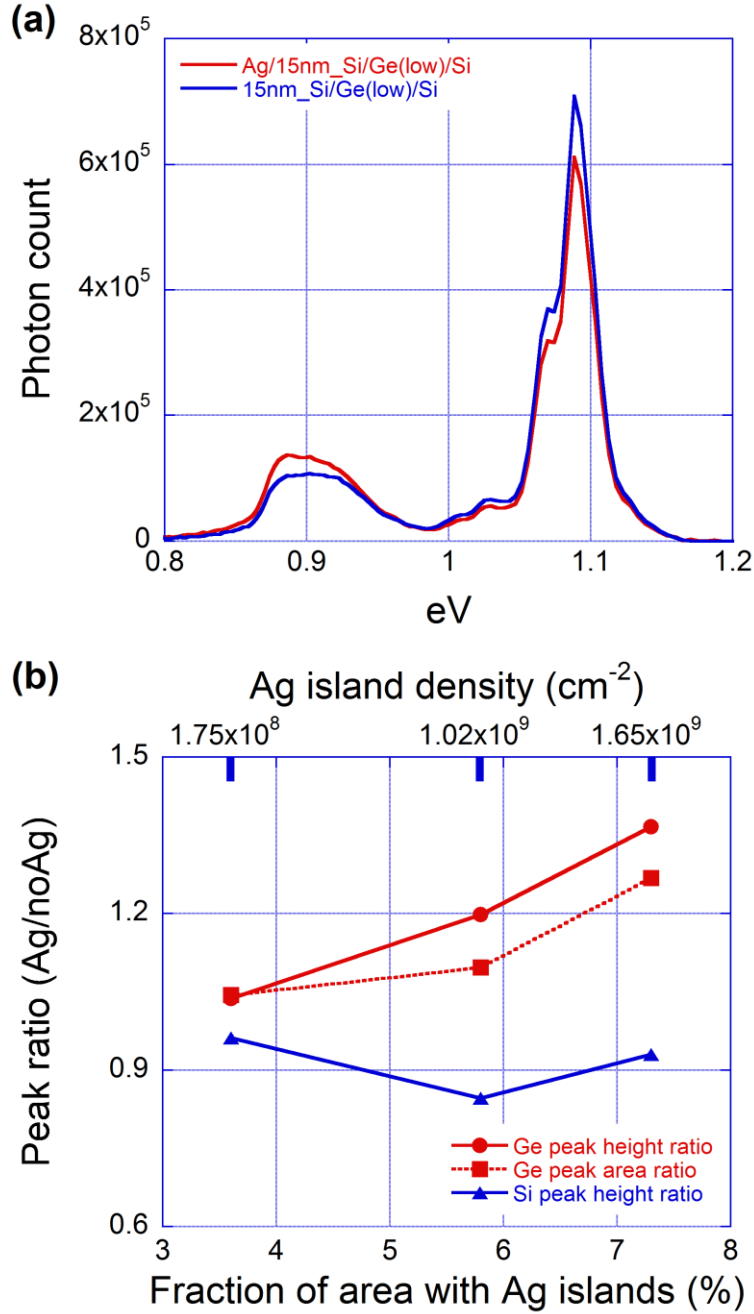


Figure 3.34. The results shown in this figure are conditional, because they are not reproducible at different conditions. (a) shows the spectra with best enhancement we have ever got. (b) shows the peak ratio of Ge dots and Si band-gap transition depends on the fraction of substrate area covered by Ag islands. The results shown in (b) are from the samples grown on highly doped Si wafers,  $\sim 6 \times 10^9 / \text{cm}^3$ , which is four orders of magnitude higher than the wafers used for 3.30 (b). The definition of peak ratio is same as that in fig. 3.29. The density of Ag islands corresponding each area fraction is labeled on the top x axis.

tune the temperature profile of the pyrometer to that of the thermocouple during the Si cap layer growth, they cannot be made identical because of their different response speeds to temperature change. It has been pointed out that the morphology of capped Ge dots is very sensitive to the growth temperature of the Si cap layer, so the difference in temperature profile during the growth of the Si cap layer could cause morphological changes of Ge dots, resulting in the different responses of charge carriers confined in Ge dots to the LSPR of Ag islands.

Besides the results in fig. 3.34, we observed that both bare Ag and Si-capped Ag islands significantly reduce the PL of Ge dots. The reducing effect of the LSPR of Ag islands decreases as the epitaxial Si cap layer becomes thicker, and increases with an increase in the fraction of substrate area covered by Ag islands. This could be because the non-radiative recombination rate is easier to be enhanced by the LSPR of Ag islands than the radiative recombination rate. For the special band alignment of Ge QD, as shown in fig. 1.6 and described in the associated discussion, the electron confinement is spatially separated from the hole confinement in Ge QDs, so it is possible that the non-radiative recombination rate is easier to be enhanced by the LSPR of Ag islands than the radiative recombination rate. Further investigation is required to fully understand this reducing effect.



## CHAPTER 4

### CONCLUSIONS AND FUTURE WORK

This doctoral research work investigated the plasmonic enhancement of Ag islands on the photoluminescence (PL) of Ge/Si(100) quantum dots (QDs). To plasmonically enhance the PL of Ge QDs with Ag islands, Ge QDs were capped with an epitaxial Si layer, and then Ag islands were grown on top of the Si cap layer, separating the Ge QDs from the Ag islands by the Si cap layer. The growth of the heterostructures was performed in a molecular beam epitaxy (MBE) system. The research project consists four topics: (i) epitaxial Ag island growth on Si(100) substrate, (ii) tuning the localized surface plasmon resonance (LSPR) of Ag islands grown on a Si(100) substrate, (iii) the heterostructure growth, (iv) the plasmonic effect of Ag islands on the PL of Ge QDs.

A brief outline of each part of this project is here given. (i) the investigation of Ag island growth on the Si(100) surface provides us a baseline for determining the effect of the Si cap layer grown atop the Ge QDs on Ag island growth. Two distinct types of Ag islands were found, and the dependence of the Ag island density and shape on the growth parameters was systematically investigated for as-grown and growth-temperature annealed samples. (ii) The plasmonic properties of Ag islands grown on Si(100) were investigated by varying the morphology, size and dielectric ambient of the Ag islands. For bare Ag islands on Si, two plasmonic modes were identified by comparing the simulated with the experimental pseudodielectric functions. The LSPR energy of Ag islands can be significantly tuned from the UV to IR range. (iii) The growth of Ge QDs on Si(100) was studied in order to find the optimum growth conditions for either solely huts/pyramids or solely coherent domes ensemble. The surface quality of the Si cap layer

and the morphology of capped dots were investigated for different recipes. A growth recipe of the Si cap layer was developed to preserve the Ge dot morphology during Si capping. The growth of Ag islands on top of the Si cap layer with different thickness was investigated. (iv) The optical properties of Ge QDs grown on Si(100) substrate have been studied with PL measurement. The effect of the LSPR of  $\alpha$ -Si capped Ag islands and bare Ag islands on the PL of Ge QDs was investigated separately. The important findings of this research project and the future outlook for each topic is summarized below.

#### **4.1 Epitaxial Ag Island Growth on Si(100)**

Two distinct families of islands form during Ag epitaxy on Si(100) heated to  $300 \leq T \leq 500^\circ\text{C}$ . The first family, big islands, is well faceted, has bases that are crystallographically aligned with the substrate, has basal dimensions in the few hundred nm to  $1\ \mu\text{m}$  range and forms with several basal shapes. From SEM imaging, these basal shapes of big islands are seen to be square, rectangular, triangular, truncated triangular and irregular. The second family, small islands, has diameters in the few 10s of nm range. Small islands are mound-like and are not clearly faceted.

For as-grown samples, the density of big islands monotonically decreases with the increase of the growth temperature. The linear dependence of the big island density on the semilogarithmic Arrhenius plot indicates that the big islands form via a nucleation and growth mechanism with a nucleation energy of 0.73 eV.

While the density of small islands is three orders of magnitude higher than that of big islands, and small islands are loosely dependent on growth temperature in the range of  $300\text{-}500^\circ\text{C}$ . Our results suggest that small islands do not exist at elevated growth and annealing temperatures. They form as excess Ag above the  $\frac{1}{4}$  ML-thick S-K layer (1

ML= $6.78 \times 10^{14}$  atoms/cm<sup>2</sup>) in between the big islands precipitates as the sample is cooled from the growth or annealing temperature to room temperature. Up to 0.8 ML of Ag can form a 2D planar layer on Si(100) at 500 °C, and the excess Ag (~ 0.6 ML) forms small islands when the samples are rapidly cooled down to room temperature.

During growth temperature annealing, the big islands exhibit unusual anti-coarsening behavior: their areal density increases and their size decreases. The analysis of the morphological evolution of big islands with annealing time at 300°C shows that islands with irregular bases are completely absent after one hour of annealing. For the remaining island basal shapes: square, rectangular, triangular and truncated triangular we find that the trend is toward a more elongated shape as the anneal progresses. The width of all of these islands decreases as the anneal time increases and, except for the triangular islands, the length does as well. We also find that the population of each island type varies as the anneal progresses, and results suggest that an elongated shape is more stable than compact one.

Another factor that may contribute to this unusual anti-coarsening behavior is defects, i.e. stacking faults and microtwins. Li, et al., attribute the decomposition of irregular islands into smaller fragments to the existence of defects [117]. Doraiswamy, et al., have found that a large fraction (~ 50%) of Ag/Si(100) islands are multiply twinned [114]. It could be possible that multiply twinned islands do decompose during the annealing to produce the higher densities that we observe. However, we very infrequently observe groups of islands that might be expected from decomposition of a larger island into smaller fragments. Clearly further work is required to determine the origin of the anti-coarsening behavior reported here.

During growth temperature annealing, we observed that the size, shape or areal density of small islands does not change with the annealing time. This is understandable because small islands do not exist at elevated temperatures and they only form when samples are rapidly cooled down to room temperature.

Understanding the microstructure of big Ag islands could be critical to explain the observation of the unusual anti-coarsening behavior, future work to determine the crystallographic structure of big Ag/Si(100) islands is necessary. In-situ investigation of big island evolution during growth temperature annealing could provide important clues to understand the physics behind the unusual anti-coarsening behavior.

We proposed the mechanism of small island formation based on careful investigation, but this mechanism was not directly proved. Future work of investigating the formation of small islands, with in-situ high resolution electron microscope or electron diffraction techniques, is essential to understand the physics of this small island formation.

#### **4.2 Tuning the Localized Surface Plasmon of Ag/Si(100) Islands**

The plasmonic properties of Ag islands grown on Si(100) was investigated with spectroscopic ellipsometry. The dependence of the Ag LSPR on the island size, shape and dielectric ambient was studied. We simulated the pseudodielectric functions by incorporating the thin island film theory to the Abeles method. The plasmonic features were identified by comparing the simulated pseudodielectric functions with experimental pseudodielectric functions.

For bare Ag islands grown on Si(100), we believe we have identified the plasmonic features, differences between the experimental pseudodielectric functions for

Ag islands on Si and that for Si, that are associated with two plasmon modes: in-plane parallel and perpendicular mode. The perpendicular mode is associated with the LSPR along the direction perpendicular to the substrate surface. Simulation results suggest that the perpendicular mode of the Ag LSPR is peaked at 3.9 eV, and that it does not significantly shift with the ratio of width to height. The parallel mode is associated with the LSPR along the direction parallel to the substrate surface. The energy of the in-plane parallel mode is lower than that of the perpendicular mode and redshifts with the increase of the width-to-height ratio, as expected from the simulation results. The LSPR energy of the parallel mode is experimentally observed to redshift from 3.1 eV to 2.8 eV as the ratio of width to height increases from 1.4 to 2.2.

Capping the Ag islands with  $\alpha$ -Si layer, the LSPR energy of Ag islands can be tuned from the UV to IR range. The peaks related with the LSPR of Si-capped Ag islands are identified by comparing the experimental pseudodielectric functions from Ag-covered samples with those with no Ag coverage. However, only one plasmonic peak was found for each ensemble of Ag islands. The investigation into the plasmonic properties of bare Ag islands shows that there are two plasmon modes observed for bare Ag islands grown on Si(100). It is difficult to conclude that the plasmon-related peak for capped Ag islands corresponds to which of the two, or both, plasmon modes observed for bare Ag islands without simulating the pseudodielectric functions for  $\alpha$ -Si capped samples.

In the simulation of pseudodielectric functions, the Ag islands were approximated as oblate spheroids. Future work to simulate the pseudodielectric functions with the actual morphology of Ag islands, shapes with rectangular base and height smaller than the basal width, will provide more realistic pseudodielectric functions, from which

additional plasmon modes may be identified. Simulating the pseudodielectric functions for samples capped with the  $\alpha$ -Si layer will be definitely beneficial in understanding the features of experimental pseudodielectric functions for  $\alpha$ -Si capped samples, and in understanding the effect of the  $\alpha$ -Si cap layer on the two plasmon modes observed for samples with bare Ag islands. In addition to the above, the results provide the guidance for utilizing the plasmonic properties of Ag islands in Si-based devices. The method used to determine the plasmonic properties of Ag islands on Si is beneficial to extend the application of spectroscopic ellipsometry from samples with thin films to those with non-uniform 3D islands.

#### **4.3 Growth of the Heterostructure**

The first thing grown on the bare Si(100) substrate is the Si buffer layer. The purpose of growing Si buffer layer is to produce an atomically flat Si(100) surface, which is critical to the success of further growth structure. The thickness of Si buffer layer is  $\sim 100$  nm, which separate the atomically flat surface far from the contaminants on Si wafer to completely eliminate the potential influence of contaminants on the nanostructure growth. AFM measurement shows that our well-developed growth recipe for the Si buffer layer produces an atomically flat surface with atomic steps with a height of 0.3 nm.

Growth of Ge QDs on the Si buffer layer has been investigated in order to determine the growth condition for either solely huts/pyramids or solely coherent domes. Depositing 5.6-6.0 ML of Ge on the Si(100) substrate heated at 550 °C produces huts/pyramids only ensembles. The density of huts/pyramids increases with the coverage of Ge in the range of 5.6-6.0 ML. Coherent domes appear when the coverage of Ge is

higher than 6.0 ML. When Ge coverage increases from 6.3 to 6.8 ML, the density of Ge coherent domes is not affected, but the density of huts/pyramids increases by an order of magnitude. The results of our investigation show that the density of huts/pyramids can be tuned by varying the coverage of Ge below 6.0 ML.

The Ge dot ensemble of solely coherent domes can be produced by depositing Ge at 600 °C. The density of Ge coherent domes can be tuned by varying the Ge coverage. If the coverage of Ge is in the range 5.2- 6.0 ML, the domes-only dot ensemble can be formed at 600°C, and the density of coherent domes increases with Ge coverage.

However, as the Ge coverage increases to 6.3 ML, the Ge dot ensemble is a mixture of huts/pyramids and coherent domes. The fraction of huts/pyramids decreases and that of coherent domes increases as the coverage of Ge continues to increase. When Ge coverage reaches 6.6 ML, about 85% of Ge dots are coherent domes, and the rest of the Ge dots are huts/pyramids. Dislocated domes start to form as Ge coverage is increased above 7 ML.

Our investigation into the Si cap layer atop Ge QDs shows that the morphology of capped Ge dots very sensitively depends on the growth recipe of the Si cap layer. Cross-sectional transmission electron microscopy (XTEM) was performed to determine the morphology of capped Ge dots. The XTEM results show that growing a Si cap layer at the growth temperature of Ge QDs results in Ge dots that are completely flattened out, leaving a uniform planar Ge layer. Therefore, capping Ge dots with Si at dot growth temperature produces a Ge quantum well (QW) structure.

A new growth recipe of Si cap layer was developed to preserve the dot morphology, which is to quench the substrate temperature from Ge QD growth temperature to 500 °C at the moment of finalizing the growth of Ge QD and initializing

the growth of Si cap layer. XTEM results show that the new Si cap layer growth recipe preserves the morphology of Ge dots, and that these Ge dots are apparently flattened during the growth of Si cap layer. The atomically flat surface of the Si cap layer can also be obtained with the new Si cap layer growth recipe when the thickness of the Si cap layer is  $\geq 15$  nm.

The growth of Ag islands on Si cap layer has been investigated, which shows that the density of as-grown Ag islands is systematically dependent on the thickness of Si cap layer. As the Si cap layer decreases from 20 to 10 nm, the density of Ag islands decreases by about two orders of magnitude. However, the density of Ag islands increases by a factor of  $\sim 2$  when the Si cap layer drops from 10 to 5 nm.

Our investigation indicates that the average strain and Ge concentration on the surface of the Si cap layer may contribute to the dependence of Ag island density on the thickness of the Si cap layer. X-ray photoelectron spectroscopy (XPS) measurements show that the Ge fraction on the surface of the Si cap layer due to Ge segregation monotonically increases with the decrease of Si cap layer thickness. Ultra violet (UV) Raman spectroscopy was employed to determine the average strain on the surface of the Si cap layer. The UV Raman results show that the average strain on the surface increases as the thickness of the Si cap layer decreases from 20 to 10 nm. It also shows that the average strain decreases when the Si cap layer drops from 10 to 5 nm. These results suggest that the increase of Ge concentration on the surface of the Si cap layer may contribute to reducing the Ag diffusion activation energy on the Si cap layer, and that the increase of the average strain on the Si cap layer may also contribute to reducing the Ag diffusion activation energy, resulting in a higher diffusion rate and a lower Ag island



density. The combination of Ge concentration and average strain change on the Si cap layer may contribute to the dependence of Ag island density on the thickness of the Si cap layer.

Even though we found that both Ge concentration and average strain on the surface of the Si cap layer affect the density of Ag islands grown on the Si cap layer, we did not determine their individual contribution to the dependence of Ag island density on the thickness of the Si cap layer. Therefore, future work to quantitatively determine the individual effect of the average strain and Ge concentration on Ag nucleation on Si cap layer will be very helpful to understanding the growth physics of Ag islands grown on a strained or alloyed surface.

We developed a new growth recipe for a Si cap layer on top of Ge coherent domes to preserve Ge dome morphology, but no recipe of preserving Ge huts/pyramids was developed. Developing new recipes of growing a Si cap layer to preserve the morphology of Ge huts/pyramids will be useful for exploring the novel electrical and optical properties of the Ge huts/pyramids. The findings about heterostructure growth provide important guidance for integrating 3D Ag islands into Si/Ge based devices.

#### **4.4 Plasmonic Effect of Ag Islands on the Photoluminescence of Ge Dots**

The emission wavelength of Ge QDs is in technologically relevant and low-loss transmission wavelength in optical fibers, 1.5  $\mu\text{m}$  (0.8 eV), but the low luminescence efficiency precludes their applications, so our research project is to solve the problem of this low luminescence efficiency through exploiting Ag plasmonic enhancement. The investigation results of the optical properties of Ge QDs will be given first, followed by the findings about the effect of the LSPR of  $\alpha$ -Si capped Ag islands on the PL of Ge

QDs. Finally, the effect of the LSPR of bare Ag islands on the PL of Ge QDs will be discussed.

The PL of samples with a Si cap layer grown at the same temperatures as Ge QDs were investigated. As discussed above, Ge QDs are completely flattened out during the growth of Si cap layer with this recipe, resulting in uniform Ge QW structures. PL measurements show that only Ge QW related peaks are observed, which again, proves that Ge QDs are completely flattened out if the Si cap layer is grown at the growth temperatures of Ge QDs. The coverage of Ge for the samples with a dot ensemble of solely huts/pyramids is 5.6 ML, and that for the samples with domes-only ensembles is 6.6 ML. The PL peak of Ge QW resulting from huts/pyramids flattening is  $\sim 1.0$  eV, which is 50 meV higher than that of Ge QW resulting from the flattening of coherent domes. This is because the Ge QW thickness resulting from huts/pyramids flattening is thinner than that of Ge QW resulting from coherent domes flattening by 1 ML.

A new growth recipe for a Si cap layer was developed to preserve the morphology of Ge QDs due to the fact that Ge QDs are completely flattened out if the Si cap layer is grown at dot-growth temperature. The new Si cap layer growth recipe is to quench the substrate temperature from dot-growth temperature to 500 °C at the moment of finalizing Ge dot growth and initializing the growth of Si cap layer. As discussed above, the Ge dot survives during Si capping, but is significantly flattened. From PL measurements, Ge dot-related PL lines, both non-phonon assisted (NP) and transverse optical (TO) lines, are observed in addition to the observation of Ge wetting layer (WL) PL peak. However, the PL intensity across the wafer is not uniform. The PL intensity of Si band-gap transition increases and the intensity of Ge dot-related PL peaks decreases as the measuring spots

moves from the wafer center to the wafer edge. This is because the density of Ge QDs is not uniform, resulting from the non-uniform substrate temperature.

To overcome the non-uniform PL problem, a new strategy of depositing Ag was developed, which was to make the boundary between the region covered by Ag islands and the region without Ag coverage very sharp ( $< 30 \mu\text{m}$ ). The whole region covered by Ag islands and enough area of the no-Ag region are in the area with  $r < 15 \text{ mm}$ . PL measurements show that the PL signal is uniform in the area with  $r < 15 \text{ mm}$ . The effect of the LSPR of Ag islands on the PL spectra can be determined by directly comparing the spectra taken from the region covered with Ag islands (2.5 mm from the boundary) with those taken from the region without Ag coverage (2.5 mm from the boundary).

Ge dot-related PL has been investigated for two samples with different dot densities,  $3.5 \times 10^9$  and  $9 \times 10^7 / \text{cm}^2$ . PL spectra show that the intensity of Ge dot-related PL peaks do not scale with the density of Ge QDs, and that the Ge dot-related PL intensity for the sample with low dot density is higher than that for the sample with high dot density. Two factors may contribute to the reduction of Ge dot-related PL intensity for the sample with high dot density. For the sample with high dot density, defects may form when some flattened dots are touching or merging with their neighbors during Si capping, which reduces the radiative recombination rate. Another possibility that may reduce the Ge dot-related PL intensity is that the density of isolated flattened dots is lower than the density of uncapped dots due to the dot merging during Si capping. For these reasons, samples with low Ge dot density were used to study the effect of Ag LSPR on the PL of Ge QDs.

The LSPR energy of Ag islands can be tuned from the UV to IR range by capping them with an  $\alpha$ -Si layer. This could significantly reduce the gap between the LSPR energy of Ag islands and the emission energy of Ge QDs, which may enhance the spontaneous recombination rate of Ge QDs due to Purcell effect. The effect of the LSPR of  $\alpha$ -Si capped Ag islands on the PL of Ge QDs has been investigated.

Our investigation shows that the PL of Si band-gap transition is reduced by  $\sim 25\%$  by the LSPR of  $\alpha$ -Si capped Ag islands. This is because the incident laser intensity on Si is reduced due to the reflection and absorption of the Ag island layer.

The effect of the LSPR of  $\alpha$ -Si capped Ag islands on the PL of Ge QDs has been investigated as a function of the Si cap layer thickness. The results show that the LSPR of Ag islands capped with an  $\alpha$ -Si layer reduces the PL intensity of Ge QDs. For the sample with a 10 nm Si cap layer, the PL intensity of Ge QDs is reduced by  $\sim 40\%$ . The reduction percentage of Ge dot-related PL by the LSPR of  $\alpha$ -Si capped Ag islands increases from 40% to 10% as the thickness of Si cap layer increases from 10 to 20 nm. This reduction percentage is saturated at 10% when the thickness of the Si cap layer increases from 20 to 30 nm. These results suggest that the Si cap layer with a thickness  $\leq 20$  nm provides the distance range between Ag islands and Ge QDs, where quenching happens. The LSPR of  $\alpha$ -Si capped Ag islands has no enhancement effect on the PL of Ge QDs, even though the thickness of the Si cap layer is above 20 nm.

The effect of the LSPR of  $\alpha$ -Si capped Ag islands on the PL of Ge QDs has been investigated as a function of Ag island density. The thickness of the Si cap layer is kept at constant, 15 nm, and the density of Ag islands is varied. Results show that the ratio of Ge

dot-related peak taken from region covered with Ag islands to that taken from region without Ag coverage decreases with the increase of the fraction of substrate surface area covered by Ag islands. As the fraction of substrate surface covered by Ag islands increases, there are more Ag islands getting close to Ge QDs, on average. This results in higher density of plasmonic modes around Ge QDs. Because 15 nm of Si cap layer is in the range where the LSPR of  $\alpha$ -Si capped Ag islands quenches the PL of Ge QDs, the increase of the electromagnetic energy density results in a stronger quenching effect.

Since the LSPR of  $\alpha$ -Si capped Ag islands does not enhance the PL of Ge QDs, we have investigated the effect of the LSPR of bare Ag islands on the PL spectra. The PL of Si band-gap transition is reduced by  $\sim 10\%$  by the bare Ag island layer, which is also a result of the reduction of incident laser intensity on Si by the Ag island layer. The intensity of incident light on the Si substrate, for samples with Ag islands capped with  $\alpha$ -Si, is less than that for samples with bare Ag islands, because the transmission coefficient of the Ag island layer to the green incident laser is reduced when the LSPR energy of Ag islands is redshifted from the UV to IR range caused by capping the Ag island layer with an  $\alpha$ -Si layer.

The effect of the LSPR of bare Ag islands on the PL of Ge QDs has also been investigated as a function of the thickness of the Si cap layer. The results show that the LSPR of bare Ag islands reduces the PL intensity of Ge QDs. The ratio of Ge dot-related peak taken from region covered by Ag islands to that without Ag coverage increases from 10% to 100% as the thickness of the Si cap layer increases from 15 to 25 nm. The peak ratio saturates as the Si cap layer increases from 25 to 30 nm. These results suggest that Si cap layers with thicknesses  $\leq 25$  nm provide the distance range between the Ag islands

and Ge QDs where quenching happens. The LSPR of bare Ag islands has no enhancement effect on the PL of Ge QDs, even though the thickness of Si cap layer is above 25 nm.

The effect of the LSPR of bare Ag islands on the PL of Ge QDs was additionally investigated as a function of Ag island density. The thickness of the Si cap layer was kept constant, 25 nm, and the density of Ag islands was varied. Results also show that the ratio of Ge dot-related peak taken from region covered with Ag islands to that taken from region without Ag coverage decreases with the increase of the fraction of substrate surface area covered by Ag islands. The explanation for  $\alpha$ -Si capped case also applies here.

With highly doped Si wafers, we observed that the optimum enhancement of Ge dot-related PL by the LSPR of bare Ag islands is  $\sim 40\%$ . This enhancement is much smaller than the theoretically predicted optimum enhancement  $\sim 8 \times 10^4$  [132]. This is because there is no clear correlation between Ge QDs and Ag islands, and that the probability for Ag islands grown atop of Ge QDs is  $\sim 1 \times 10^{-3}$ . The reason we don't see the enhancement for lightly doped wafers could be explained by considering the Schottky barrier at the Ag-Si interface. Calculation shows that the depletion width for high doping wafers is  $\sim 3$  nm (less than the thickness of the Si cap layer,  $>10$  nm), and that the depletion width for lightly doped wafers is  $\sim 500$  nm (much larger than the Si cap layer thicknesses,  $< 30$  nm). It is therefore possible that a built-in electric field in the depletion region for lightly doped wafers provides additional path for, or enhances, the non-radiative electron-hole recombination in Ge QDs.

Our results show that the PL of Ge QDs is sensitively dependent on the growth recipe of the Si cap layer, suggesting that future work on optimizing the growth recipe of the Si cap layer by exploring the variation of the substrate temperature and deposition rate would be beneficial. Our results also indicate that the doping level of the Si wafers used may affect the plasmonic effect of Ag islands on the PL of the Ge QDs. Therefore, future work on using even higher doping level of Si wafers may result in a higher enhancement factor. Another direction for future work would be to find a way to template Ag islands with the Ge QDs, because the enhancement can be improved by growing Ag islands directly atop of Ge QDs. Finally, other metallic materials, i.e. Au, Al and Cu, can also be explored, because it is possible that Ge QDs may perfectly template the epitaxial island growth of these materials.

## REFERENCES

- [1] The International Technology Roadmap for Semiconductors: 2014 edition.  
<http://www.itrs.net/>.
- [2] P. Siffert and E. Krimmel, editors , *Silicon Evolution and Future of a Technology* (Springer, 2004).
- [3] R. A. Soref and S. Member, Proc. IEEE **81**, 1687 (1993).
- [4] D. C. Tsui, A. C. Gossard, G. Kaminsky, and W. Wiegmann, Appl. Phys. Lett. **39**, 712 (1981).
- [5] H. L. Störmer, A. C. Gossard, W. Wiegmann, and K. Baldwin, Appl. Phys. Lett. **39**, 912 (1981).
- [6] T. J. Drummond, H. Morkoç, and A. Y. Cho, J. Appl. Phys. **52**, 1380 (1981).
- [7] B. Yu, M. Zebarjadi, H. Wang, K. Lukas, H. Wang, D. Wang, C. Opeil, M. Dresselhaus, G. Chen, and Z. Ren, Nano Lett. **12**, 2077 (2012).
- [8] J. Bardeen and W. Shockley, Phys. Rev. **80**, 72 (1950).
- [9] J. Greil, A. Lugstein, C. Zeiner, G. Strasser, and E. Bertagnolli, Nano Lett. **12**, 6230 (2012).
- [10] K. H. Hong, J. Kim, S. H. Lee, and J. K. Shin, Nano Lett. **8**, 1335 (2008).
- [11] Y. Sun, S. E. Thompson, and T. Nishida, J. Appl. Phys. **101**, 104503 (2007).
- [12] D. J. Lockwood, J. Mater. Sci. Mater. Electron. **20**, S235 (2009).
- [13] W. Zheng, Growth and Study of Si / SiGe Multiple Quantum Wells for Mid-Infrared Applications, Princeton University, 2007.
- [14] R. K. Schaevitz, J. E. Roth, S. Ren, O. Fidaner, and D. A. B. Miller, IEEE J. Sel. Top. Quantum Electron. **14**, 1082 (2008).
- [15] G. Dehlinger, L. Diehl, U. Gennser, and H. Sigg, Science (80). **290**, 2277 (2000).
- [16] E. C. Garnett, M. L. Brongersma, Y. Cui, and M. D. McGehee, Annu. Rev. Mater. Res. **41**, 269 (2011).
- [17] L. Tsakalakos, J. Balch, J. Fronheiser, B. A. Korevaar, O. Sulima, and J. Rand, Appl. Phys. Lett. **91**, 233117 (2007).



- [18] J. Drucker, IEEE J. Sel. Top. Quantum Electron. **38**, 975 (2002).
- [19] J. S. Biteen, N. S. Lewis, H. A. Atwater, H. Mertens, and A. Polman, Appl. Phys. Lett. **88**, 131109 (2006).
- [20] R. A. Soref, J. Vac. Sci. Technol. A **14**, 913 (1996).
- [21] S. A. Chaparro, Y. Zhang, J. Drucker, D. Chandrasekhar, and D. J. Smith, J. Appl. Phys. **87**, 2245 (2000).
- [22] S. A. Chaparro, J. Drucker, Y. Zhang, D. Chandrasekhar, M. R. McCartney, and D. J. Smith, Phys. Rev. Lett. **83**, 1199 (1999).
- [23] M. Tomitori, K. Watanabe, M. Kobayashi, and O. Nishikawa, Appl. Surf. Sci. **76/77**, 322 (1994).
- [24] G. Medeiros-ribeiro, A. M. Bratkovski, T. I. Kamins, D. A. A. Ohlberg, and R. S. Williams, Science. **279**, 353 (1998).
- [25] S. Ketharanathan, S. Sinha, J. Shumway, and J. Drucker, J. Appl. Phys. **105**, 044312 (2009).
- [26] L. Li, S. Ketharanathan, J. Drucker, and M. R. McCartney, Appl. Phys. Lett. **94**, 232108 (2009).
- [27] M. W. Dashiell, U. Denker, C. Müller, G. Costantini, C. Manzano, K. Kern, and O. G. Schmidt, Appl. Phys. Lett. **80**, 1279 (2002).
- [28] E. Palange, G. Capellini, L. Di Gaspare, and F. Evangelisti, Appl. Phys. Lett. **68**, 2982 (1996).
- [29] G. Sun, J. B. Khurgin, and R. A. Soref, Appl. Phys. Lett. **94**, 101103 (2009).
- [30] A. O. Govorov, G. W. Bryant, W. Zhang, T. Skeini, J. Lee, N. A. Kotov, J. M. Slocik, and R. R. Naik, Nano Lett. **6**, 984 (2006).
- [31] J. H. Song, T. Atay, S. Shi, H. Urabe, and A. V Nurmikko, Nano Lett. **5**, 1557 (2005).
- [32] V. N. Lutsikii, Phys. Status Solidi **1**, 199 (1970).
- [33] P. M. Petroff and G. Medeiros-Ribeiro, MRS Bull **20**, 50 (1996).
- [34] A. I. Ekimov and A. A. Onushchenko, JETP Lett. **40**, 1136 (1984).

- [35] A. P. Alivisatos, A. L. Harris, N. J. Levinos, M. L. Steigerwald, and L. E. Brus, *J. Chem. Phys.* **89**, 4001 (1988).
- [36] L. E. Brus, *J. Chem. Phys.* **80**, 4403 (1984).
- [37] M. Danek, K. F. Jensen, C. B. Murray, and M. G. Bawendi, *Chem. Mater.* **8**, 173 (1996).
- [38] F. A. Ponce and D. P. Bour, *Nature* **386**, 351 (1997).
- [39] F. C. Frank and J. H. van der Merwe, *Proc. R. Soc. London. A* **198**, 205 (1949).
- [40] M. Volmer and A. Weber, *Z. Phys. Chem.* **119**, 277 (1926).
- [41] I. N. Stranski and L. Krastanow, *Akad. Wiss. Lit. Mainz Math. Natur. Kl. IIb* **146**, 797 (1938).
- [42] D. J. Eaglesham and M. Cerullo, *Phys. Rev. Lett.* **64**, 1943 (1990).
- [43] A. Vailionis, B. Cho, G. Glass, P. Desjardins, D. Cahill, and J. Greene, *Phys. Rev. Lett.* **85**, 3672 (2000).
- [44] Y. W. Mo, D. E. Savage, B. S. Swartzentruber, and M. G. Lagally, *Phys. Rev. Lett.* **65**, 1020 (1990).
- [45] G. Medeiros-Ribeiro, T. Kamins, D. Ohlberg, and R. Williams, *Phys. Rev. B* **58**, 3533 (1998).
- [46] F. M. Ross, R. M. Tromp, and M. C. Reuter, *Science* **286**, 1931 (1999).
- [47] M. Krishnamurthy, J. S. Drucker, and J. A. Venables, *J. Appl. Phys.* **69**, 6461 (1991).
- [48] J. Drucker, *Phys. Rev.* **48**, 18203 (1993).
- [49] J. Floro, G. Lucadamo, E. Chason, L. Freund, M. Sinclair, R. Twisten, and R. Hwang, *Phys. Rev. Lett.* **80**, 4717 (1998).
- [50] F. M. Ross, J. Tersoff, and R. M. Tromp, *Phys. Rev. Lett.* **80**, 984 (1998).
- [51] T. I. Kamins, G. Medeiros-Ribeiro, D. A. A. Ohlberg, and R. Stanley Williams, *J. Appl. Phys.* **85**, 1159 (1999).
- [52] Y. Zhang and J. Drucker, *J. Appl. Phys.* **93**, 9583 (2003).

- [53] G. Capellini, M. De Seta, and F. Evangelisti, Appl. Phys. Lett. **78**, 303 (2001).
- [54] O. Kienzle, F. Ernst, M. Rühle, O. G. Schmidt, and K. Eberl, Appl. Phys. Lett. **74**, 269 (1999).
- [55] A. Rastelli, E. Müller, and H. von Känel, Appl. Phys. Lett. **80**, 1438 (2002).
- [56] A. Rastelli, M. Kummer, and von H. Känel, Phys. Rev. Lett. **87**, 256101 (2001).
- [57] G. Patriarche, I. Sagnes, P. Boucaud, V. Le Thanh, D. Bouchier, C. Hernandez, Y. Campidelli, and D. Bensahel, Appl. Phys. Lett. **77**, 370 (2000).
- [58] E. Mateeva, P. Sutter, J. C. Bean, and M. G. Lagally, Appl. Phys. Lett. **71**, 3233 (1997).
- [59] O. G. Schmidt and K. Eberl, Phys. Rev. B **61**, 13721 (2000).
- [60] E. Palange, G. Capellini, L. Di Gaspare, and F. Evangelisti, Appl. Phys. Lett. **68**, 2982 (1996).
- [61] J. H. Seok and J. Y. Kim, Appl. Phys. Lett. **78**, 3124 (2001).
- [62] O. G. Schmidt, K. Eberl, and Y. Rau, Phys. Rev. B **62**, 16715 (2000).
- [63] S. K. Zhang, H. Zhu, F. Lu, Z. Jiang, and X. Wang, Phys. Rev. Lett. **80**, 3340 (1998).
- [64] K. Schmalz, I. Yassievich, P. Schittenhelm, and G. Abstreiter, Phys. Rev. B **60**, 1792 (1999).
- [65] C. Miesner, T. Asperger, K. Brunner, and G. Abstreiter, Appl. Phys. Lett. **77**, 2704 (2000).
- [66] C. M. A. Kapteyn, M. Lion, R. Heitz, D. Bimberg, C. Miesner, T. Asperger, K. Brunner, and G. Abstreiter, Appl. Phys. Lett. **77**, 4169 (2000).
- [67] A. I. Yakimov, A. V. Dvurechenskii, and A. I. Nikiforov, JETP Lett. **73**, 598 (2001).
- [68] A. I. Yakimov, A. V. Dvurechenskii, A. I. Nikiforov, A. A. Bloshkin, A. V. Nenashev, and V. A. Volodin, Phys. Rev. B **73**, 115333 (2006).
- [69] A. I. Yakimov, A. I. Nikiforov, and A. V. Dvurechenskii, Appl. Phys. Lett. **89**, 163126 (2006).

- [70] S. Ketharanathan, S. Sinha, J. Shumway, and J. Drucker, J. Appl. Phys. **105**, 044312 (2009).
- [71] O. G. Schmidt, U. Denker, K. Eberl, O. Kienzle, and F. Ernst, Appl. Phys. Lett. **77**, 2509 (2000).
- [72] J. Weber and M. I. Alonso, Phys. Rev. B **40**, 5683 (1989).
- [73] P. Boucaud, S. Sauvage, M. Elkurdi, E. Mercier, T. Brunhes, V. Le Thanh, D. Bouchier, O. Kermarrec, Y. Campidelli, and D. Bensahel, Phys. Rev. B **64**, 155310 (2001).
- [74] O. G. Schmidt, C. Lange, and K. Eberl, Appl. Phys. Lett. **75**, 1905 (1999).
- [75] H. Sunamura, N. Usami, Y. Shiraki, and S. Fukatsu, Appl. Phys. Lett. **66**, 3024 (1995).
- [76] P. Schittenhelm, M. Gail, J. Brunner, J. F. Nützel, and G. Abstreiter, Appl. Phys. Lett. **67**, 1292 (1995).
- [77] V. Le Thanh, P. Boucaud, D. D'Amore, Y. Zheng, D. Bouchier, and J.-M. Lourtioz, Phys. Rev. B **58**, 13115 (1998).
- [78] V. Yam, V. Le Thanh, Y. Zheng, P. Boucaud, and D. Bouchier, Phys. Rev. B **63**, 033313 (2001).
- [79] H. Sunamura, S. Fukatsu, N. Usami, and Y. Shiraki, J. Cryst. Growth **157**, 265 (1995).
- [80] K. Eberl, O. G. Schmidt, R. Duschl, O. Kienzle, E. Ernst, and Y. Rau, Thin Solid Films **369**, 33 (2000).
- [81] J. Wan, G. L. Jin, Z. M. Jiang, Y. H. Luo, J. L. Liu, and K. L. Wang, Appl. Phys. Lett. **78**, 1763 (2001).
- [82] O. G. Schmidt, C. Lange, and K. Eberl, Phys. Status Solidi **215**, 319 (1999).
- [83] K. R. Catchpole, in *2010 Conf. Optoelectron. Microelectron. Mater. Devices* (Ieee, 2010), pp. 121–122.
- [84] S. Pillai, K. R. Catchpole, T. Trupke, and M. A. Green, J. Appl. Phys. **101**, 093105 (2007).
- [85] K. R. Catchpole and a. Polman, Appl. Phys. Lett. **93**, 191113 (2008).

- [86] J. R. Heath, Phys. Rev. B **40**, 9982 (1989).
- [87] T. R. Jensen, M. D. Malinsky, C. L. Haynes, and R. P. Van Duyne, J. Phys. Chem. B **104**, 10549 (2000).
- [88] C. Collazo-Davila, D. Grozea, and L. D. Marks, Phys. Rev. B **80**, 1678 (1998).
- [89] R. J. Wilson and S. Chiang, Phys. Rev. Lett. **59**, 2329 (1987).
- [90] Y. G. Ding, C. T. Chan, and K. M. Ho, Phys. Rev. Lett. **67**, 1454 (1991).
- [91] R. J. Wilson and S. Chiang, Phys. Rev. Lett. **58**, 369 (1987).
- [92] T. Ichinokawa, H. Itoh, A. Schmid, D. Winau, and J. Kirschner, Ultramicroscopy **54**, 116 (1994).
- [93] A. Brodde, D. Badt, S. Tosch, and H. Neddermeyer, J. Vac. Sci. Technol. A **8**, 251 (1990).
- [94] K. Nishimori, H. Tokutaka, T. Tamon, S. Kishida, and N. Ishihara, Surf. Sci. **242**, 157 (1991).
- [95] Y. Borensztein and R. Alamech, Appl. Surf. Sci. **65/66**, 735 (1993).
- [96] H. W. Yeom, I. Matsuda, K. Tono, and T. Ohta, Phys. Rev. B **57**, 3949 (1998).
- [97] Y. Kimura and K. Takayanagi, Surf. Sci. **276**, 166 (1992).
- [98] D. Winau, H. Itoh, A. K. Schmid, and T. Ichinokawa, Surf. Sci. **303**, 139 (1994).
- [99] W. S. Cho, J. Y. Kim, N. G. Park, K. H. Chae, Y. W. Kim, I. W. Lyo, S. S. Kim, D. S. Choi, and C. N. Whang, Surf. Sci. **439**, L792 (1999).
- [100] S. M. Shivaprasad, T. Abukawa, H. W. Yeom, M. Nakamura, S. Suzuki, S. Sato, K. Sakamoto, T. Sakamoto, and S. Kono, Surf. Sci. **344**, L1245 (1995).
- [101] N. G. Park, Y. W. Kim, W. S. Cho, J. Y. Kim, D. S. Choi, K. Jeong, K. H. Chae, and C. N. Whang, Surf. Sci. **414**, L945 (1998).
- [102] M. Hanbucken, M. Futamoto, and J. A. Venables, Surf. Sci. **147**, 433 (1984).
- [103] K. Kimura, K. Ohshima, and M. Mannami, Phys. Rev. B **52**, 5737 (1995).
- [104] D. E. Starr, J. T. Ranney, J. H. Larsen, J. E. Musgrove, and C. T. Campbell, Phys. Rev. Lett. **87**, 106102 (2001).

- [105] D. Winau, H. Itoh, A. K. Schmid, and T. Ichinokawa, *J. Vac. Sci. Technol. B* **12**, 2082 (1994).
- [106] X. F. Lin, K. J. Wan, and J. Nogami, *Phys. Rev. B* **47**, 13491 (1993).
- [107] X. F. Lin, K. J. Wan, and J. Nogami, *Phys. Rev. B* **49**, 7385 (1994).
- [108] G. G. Hembree and J. A. Venables, *Ultramicroscopy* **47**, 109 (1992).
- [109] J. C. Glueckstein, M. M. R. Evans, and J. Nogami, *Phys. Rev. B* **54**, R11066 (1996).
- [110] J. Tersoff and R. M. Tromp, *Phys. Rev. Lett.* **70**, 2782 (1993).
- [111] F. K. LeGoues, M. Liehr, M. Renier, and W. Krakow, *Philos. Mag. Part B* **57**, 179 (1988).
- [112] T. Ichinokawa, H. Itoh, A. Schmid, D. Winau, and J. Kirschner, *J. Vac. Sci. Technol. B* **12**, 2070 (1994).
- [113] Y. W. Kim, N. G. Park, W. S. Cho, K. H. Chae, C. N. Whang, K. S. Kim, S. S. Kim, and D. S. Choi, *Surf. Sci.* **396**, 295 (1998).
- [114] N. Doraiswamy, G. Jayaram, and L. D. Marks, *Phys. Rev. B* **51**, 10167 (1995).
- [115] H. Tokutaka, K. Nishimori, N. Ishihara, and T. Seki, *Jpn. J. Appl. Phys.* **25**, 1584 (1986).
- [116] D. Kong and J. Drucker, *J. Appl. Phys.* **114**, 144310 (2013).
- [117] B. Q. Li, W. Swiech, J. A. Venables, and J. M. Zuo, *Surf. Sci.* **569**, 142 (2004).
- [118] J. A. Venables, G. D. T. Spiller, and M. Hanbucken, *Reports Prog. Phys.* **47**, 399 (1984).
- [119] J. A. Venables, *Surf. Sci.* **299/300**, 798 (1994).
- [120] G. Mie, *Ann. Phys. Berlin* **25**, 377 (1908).
- [121] J. S. Biteen, L. A. Sweatlock, H. Mertens, N. S. Lewis, A. Polman, and H. A. Atwater, *J. Phys. Chem. C* **111**, 13372 (2007).
- [122] X. Xu and M. B. Cortie, *Adv. Funct. Mater.* **16**, 2170 (2006).
- [123] A. Brioude, X. C. Jiang, and M. P. Pileni, *J. Phys. Chem. B* **109**, 13138 (2005).

- [124] Y. Y. Yu, S. S. Chang, C. L. Lee, and C. R. C. Wang, *J. Phys. Chem. B* **101**, 6661 (1997).
- [125] C. Noguez, *J. Phys. Chem. C* **111**, 3806 (2007).
- [126] L. D. Landau and E. M. Lifshitz, *Electrodynamics Of Continuous Media* (Oxford, New York, Pergamon Press., 1960).
- [127] G. Xu, M. Tazawa, P. Jin, S. Nakao, and K. Yoshimura, *Appl. Phys. Lett.* **82**, 3811 (2003).
- [128] A. Urbanićzyk, F. W. M. van Otten, and R. Nötzel, *Appl. Phys. Lett.* **98**, 243110 (2011).
- [129] H. A. Atwater and A. Polman, *Nat. Mater.* **9**, 205 (2010).
- [130] K. Okamoto, I. Niki, A. Shvartser, Y. Narukawa, T. Mukai, and A. Scherer, *Nat. Mater.* **3**, 601 (2004).
- [131] K. Kneipp, Y. Wang, H. Kneipp, L. T. Perelman, I. Itzkan, R. R. Dasari, and M. S. Feld, *Phys. Rev. Lett.* **78**, 1667 (1997).
- [132] G. Sun, J. B. Khurgin, and R. A. Soref, *Appl. Phys. Lett.* **94**, 101103 (2009).
- [133] H. Mertens, A. F. Koenderink, and A. Polman, *Phys. Rev. B* **76**, 115123 (2007).
- [134] C. Nahm, D. R. Jung, S. Nam, H. Choi, S. Hong, T. Hwang, T. Moon, and B. Park, *Appl. Phys. Express* **6**, 052001 (2013).
- [135] E. M. Purcell, H. C. Torrey, and R. V. Pound, *Phys. Rev.* **69**, 37 (1946).
- [136] D. R. Jung, J. Kim, S. Nam, C. Nahm, H. Choi, J. I. Kim, J. Lee, C. Kim, and B. Park, *Appl. Phys. Lett.* **99**, 041906 (2011).
- [137] A. E. Ragab, A. S. Gadallah, T. Da Ros, M. B. Mohamed, and I. M. Azzouz, *Opt. Commun.* **314**, 86 (2014).
- [138] E. Dulkeith, M. Ringler, T. A. Klar, J. Feldmann, A. Muñoz Javier, and W. J. Parak, *Nano Lett.* **5**, 585 (2005).
- [139] Z. Gueroui and A. Libchaber, *Phys. Rev. Lett.* **93**, 166108 (2004).
- [140] J. R. Arthur, *J. Appl. Phys.* **39**, 4032 (1968).

- [141] K. A. Reinhardt and W. Kern, *Handbook of Silicon Wafer Cleaning Technology*, 2nd ed. (William Andrew, Norwich, NY, 2008).
- [142] N. Herbots, J. Shaw, Q. Hurst, M. Grams, R. Culbertson, D. J. Smith, V. Atluri, P. Zimmerman, and K. Queeney, *Mater. Sci. Eng. B* **87**, 303 (2001).
- [143] [Http://cmrf.research.uiowa.edu/scanning-Electron-Microscopy](http://cmrf.research.uiowa.edu/scanning-Electron-Microscopy).
- [144] J. Vlieger and D. Bedeaux, *Thin Solid Films* **69**, 107 (1980).
- [145] T. W. H. Oates, H. Wormeester, and H. Arwin, *Prog. Surf. Sci.* **86**, 328 (2011).
- [146] M. Bohmer, E. Zeeuw, and G. Koper, *J. Colloid Interface Sci.* **197**, 242 (1998).
- [147] E. S. Kooij, H. Wormeester, E. A. M. Brouwer, E. Van Vroonhoven, A. Van Silfhout, and B. Poelsema, *Langmuir* **18**, 4401 (2002).
- [148] D. Bedeaux and J. Vlieger, *Physica* **67**, 55 (1973).
- [149] P. A. Bobbert and J. Vlieger, *Physica A* **147**, 115 (1987).
- [150] M. Valamanesh, Y. Borensztein, C. Langlois, and E. Lacaze, *J. Phys. Chem. C* **115**, 2914 (2011).
- [151] Y. Zhang, *Island Evolution of Self-Assembled Germanium / Silicon ( 100 ) Quantum Dots*, Arizona State University, 2002.
- [152] S. Ketharanathan, *Electron Charging in Epitaxial Germanium Quantum Dots on Silicon ( 100 )*, Arizona State University, 2007.
- [153] M. Gavelle, E. M. Bazizi, E. Scheid, P. F. Fazzini, F. Cristiano, C. Armand, W. Lerch, S. Paul, Y. Campidelli, and A. Halimaoui, *J. Appl. Phys.* **104**, 113524 (2008).
- [154] J. C. Tsang, P. M. Mooney, F. Dacol, and J. O. Chu, *J. Appl. Phys.* **75**, 8098 (1994).
- [155] J. Groenen, R. Carles, S. Christiansen, M. Albrecht, W. Dorsch, H. P. Strunk, H. Wawra, and G. Wagner, *Appl. Phys. Lett.* **71**, 3856 (1997).
- [156] H. Chen, Y. K. Li, C. S. Peng, H. F. Liu, Y. L. Liu, Q. Huang, J. M. Zhou, and Q.-K. Xue, *Phys. Rev. B* **65**, 233303 (2002).
- [157] S. Nakashima, T. Mitani, M. Ninomiya, and K. Matsumoto, *J. Appl. Phys.* **99**, 053512 (2006).



- [158] F. Pezzoli, E. Bonera, E. Grilli, M. Guzzi, S. Sanguinetti, D. Chrastina, G. Isella, H. von Känel, E. Wintersberger, J. Stangl, and G. Bauer, J. Appl. Phys. **103**, 093521 (2008).
- [159] D. A. Shirley, Phys. Rev. B **5**, 4709 (1972).
- [160] A. W. Dweydari and C. H. B. Mee, Phys. Status Solidi **27**, 223 (1975).
- [161] A. Novikov, Solid. State. Electron. **54**, 8 (2010).
- [162] B. L. Smith and E. H. Rhoderick, Solid. State. Electron. **14**, 71 (1971).